UNIVERSITY OF
BIRMINGHAM

MARITIME FORWARD SCATTER RADAR: DATA COLLECTION AND CLUTTER ANALYSIS

by

Kalin Hristov Kabakchiev

A thesis submitted to the School of Electronic, Electrical and System Engineering of The University of Birmingham
for the degree of
DOCTOR OF PHILOSOPHY

December 2014

Abstract

This thesis is the result of study into development, experimental testing and clutter analysis in a Forward Scatter Radar (FSR) designed to detect low reflectivity maritime targets at low grazing angles. The concept of such kind of maritime system is presented; its advantages for surveillance applications are described. Scattering of Electromagnetic (EM) Waves over the sea surface at different radar configurations is outlined with the focus made on forward scattering and appropriate sea clutter models. Phenomenology of the signals in FSR is examined and explained. The development of an experimental FSR hardware operating in X- and K- frequency bands for target detection and clutter analysis and its performance are described in details. It follows with the comprehensive analysis on the measured sea clutter which includes study of influence of a large number of parameters of the radar and sea conditions on the clutter spectral and statistical properties. Finally preliminary analysis of radio frequency (RF) target signatures made with the prototype radar is presented.

Acknowledgements

Firstly, I would like to express my gratitude to my supervisors Prof. M. Cherniakov and Dr. M. Gashinova for the inspiration, guidance and support they provided me throughout the whole process of my studies and research.

I would also like to thank Dr. E. Hoare, Dr. V. Sizov and Mr. L. Daniel for the support, knowledge and skills that I acquired from them.

Glossary of Abbreviations

ACC	Autonomous Cruise Control
ADC	Analog-to-Digital Convertor
AEW	Airborne Early Warning
ATC	Air Traffic Control
ATDT	Automatic Target Detection and Tracking
AWG	Arbitrary Waveform Generator
BPF	Band Pass Filter
BRSC	Bistatic Radar Cross Section
CDF	Cumulative Distribution Function
CLT	Central Limit Theorem
DPO	Digital Phosphor Oscilloscope
DRC	Doppler Receiver Channel
EEZ	Effective Economic Zone
EM	Electromagnetic
FS	Forward Scattering
FS CS	Forward Scatter Cross Section
FSML	Forward Scatter Main Lobe
FSR	Forward Scatter Radar
GIT	Georgia Institute of Technology
HF	High Frequency
HPF	High Pass Filter
ISAR	Inverse Synthetic Aperture Radar
LOS	Line Of Sight
MLE	Maximum Likelihood Estimation
MIMO	Multiple-Input and Multiple-Output
MISL	Microwave Integrated Systems Laboratory
NMRCS	Normalised Monostatic Radar Cross Section
NRCS	Normalised Radar Cross Section
OTH	Over-the-Horizon Radar
PDF	Probability Density Function
PO	Physical Optics

PRF	Pulse Repetition Frequency
PSD	Power Spectral Density
PTD	Physical Theory of Diffraction
RF	Radio Frequency
ROTHR	Raytheon's Relocatable Over-the-Horizon Radar
RCS	Radar Cross Section
Rx	Receiver
SAR	Synthetic Aperture Radar
SCR	Signal-to-Clutter Ratio
SNR	Signal-to-Noise Ratio
SS	Sea State
T/R	Transmit/Receive Device
TLR	Target-to-Leakage Ratio
TRP	Two-Ray Path
Tx	Transmitter
VSWR	Voltage Standing Wave Ratio
WMO	World Meteorological Organisation

List of Symbols

α	Azimuth of the target
A	Effective aperture of the receiving antenna
A_{DP}	Phase Signature Amplitude for the Direct Path Signal
A_{TG}	Phase Signature Amplitude for the Scattered Signal
B_n	Receiver bandwidth
β	Bistatic angle
c	Speed of light (c = 3.10^8 m/s)
D	Baseline Length
D_{ed}	Effective Target Dimension
Δf_M	Fluctuation Spectrum Bandwidth
$\Delta\tau_M$	Coherent Analysis Time
$\Delta\tau_{FS}$	Target Visibility Time in FSR
E_{dir}	Intensity of the electric component of the direct field
E_{scat}	Intensity of the electric component of the scattered field
E_S	Electric component of the shadow field
E_Σ	Full scattered field
f_B	Bistatic Doppler shift
f_d	Doppler frequency shift
f_0	Transmitted frequency
f_{Tgt}	Bistatic Doppler shift caused by the target motion
F	Propagation Gain
h_R	Receiver antenna height
h_T	Transmitter antenna height

h_{tg} Target height

v Target speed

v_r Radial velocity of the target

ν_{tg} Speed of Moving Target

λ Wavelength of the radio waves

σ Radar Cross Section

σ^0 Normalised Radar Cross Section

σ_{tot} Total Scattering Cross Section

δ Elevation of the target

δ_T Aspect angle of Tx

δ_R Aspect angle of Rx

N Overall noise power

G_t Transmitted antenna gain

G_r Received antenna gain

k The wave number defined by $k = 2\pi/\lambda$

L_a Propagation loss

τ Radar Pulse Width

$L_{T\text{-}tg}$ Transmitter-to-target propagation loss

$L_{tg\text{-}R}$ Target-to-receiver propagation loss

ρ Signal-to-noise ratio

$P_{coherent}$ Mean Value of the Received Signal

$P_{coherent}$ Mean Signal Variance

P_r	Power returning to the receiving antenna
P_t	Transmitted power
R	Range to the target in meters
R_t	Range from Tx to target
R_r	Range from Rx to target
R_X	Receiver Position
ΔR	Range Resolution
S_{DP}	Direct Path Signal
S_{RI}	Receiver Input
S_{TG}	Scattered Target Signal
$\underline{O}$	Order
t	Time of Direct Signal Arrival at the Receiver
t_{sh}	Delay Time of the Signal from Moving Target
ΔT	Round-trip time delay
T_X	Transmitter position
T_s	System noise temperature in Kelvin
T_V	Target Visibility Time
V	Magnitude of velocity vector of the target
V_R	Receiver's velocity vector of magnitude
V_T	Transmitter's velocity vector of magnitude
ω_0	Carrier Frequency
ω_d	Doppler angular Frequency
ω_{dp}	Doppler Frequency Shift of the Moving Target.
θ	Angle made by the target trajectory and the line joining radar and target
x, y, z	Cartesian coordinates

Table of Contents

List of Figures

List of Tables

Chapter 1 Introduction

1.1 Radar Basic Operation and Definition.

In the past the main goal of Radars have been to detect target and to measure range to it. As a matter of fact, Radar is an acronym for Radio Detection and Ranging [1]. But much has been improved in the development and purpose of modern radar systems. Present-day radars are incredibly complex tranducers/computer devices which detect various objects in space and establish their current position but they could also identify, track, image and classify these objects. These systems are also robust to interference and countermeasures. Such radar systems are used in various applications such as traditional military radar, civilian radar for tracking aircrafts and vehicles, earth resources monitoring, autonomous cruise control systems (ACC), and many more.

1.1.1 General Properties of Radar Systems

A basic modern radar includes Transmitter (Tx), Receiver (Rx), antenna and signal processor which is an essential sub-unit for detection and localisation of targets. Depending on the transmitter-receiver topology, radar systems could be divided in a few groups. Monostatic radar is the most common type of radar and in this configuration the transmitter and receiver are co-located [2], [3] as shown on Figure 1.1.1 (a) where R is the range to the target. Bistatic radar is a category of radar which encompasses one transmitter and one receiver device separated in space as shown on Figure 1.1.1 (b). The angle that is formed between the transmitter, target

and receiver is called bistatic angle β, the range from the transmitter to the target is R_t and the distance from the target to the receiver is labelled R_r [4], [5]. Multistatic radar is the type of radar which uses multiple transmitting points and numerous receiving systems separated in space. The collected data from all the receivers can be processed jointly or independently. Multistatic radar is often referred to as 'multisite' or 'netted' radar and according to [6] the definition of 'multistatic radar' is not completely consistent within the literature of the subject.

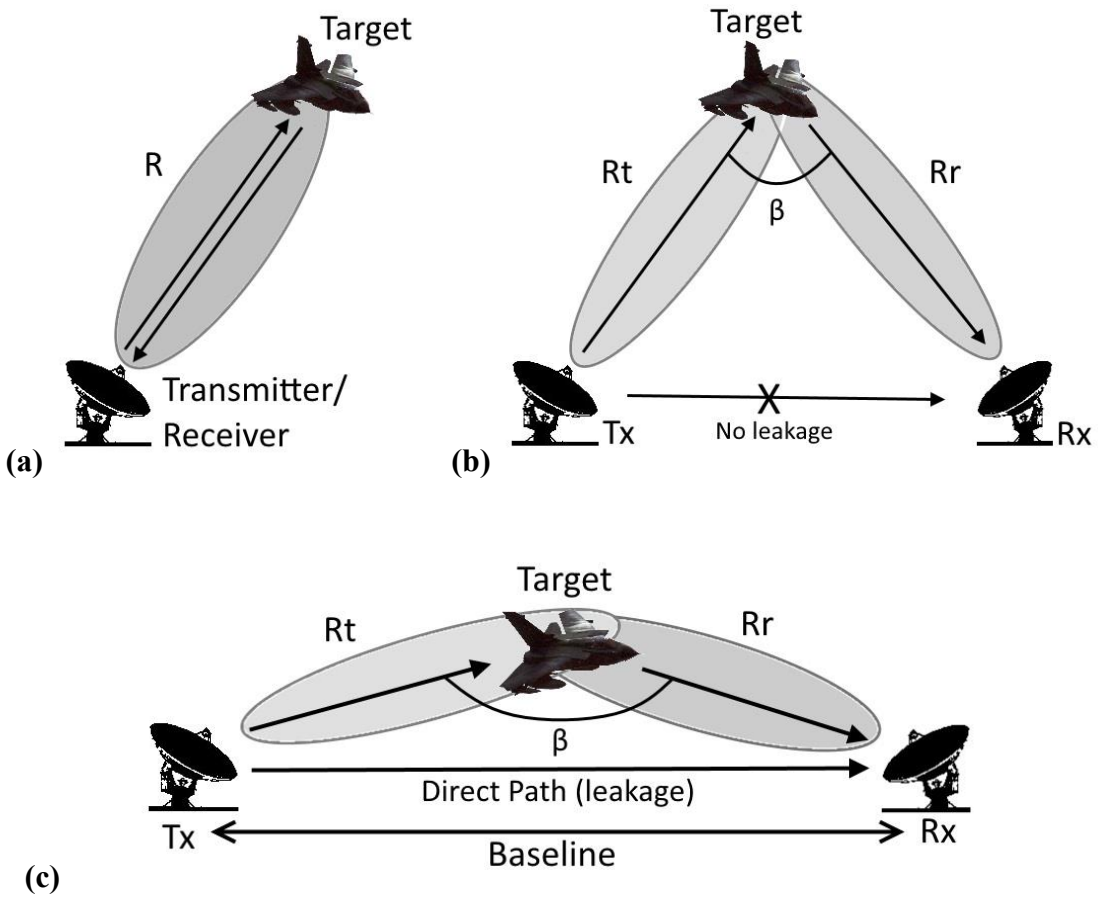

Figure 1.1.1 (a) Monostatic radar (b) Bistatic radar and (c) Forward scatter radar

MIMO radar systems is a novel radar method in which MIMO stands for Multiple Input Multiple Output. Such kind of system uses multiple antennas where each transmit antenna radiates an arbitrary waveform independently of the other transmitting antennas and each

receive antenna can receive these signals. Due to the different wave forms, the echo signals can be re-assigned to the single transmitter. MIMO radar systems can be used to improve the spatial resolution, and they provide a substantially improved immunity to interference [7].

This thesis is dedicated only to a special case of bistatic radar when the bistatic angle is equal or near 180 degrees ($\beta \approx 180°$) and the target dimensions are larger than the transmitted wavelength [5]. In this scenario the radar system uses the diffraction phenomenon [8], [9]. The system which uses this phenomenon is called the Forward Scatter Radar (FSR) shown on Figure 1.1.1 (c) and this thesis is dedicated to study the FSR phenomenology. The FSR has been widely discussed in [9] and its characteristics will be explained in details later in this chapter.

1.1.2 Monostatic Radar Block Diagram and Operation

A typical monostatic radar includes transmitter, receiver, antenna and signal processor [1], [10], [11]. Following the block diagram on Figure 1.1.2, the transmit device generates electromagnetic (EM) waves and then passes them to the antenna which emits these waves in space. In monostatic radar where only one antenna is used for transmitting and receiving radio frequency (RF) signals, a transmit/receive (T/R) device is used in the radar configuration.

The purpose of T/R (usually circulator or switch) is to connect both Tx and Rx with the antenna and to isolate the transmitted high power signal from entering into the very sensitive receiving unit. Once the EM signal is transmitted and propagates the region of interest, a portion of this signal is intercepted by a reflective target. Target reflects the EM waves in all directions including the direction to the receive antenna. Besides the targets of interest, RF signals are reflected by other surfaces and objects. These unwanted signals are called clutter.

The receive antenna collects a certain amount of EM waves from the targets of interest and from the unwanted objects and surfaces. The portion of energy that will be reradiated to the receive antenna depends on the physical characteristics of the radiated object or surface and the Rx antenna. Once the EM signal has reached the receiver antenna, it passes to the receiver unit.

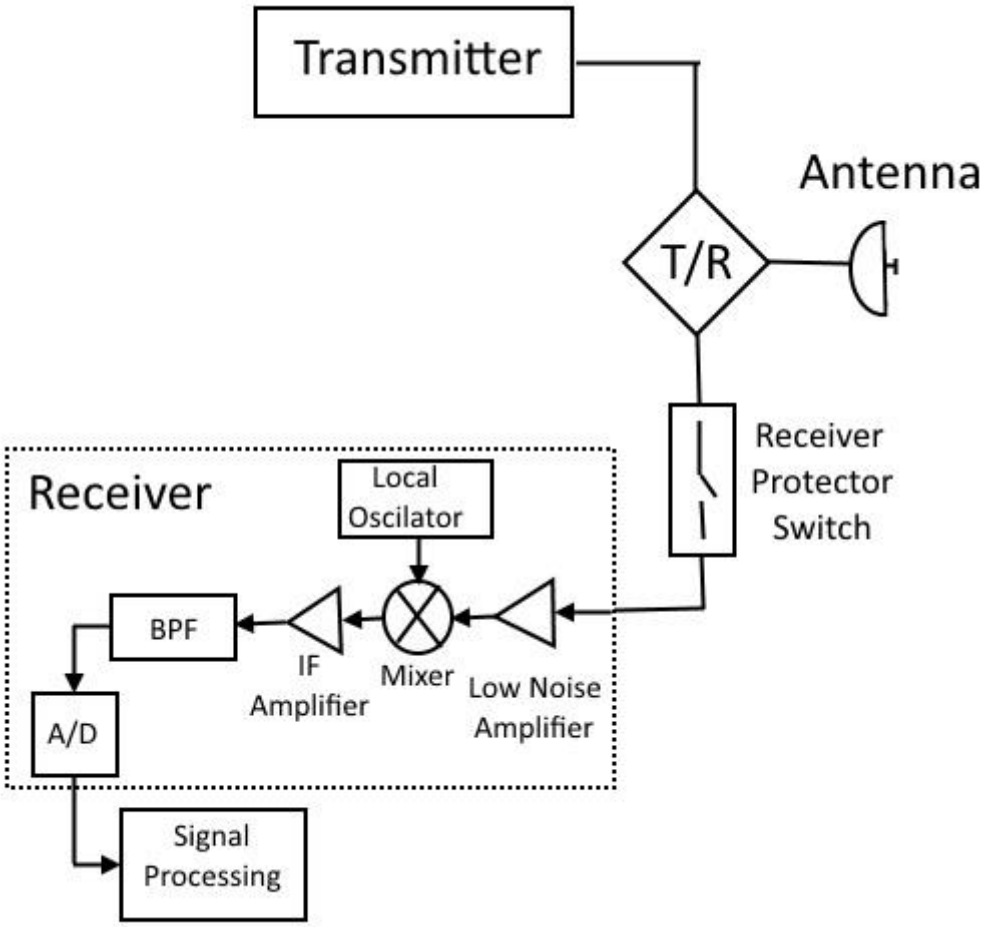

Figure 1.1.2 Block diagram of monostatic radar

The main function of superheterodyne receiver module is to amplify the received signal, then to convert it to intermediate frequency and to pass it to the band pass filter (BPF). The receiver is used for separating and removing the carrier frequency from the modulated target return

signal. Next step in the receiver box is to pass the signal trough an analog-to-digital convertor (ADC) which will allow data to be analysed by signal processor. In former radar systems the received data is presented on displays/indicators and analysis and target recognition is performed by human operators. In modern radars automatic target detection and tracking (ATDT) and air traffic control (ATC) are performed by computer system but still display targets for human recognition.

Despite the fact that radars have evolved so much during the past few decades, still one of the most important characteristics of radar is its ability to measure distance. The simplest way to express the range to a detected object is by taking into account the time, that is needed for a EM wave to propagate from the transmitter, reflect from the target and get back to the receiver unit. This relationship is expressed by Equation (1.1) [1], [9], [11]:

$$R = \frac{c\Delta T}{2} \tag{1.1}$$

where c is the speed of light (c = 3.10^8 m/s) and ΔT is the round-trip time delay.

1.1.3 The Radar Equation

The radar range equation (hereafter referred to as the radar equation) represents the fundamental relationship between the radar characteristics, the target and the transmitted and received signal [1], [9]–[11]. By using the fundamental range equation which has been consider in [9], [12], the power P_r returning to the receiving antenna is expressed by:

$$P_r = \frac{P_t G_t G_r \lambda^2 \sigma}{(4\pi)^3 R_t^2 R_r^2} \tag{1.2}$$

This power depends on the initial transmitted power P_t, the transmitted and received antenna gain G_t and G_r, λ is the wavelength of the radio waves, the reflective characteristics of the target (defined as the radar-cross-section (RCS) (σ) and the range to the target R (in cases where the radar system is monostatic $R_t = R_r = R$ and $G_t = G_r$). It is important to note that the equation considers bistatic radar configuration for propagation in free space.

Equation (1.2) does not take into account miscellaneous losses which are always present in radar. So that in Equation (1.3) extra dimensionless factor $L_a < 1$ is used.

$$P_r = \frac{P_t G_t G_r \lambda^2 \sigma L_a}{(4\pi)^3 R_t^2 R_r^2} \tag{1.3}$$

There are two main sources of noise in the receiving system according to [4], [12]: environmental noise received by the receiving antenna and receiving system internal noise.

In the latter case the overall noise power is:

$$N = kT_S B_n \tag{1.4}$$

where k is the Boltzmann constant, T_s is the system noise temperature in Kelvin and B_n is the receiver bandwidth.

Following the range Equation (1.3), the theoretical maximum range can be calculated if radar parameters are known. For accurate calculation of maximum range, it is important to include in the equation the Signal-to-Noise ratio (SNR) referred to the receiving input:

$$\rho = \frac{P_r}{N} = \frac{P_t G_t G_r \lambda^2 \sigma L_a}{(4\pi)^3 R_t^2 R_r^2 k T_S B_n} \tag{1.5}$$

where ρ is the signal-to-noise ratio. For desired target detection performance, ρ should be less than a certain value ρ_r [9].

Depending on the type of the radar two maximum range equations are shown below [9]:

- bistatic radar equation

$$(R_t R_r)max = \sqrt{\frac{P_t G_t G_r \lambda^2 \sigma L_a}{(4\pi)^3 \rho_r k T_s B_n}} \tag{1.6}$$

- monostatic radar equation

$$R_{max} = \sqrt[4]{\frac{P_t G_t G_r \lambda^2 \sigma L_a}{(4\pi)^3 \rho_r k T_s B_n}} \tag{1.7}$$

1.1.4 Radar Resolution

The definition of monostatic radar resolution is the same as for bistatic radar resolution and more specifically it is the degree to which two or more targets which are roughly equal amplitude and arbitrary persistent phase, may be separated in one or more dimensions, such as range, angle, velocity (Doppler) and acceleration [8], and be still distinguished from each other. In the monostatic scenario, the target separation is referenced to the radar-to-target line of sight (LOS) and in the bistatic case, it is related to the bistatic bisector [8]. In both type of radars range resolution, a reasonable degree of separation between two target returns at the receiver is expressed by $c\tau/2$, where τ is the radars pulse width. In monostatic radar the range resolution equation is defined as:

$$\Delta R = \frac{c\tau}{2} \tag{1.8}$$

The bistatic physical range resolution (also called bistatic range cell) is explained as the separation, ΔR, between two confocal concentric isorange contours shown on Figure 1.1.3. It can be observed from the segregation between the two contours that it varies depending on the target location [9].

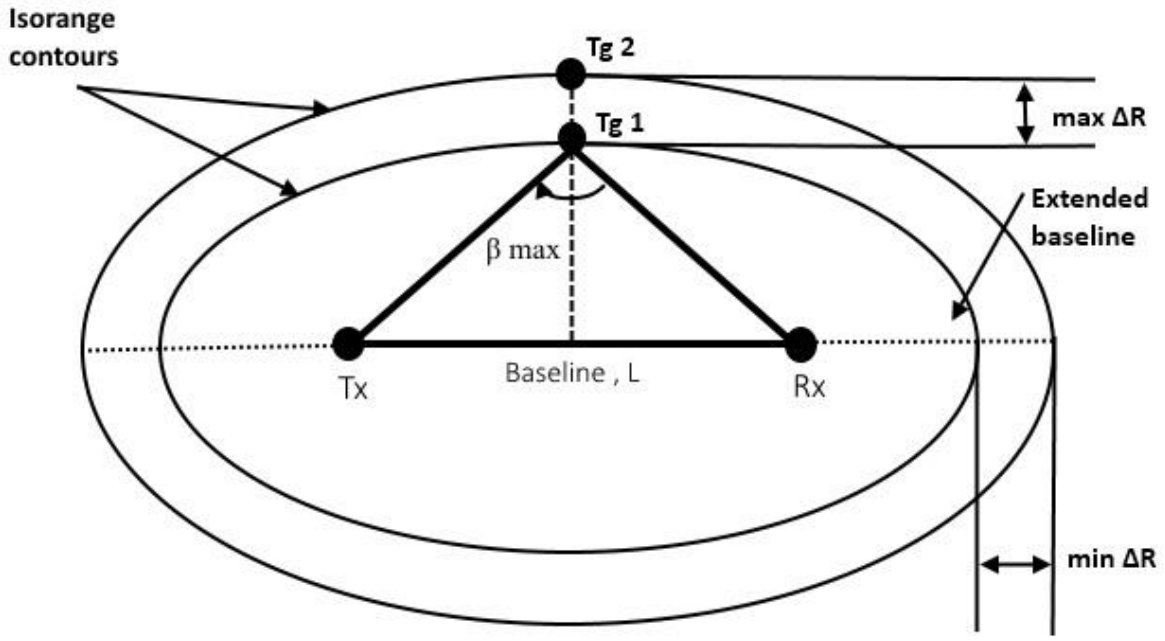

Figure 1.1.3 Geometry for bistatic range resolution

The separation is maximum at the bisector of the baseline and minimum at the extended baseline. The bistatic physical range resolution, ΔR, is expressed as in [9]:

$$\Delta R = \frac{c\tau}{2\cos(\beta/2)} \tag{1.9}$$

Following Equation (1.8) it can be seen that the bistatic range resolution width degrades by $\cos(\beta/2)$ in comparison with monostatic radar. In the cases when β = 0, the bistatic radar

range resolution width is equal to the width of the monostatic one and in such situations the bistatic radar is known to have pseudo-monostatic geometry.

As described in References [4], [8], [10], [13] when bistatic radar operates exactly at $\beta = 180$,or forward scatter, it provides information only that the target is somewhere between the transmitter and receiver. Target range is unspecified; target Doppler shift is zero for all target velocity vectors; and both Doppler and range resolution are lost.

1.1.5 Target Radar Cross Section

Radar cross section (RCS) characterises the electrical dimensions and ability of a target to re-radiate radar EM signal in the direction of the receiver. The RCS relates to target characteristics because it is a ratio and it is not taking in to account the transmit power, receiver sensitivity and the range or position of the transmitter and receiver as discussed in [1]. The target radar cross section can be calculated according to Equation (1.10) which is defined by the Institute of Electrical and Electronics Engineers (IEEE) [14] as:

$$\sigma = \lim_{R \to \infty} 4\pi R^2 \frac{\lfloor E^{Sc} \rfloor^2}{\lfloor E^{In} \rfloor^2} \tag{1.10}$$

where R the distance between target and radar is, E^{Sc} is the scattered electric field and E^{In} is the strength of the incident field at the target. This equation allows the calculation of RCS of objects with simple geometry such as sphere, infinite cylinder, flat plate and others. The cross sections of simple scattering objects are of interests not only because of the insight they give to the scattering properties of more complex radar targets, but they are characteristic of such important targets such as meteorological objects such as rain, snow and ice and certain classes of space objects [10]. But for most radar targets such as aircrafts and ships, this method of RCS

evaluation is ineffective [1], [4], [9] and does not bear a simple relationship to the physical area, except that the larger the target size, the larger the cross section is likely to be. A complex target such as ships, aircraft, cities, and terrain may be considered as comprising a large number of independent objects that scatter energy in all directions. The RCS of such complex targets are complicated functions of the viewing aspect and the radar frequency. Target cross sections may be calculated with the help of computers or be measured experimentally. Also target CS could be measured with full scale targets, but it is easier to use scale models at the proper scaled frequency. Most radar cross section analysis concerning complex targets are acquired by this manner.

In general the target radar cross section depends on:

- Position of transmitter/receiver relative to the target.
- The radar transmitter frequency.
- Object physical geometry and material composition.
- Transmitter and receiver polarisation.

Three cases of radar cross section are defined which based on: (1) backscattering (Monostatic radar); (2) bistatic scattering (Bistatic radar) and (3) forward scattering (Forward Scatter Radar). Forward scatter radar cross section is discussed further in this chapter and is in the focus of this research.

1.2 Doppler Relationships

As previously discussed radar is a device that detects the presence of objects and determines their location in space by transmitting EM energy and observing the return echo. Pulse radar operation has been reviewed in Section 1.1.2 where the radar transmits a relatively short burst of EM wave, after which the receiver is turned on to listen for the echo. The echo not only indicates that a target is present, but the time that elapses between the transmission of the pulse and the receipt of the echo is a measure of the distance to the target.

Another mode that the radar transmitter can work is continuously (also called continuous wave) rather than pulsed if the strong transmitted signal can be separated from the weak echo. The weak received echo signal power could be as little as 10^{-18} that of the transmitted power. A method for splitting the weak received signal from the strong transmitted one is by using separate transmit and receive antennas but this is not very successful because of isolation issues. A possible technique for separating the received signal from the transmitted signal when there is relative motion between radar and target is based on recognising the change in the echo-signal frequency caused by the Doppler effect as described in [10].

It is well known/observed in the fields of acoustics and optics that if either the source of oscillation or the observer of the oscillation is in motion, then an apparent shift in frequency will result [10]. This is the Doppler frequency and is the basis of the continuous- wave (CW) radar. Following the previous discussions, Equation (1.11) presents the Doppler angular frequency ω_d.

$$\omega_d = 2\pi f_d = \frac{d\varphi}{dt} = \frac{4\pi}{\lambda}\frac{dR}{dt} = \frac{4\pi v_r}{\lambda} \tag{1.11}$$

where f_d is the Doppler frequency shift and v_r is the relative (or radial) velocity of the target with respect to radar. The Doppler frequency shift is

$$f_d = \frac{2v_r}{\lambda} = \frac{2v_r f_0}{c} \tag{1.12}$$

where f_0 is the transmitted frequency.

The relative velocity's equation would be $v_r = v\cos\theta$, where v is the target speed and θ is the angle made by the target trajectory and the line joining radar and target. When $\theta = 0°$, the Doppler frequency is maximum and when $\theta = 90°$ (the trajectory is perpendicular to LOS), the Doppler is zero [10].

In bistatic radar configuration, it is observed specific example of the Doppler Effect called Bistatic Doppler shift. The definition of bistatic Doppler, or Doppler shift, f_B, is the time rate of change of the total path length of the scattered signal, normalised by the wavelength λ [8], [10]. The total path length is the distance sum, $R_t + R_r$,

$$f_B = \frac{1}{\lambda}\left[\frac{d}{dt}(R_t + R_r)\right] = \frac{1}{\lambda}\left[\frac{dR_t}{dt} + \frac{dR_t}{dt}\right] \tag{1.13}$$

Figure 1.2.1 presents the geometry for bistatic Doppler when the transmitter, receiver and target are moving. The velocity vector of the target has magnitude V and aspect angle δ referenced to the bistatic bisector as described in [8]. The transmitter and receiver have velocity vectors of magnitude V_T and V_R and respectively aspect angles δ_T and δ_R.

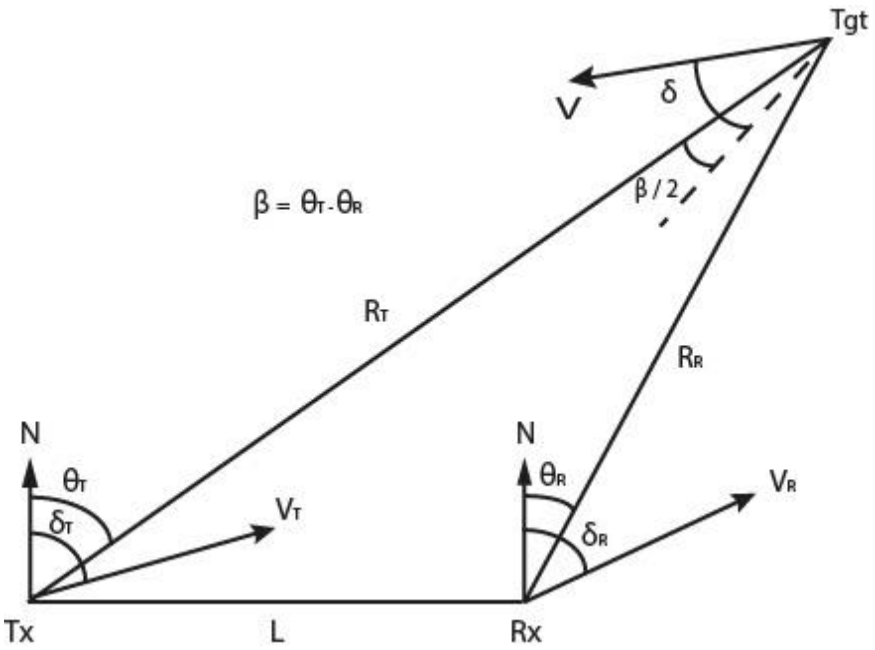

Figure 1.2.1 Geometry of bistatic doppler

In scenarios when the Tx and Rx are fixed ($V_T = V_R = 0$) and the target is moving ($V \neq 0$), the target's bistatic Doppler at the Rx site is:

$$f_B = f_{Tgt} = (V/\lambda)[\cos(\delta - \beta/2) + \cos(\delta + \beta/2)] = (2V/\lambda)\cos\delta\cos(\beta/2) \tag{1.14}$$

where f_{Tgt} is the bistatic Doppler shift caused only by the target motion [8]. When $\beta = 0°$, Equation 1.14 reduces to monostatic case for monostatic radar located on the bistatic bisector where δ is now the angle between the target velocity vector and the monostatic radar-to-target LOS. When $\beta = 180°$, the forward scatter radar case, $f_{Tgt} = 0$ for any δ [8].

1.3 Radars used for Maritime Surface Observation

The history of maritime radar begins around the 1930s when the short-wave radio technology has been developed. Several countries which began experiments for target detection using radio

were especially interested in maritime collision avoidance. The first marine commercial radars were built in 1946 [15] and they were not particularly reliable. However, most of the system issues were resolved within a short time and maritime radar became mandatory part of the maritime and later on the waterways transport.

Marine radars are radar systems installed on merchant ships, leisure crafts, fishing vessels, oil industry support vessels, search and rescue crafts, warships and many more as described in [15] providing them with information about traffic situation, collision avoidance, the ship's position relative-to sea-marks or coastal features, ice, uncharted wrecks and other obstructions.

Two frequency bands are used for marine radars according to the IEEE standard:

- S band radar operates at frequencies around of 3 GHz (10 cm wavelength) and provide good performance in severe rain condition.
- X band radar operates at frequencies around of 9 GHz (3 cm wavelength) and is the most established type of the radar delivering needed capabilities in most cases.

Another widespread type of the radar used mainly for surveillance from the coastal line is Over-the-Horizon Radar (OTH). OTH operate in HF frequency band (3-30 MHz) and use skywave propagation over the horizon. Clearly such radar requires large antenna installation as the operational wavelength is just below of 100 m and they are characterized by the large coverage area and low range resolution.

In this section the main focus will be on maritime radar systems which can provide safety surveillance of coastal and offshore areas protecting them from drug trafficking, piracy and intruders. Such systems are the coastal surveillance radars used by the coastguards and the Vessel Traffic Services (VTS). An example for a coastal radar for surveillance and control is

the Marconi's S124 coastal HF (4-7 MHz) surface-wave radar which is intended to detect low flying aircrafts out to 150km and ships out to 370 km within 120-degree sector. S124 uses 50m wide transmitting antenna and 800m wide receiving array. It has range resolution of 15km at 200km as described in [16]. Another example and one of the main coastal radars today is the Furuno large-scale surveillance radar system which is suitable for monitoring activities for wide areas such as Maritime Traffic Control Service, Hazardous Area monitoring, Patrol for unidentified vessels, Port monitoring and etc. There is variety of radar sensors that could be used but the most powerful one is Furuno NavNet TZtouch2 3D DRS25A radar sensor which is an X-band (9410 MHz ± 30 MHz) radar with peak power 25 kW. The maximum detecting range is 96 nautical miles and the minimum 25 m. The range resolution for this radar sensor is 20m. The horizontal beam width is 1.9° or 1.4° and the vertical is 22°. The DRS25A weights 25 kilograms [17].

Search and surveillance crafts is another way for providing protection of borders and offshore assets. Searchwater airborne early warning (AEW) radar is an example for surveillance system mounted on a helicopters (Sea King AEW) and aircrafts (Nimrod Mk 2 maritime reconnaissance aircraft). It is an X-band radar with peak power of 65 kW. As described in [16] the radar claimed detection performance is: 28+ nautical miles on a submarine snorkel, 60+ nm on a fast attack boat, and 130+ nm on a medium size ship.

Marconi S810 is an X-band (8.6 - 9.5 GHz) lightweight surveillance radar [16] and it is an example of a naval radar mounted on a warship. This kind of radar could detect a 5 m^2 airplane at 28km at 2000m above the sea level. S810P radar, which is used for lower altitude coverage can detect 0.1 m^2 target at 15km. Marconi S810 weights around of 1 tonne, including 250 kg of antenna and about 695 kg of transmitter and receiver.

Over-the-horizon radar deliver good detection capabilities but uses huge antennas and experiences difficulties in detecting small targets. An example of such kind of system is the Raytheon's Relocatable Over-the-Horizon Radar (ROTHR) which is able to detect both ships and aircrafts. This radar covers 64-deg wedge between 500 and 1600 nm range and it is incapable of detecting anything closer than that because it is working on the principle of ionospheric bounce technique. The transmitter is 200 kW FMCW and the receive array is 372 pairs of 19 ft monopoles distributed over 1.6 mile line.

Another way to provide maritime surveillance is by use of the radar images from satellites but the revisit time of satellites is a significant issue. For example Maritime satellite surveillance system provided by Airbus defence and space [18] has a revisit time few times daily (radar satellites passing at 6AM or 6PM, optical ones in the frame of 10 -11 PM).

Something that all previously mentioned systems working in maritime conditions have in common is sea clutter. Sea clutter is the reflected EM waves from rough sea surface in the region of interest. Because of its nature this type of clutter is difficult to predict and it may cause a severe problem, especially to the 9 GHz band radar. The reason is that the statistics of the clutter produce many high intensity returns which cause increased false alarm rates and it is non-Gaussian. More detailed explanation on sea clutter is presented further in this Chapter and in Chapter 2.

1.4 Maritime Clutter Problems and Basic Models

Radars operating in maritime conditions certainly detect scattered signals from the sea surface, typically defined as sea clutter [19]. Usually this sea clutter is unwanted and in the cases where target detection is of interest, the radar system will be clutter limited rather than noise limited

[20]. The amount and level of the sea clutter seen by the radar will rely not only on the sea characteristics but on the radar frequency, aspect angle, Tx/Rx topology, height as well [10]. Further discussion on sea clutter are presented in Chapter 2.

1.5 Forward Scatter Radar Brief History, Basic Operation and Definition

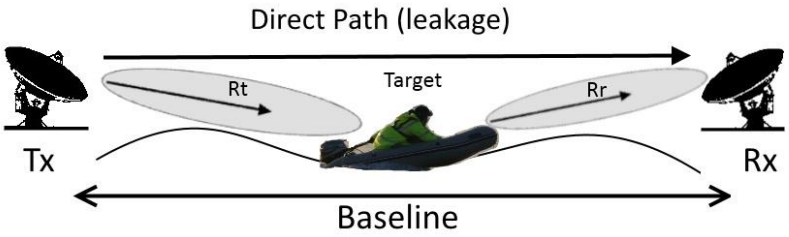

Figure 1.5.1 Forward scatter radar for maritime applications

Forward scatter radar (Figure 1.5.1) is a special case of bistatic radar where the bistatic angle is approaching 180º [8], [21], [22]. The physical operational principle of FSR however is essentially different from that of bistatic radar, which is inherently a backscatter radar as it is described in [23]. In the FSR case the transmitter and receiver antenna are facing each other. When a target crosses the baseline, it introduces a perturbation of the direct path signal (the leakage signal between transmitter and receiver) and produces a Doppler phase signature.

The forward scatter radars have some drawbacks, such as absence of range resolution and narrow operational corridor. However the system provides significant benefits in terms of target radar cross section enhancement in comparison with the backscatter radar, excellent Doppler resolution and long coherent integration time equal to the target observation time. This effect has been explained in details in Chapter 2.2.1. Also the system offers increase in power budget, because of its one way propagation, anti-stealth capabilities and reduction in fluctuations of signals which occur in monostatic radars as signal is defined by shadow contour

in FSR. Additionally to this the modern digital signal processing techniques now allow significant improvement in capability and performance of target detection and classification [24], including the ability to measure target crossing velocity, crossing angle, baseline crossing range.

1.5.1 Brief History of Forward Scatter Radar

The forward scatter radar has been used in fence applications since the early 20th century [8] and it is historically thought of as the first type of bistatic radar [25].

The FS phenomenon reported for first time by Alexander Popov in 1897 was that a disruption of the signal continuously transmitted between two battleships had been observed every time a third ship was crossing the line of sight shadowing the receiver. This observation created the idea to use FSR as an "electronic fence" for target detection in the cases the direct signal is blocked by the extended target as described in [25], [26] This idea was implemented by France, Japan and the Soviet Union who actually deployed bistatic forward scatter fences before and during the World War 2. These FSR fences used CW transmitters, so the receiver detected a beat frequency formed between the direct signal from the transmitter and the Doppler frequency shift scattered by the moving target. Because of the complex nature of these systems and their coverage area was very narrow, by the end of World War 2 all the FSR have been replaced by the monostatic radars better spatial coverage area and location accuracy [8].

The United States designed and used CW radar fence called as AN/FPS-23 (Fluttar) in the mid-20th century. This system had very similar geometry as a forward scatter radar and it was used for the distant early warning air defence line in the Arctic. This system was operational in the following 5 years. Afterwards, three forward scatter over the horizon fences for detecting ballistic missiles launched from the Soviet Union were developed. However, at that time the

full advantage of the RCS enchantment was not known. Once the benefits of the FSR system became clear, many efforts have been devoted and concentrated in this area during the past two decades [8], [27].

Presently, electronic fences or microwave fences are broadly used in security applications to protect large territories [28]. Also research in Russia for the development for air defence systems has been produces by Blyakhman [29], [30].

Further investigation on FSR research in maritime condition is available in Chapter 2.

1.5.2 Forward Scatter Phenomenon

FSR uses the so-called forward scattering effect for improved target detection [8], [31], [32], which take place if the target's electrical size produces scattering in the Mie and optical regions. As it is specified in [23], [33], [34]:

'*The FS effect is the strong increase of RCS in the forward direction caused by the co-phase interference of the waves arising from shadow contour of the scatterer. This results in a field focussing on the line perpendicular to the object aperture in the shadow area. With an increase in frequency the main shadow lobe narrows and its peak intensity becomes significantly larger than that of the backscattering lobe, with maximum along the axis of the main shadow lobe, that is when the transmitter, receiver and the target form ~180° bistatic angle.*'

The forward scatter effect was firstly investigated in optics, where it was predicted by Mie [35], reported to be observed for the Mie scattering region [36] and quantitatively evaluated by the optical theorem for particles [37]. Afterwards, the phenomenon was examined in studies dedicated to the approximations of bistatic RCS of objects [32] for microwaves and Ufimtsev [38] created the physical theory of diffraction.

1.5.3 Forward Scatter Radar Cross Section

Forward scatter radars are built to detect targets which are moving in the narrow region between the transmitter and receiver [21]. In this zone, the RCS of the targets raise sharply because of the 'forward scatter effect'. On Figure 1.5.2 the topology of FSR is shown, where Tx is the transmitter position, Rx is the receiver position, x, y, z are Cartesian coordinates with the origin corresponding to the phase centre of the receiving antenna, b is the base of the system, Tg is a target, V is velocity vector of the target, φ is an array of trajectory inclination towards the baseline in the horizontal plane, γ is an array of trajectory inclination towards the horizontal plane, α is azimuth of the target and δ is the elevation of the target.

In equation (1.10) of this chapter the RCS of a target has been described on a basis of incident and reflected waves electric fields intensity. This equation is true for both monostatic and bistatic radar but we will focus on the bistatic case where the targets RCS is defined as bistatic RCS (BRCS).

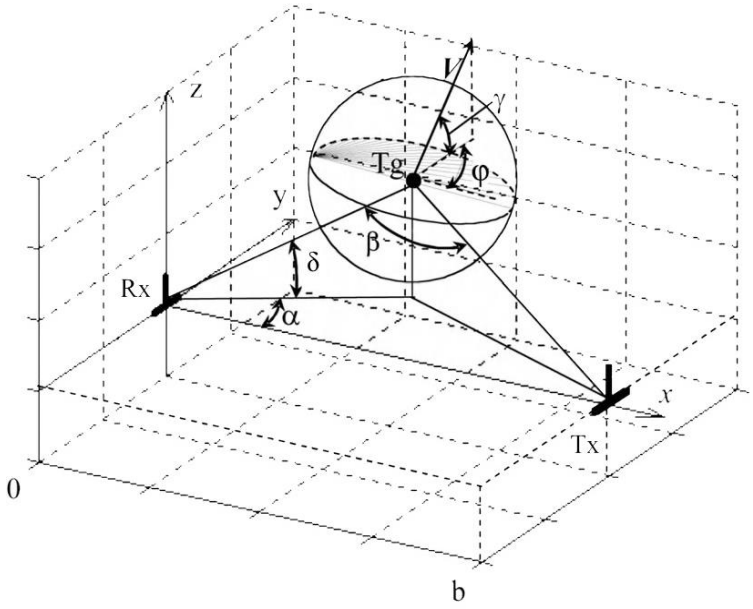

Figure 1.5.2 FSR topology

It is important to describe the process of forming the electromagnetic field scattered by a target in a bistatic case. This field contains two components. The first one describes the self-scattering field formed by any target. The intensity of the electric component of the scattered field is expressed by *Es*. The second one following the electromagnetic fields and waves theory [39] describes as in [21] the electric component of the shadow field E_{SH}:

'*if an absolute black body of finite size, which is larger or comparable with the wavelength λ, is placed in the way of wave propagation, then a scattering field or shadow field appears behind the body. The field appears as a result of a primary field disturbance (the shadow part of the incident wave front).*'

This allowed to determine the full scattered field:

$$E_{\Sigma} = E_S + E_{SH} \tag{1.15}$$

Targets which are bigger than the wavelength have both self-scattering and shadow fields. But at bistatic angles very close to 180 degrees the main contributor in the scattering field is the shadow field. This region is specified as the forward-scattering (FS) field. In this region a real target can be considered to be an absolutely black body, allowing to neglect the effects of the currents on the surface of the target.

Babinet's principle is used for numerical assessment of the FS RCS. This principle is explained [5], [21], [37] as:

'*the diffraction pattern from an opaque body is identical to that from a hole of the same size and shape, except for the overall forward beam intensity'*

Following the analysis, the radar cross section of a target increases sharply in the FS region and this phenomenon is called forward-scatter effect.

1.5.4 Block diagram of CW FSR

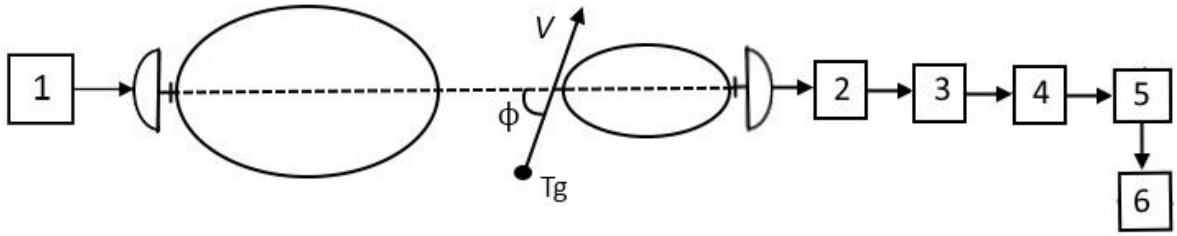

Figure 1.5.3 Block diagram of continuous wave FSR

A basic block diagram of CW FSR is presented in Figure 1.5.3 where the following are titled as:1, transmitter; 2, analogue receivers in the receiving channels of each directional pattern partial beam; 3, Amplitude detectors (ADs); 4, ADC converters; 5, module of digital signal processing; 6, tracing module; Tg is target and V is the vector of velocity.

1.6 Possible Applications of FSR in Maritime Environment

The defence and protection of a country's coastal area, exclusive economic zone and offshore assets, including wind farms, fisheries, oil rigs and high value military assets such as warships and aircraft carriers, is a significant issue for national homeland security. Recent examples: lack of maritime security in the Persian Gulf has created an open market for piracy in a region with billions of pounds of merchant traffic annually; another example was the suicide attack on the warship USS Cole on 12 October 2000 in the Yemeni port of Aden [40]. Such failures in security not only have political repercussions but also huge financial implications and should be minimised wherever possible. Also maritime vessels face a variety of threats to safety at

sea, including a growing number of submerged objects such as freight containers lost from large cargo vessels.

Nowadays, there are multiple surveillance systems which attempt to provide effective maritime protection, each with its own advantages and limitations [41], [42]. Coastal radars and radars mounted on offshore platforms, such as oil rigs, are used for monitoring surrounding areas but they all suffer from limited performance by the local horizon surveillance range [15]. Another way of obtaining surveillance of a perimeter of interest is by using radars mounted on ships and aircrafts but this method is expensive, weather dependant and cannot provide continuous surveillance. As discussed previously, satellites radar imaging is another promising way to provide surveillance of an area but the long revisit time of the satellites is a major issue. HF radars working at over-the-horizon range provide good compromise but use colossal antennas and experience difficulties in detecting small targets – potentially the most dangerous type.

Conventional maritime radars do not solve the problem of automatic non-cooperative target identification, specifically where relatively small (inflatable boat, Jet Ski, swimmer and etc.) and a priori unknown targets need to be automatically identified in the presence of strong sea clutter. A way to solve such kind of problem is the use of electro-optical sensors mounted on ships and aircrafts which provide adequate identification level but these systems are weather dependant. It appears that building a system which provides all of the needs of sea monitoring with a satisfactory resolution allowing automatic target detection and identification of small maritime targets, is quite unlikely. Ultimately it is clear the solution lies in an combination of various existing systems, all working in synergy with each other [43]. This is one of the motivation factors behind looking for new system which can provide improved capabilities to current surveillance systems.

1.7 Buoys/Shore Mounted FSR Sensors – The Concept

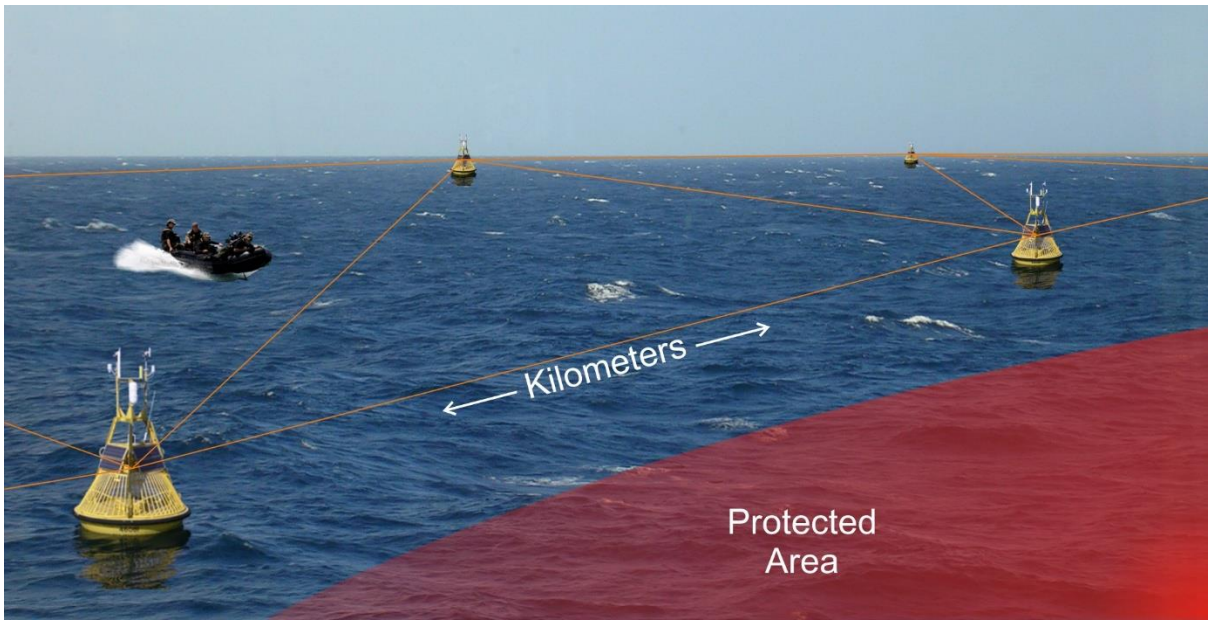

Figure 1.7.1 FSR buoy mounted network topology

This thesis therefore presents the progress, initial results and analysis of research to develop a brand new, cost effective surveillance sensor network for maritime applications. The network concept consists of buoy mounted FSR sensors equipped with omni-directional antennas in a zigzag structure spread over many kilometres, forming a fence or perimeter to keep safe any maritime asset [42], [43]. The proposed network configuration is shown on Figure 1.7.1. Target crossing between sensors in the network will be detected through changes in both amplitude and frequency of the received signal. These FS sensors are designed to provide early automatic detection and identification of low visibility, small, potentially low speed maritime targets such as boats (being used for suicide missions, people, drugs and weapons smuggling), semi-submerged objects (lost containers or icebergs that pose danger to maritime traffic and off-shore installations) and environmental control (oil spill detection) in all weather conditions. The system is proposed to be deployed in areas where more traditional monitoring devices are

incapable to operate and may either replace or complement them. The aforementioned will be effectively applicable for surveillance of effective economic zones (EEZ), offshore assets such as wind energy farms (wind farms, being presumably within the range of ground based radar, extremely difficult to monitor by conventional radars due to the strong Doppler clutter generated by the rotating blades) and oil rigs, including tracking pirates boats routes[1] to and from the coast and serve as a radar fence around high value maritime assets such as aircraft carriers and warships. Such a system has the potential to be transportable and relocatable [42].

There are key advantages to the use of FSR as a fence and the practicalities of such systems are well documented [20], [21], [44], [45]. Benefits include an increased ability to detect stealth targets and the enhanced cross section of conventional targets. In the forward scatter region radar cross section tends to rely more heavily on an object's physical shape and size rather than their electromagnetic attributes.

1.7.1 Foundation work

Previous work within the Microwave Integrated Systems Laboratory (MISL) in remote sensing technology has developed an innovative ground target detection network which has demonstrated an extremely high efficacy in operations by using a network of VHF forward scattering micro sensors [44], [46], [47]. In the study described in this thesis the operation of FSR has been translated to the maritime domain [43]. Whilst the automatic target detection and identification principles remain similar at the phenomenological level to ground target detection, the fundamental theory, technology and technique behind the maritime network is essentially different [42].

[1] In contrast to a traditional maritime surveillance task in this case we need to monitor boats out coming from the shore to blue water and have no access to the shore to install surveillance radars

This is dictated by the presence of strong sea clutter, therefore the operational wavelength employed and signal processing developed for the ground application system cannot be used for the maritime application. To address the issue of very high levels of sea clutter, whilst keeping the system cost effective, the system uses microwave CW signal transmission in forward-scatter operation mode.

Research conducted by the MISL group has shown that a chain of FSR sensors mounted on anchored buoys could resolve the sea clutter issues and be able to detect small objects such as boats and jet skis in maritime conditions [47], [48]. For this particular reason, forward scatter cross section (FS CS) analysis have been undertaken for typical small maritime targets which provided deeper understanding of the radar system performance investigated in [33].

1.7.2 Forward scattering of microwaves above sea surface

Close observation of sea clutter leaded the creation of some basic terms which describe the sea surface [4]. The wind wave is an outcome of the action of the wind over the water surface. The gravity wave could be explain as a wave whose speed of propagation is controlled mainly by the gravity. Therefore every water wave bigger that 5 cm is seen as gravity waves. Capillary wave which is also called a ripple is a water wave which is smaller than 2.5 cm. This is a wave whose velocity propagation is controlled mainly by the surface tension of the liquid in which wave is travelling [19]. A very important characteristic of the sea surface is the sea state (SS) which is the numerical description of the ocean surface roughness. The Douglas Sea State scale [49] is used as a standard estimate of a wave height and it is presented on Table 1.1. Another important scale for estimating the sea state is based on Beaufort's wind force scale. The Beaufort scale is an empirical measure that relates to wind speed to observed conditions at sea or land [50].

Particular attention on the scattering conditions is necessary in the case of forward scattering of EM above the sea surface at low grazing (near zero) angles. There are three well defined scattering mechanisms which are explained below and most of the material below has been published in [20].

Table 1.1 Douglas sea and swell scale

State of the sea				Swell
Code figure	Height (m)	Description	Code figure	Description
0	0	Calm (glassy)	0	No swell
1	0 – 0.1	Calm (rippled)	1	Very low (short and low wave)
2	0.1 – 0.5	Smooth (wavelets)	2	Low (long and low wave)
3	0.5 – 1.25	Slight	3	Light (short and moderate wave)
4	1.25 – 2.5	Moderate	4	Moderate (average and moderate wave)
5	2.5 – 4.0	Rough	5	Moderate rough (long and moderate wave)
6	4.0 – 6.0	Very rough	6	Rough (short and heavy wave)
7	6.0 – 9.0	High	7	High (average and heavy wave)
8	9.0 – 14.0	Very high	8	Very high (long and heavy wave)
9	Over 14.0	Phenomenal	9	Confused (wave length and height indefinable)

The first case could be specified as dominant coherent scattering. In situations when the sea is relatively calm (SS 0 to 2), the reflections from the smooth surface are expected to be specular representing coherent scattering (Figure 1.7.2 (a)). The appearance of ripples on the sea surface will decrease the signal power scattered in forward direction due to the diffuse scattering.

Second case is named dominant diffuse scattering shown on Figure 1.7.2 (b) where sea states are high but there is still line-of-sight (SS 3). In this scenario diffuse scattering becomes the dominant component and it is mostly true for large grazing angle (around 4-5°) as underlined in [51], [52]. Strong wind and higher seas decrease the scattering in specular direction and received coherent power practically disappear for high grazing angles. But this is not the situation for low grazing (near zero) angle where there is little or no change in the Fresnel reflection coefficient explained in [51].

Shadowing with intermittent loss of signal presented in Figure 1.7.2 (c) is the case where very high sea states such as SS 4 and higher are present. Sea state 4 present the formation of small waves with breaking crests and scattered whitecaps. Direct and reflected EM are shadowed by the sea surface and this may cause an intermittent loss of signal which has been discussed in [20].

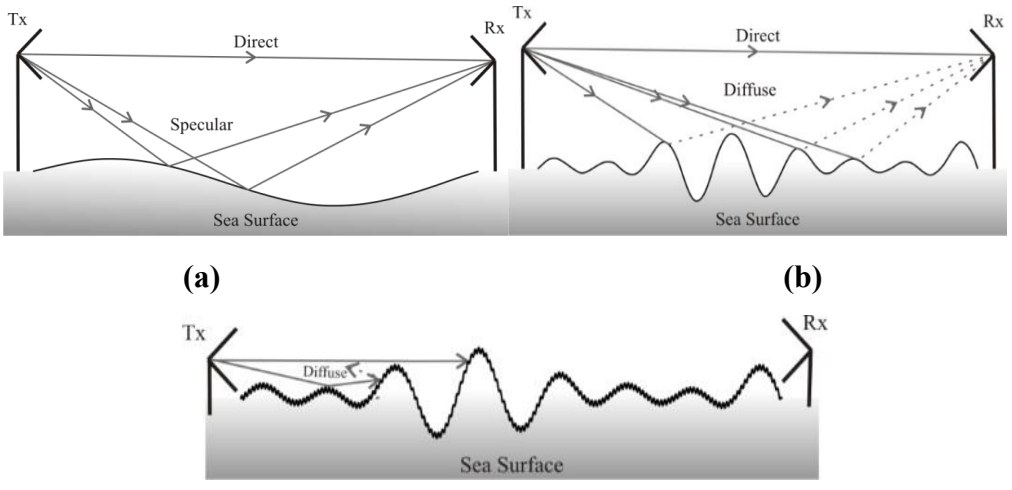

Figure 1.7.2 Geometry of ray paths over the sea surface. (a) dominant coherent scattering (b) dominant diffused scattering when grazing angles are large; (c) illustrate the shadowing with intermittent loss of signal

With respect to the detection of the previously mentioned 'difficult' sea targets, the situation actually only occurs for the first two cases in which the sea state will allow small target vessels to be safely at sea (up to SS 3).

1.8 PhD Research Problem Setting (aim, objectives)

The aim of this thesis is FSR experimentation at the sea at very low grazing angles and subsequently looking at and performing comprehensive analysis of the sea clutter data conducted with the prototype FSR system.

Currently there is a lack of experimental data and models for the maritime forward-scatter radar which must be addressed. Furthermore at very low grazing angles (as would be applicable for such a sea based, buoy mounted network), shadowing of areas of the sea surface by very large dominant waves can be expected to be common (schematically shown in Figure 1.8.1), creating complexities in estimating signal to clutter ratio, as the clutter source area is constantly changing [42]. This may increase a false alarm rate, while shielding an actual target in rough seas.

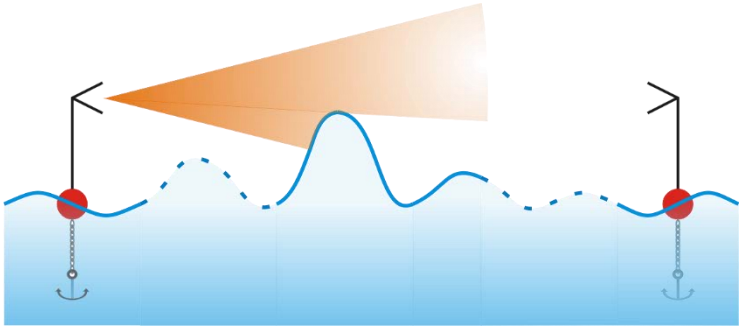

Figure 1.8.1 Surface shadowing of the sea by large dominant waves

Considering the deficit of both experimental data and verified models for maritime FSR, the FSR experimentation at the sea at very low grazing angle (0.05° – 0.7°) is the most important

research stage. In order to accomplish such measurements a prototype FSR transceiver has been developed [42], [43]. The radar was developed to work at the 7.5GHz band in both continuous wave (CW) and Pulse mode (Chapter 3.1 and Appendix A). Further on in the research a 24 GHz FSR equipment working only in CW mode has been developed and used in maritime measurements. In this thesis full description of the developed system is provided, including the stages of improvements.

Initially experiments were conducted in laboratory environment and more specifically in anechoic chamber to test the Doppler frequency measurements capabilities of the maritime FS radar. Afterwards the system power budget performance has been tested over various surfaces including sea water. The first maritime FSR experiments were performed in November 2009 and since then a number of sea trials have been conducted in the UK, Bulgaria and recently in Italy providing large database of sea clutter data and records of various targets.

In this work, vast number of sea clutter signals and target signals were organised into databases allowing more efficient way for further systematic analysis of the data.

The original contributions in this research thesis are:

- Designed numerous databases for storing the information acquired during the maritime trial.
- Perform comprehensive analysis of the sea clutter data generated with the prototype FSR systems. Spectral and statistical analysis over the FSR sea clutter data depending on the radar operational regimes, environment and scenarios, was completed.
- Preliminary analysis on the FSR target signals were performed.

1.9 Thesis Structure

Chapter 2 focus on current sea clutter models. Initially sea clutter models for monostatic radar systems are discussed and later on description of the existing models of sea clutter in bistatic and forward-scatter cases are presented. Also Chapter 2 describes in more detail the phenomenology of FSR. Information about the maritime forward scatter radar architecture, configuration and frequencies is given and typical targets of interest are specified. Chapter 3 gives a detailed description of the test equipment and the stages of development including block diagrams, calibration curves etc. Environmental conditions monitoring devices used during the experiments are described in the same chapter. Then databases structure is explained. Chapter 4 provides spectral and statistical analysis of sea clutter depending on the FSR operational regimes, environment and FSR layouts. Chapter 5 focuses on a basic analysis of FSR target signatures. Specific attention is paid to the target signatures of the MISL boat which was repeatedly used in all experiments allowing control of target motion parameters and RCS. Finally, in chapter 6 outline of the completed work is given and important conclusions are made. Future work is discussed as a final part of the thesis.

Chapter 2 Sea Clutter Models and Phenomenology of Signals in Maritime FSR

2.1 Sea Clutter Models

In this section of the chapter, a brief review of the monostatic, bistatic and forward scatter radar sea clutter models has been presented. Monostatic and bistatic radars have different parameters of EM scattering but essentially they use the same physical mechanism, i.e EM scattering from the sea clutter cell area is reflected towards the receiver. This is not the case in the FSR where the EM waves are shadowing from the sea clutter cell surface in direction the receiver [8].

2.1.1 Backscatter Sea Clutter and Sea Clutter Models

Different types of radar experience backscatter from the sea, either as desired signal or unwanted sea clutter [19]. For example, the purpose of some remote sensing systems could be the reception of the backscattered sea clutter signal such as space-bourne synthetic aperture radars (SAR) used for oceanographic studies. But for almost every other application reflections from the sea are considered as clutter and are unwanted as it affects the performance of the radar.

Depending on the radar applications, sea clutter properties may vary quite widely. To be able to understand what is the impact on the maritime radar efficiency under different condition

from the sea clutter signal, development of accurate statistical models of the clutter return is necessary. This is explained in [19]:

'*These models must be able to incorporate the spatial and temporal properties of the backscatter, under a wide range of environmental conditions and for different radar waveforms and viewing geometries'*

The clutter returns can be characterized by a couple of features such as the normalised radar cross section (NRCS) σ^0, the amplitude distribution of the clutter power, the Doppler spectrum of the clutter returns, the spatial variation of the clutter return, the polarization scattering matrix and the discrete clutter spikes. The NRCS expresses the average radar cross-section of the energy scattered from a clutter cell area. So for surface area A restricted by radar resolution, the RCS of the clutter will be expressed by $\sigma^0 A$ [19]. Taking into account sea surface complex nature and continuous change, the momentous RCS from the reflected sea area fluctuates broadly around the average value determined by σ^0. Taking into account the statistics of this variations is essential parameter for the clutter characterization. Families of probability density functions (PDF) have been used for describing the single point amplitude statistics and more specifically for each set of observations a specific set of PDF has been applied. The spectrum of the sea clutter returns have been used to characterize the variations of the amplitude fluctuations.

It is also important to stress as in [4]:

'*In modeling sea clutter, there is a difference between a theory, which relates the physical scattering properties of the sea surface to the received signal, and a characterization, which provides a description of sea clutter data in terms of statistical model (e.g., Rayleigh,*

lognormal, Weibull, and K- distribution) that, although sometimes suggestive of physical process in the underlying scattering, is of greater direct interest of the radar system designer in providing detection probabilities and false alarm rates.'

Rayleigh distribution, named after Lord Rayleigh, is a continuous distribution for positive-valued random variables. This is distribution of the magnitude of two dimensional random vector whose coordinates are independent, identically distributed, mean 0 normal variables. The probability density function of the Rayleigh distribution is [53]:

$$y = f(x; b) = \frac{x}{b^2} e^{\left(\frac{-x^2}{2b^2}\right)}, \qquad x \geq 0 \tag{2.1}$$

where b is the scale parameter of the distribution. And the cumulative distribution function is:

$$F(x) = 1 - e^{\left(\frac{-x^2}{2b^2}\right)}, \qquad x \in [\,0, \infty) \tag{2.2}$$

The lognormal (or log-normal) distribution is a continuous probability distribution of random variable whose logarithm is normally distributed. Accordingly, if the random variable *X* is log-normally distributed, then $Y = \ln(X)$ has a normal distribution [54]. The lognormal probability density function is:

$$\ln N(x; \mu, \sigma) = \frac{1}{x\sigma\sqrt{2\pi}} exp\left[-\frac{(\ln x - \mu)^2}{2\sigma^2}\right], \qquad x > 0 \tag{2.3}$$

where x is random positive variable, μ is location parameter and σ is scale parameter. And the lognormal cumulative distribution function is:

$$\int_0^x \ln N(\xi;\mu,\sigma)\,d\xi = \frac{1}{2}\left[1 + erf\left(\frac{\ln x - \mu}{\sigma\sqrt{2}}\right)\right] = \frac{1}{2} erfc\left(-\frac{\ln x - \mu}{\sigma\sqrt{2}}\right) = \Phi\left(\frac{\ln x - \mu}{\sigma}\right) \tag{2.4}$$

where erfc is the complementary error function, and Φ is the cumulative distribution function of the standard normal distribution.

The Weibull distribution, named after Waloddi Weibull, is as well continuous probability distribution. The probability density function of a Weibull random variable is:

$$f(x;\lambda,k) = \frac{k}{\lambda}\left(\frac{x}{\lambda}\right)^{k-1} e^{-\frac{x}{\lambda}}, \qquad x \geq 0 \tag{2.5}$$

Where k > 0 is the shape factor and λ is the scale parameter of the distribution [53]. And the cumulative distribution function is stretched exponential function.

$$f(x;\lambda,k) = 1 - e^{-\frac{x}{\lambda}}, \qquad x \geq 0 \tag{2.6}$$

The Weibull distribution is associated to a number of other probability distributions, more specifically, it interpolates between the Rayleigh distribution (shape factor equals to 2) and exponential distribution when k = 1.

K-distribution is a probability distribution that arises as the result of a statistical or probabilistic model used in SAR imagery [55]. The K-distribution is created by compounding two separate probability distributions, one describing speckle that is a characteristic of coherent imaging, and the other representing the radar cross-section. The probability density function is:

$$f_x(x;\mu,\nu,L) = \frac{2}{x}\left(\frac{L\nu x}{\mu}\right)^{\frac{L+\nu}{2}} \frac{1}{\Gamma(L)\Gamma(\nu)} K_{\nu-L}\left(2\sqrt{\frac{L\nu x}{\mu}}\right), \quad x > 0 \qquad (2.7)$$

where X is that random variable which has a gamma distribution with mean σ and a shape parameter *L,* with σ being treated as a random variable having another gamma distribution, this time with mean μ and shape parameter ν and *K* is a modified Bessel function of the second kind.

Sea clutter modelling has been performed since the early ages of radar. Simple models such as Kirchoff approximation and Gaussian model have been effectively used for analysis of the sea clutter in high grazing low resolution radars. According the central limit theorem (CLT) [56] it could be concluded that in low resolution radars many scatterers contribute to a Gaussian like distribution. While in high resolution radars few scatterers contribute and hence the distribution moves away from being Gaussian. Advanced modelling techniques have introduced during the past 3 decades, allowing to create correct models for low grazing angle, high resolution radar sea clutter case. New non-Gaussian statistical models were presented but it wasn't until the 70s when the K distribution model was proposed. This model was initially suggested by Jakeman and Pusey in [57]. A few years later detailed analysis of the sea clutter using the K distribution were published by [58]. The significance of the K distribution is explained in [19], [59], [60] :

'*This approach highlighted the usefulness of the compound representation of the clutter process, which in the hands of Ward, Watts and others, made possible the systematic analysis of effects of thermal noise and the spatial and temporal correlation properties displayed by the clutter and their impact on maritime surveillance radar'*

As previously mentioned the EM reflection by the sea surface at low grazing angles radars introduce many issues. One of the most uncomplicated way to explain both the EM theory and the statistical description of the sea surface at low grazing angle is by using Rice's perturbation theory [61]. Composite models [62] have been introduced as well as attempts to include shadowing and multipath effects on the low grazing sea clutter into models. Most of the work in backscatter low grazing angle radar sea clutter has been presented in [19], [63].

2.1.2 Bistatic Sea Clutter Models

Presently, bistatic radar is a subject of great interest and that is the reason why understanding the bistatic clutter properties is of a great importance [64]. Outstanding summary of the work done in the past 40 years in bistatic sea clutter is described in [22], [64]. One of the first published maritime experiments with C-band and X-band bistatic radar were performed in 1966 and 1967 by Pidgeon where he used land-based CW transmitter and receiver mounted on an aircraft [65]. Shortly after the GEC Electronics and more specifically Domville published his results from experiments with bistatic X-band over several surfaces including sea surface [66]. During the trials though measurements of the sea state haven't been performed which is a significant drawback [8]. Nevertheless, his results provoked interest and have been discussed by [4], [8], [67]. Further analysis on the aforementioned sea clutter data have been performed in [8].

Having in mind the lack of measurements of the statistical properties of bistatic sea clutter Ewell and Zehner performed low grazing angle sea clutter measurements with X-band (9.38 GHz) pulsed land based bistatic radar [68]. They demonstrated that the amplitude distribution of both the monostatic and bistatic sea clutter followed the lognormal distribution [64]. Their analysis also showed that monostatic clutter echoes amplitude tend to be higher than the bistatic

one. The compound K-distribution model was applied by Yates to experiments with simultaneous monostatic and bistatic synthetic aperture radar imagery and her results demonstrated reasonable agreement with the model [69]. Also results showed that the bistatic clutter is less spiky than monostatic.

In 1991 Kochanski and the M.I.T Lincoln Laboratory performed low grazing bistatic sea clutter backscatter experiments at X-band (10 GHz) using CW land-based transmitter and receiver mounted on an aircraft [70]. The measurements were performed over broad variety of receiver angles. His work has presented that the smaller of Tx and Rx grazing angle tend to prevail the resulting normalized radar cross section.

In 2010 Griffiths published the results from measurements and modeling of bistatic sea clutter [64]. His work examined the possibility of using models that have been developed for monostatic sea cluter sea clutter such as the Georgia Institute of Technology (GIT) model [71] and the compound K-distribution [19] for amplitude statistics. In addition, analysis of the existing bistatic clutter data have been presented.

The GIT sea clutter model is used to predict the normalised monostatic radar cross-section (NMRCS). Since this model was devised for low grazing angles it places an upper limit of around 10 degrees on the grazing angle, although use of other monostatic models could extend the application to higher grazing angles, and land of clutter. The GIT returns the NMRCS of sea surface given the radar wavelength average wave height, wind speed, radar look angle with respect to the wind direction and the grazing angle as described in [64], [71].

In [72], [73] continuation of Griffiths work is presented where they have compared monostatic and bistatic datasets to the K-distribution. The results showed the shape factor of the compound

K-distribution model applied to the experimental data tends to be lower for the monostatic clutter data than for the corresponding bistatic clutter. The results in [73] also demonstrated that the Power Spectral Density (PSD) is comparable between monostatic and bistatic case, but some differences were noted. The monostatic spectral shape was less spikey in comparison with bistatic PSD and it had increase of double edged in spikiness, where the bistatic clutter has more developed single edged one. Also the monostatic clutter presents on average more spiky distribution.

2.1.3 Forward Scatter Sea Clutter Models

Following the discussions in Chapter 1 concerning the scattering mechanism in Forward Scatter mode, observations have concluded that when low grazing angles are inherent, it is likely that coherent scattering will be dominant even in high sea states (measured throughout thesis by the Douglas scale [49]) because shadowing will block most of the received diffuse scattering as shown in Figure 2.1.1 (b) [20]. Specular reflections are expected from the tops of the waves (which will be the only visible parts between transmitter and receiver) and they will be the major contributors of the received signal. The aforementioned case is not taking into account the breaking waves and white caps, which are usually present above sea state 3 and could change the scattering situation.

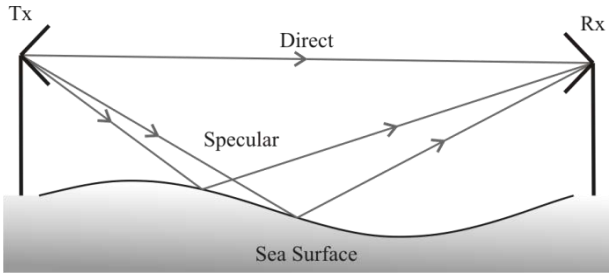

(a)

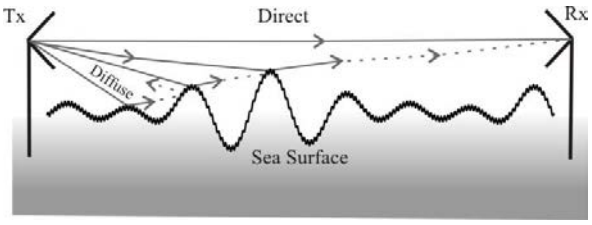

(b)

Figure 2.1.1 Geometry of ray paths over the sea surface. Figures illustrate (a) dominant coherent scattering (b) dominant coherent scattering in high sea states;

Analytical approaches and computer simulation of the time-spatial scattering processes have been widely used for estimation of radio propagation characteristics [51], [52], [74]–[80]. However there is rather limited amount of research on experimental observation of radar scattering at low grazing angles [74], [81]–[85]. During the mid-1950s several propagation experiments were conducted across the Golden Gate in San Francisco [74], [81], [82] where sea wave spectral analysis and radio spectra in X-band were estimated for different grazing angles starting as small as 0.6° which has been described in [20].

In the experimental study in [83], the propagation characteristics of X-band CW over a surface of artificially generated gravity waves in an indoor wave tank were thoroughly investigated. In this study, the waves were scaled to be $1/10^{th}$ of the actual significant wave height for a given sea state and due to the generation method (no wind effects), no capillary waves were generated on the surface. Gradual increase of the sea state led to a smearing out the typical two-ray path interference pattern, clearly indicating the transition from dominant coherent to rather diffuse reflection even in the absence of capillary waves. At sea state 0 a clear coherent reflection for the glassy sea surface was observed, at sea state 3 with larger than 5° grazing angle the time averaged power/mean interference pattern demonstrates typical constructive-destructive behaviour with frequency and, finally, sea state 5 produced entirely diffuse

scattering at the same grazing angle [20]. A shift in the mean interference pattern for higher sea states was also observed, with the most pronounced shifts at smallest grazing angles due to the height of the illuminated water surface responsible for specular reflections being higher than the mean water surface level.

A majority of papers on forward scattering have been published in the context of shipboard and coastal communications to estimate the received power reduction due to the presence of the rough dynamic surface which have been discussed in [20]. Therefore the main focus was on average characteristics, such as the average power scattered per unit area of sea surface, or average specular reflection coefficient [51], [77], [85]–[88]. In the two fundamental models of Ament [86] and Miller-Brown-Vegh (MBV) [88] the procedure of coherent equivalent reflection coefficient estimation was suggested based on an ensemble average over the illuminated height of the waves obeying some specific statistics.

The Ament model assumes that only the coherent scattered power contributes to the total scattered power. The Ament model is a fast and simple model that describes the forward radar propagation over rough surfaces and is used for low grazing incidence angles. The Ament model, which is based on a ray approach, uses the Rayleigh roughness parameter to describe the scattering from a rough interface for grazing angle in a simple way [89]. Ament reflection coefficient, r_A, is defined by:

$$r_A(\theta_i) = r_{12}(\theta_i) exp(-2R_a^2) \tag{2.8}$$

Where it takes the surface roughness into account by multiplying the Fresnel reflection coefficient of a plane surface r_{12}, by the term $exp(-2R_a^2)$ (for Gaussian statistics, with R_a the Rayleigh roughness parameter).

The MBV model was commonly used to describe scattering from the ocean surface. The model has been adopted by the US Navy for propagation over the ocean and it was considered to be more realistic than previous models [86], [90]. The MBV model was proposed in response to observations by Beard [74], suggesting that the Gaussian assumption for the probability density distribution of sea surface elevation may under- predict the scattered field. The model has been built on two essential elements: the Kirchhoff approximation is the electrodynamic element and an assumption regarding the probabllity distribution of the ocean surface elevations is the fluid-mechanical element.

Later discussion of Ament and MBV models [77], [85] analysed the suitability of the suggested statistics and estimates to describe coherent equivalent propagation as authors have described it in [20].

Direct numerical simulations of near zero grazing angle forward scatter have been performed in [52] where in addition to coherent and incoherent power estimations at various angles, the spectral and statistical properties of clutter were discussed. Though this study has been performed for shipboard communication systems at a different frequency band (1 GHz), it suggested quite useful qualitative and quantitative explanations of expected phenomena.

In contrast to the main goal in the modelling of communications systems, which aims to give accurate estimation of average received power, in the thesis the focus is on the statistical and spectral properties of the measured sea clutter [20]. FS sea clutter is a time-varying modulation of the average coherent power due to the presence of incoherent diffuse reflections and shadowing, where interference of the direct signal and multipath arriving from all areas of the illuminated surface footprint produce random deviations from the coherent received power. Clutter may mask the signal scattered by a target no matter how greatly the target cross section

is enhanced by the FS effect [23] and therefore the ability to eliminate clutter in either time or frequency domain largely governs radar target detection performance.

2.1.4 Scattering Mechanism in Sea FSR

In FSR as published in [20], clutter is received from a large area of the sea surface illuminated by the Rx and Tx antennas, which face each other. Spatially distributed dynamic sea waves may be generally considered as obstacles forming backscatter, bistatic and forward scatter signal interference with the direct signal. Indeed, it has been confirmed experimentally that the average values and amplitude fluctuation characteristics of signals scattered over a sea surface path at centimetre and millimetre wavelengths can be satisfactorily described by the model of the interference of direct and scattered beams [19], [20], [51], [52], [78], [79], [91] as illustrated in Figure 2.1.1.

Such a model describes the electromagnetic field at the reception point as the superposition of the coherent component (the sum of the direct beam and the specular reflected beam) and the incoherent component that corresponds to the diffuse scattered field.

The propagation gain *F* [52] is used to present the characteristics of the received signal:

$$F = \frac{E_{dir} + E_{scat}}{E_{dir}} \tag{2.9}$$

where E_{dir} is the direct field which would be received in free space without considering the surface and E_{scat} corresponds to the scattered field, which is radiated from the induced currents of the surface. Since the total field at the Rx is the sum of these two, multipath fading effect caused by the interference between each other is possible.

For our convenience and to adopt communications terminology, we will completely redefine (2.9) in terms of coherent ($E_{coherent}$) and incoherent fields ($E_{incoherent}$):

$$F = \frac{\mathbf{E}_{coherent} + \mathbf{E}_{incoherent}}{\mathbf{E}_{coherent}}$$

where

$$\mathbf{E}_{coherent} = \mathbf{E}_{\mathbf{d}ir} + \mathbf{E}_{spec}$$

$$\mathbf{E}_{incoherent} = \sum_{n} \mathbf{E}_{n} \tag{2.10}$$

In Equation (2.10) the coherent field is the sum of the field that propagates directly and the field that specularly reflects off the surface. The incoherent field is the sum of the diffuse scattered field from a big number (*n* represents that number) of independent individual scatterers.

According to [51], the magnitude of the coherent field is:

$$\left|\mathbf{E}_{coherent}\right| = \left|\mathbf{E}_{\mathbf{d}ir}\right| \left[\left(1 - \left|R\right|\right)^2 + 4\left|R\right| \cos^2\left(\frac{\Phi}{2}\right) \right]^{1/2}, \tag{2.11}$$

where R is the complex Fresnel coefficient and $\Phi = kd + \phi$ is the phase shift of the reflected wave due to path difference *d* and the phase of the reflection coefficient ϕ; $k = \frac{2\pi}{\lambda}$ is the wavenumber.

In general, coherent and incoherent power can be expressed in the form [52]:

$$P_{coherent} = |\langle F \rangle|^2;$$

$$P_{incoherent} = \langle |F - \langle F \rangle|^2 \rangle = \frac{\langle |E_{incoherent} - E_{incoherent}|^2 \rangle}{|E_{coherent}|^2} \tag{2.12}$$

where the $\langle \cdot \rangle$ operator denotes the ensemble average (or mean value) and therefore, $P_{coherent}$ represents the mean value of the received signal, while $P_{incoherent}$ is the mean signal variance.

For a rough sea, when the coherence between the direct and reflected field is reduced, the reduction factor ρ for the average reflection coefficient is introduced and the effective reflection coefficient is [51]:

$$R_{eff} = \rho R \tag{2.13}$$

Different approximations for the roughness reduction factor ρ according to Ament [86] and Miller-Brown-Vegh [88] were obtained:

$$\rho_{Ament} = exp\left[-\frac{1}{2}(2kh_{rms}\sin\gamma)^2\right] \text{ and}$$
$$\rho_{MBV} = \rho_{Ament} I_0\left[\frac{1}{2}(2kh_{rms}\sin\gamma)^2\right] \tag{2.14}$$

where h_{rms} and α are the rms deviation of surface height and grazing angle respectively, I_0 is a modified Bessel function of the first kind of zero order. Grazing angle is defined by geometry and the mean surface level. It is important to stress here that whatever the deviation of the surface h_{rms}, if grazing angles tend to zero both reduction factors tend to 1, and there is no reduction due to the roughness of the sea [20]. Indeed the reflection in the forward direction will take place from the tops of the waves (bottoms and slopes of the wave troughs are not "visible" from Tx/Rx), defining coherence of the reflected waves for the ensemble average sea surface. Moreover as pointed out in [51], reflection from the wave tops decreases the reflected wave path length relative to that from points at mean sea level and, therefore, the interference pattern of the received power from the coherent component is shifted down. This conclusion was confirmed by both measurements [83] and simulations [51], [52], [77].

2.2 Phenomenology of Signals in Maritime FSR

Optimal radar system design and performance prediction requires knowledge of the physics of the system operation. In this Chapter an in-depth view on the target signature analysis in FSR has been provided, merging the physical optics results with the RF engineering approach [23], [26].

The effect first reported by Alexander Popov in 1897 [25] was that a disruption of the signal continuously transmitted between two battleships had been observed every time a third ship was crossing the line of sight shadowing the receiver. This observation led to the straightforward idea to use FSR as an "electronic fence" for target detection when the direct signal is blocked by the extended target.

2.2.1 FSR Surface Target Detection

This chapter is focused with the analysis of such a type of FSR when the target actually crosses the baseline introducing a perturbation of the direct path signal and producing a Doppler phase signature with reasonably long integration time. Whilst the lack of range resolution is an apparent drawback of FSR, it does however give rise to a non-fluctuating target signal, even for highly manoeuvrable targets. As a result, the maximum coherent analysis time in FSR may be equal to the target visibility time T_V. Therefore an absence of range resolution is partly compensated by the excellent frequency resolution. A comparison between two extreme scenarios such as monostatic radar (MR) and FSR is made. In MR, the target fluctuation spectrum bandwidth Δf_M and coherent analysis time $\Delta\tau_M$ are estimated as [32].

$$\Delta f_M = \left(\frac{D_{ed}}{\lambda}\right)\left(\frac{\Delta\varphi}{\Delta t}\right) \; and \; \Delta\tau_M = \frac{1}{\Delta f_M} \tag{2.15}$$

where D_{ed} is an effective target dimension and $\Delta\varphi/\Delta t$ is the rate of change of change the aspect angle φ. Effectively Δf_M corresponds to a frequency resolution limit in MR and $\Delta\tau_M$ is the maximum coherent integration time.

In FSR the target visibility time $\Delta\tau_{FS}$ is equal to the target coherent analysis time. If a target moving with speed v_{tg} is within the forward scatter main lobe (FSML) its visibility time could be estimated as [92],

$$\Delta f_{FS} = \frac{\lambda R_0}{2D_{ed}v_{tg}} \tag{2.16}$$

So as an example for comparison, for a 0.75 m wavelength, the maximum coherent integration time increases from 0.16 in MR (aspect angle rate 0.4 °/s) to 19 seconds in FSR. In terms of frequency resolution, this equates to 0.05 Hz for FSR but ~6 Hz for MR. The very high frequency resolution of FSR enables development of efficient automatic target classification algorithms based on inverse shadow aperture synthesis and this even allows target profile reconstruction [31], [93].

Strictly speaking the radar under analysis is special purpose radar intended to detect low profile, "stealth", low speed targets, representing class of so called difficult targets, where traditional monostatic radar has limitations.

FSR exploits the forward scattering (FS) effect for enhanced target detection [22], [31], [32] which arises if the target's electrical size generates scattering in the Mie and optical regions.

The forward scatter phenomenon is the strong increase of RCS in a forward direction caused by the co-phase interference of the waves arising at the shadow contour of the scatterer which

results in a field focusing on the line perpendicular to the aperture in the shadow area. With the increase of frequency the main shadow lobe narrows and its peak intensity becomes significantly larger [31], [33] with a maximum along the axis of the main shadow lobe, that is, when the transmitter, receiver and target form approximately 180 degree bistatic angle [23], [32], [94]. Figure 2.2.1 demonstrates the nature of forward scattering and shows the directivity pattern of the field scattered by an acoustically hard cylinder with flat bases. This Figure shows both the total PO field and the shadow radiation. It is seen that the shadow radiation really represents the scattered field in the vicinity of the forward direction.

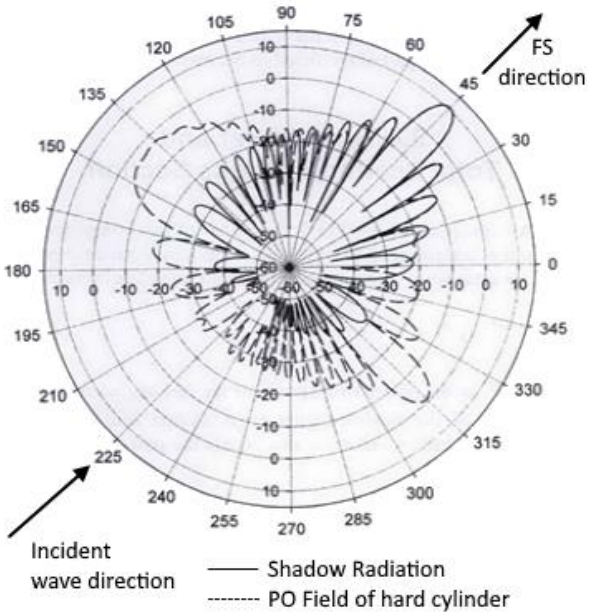

Figure 2.2.1 Shadow radiation focusssed in FS direction (45° in this Figure) as a constitutive part of the phisical optics far field of a cylinder

The forward scattering power is equal to the total power incident on a scattering object, which is much greater than a wavelength and it does not depend on the object reflections coefficients [95].

At present most radar applications use bistatic or monostatic configurations when bistatic angles are considerably less than 180^0 and, consequently, the FS effect is not fully exploited.

FSR could demonstrate unique detection capability as an "electronic fence", in particular, overcoming the problem of strong ground clutter. Indeed, it was shown [9], [91], [96], that in spite of the absence of range resolution in FSR the most critical clutters from vegetation, dynamic sea surface and similar are mainly concentrated in a low Doppler frequency band up to 1 Hz which enables efficient clutter rejection in the frequency domain.

In addition an efficient FSR system should be capable not only for target detection, but also for trajectory parameters estimation and target recognition [97].

FS effect is observable within a relatively narrow area defined by the shadow main lobe. If its width coincides with the so called "dead zone" of zero or nearly zero Doppler shift and there is no direct path signal at the receiver, then there is no benefit in the use of the FS effect. In this case detection is unfeasible and, therefore, this region is typically excluded from the FSR consideration [26]. However in presence of the direct path signal it will be modulated with respect to the speed and trajectory of the target producing a scattered signal, and the middle part of the chirp-like Doppler signal, corresponding to the "dead zone", plays an important role in optimal processing when matching filtering is applied for estimating trajectory parameters.

In general such a signature is the result of interference of the direct path and diffracted (or scattered) target signals. Diffraction from the moving target can be analysed using the analytical approach presented in [97]. However it is interesting to consider such a signature from the point of view of transition between different scattering mechanisms: from bistatic scattering when target is outside of the main shadow lobe (far from the baseline) to a purely

forward scattering mechanism when the target is crossing the baseline and the receiver is in the shadow. This view is useful for analysis of response from so called "stealth target" which caused the recent rise of interest in FSR where detection is always possible whatever shape or material may be used to suppress backscattering [26].

Physical theory of diffraction [31] allows analytical estimation of the target signature and 3D electromagnetic modelling can be used for simulation of the scattering field for a few discrete positions of the target in the process of movement. However such approaches introduce essential fundamental and computational problems to derive the targets signature in real time. An accurate yet uncomplicated analytical model of the received signal, which covers intended range of surface targets trajectories and speeds, will, therefore, benefit FSR system performance analysis and signal processing algorithms development. An appropriate model is presented and the margins of applicability are defined in Section 2.2.4 of this Chapter.

2.2.2 FSR Phenomenology

In conventional bistatic radar configuration spatially separated Tx and Rx antennas are pointed to the area where the target of interest appears (Figure 2.2.2 (a)) and it is assumed that the baseline distance is comparable to the distances from Tx/Rx to target. Signal at the input of the receive antenna represents mainly bistatic reflections of the transmitted signal from the interrogated target and only such reradiated signal is required to extract information about the target if the transmit and receive signals are synchronised [26].

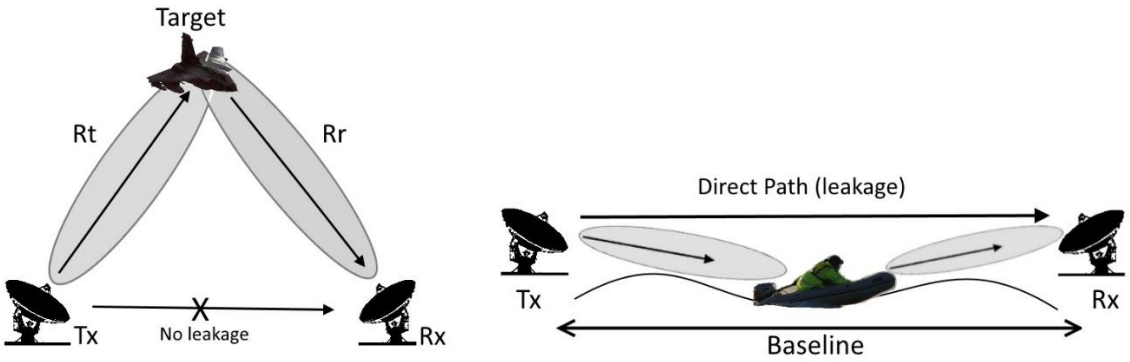

(a) (b)

Figure 2.2.2 The difference between bistatic (a) and forward scatter (b) radar configurations

In contrast, in FSR the Rx and Tx antennas are facing each other (Figure 2.2.2 (b)) and there are two signals which play equally important roles in forming the sensed interference or 'beat' [22] signal: first is the strong direct signal, or 'leakage' signal between the transmitter and the receiver and the second is the presumably much weaker forward scatter signal 'modulating' the leakage. Thus the key point of FSR is availability of both signals at the input of the receive antenna.

In order to provide presence of both leakage and scattered signal the target-to-radar topology should satisfy conditions of Fraunhofer zone scattering: the electrical size of the target should be significantly smaller than distances to the both Tx and Rx and to the radius of the first Fresnel zone. The target characterises a source of secondary radiation with respect to primary radiation from Tx according to Huygens-Fresnel principle.

Using Fresnel parameter $S = D^2/(4\lambda)$, where D is effective size of target and λ is a wavelength we will consider scattering mechanism as a Fraunhofer diffraction in the case when ranges to/from target are larger than S. Nevertheless when considering the time-varying Doppler signature of a moving target, one should not confuse Fraunhofer diffraction on the individual

target with the Fresnel-like diffraction on the effective inverse aperture defined by the whole path of the moving target which is received by the radar.

Measured signatures of targets with sizes defining different diffraction mechanisms are shown in Figure 2.2.3 for 7.5 GHz carrier [23], [26]: (a) Fraunhofer (far field) diffraction from a small inflatable boat of size 2.9 m x 1 m (length and height above the surface), **S=** 60 m and baseline around 1.2 km; (b) boundary Fresnel to Fraunhofer, medium size sailing yacht (5m x3m), S=160 m and distance between Tx and Rx was 350 m; (c) Fresnel diffraction from large motor boat (10m x4 m), S=630 m and baseline approximately 350m.

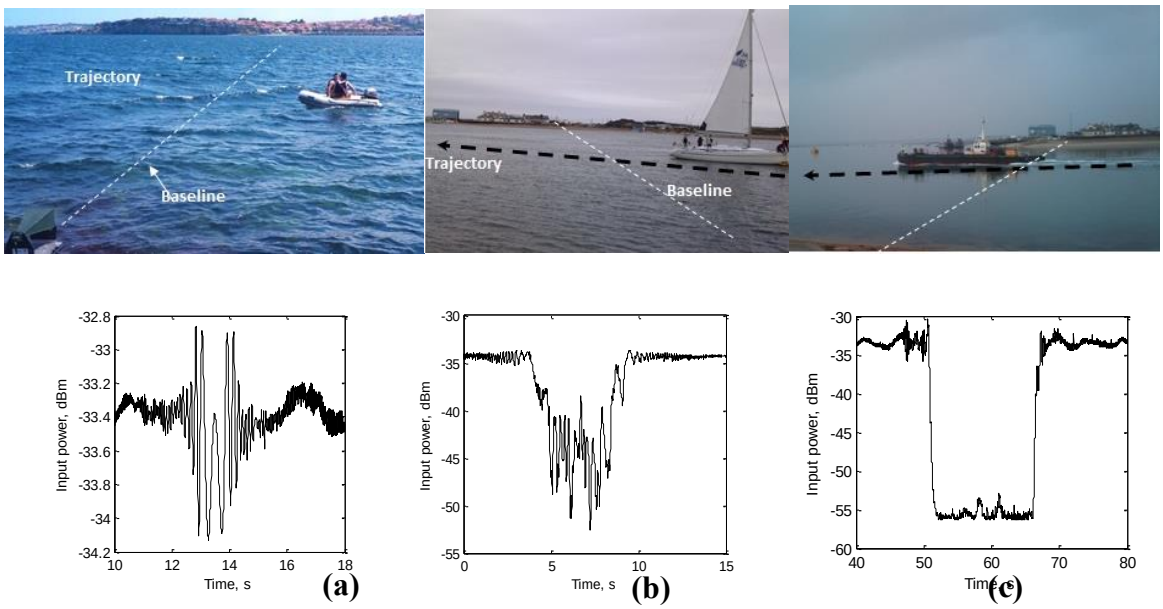

Figure 2.2.3 Doppler signature of from a target crossing in the middle: (a) small inflatable boat, (b) medium size yacht, (c) large motor boat

Shown measured signals are in fact the RSSI (Received Signal Strength Indicator) signals, which contain the oscillating Doppler signature on top of a DC level indicating the strength of the direct path signal [26]. In all signatures the typical diffraction behaviour (positive and negative contribution of phases of interfered signals) is visible at least at the edges of the target signal. Obviously all three signals are liable to detection. However, only the first signal is

suitable for the extraction of target motion parameters. Indeed, its waveform is fully defined by diffraction reflecting specific positions and speed of the target passing through the constructive (in phase) and destructive (out of phase) zones over the path. Let's stress that in the middle of the two-sided chirp-like signal the signal intensity is the same as an intensity of incident (direct path) signal, though intuitively there should be a global minimum due to shadowing. This phenomenon is similar to the Poisson phenomenon (Arago spot) known in optics for the Fresnel diffraction.

Observed in optics, Arago spot or Poisson spot is a bright point that appears at the centre of a circular object's shadow due to Fresnel diffraction [98]–[100]. Arago spot is rather a challenge to observe in optics where very small wavelength impose following conditions (i) target to be small, perfectly symmetrical and having ideal edges, (ii) distances to the source and the illuminated screen to be in the Fresnel zone and (iii) source of light to be point-like. However scaling up the wavelength we can expect a pattern that is similar to Fresnel rings to appear, reflecting constructive or destructive contribution from particular zones if target/wavelength ratio defines Mie scattering and the total ranges of moving objects satisfy the condition of Fresnel diffraction zone. Moreover the much larger scale and the use of Doppler signature instead of total carrier-frequency signals weakens strict conditions on the symmetry and smooth edges of the target on the line of sight so that the Arago-Poisson spot appears as soon as the target is on the line of sight [26]. Mathematically it is expressed by the presence of the non-zero imaginary part of the forward scattering amplitude $f(\theta = 0)$ which relates to the total scattering cross section σ_{tot} as

$$\mathrm{Im}\, f(\theta = 0) = \frac{k\sigma_{tot}}{4\pi} \tag{2.17}$$

and explained by Optical theorem [101], [102].

It is important to stress that the symmetry of the target silhouette to the incident wave is still required for the quasi-optical region; nevertheless, it is less strict when we move down in frequency [23]. An assumption could be made that if the wavelength is nearly comparable to the effective target dimensions its asymmetry will be not resolved by the incident and diffracted waves.

When target moves, continuously crossing constructive and destructive zones, the time domain waveform of the Doppler signature develops in time in the same way as the Fresnel rings progress in space. The larger electrically the target the less observable is the Arago spot and the target intensity of shadow radiation.

2.2.3 Doppler Signature at the Output of RSSI Receiver

Following Ufimtsev [31] the simple interpretation of the shadowed direct path signal can be understood by considering the field at the receiver as a result of interference of the incident electromagnetic field and imaginary shadow radiation from the scattering body.

Several assumptions are made in our analysis [26]:

(1) Target moves uniformly along linear trajectories. These assumptions are nearly always true for a surface targets: they have a relatively narrow FS CS pattern, consequently, visibility time in the order of seconds, i.e. signature duration, and it is not likely that they will make an essential manoeuvre or a change of speed.

(2) Signal scattered by a target corresponds to the forward scattering with the maximum of the shadow radiation along the Tx-Rx, when the target in on the baseline

(3)The 'shadow' of the forward scatter signal is $\pi/2$ phase shifted (imaginary along the FS axis) relative to the direct path signal [31], [102].

At this stage we omit consideration of the amplitude modulation of the signal caused by propagation loss and by FS CS pattern. Only the phase signature of the point-like target (yet casting shadow on the receiver) will be initially derived.

The total target signature will be presented later on as a result of superposition of the phase signature from the "point target" and complex envelope defined by FS CS of the extended target.

The receiver input as a composition of the direct path signal and delayed scattered signal from the moving target as described in [23] is

$$S_{RI}(t) = S_{DP} + S_{TG} = A_{DP}\cos(\omega_0 t) + A_{TG}\sin\big(\omega_0(t + t_{sh})\big) \qquad (2.18)$$

where ω_0 is the carrier, t is the time of direct signal arrival at the receiver, t_{sh} is the delay time of the signal from moving target, S_{DP} and S_{TG} are direct path signal and scattered target signal respectively, A_{DP} and A_{TG} is the phase signature amplitude for the direct path signal and the scattered signal. The initial phase of coherently acquired signals can be omitted without loss of generality.

After passing through the square law detector (SLD) of the receiver with following low-pass filtering (LPF) the signal transforms into:

$$S_{RI}(t) \overset{SLD}{\approx} \left[A_{DP}\cos(\omega_0 t) + A_{Tg}\sin\left(\omega_0 (t+t_{sh})\right)\right]^2 = \\ \overset{LPF}{\approx} DC - A_{Sc}\sin\left(\omega_0 t_{sh}\right)|_{t_{sh}=\left(R(t)+R(t)-L/c\right)} = DC - A_{Sc}\sin\left(\frac{2\pi\left(R_t(t)+R_r(t)-L\right)}{\lambda}\right) \quad (2.19)$$

where $DC = (A_{DP}^2 + A_{Tg}^2/2) \overset{A_{Tg} \ll A_{DP}}{\simeq} \left(A_{DP}^2/2\right)$ is the power of the leakage signal, $A_{Sc} = A_{DP}A_{Tg}$ characterises phase signature amplitude, L is baseline distance, $R_t(t)$ and $R_r(t)$ are time dependant ranges Tx-to-target and target-to-Rx accordingly.

In terms of Doppler phase shift:

$$S_{RI}(t) \overset{SLD}{\simeq} \left[A_{DP}\cos(\omega_0 t) + A_{Sc}\sin\left(\left(\omega_0 + \omega_{dp}\right)t\right)\right]^2 \overset{LPF}{=\simeq} DC + A_{Sc}\sin(\omega_{dp} t) \quad (2.20)$$

where ω_{dp} is the Doppler frequency shift of the moving target.

Thus

$$\omega_{dp} t \equiv -\frac{2\pi}{\lambda}\left(R_t(t) + R_r(t) - L\right) + 2\pi n, \quad \mathrm{n} \in \mathbb{Z} \quad (2.21)$$

where $\mathrm{n} \in \mathbb{Z}$ defining constant phase shift which we will omit without loss of generality [23].

2.2.4 Forward Scatter Cross section Approximation

Analytical solutions for the FS CS are only available for few convex shapes using physical optics (PO) and Physical Theory of Diffraction (PTD) approaches [102]–[104]. Thus either approximated models or 3D EM simulation methods must be used for target FS CS estimation. However without *a prior* knowledge of the target shape it is only the phase target signature which can be used for extraction of information on the target motion. Yet FS CS indicates the

size of the target and enables rough classification based on comparison with the database of known targets [105]. An appropriate rectangular aperture approximation of a target silhouette will be applied as presented in [23], [26].

It was shown in [33] that the peak intensity of the forward scattering lobe of the RCS is directly proportional to the frequency (squared) and from some point it will be greater than backscattering lobe. This fact reflects gradual change of the scattering mechanism from Rayleigh (small effective electrical size target) to Mie (comparable electrical size and wavelength) and eventually to optical scattering (target is significantly larger than wavelength). In Figure 2.2.4 we demonstrate dependence of the forward and backscatter RCS (left vertical axis) as well as beamwidth of the main shadow lobe (right vertical axis) of the sphere on the sphere's electrical size as in [26].

In [33] it was shown that for the rough estimation of the RCS the equivalent rectangular shape can be used instead of complex shape of the target.

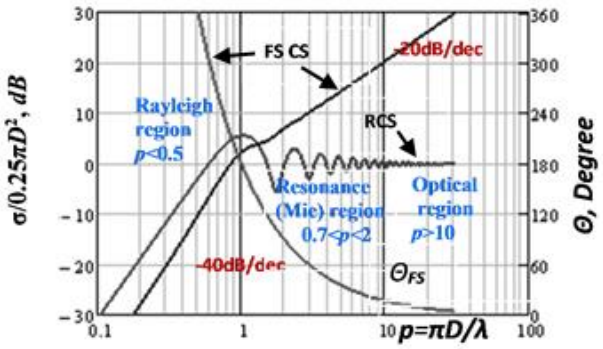

Figure 2.2.4 Width of main forward scatter lobe (right axis) and normalized RCS for the sphere (left axis). The slope of both FS and backscatter CS are -40 dB per decade in Rayleigh region, while it became -20 dB/dec in Mie and optical resonance for FS CS

According to Babinet's principle and Shadow Contour Theorem [31] the shadow radiation in the optical case is completely determined by the size and geometry of the shadow contour. Thus scattering on the target with the rectangular cross-section is equivalent to the radiation by a rectangular aperture antenna.

In far field approximation the target can be considered as an independent source of the radiation, presented by rectangular aperture antenna and magnitude of the σ_{tg} in the direction of Rx will be defined by the attitude of the aperture at every moment of motion to the incidence from the transmitter and viewing geometry from the receiver.

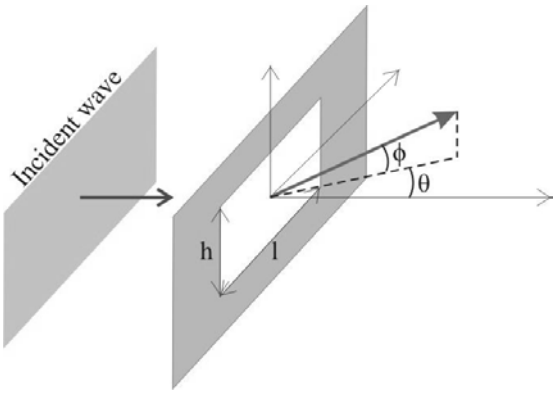

Figure 2.2.5 Plane wave incidence on the rectangular plate /aperture

For the rectangular aperture (Figure 2.2.5) FS CS is defined by:

$$\sigma_{fs}(\theta,\phi) = 4\pi \frac{\boldsymbol{A}_{\boldsymbol{eff}}{}^2}{\lambda^2} \left(\frac{\sin(\frac{\pi \boldsymbol{l}_{\boldsymbol{eff}}}{\lambda}\sin\theta)}{\frac{\pi \boldsymbol{l}_{\boldsymbol{eff}}}{\lambda}\sin\theta} \right)^2 \left(\frac{\sin(\frac{\pi \boldsymbol{h}_{\boldsymbol{eff}}}{\lambda}\sin\phi)}{\frac{\pi \boldsymbol{h}_{\boldsymbol{eff}}}{\lambda}\sin\phi} \right)^2 \tag{2.22}$$

where A_{eff}, l_{eff}, h_{eff} are time-dependant effective aperture area, effective length and effective height of target viewed from the Rx (incidence direction) [26].

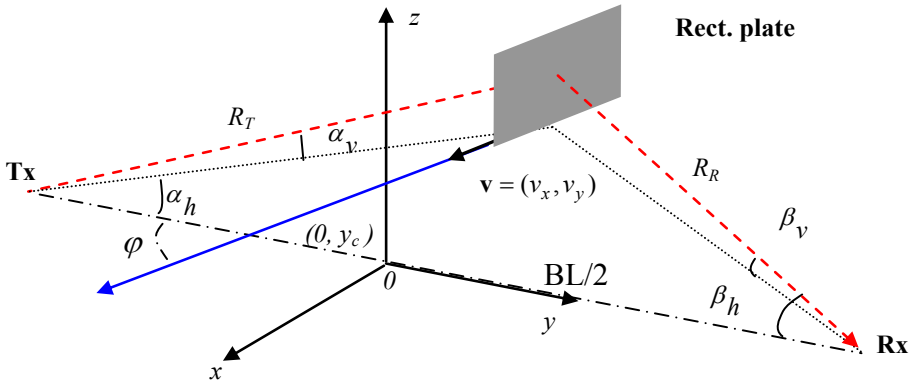

Figure 2.2.6 Geometry for rectangular aperture CS estimation

$\sigma_{fs}(\theta,\phi)$ at the receiver as a function of time for moving rectangular plate at a speed v using geometry of Figure 2.2.6 is:.

$$\begin{aligned}\sigma_{fs}(t) &= 4\pi \frac{(\boldsymbol{l}\cdot\boldsymbol{h})^2 \sin^2(\varphi-\alpha_h)\cos^2(\alpha_v)}{\lambda^2} \\ &\times\left(\operatorname{sinc}\left(\frac{\pi \boldsymbol{l}\cdot\sin(\varphi-\alpha_h)}{\lambda}\sin(\alpha_h+\beta_h)\right)\right)^2 \\ &\times\left(\operatorname{sinc}\left(\frac{\pi \boldsymbol{h}\cdot\cos(\alpha_v)}{\lambda}\sin(\alpha_v+\beta_v)\right)\right)^2\end{aligned} \tag{2.23}$$

where $\varphi,\alpha_h(t),\beta_h(t),\alpha_v(t),\beta_v(t)$ are angles representing direction of target motion and time-varying viewing azimuth and elevation angles, respectively. Doppler phase signature modulated according to rectangular plate CS is shown in Figure 2.2.7 [26].

Now we have both FS CS of extended target by Equation (2.23) and Doppler phase signature (2.19) of a point like target. Thus for the rectangular aperture target we can assume the Doppler signature to have a form [26]:

$$\boldsymbol{S}(t) = \boldsymbol{S}_{RI}(t,)\cdot\sigma_{fs}(t) \tag{2.23}$$

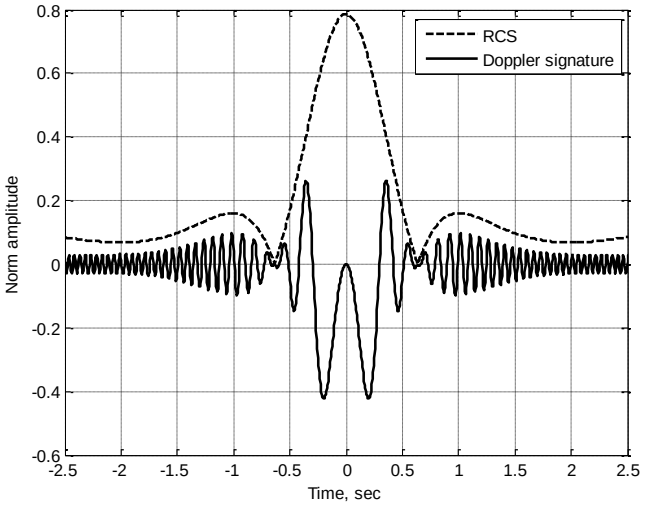

Figure 2.2.7 Signature of a rectangular plate crossing BL in the middle at 90º

2.2.5 Typical Maritime Targets of Interest

Before collecting any data from real seaborne targets and sea clutter using FS radar, vast amount of simulation work have been performed in the laboratory [26], [33], [48]. One vital part of simulation process was the calculation of the forward scatter cross section on targets of interest. To validate the use of the simplified analytical model discussed in the previous section a CST Microwave studio [106] was used for producing the RCS models of 3 typical examples of small, and potentially most dangerous targets. 3D models of manned jet-ski with usual dimension of 230cm long by 74cm wide by 130 cm high, a small inflatable boat with one man crew (230cm x 135 cm x 107cm) and an interesting case of a head of a swimmer (9 cm radius) have been calculated by [48] but only the first 2 cases will be discussed in this thesis (Figure 2.2.8).

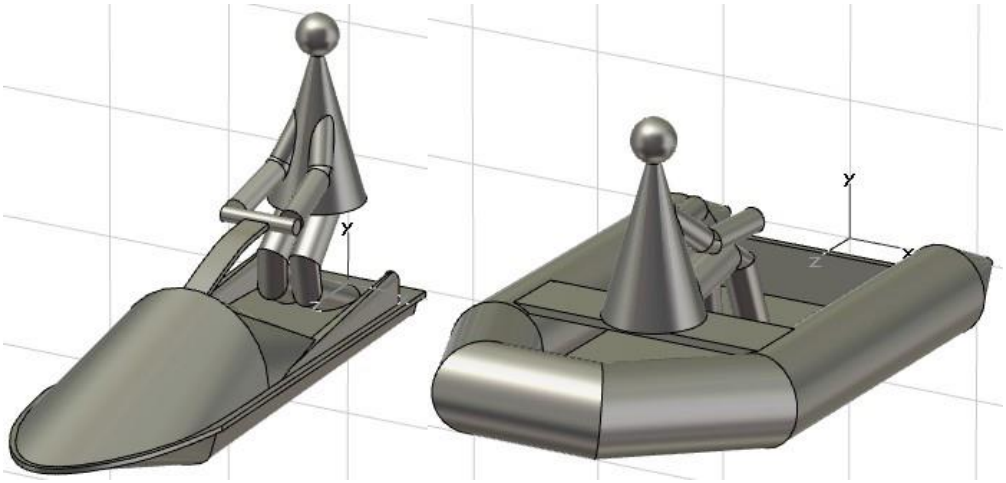

Figure 2.2.8 Jet Ski and inflatable boat models for cross section simulations[2]

Simulated targets have been considered as perfect electrical conductors, real life targets will be covered in sea water, so this seems a realistic simplification at present.

The RCS of the inflatable boat and Jet Ski have been also calculated using the simplified analytical model (Section 2.2.4) and compared with the results from the 3D simulations. The results have been shown on Figure 2.2.9 and they indicated that there is a reasonable agreement between the two RCS's calculation methods [48]. This correspondence between the two methods is good for the system study and confirmed that the analytical model is suitable for use as an approximation in further calculations.

[1] The presented models and appropriate CST modelling has been done by Mr. L. Daniel and the results are published with his permission.

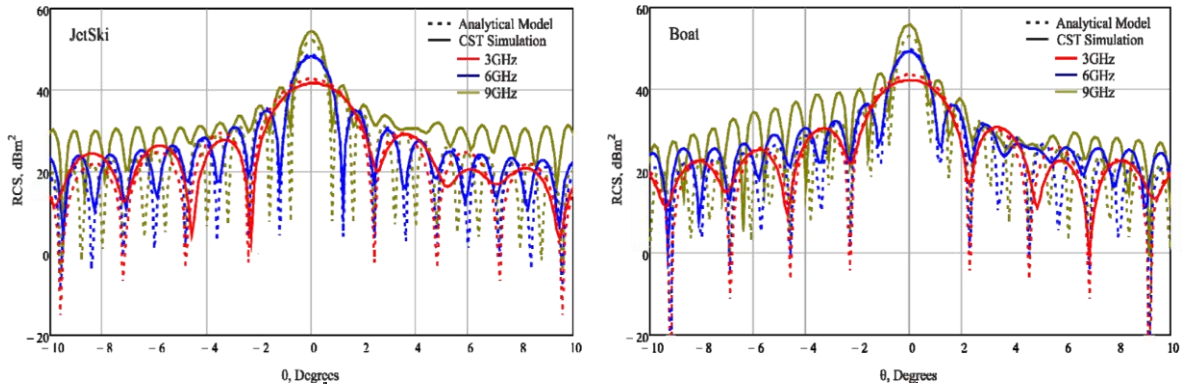

Figure 2.2.9 Comparison of simplified analytical model RCS and CST comprehensive model RCS simulation for Jet Ski and manned Boat at three discrete frequencies

2.3 Conclusions

In this Chapter a view has been given on the target Doppler phase signature analysis in FSR which merges the physical optics results with the RF engineering approach.

A concept of FSR has been described which explains a Doppler phase signature as a combination of the direct path signal and a shadow signal due to forward scattering. Analytical formulas for Doppler phase signature at the output of RSSI receiver as well as simplified Forward Scatter Cross Section (FS CS) model have been presented [26].

Analysis and simulations of the FS RCS of small seaborne targets such as Jet Ski and inflatable boat has been applied by [48] using CST modelling. A simple analytical approach has been proposed for replacing a real complex shaped target by a rectangular aperture and it has been justified.

Chapter 3 Test Equipment and Methodology

Considering the deficit of information, experimental data and therefore verified models, the next step in this research was to undertake an experimental program of very low grazing angle, forward scatter, land and sea based measurements. In order to accomplish these measurements a prototype FSR transceiver was developed (essentially one link in the network chain) by the MISL [42], [43], [48].

The radar was used to characterise and understand forward-scatter sea clutter by an experimental study program, starting with a relatively narrow beam antenna and CW modulation.

3.1 Experimental Systems

The main goal was the development of prototype low grazing angle maritime FSR which could be used for testing in maritime environment and demonstrate that the radar could be used for detection of difficult small targets (such as small inflatable boat and Jet Ski) in relatively rough sea conditions. Initially, a prototype 7.5 GHz FSR equipment has been developed and further on in the process 24 GHz radar system has been built. Presently, a prototype 434 MHz equipment has been designed but it is not of interest of this thesis. A database showing all the development stages and FSR equipments is presented on Table 3.1.

Table 3.1 Radar upgrades database

Year	Version	TX	Rx	Changes in the system	Calibration Curves
Nov 2009	1.0	AWG	Oscilloscope and First Doppler Box	N/A	Old
Aug 2010	2.0	Prototype Tx7.5 V1	Oscilloscope and Receiver V1(Receiver and Doppler box)	N/A	Old
Oct 2010	3.0	Prototype Tx7.5 V1	Receiver V2(Same receiver and improvement ii Doppler box)	N/A	New
Nov 2011	4.00	Prototype Tx7.5 V1 and 24GHz prototype Tx24 V1	Rx7.5 V2 and new Rx24 V1	N/A	None
Apr-13	5	Prototype Tx7.5 V1, 24GHz prototype Tx24 V1 and 430MHz Tx V1 prototype	Rx7.5 V2, Rx24 V1 and 430MHz prototype	N/A	Newest

7.5 GHz FSR Test Equipment

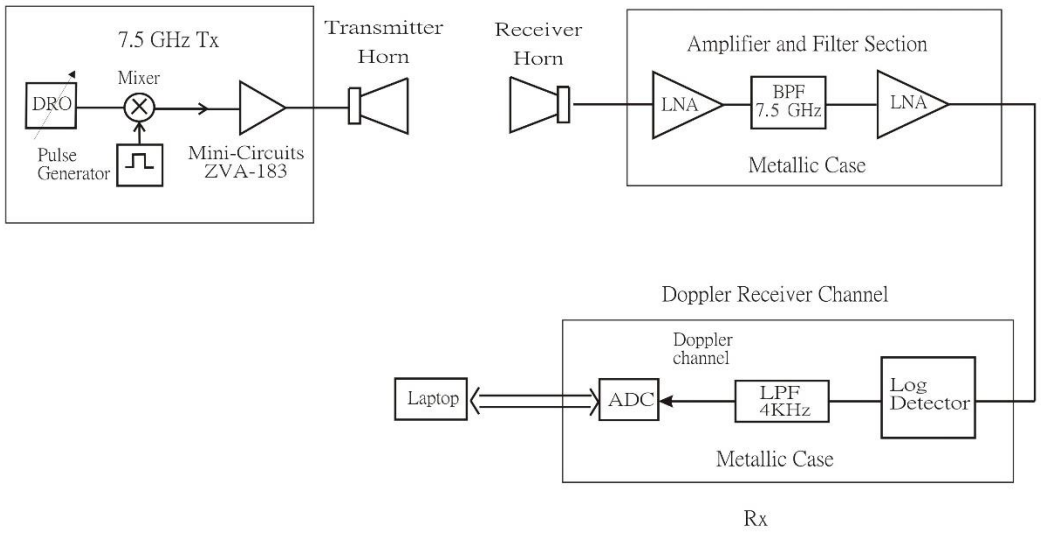

Figure 3.1.1 Block diagram of the 7.5 GHz prototype FSR equipment

The development of the 7.5 GHz FSR passed through a few hardware versions among the years of 2009 and 2012 as shown on Table 3.1. The present 7.5 GHz FSR equipment is presented here and a complete description of the development stages, radar subsystems, used antennas etc. is given in Appendix A.

Block diagram of the current 7.5 GHz radar equipment including the transmitter and receiver modules is presented on Figure 3.1.1. The low cost and portable transmitter was developed by Dr. E. Hoare and the receiver unit was developed by Dr. E. Hoare and Dr. V. Sizov. The transmitter works in 7.5 GHz CW mode and also in 30 MHz, 100 MHz and 1 GHz bandwidth Gaussian modulated pulse centred at 7.5 GHz. A hardware switch is used for changing the transmitting bandwidths and pulse repetition frequencies (PRF) shown on Figure 3.1.2.

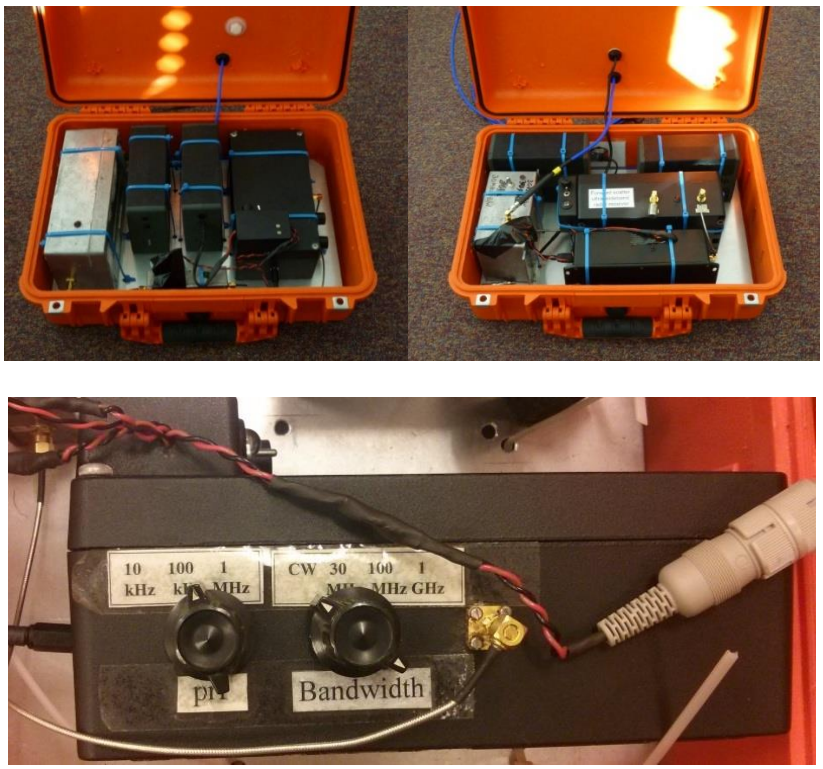

Figure 3.1.2: 7.5 GHz prototype transmitter (on the top left) and receiver (on the top right) and 7.5 GHz Wave Generator box (bottom) part of the Tx

The transmitter and receiver are fitted in portable, water light, crushproof and dustproof cases (as shown on Figure 3.1.2). This gives 2 possible experimental configurations for placing the transmitter and receiver: one is with directional or omni-directional antennas on the on the shore next to the sea/ocean as shown on Figure 3.1.3; and another opportunity is mounted on a 60 inch Ringo and released in open sea.

Figure 3.1.3 7.5 GHz transmitter placed on the shore using directional antennas mounted on a tripod (left) and 7.5 GHz transmitter mounted on a 60 inch Ringo (right)

The 7.5 GHz transmitter case is being held in place by compression from the surrounding Ringo tube as shown on Figure 3.1.3. To keep the Ringo in a stable position on the sea surface, it was attached to two anchors at the ends of 40 m. rope. The antenna is mounted on a pole approximately 1.5 meters above the sea surface. Measurements of the maximum deviation of the transmitter position have been made using a GPS recording device [107] mounted on the Ringo. The anchored Ringo was left for 6 hours in open sea with the GPS logger turned on (recording every second) in order to make sure that it won't shift much from the initial position. Figure 3.1.4 presents the GPS logger data applied on Google Maps and it could be observed that the maximum deviation was 8 meters over the tested period of time.

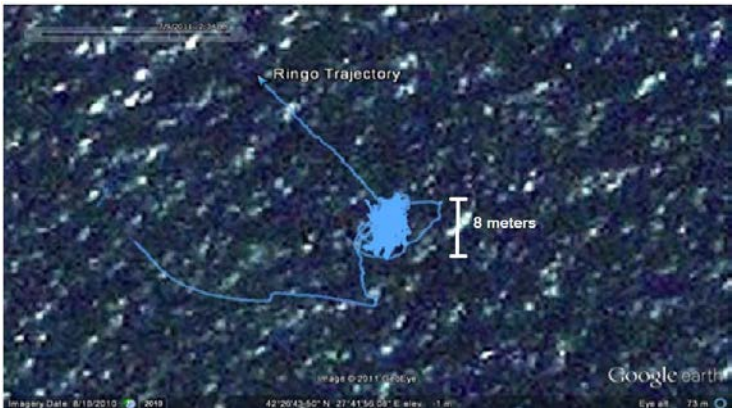

Figure 3.1.4: Six hour GPS track of the anchored Ringo tube in open sea

24 GHz FSR Equipment

During 2011 MISL was in the process of developing a 24GHz Forward Scatter Radar for comparative testing with the 7.5 GHz system. A block diagram of the complete experimental 24 GHz hardware for data acquisition is given in Figure 3.1.5.

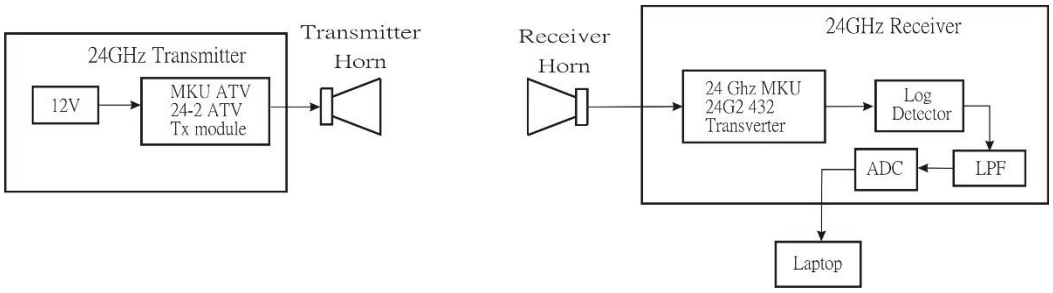

Figure 3.1.5 Block diagram of the 24 GHz equipment

The transmitter configuration is simplified by using off the shelf 24 GHz transmitting module - MKU ATV 24-2ATV built by company called 'Kuhne Electronic Microwave Components' [108] and a horn antenna designed by Dr. E. Hoare. These antennas have 20 degrees beamwidth in both planes. The output power of this module is typically 300mW. Photos of the 24 GHz transmitter and receiver are shown on Figure 3.1.6.

Figure 3.1.6 24 GHz FSR transmitter mounted next to the 7.5 GHz Tx

The receiver uses off the shelf 24 GHz MKU 24G 2 432 USA Transverter module designed by the same company as the transmitting module [109]. Then the signal is passed to log detector, followed by the 16-bit, 200 Hz analog-to-digital converter USB-1608FS (detailed information is provided in Appendix C) and afterwards the received signal is processed by computer.

3.2 Experimental Sites

3.2.1 Equipment laboratory testing and calibration

The process of experimental testing has been progressive. Initially testing was performed in an anechoic chamber to measure system performance and establishes that all equipment functioned as designed before moving to more extreme environments. Following this field trials were carried out on solid ground (grass pitch) to validate the power budget and operation at larger ranges and ultimately sea trials were carried out. A summary of some of the results follows and data is shown which is received using the DRC [42], [43].

System measurements in the anechoic chamber

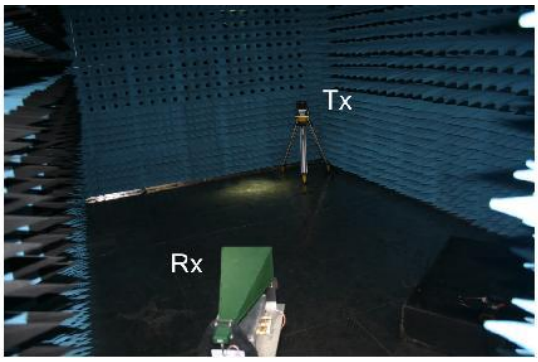

Figure 3.2.1 Initial experiment arrangement in the anechoic chamber

Anechoic chamber tests were used to measure the initial performance of the FSR. The measurement arrangement is shown in Figure 3.2.1, with the transmitter and receiver facing each other at a separation of approximately 6m. The AWG was used as the signal source and the received data was recorded on the DPO [110].

A number of experiments were carried out using targets including a swinging pendulums and fan agitated strips of aluminium foil of different lengths to generate broadband clutter as shown on Figure 3.2.2.

Figure 3.2.2 Controlled Doppler generation from a) swinging pendulums b) fan agitated strips of aluminium foil of different lengths to generate broadband clutter

One of the significant benefits of this FS radar system is the ability to measure Doppler frequencies to below 1 Hz. In conventional radar this would be masked by the noise contributions from the transmitter/receiver system.

Very low Doppler frequencies were generated by a low RCS rotating target for repeatable single frequency target simulation measurements, a swinging pendulum was also used to simulate complex motion targets and broadband clutter was generated using fan agitated aluminium strips of progressively decreasing length. Results of the Doppler processing of single frequency, low RCS targets shows that extremely low Doppler frequencies (<1Hz) can be measured with this system. Figure 3.2.3 shows separate superimposed measurements of the Doppler target at frequencies from 5 Hz to less than 1Hz [42], [43].

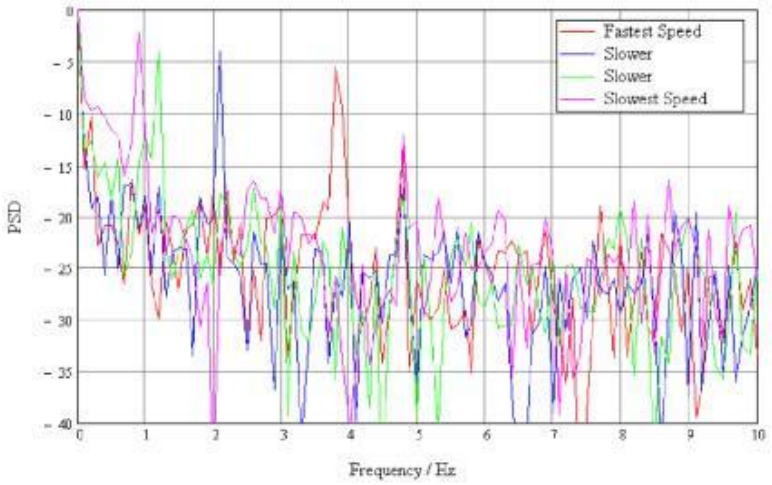

Figure 3.2.3 Superimposed Doppler frequency measurement

3.2.2 Equipment measurements on field

Outdoor measurements were made initially over tarmac using a 60 m range at the rear of the department as shown on Figure 3.2.4 and Figure 3.2.5. This was to evaluate the field operation of the equipment, including petrol generators, Tektronix units, radars and all

ancillary equipment needed for autonomous trials. This also included arranging for all of the necessary equipment and personnel to be able to be transported in a single Land Rover. Subsequently the loaded vehicle was taken to one of the University sports fields for long range measurements [42], [43].

Figure 3.2.4 Sports field power budget measurements: a) AWG, generator and transmitter. b) receiver, scope, Doppler receiver & generator

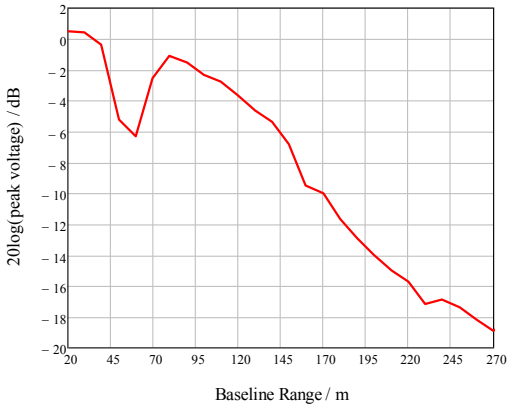

Figure 3.2.5 First range profile over grass, range 300 m

Further trials were undertaken to measure the Doppler signature of different targets over grass at Hornton Grange gardens within the university premises. Figure 3.2.6 shows the CW measurement of a running human from the first Doppler trials [42].

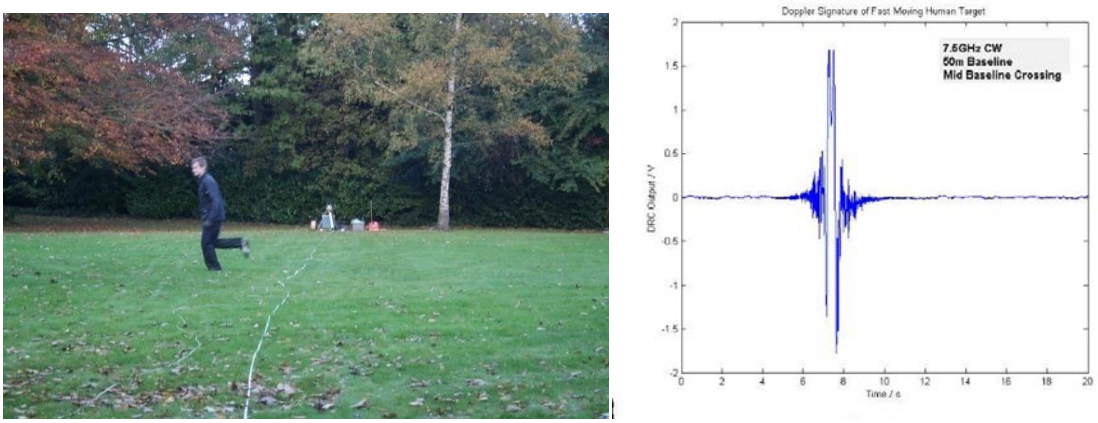

Figure 3.2.6 Running human target over grass and CW Doppler signature

Targets crossed the middle of a 50 m baseline on a trajectory perpendicular to the baseline. The results indicated that the clutter level is significantly lower than that obtained using the low frequency ground NB system [96]. This is due to the much higher operating frequency and the use of highly directional antennas.

3.2.3 Maritime environment measurement locations

Langstone Harbour measurements

Once the equipment was proved to be working effectively for ground data acquisition, the next experimental phase was the first sea trials. Many test sites were investigated prior to selecting the one most appropriate for initial maritime experiments. At each location spectrum surveys showed high powered marine radars in place, operating close to the frequency band used by the FSR system, indeed in the very first tests, the receiver was saturated due to these transmissions. There was a clear need to develop very specific band pass filters with deep notches at this marine radar frequency for placement at the front end of the radar receiver [42].

Figure 3.2.7 Brixham harbour, high breakwater and no waves

Figure 3.2.7 shows Brixham harbour which is characteristic of many of the sites assessed and illustrates some of the difficulties in site selection. The breakwater is much too high above the water to enable the radar to be placed close to the sea, there is difficulty getting down to the waterside, there is no vehicular access to beach or breakwater area (either impractical or prohibited) and finally water inside the breakwater has no significant waves to generate clutter [42].

Figure 3.2.8 Langstone Harbour test site

After evaluating many sites Langstone Harbour entrance, near Portsmouth was chosen as the test site (Figure 3.2.8). This site had a clear 300m of open sea with the ability to place the radars at the edge of the sea and gain vehicular access and sea waves were unobstructed.

Figure 3.2.9 shows the position of transmit and receive antennas, the baseline distance was approximately 300m. Also indicated in the figure is the marine radar for which the notch filter on the receiver is required.

Figure 3.2.9 Sea trials site across the entrance to Langstone Harbour

This site was chosen due to the relative ease of access to either side of the seaway and also as access could be gained right to the water edge.

The experimental goal was not solely to measure target signatures, but to make measurements of the sea surface clutter. The following photographs on Figure 3.2.10 and Figure 3.2.11 illustrate the trials arrangements at Langstone Harbour entrance between Hayling Island and Portsmouth [42].

Figure 3.2.10 Transmit site at Langstone Harbour

Figure 3.2.11 Data collection using the DPO and Doppler receiver at Langstone Harbour

Coniston Water – Lake District, Cumbria, UK

During 2010 three day measurements has been accomplished on fresh water at Coniston Lake in the Lake District. The purpose of the trials was to measure the maximum effective detection range for the newly acquired MISL small boat target (further information about the boat in Appendix B) and such kind of measurement would have been impossible to perform in the Langstone Harbour. With its max length of 8.8km (5.5mi) and max width of 793m (0.49mi) Coniston Lake was just the right size for taking trial at long baselines. On

Figure 3.2.12 are shown the Receiver and Transmitter positions during the measurements. On Figure 3.2.13 (a) and (b) photos from the measurements are presented.

Figure 3.2.12 Sea trials site on the Coniston water lake

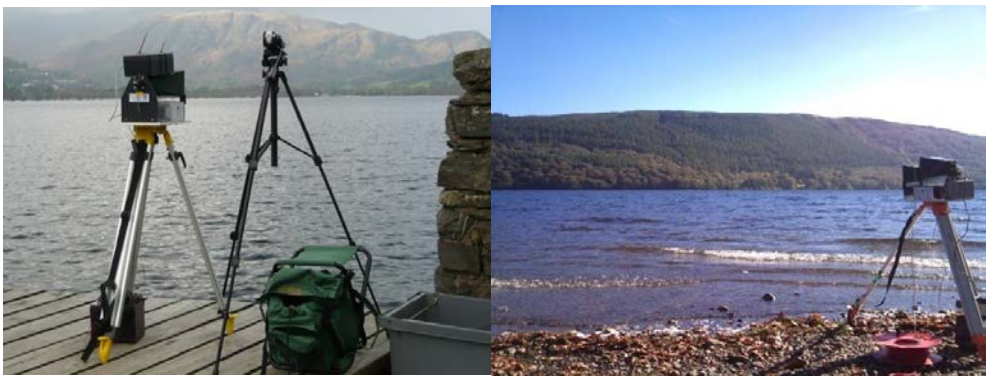

a) **b)**

Figure 3.2.13 FSR transmitter (a) and receiver (b) mounted on the shore of the lake

It was also an opportunity to do measurements in lake conditions where the waves would have different shape and much lower height. During the trials, lake clutter data was recorded where the water was extremely calm (mirror). The pointing accuracy between the transmitter and receiver during the Lake Coniston measurements was assessed by using monoculars mounted next to the Tx and Rx antennas.

Sozopol, Bulgaria measurements

During 2011 MISL group collaborated on a project with Prof H. Kabakchiev from Sofia University, Bulgaria. A major part of the project was organising open sea trial measurements using FSR system in Black Sea. This was opportunity for the MISL team to test the efficiency of the omni-directional antennas on the newly designed buoy mounted transmitter and stationary receiver. All the specifications of the radar system have been mentioned previously in the chapter.

Figure 3.2.14 Position and photo of the Transmitter in open sea. The position of the Receiver is also shown on land

Various locations on the Black Sea coast have been investigated as a potential trials site. After sequence of discussion Sozopol city shown on Figure 3.2.14 seemed to be very convenient location for performing measurements with its two islands nearby (St. Ivan and St. Peter) and with the relatively big harbour for the area. Nevertheless, a team needed to be sent to double check the location before performing measurements for a week. An old naval base situated next to the harbour was one of the major concerns.

After significant efforts in short time for redesigning the existing maritime system and in transportation of the equipment (around 270 kilogram pallet filled with boat, engine, Ringo, anchors, transmitter, receiver, repair kit and much more), seven day trials were performed in the beginning of the summer of 2011 around the area of Sozopol, Bulgaria.

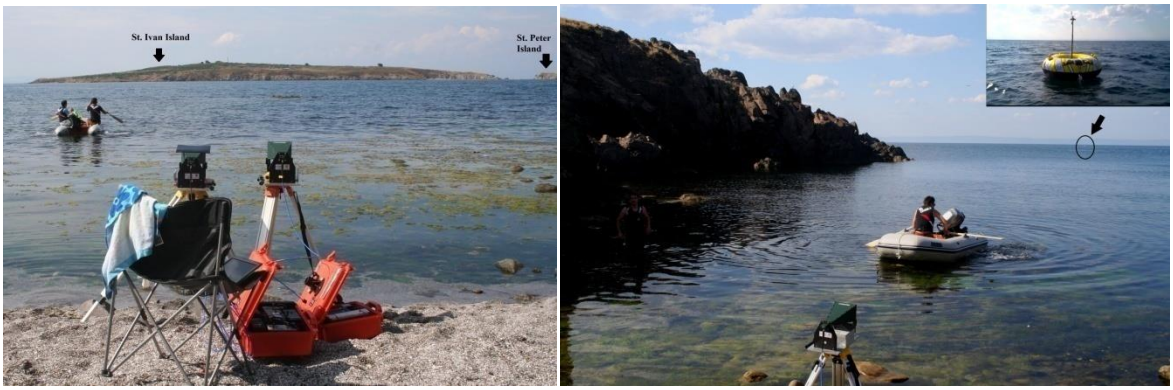

Figure 3.2.15 Photos taken throughout two measurements around Sozopol and the islands around

The figures above (Figure 3.2.15) are example for positioning of the system during the trials. Both St. Ivan and St. Peter Island were inhabited by thousands of seagulls which introduced interference in the recorded data.

The sea trials were completed in the beginning of the summer when the average temperatures in the area were 23 degrees Celsius. This was in advantage for the MISL lab enabling the team to work in good weather conditions. However there were trial days spent on the St. Ivan and St. Peters islands where the temperatures were getting much higher and respectively the laptop used for recording the data had overheating problems.

Weymouth, UK

Weymouth site (shown on Figure 3.2.16) was chosen due to easy access to the shore and the Weymouth Harbour. This was giving us the opportunity to do various distance sea clutter measurements (600m up to 3.5 km) but also it was thought to be a good place to record high sea states during the winter season. As in Lake Coniston case, monoculars were used in order to point the Tx and Rx in the same direction.

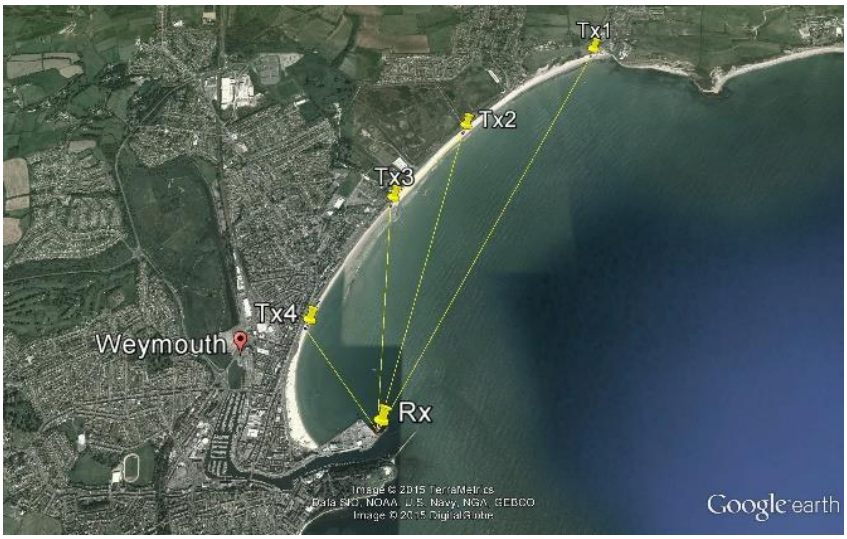

Figure 3.2.16 Tx and Rx locations during trials in Weymouth, UK

3.2.4 Condition monitoring and data truth.

A fundamental part for each experiment was monitoring of the weather conditions, photo and video records of the trials and GPS coordinates of the radar system and the MISL target boat. These monitoring devices provide information about the accuracy of the FSR Sea based measurements. Respectively this allowed more precise further analysis of the data.

Tide tables of the sea area of interest were collected and monitored between and during every trial measurement. This was extremely important for Langstone harbour where the difference between the low and high tide could have been more than 4m.

MISL portable land based weather station was used for observing the atmospheric condition and providing the group with data about the wind speed and direction, temperature and rain level.

Different video recording devices have been used through the trials. CCTV camera mounted on the top of our university vehicle was recording the first FSR measurements. The camera was using the car battery as an energy supply and the video records were directly recorded on a laptop. A replacement of the CCTV camera was a portable video camera which offered relatively long lasting and removable battery and enough memory storage. The next generation cameras were waterproofed GoPro's Generation 2 with 170 degree viewing angle and excellent video resolution [111].

Photographs were made throughout the trial using two semi-professional cameras – Nikon D5100 with 18-55mm lens [112] and Cannon camera with similar lens [113]. Depending the configuration of the measurement the cameras could have been used from both transmitter and receiver side.

Software has been provided with the devices giving you the opportunity to overlay the tracking data on Google earth map.

Figure 3.2.17 Condition monitoring throughout maritime trials.Compact waterproof GPS tracking devices has been purchased and used for recording the position of the Radar system and the MISL boat

Compact waterproof GPS tracking devices has been purchased and used for recording the position of the Radar system and the MISL boat.

Software has been provided with the devices giving you the opportunity to overlay the tracking data on Google Earth map.

3.3 Experimental Programme and Methodology

Experiments were performed using a prototype maritime FSR system developed by the MISL. The trials were executed at different places which have been explained in the previous sub chapter.

The objective of the experiments was to characterise and understand forward scatter sea clutter, test the system parameters of the radar and record maritime targets of opportunity crossing the baseline.

Table 3.2 Maritime experiments - different test sites

Date and Time	Experiment Location	Water	Depth, m	Number of Records
25-26 Nov 09 16-18 Feb 10 21-23 Mar 10 1-3 Aug 10 20-22 Nov 11	Portsmouth area, UK	Littoral water, across Langstone harbour	10-15	543
3-4 Aug 10	Portsmouth, Hampshire, UK	Littoral water, off coast	10-15	47
5-11 Jul 11	Sozopol, Bulgaria	Deep water	25-35	213
7-9 Oct 10	Coniston Water, Cumbria, UK	Fresh water	10-20	85
30 Apr- 2 May 13	Weymouth , Portland,UK	Littoral water	10-15	146

The prototype FSR equipment has been deployed at different maritime sites providing a wide set of environmental conditions ranging from almost perfect mirror surface (Lake Coniston, UK) to rough, long range, deep water sea states (Sozopol, Bulgaria). The maritime experimental locations, dates and number of records are summarised in Table 3.2 and detailed information is provided further in the Section.

3.3.1 Maritime Experimental Set-up

Figure 3.3.1 illustrates the configuration of the low grazing angle forward scatter radar for maritime application during one of the first sea based measurements across the entrance of Langstone Harbour.

The AWG has been used as a transmitting device followed by amplifier and variety of horn antennas. The transmitter generated CW signal at H band carrier frequency, fc of 7.5GHz. The Tx and Rx antennas were mounted on tripods and their characteristics (height and polarisation) have been changed throughout the experiments. A petrol generator has been used for power supply of the AWG and a 12V battery for the amplifiers [42], [43].

On the other side of the shore two output channel low noise receiver with 60 dB gain was mounted to the Rx antenna. The first RF channel fed the DPO as a raw signal capture device. The other one was used by a Doppler processor to allow simultaneous capture of Doppler data on a PC along with the raw RF signal in the oscilloscope. In this thesis we are mainly focused on the data from the Doppler receiver so all measurements from the Oscilloscope will not be discussed. The Doppler receiver has been explained in details in Appendix A. Data from both RSSI and Doppler channel of the Doppler box is digitalised and transferred on computer via USB and stored on a PC hard drive. Matlab GUIs has been used for communication with the hardware and later processing of the experimental data [114]. The communication software have been designed by Dr. M. Gashinova and Mr. L. Daniel and used for controlling the parameters of the Doppler box and the transfer of data. Two of the programs were used for acquiring data with the FSR equipment.

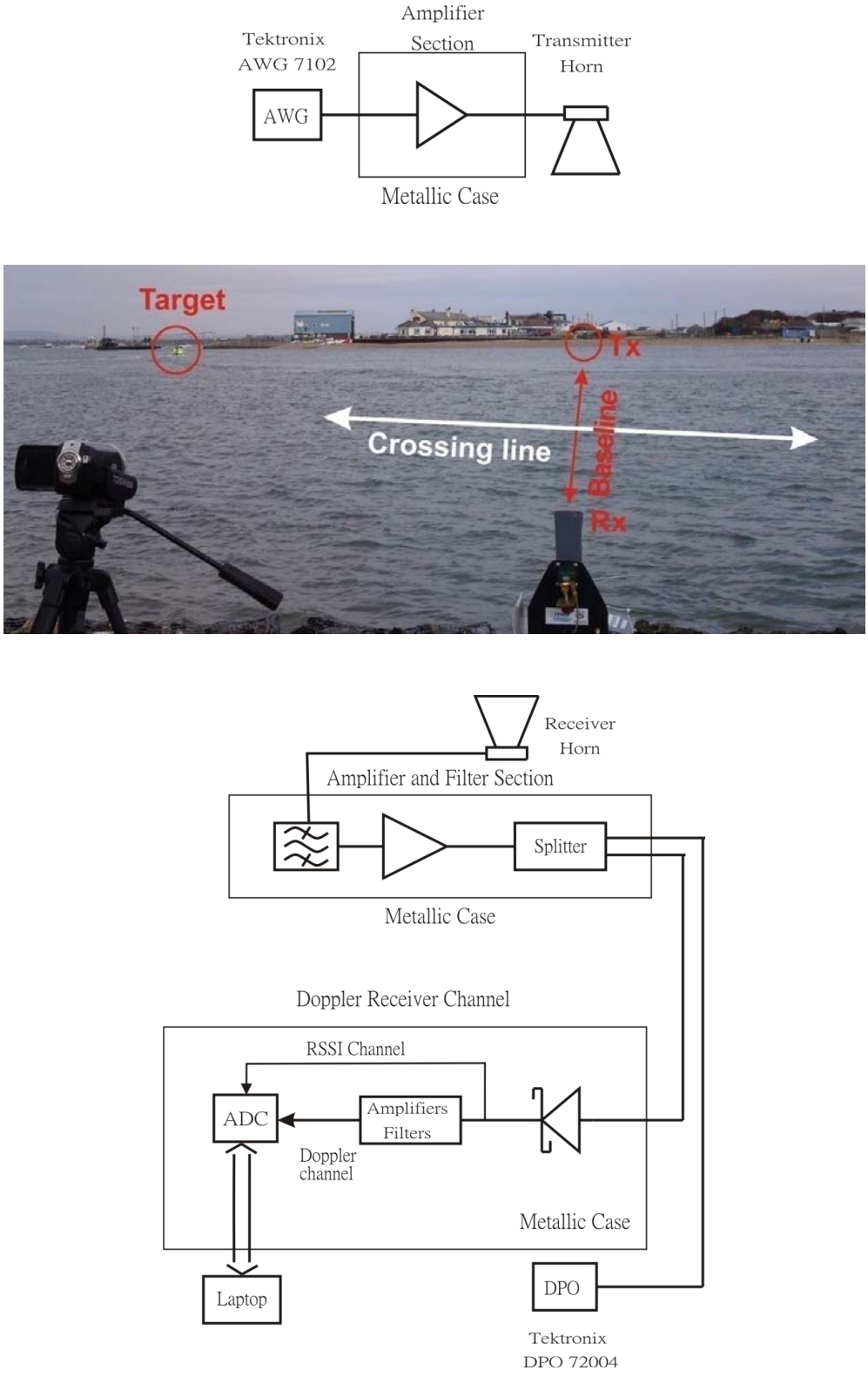

Figure 3.3.1 Forward scatter radar configuration for experiments in maritime condition

3.3.2 Collection Process

26 November 2009 Langstone Harbour

The collection of data started late 2009 in the area of Langstone Harbour entrance, near Portsmouth. During these trials FSR "Version 1" equipment has been used (according Table 3.1). One day measurements were conducted where the main goal was testing the system, recording sea clutter and target of opportunities. A large number of clutter measurements were recorded. A 316m has been set as a baseline of the measurements. 'Flann' and 'Wide' antennas (Appendix A) at different heights and polarisations have been used throughout the day. An example of clutter record from both channels is shown on Figure 3.3.2.

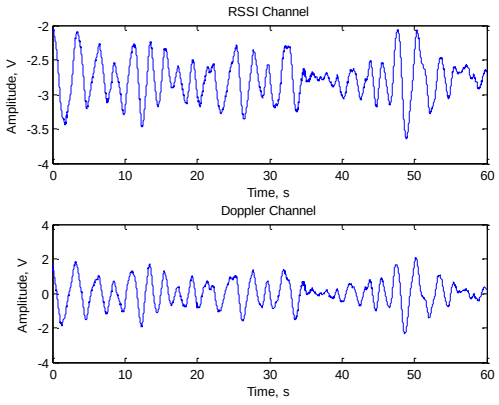

Figure 3.3.2 Sea clutter on the output of the RSSI and Doppler channel

The wind speed for the clutter measurements varied between 3.7-4.5mph (gusts of 6-8.3 mph), however in the littoral area, it is very hard to classify the sea surface in terms of a sea state (normally deep, open developed seas are required). In this test site there was a high degree of tidal influence on the surface structure [42].

The sea clutter records have been compared with the clutter records previously acquired at the open field (Section 3.2.2). First observation on the sea clutter showed that it is less

spikier and following more sinusoidal shape in time domain compared to the surface land clutter. Also the clutter magnitude was lower at the observed sea condition compared to open field. This effect could be explained by the strong contribution of wind, trees and grass in surface land clutter as observed [115]. Further investigation in this direction is needed.

During measurements at Langstone, a small rigid inflatable, with two man crew crossed the radar baseline and Figure 3.3.3 shows the DRC output signal for this transit. The signature of the boat itself is very much above the surface clutter level and the boat is clearly detectable. An image taken of the boat during data capture is shown in Figure 3.3.4 [42], [43].

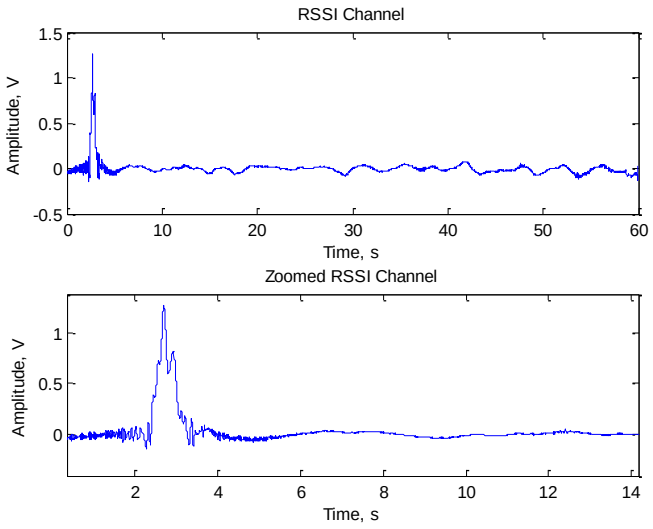

Figure 3.3.3 Doppler signature of small inflatable with 2 man crew

Figure 3.3.4 Small inflatable with 2 crew crossing baseline (Tx is 2 yellow dots)

21-23 March 2010 Langstone Harbour

Three day measurements have been completed few months later. The objective of the trials was collecting more sea clutter data and to record crossing of radar baseline with a reference target at different distances – The MISL boat (Figure 3.3.5 and Figure 3.3.6). Targets of opportunity such as ships, yachts and jet ski were recorded as well.

Figure 3.3.5. MISL boat crossing the baseline

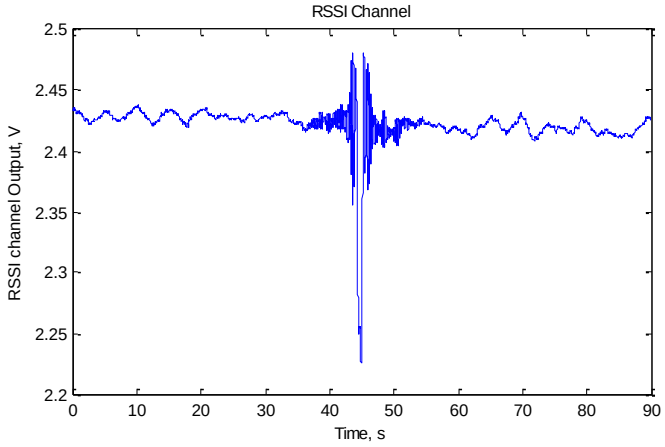

Figure 3.3.6 MISL boat target signature and clutter

FSR "Version 1" equipment has been used as presented on Table 3.1. "Flann" antennas have been used throughout the 3 days of the measurements. The height of the antennas was varying from 1 up to 3 meters and both vertical and horizontal polarization has been used. The result from these measurements could be found in Section 1.3 of Chapter 4.

Two set baselines between transmitter and receiver have been used during the tests – 330m and 550m shown on Figure 3.3.7.

The wind speed throughout the days varied from less than one mile till up to 5mph. A waterproof GPS device has been used for tracking the reference inflatable boat during the crossings and to record the positions of transmit and receive devices.

Figure 3.3.7 Two of the baselines throughout measurements on the Langstone harbour 1-4 August 2010 Langstone Harbour

Measurements with a new transmitting device have been accomplished later that year. It was a replacement of the substantial wave generator which allowed more flexibility in the positioning of the Transmitter (FSR "Version 2" according to Table 3.1). The coordinates were recorded by the GPS device mounted on the system. The receiver coordinates have been collected as well.

Crossings of the baseline with a 65cm metallic sphere (another reference target) towed by the MISL boat has been completed during that trials in the Langstone Harbour (Figure 3.3.8) [91].

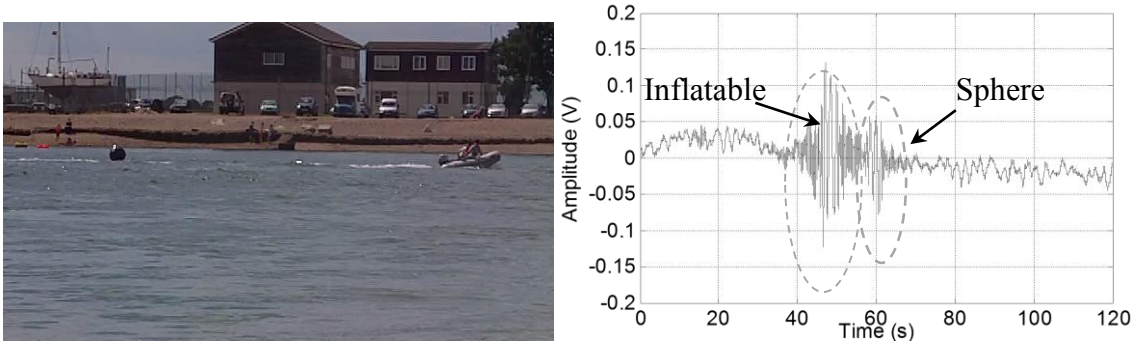

Figure 3.3.8 (a) Small inflatable boat towing the target sphere, crossing a 300m baseline across Langstone harbour (site A); (b) FSR Doppler signatures of the inflatable boat and the towed calibration sphere measured at 7.5 GHz

During the third day of the measurements, the sea state was much higher than the MISL team has experienced before. Records of sea clutter and targets crossing the baseline have been recorded. The sea state was roughly calculated to be between 2 and 3 by the Douglas scale [49]. Figure 3.3.9 (a), (b) and (c) is showing respectively a photo of the crossing, the RSSI output from the Receiver with birds, MISL boat and Harbour master boat crossing the baseline and high pass filter (HPF) RSSI output.

(a)

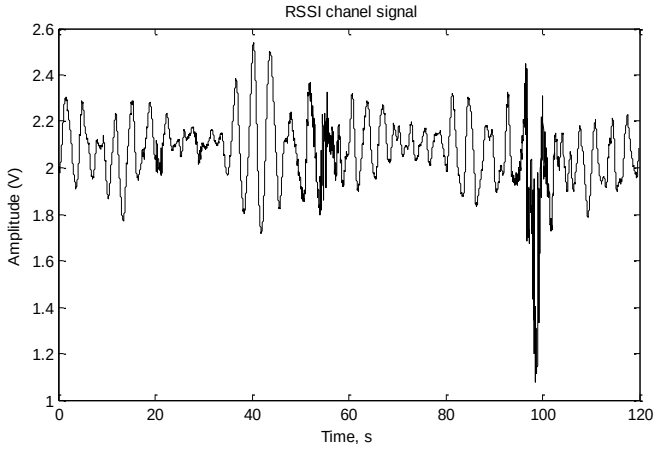

(b)

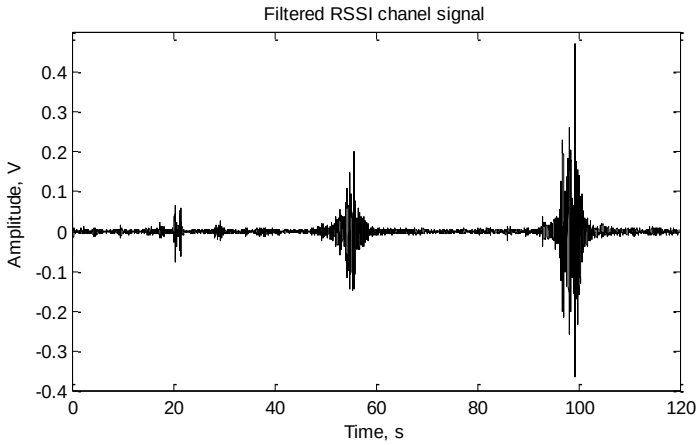

(c)

Figure 3.3.9 a) Photo during one of the FSR measurements – seagulls (15-25s), MISL boat (50-65s) and target of opportunity (90-100s) crossed the radar baseline; b) the RSSI output from this signal and c) RSSI output after applied HPF

In order to provide insight in to how clutter power depends upon the transmitter-receiver distance, the 7.5GHz radar equipment has been tested over ranges up to 2 km. The measurements have been conducted on the Portsmouth shore – about a mile South West from the Langstone harbor. The stationary receiver has been located on the Portsmouth beach and the transmitter has been mounted on the MISL inflatable boat in open sea. This allowed increasing relatively fast the radar baseline so the records had the same or very similar sea and weather conditions. During the measurements the boat/Tx device changed 5 location

shown on the Figure 3.3.10. During the records the inflatable boat was anchored for more stability.

Figure 3.3.10 Location of the trial and the positions of the Tx and Rx

Figure 3.3.11 show preliminary results of the leakage and clutter powers as function of the baseline distances shown on Figure 3.3.10 and measured at 7.5 GHz. The effect is yet to be explained and further analysis are presented in Chapter 4.

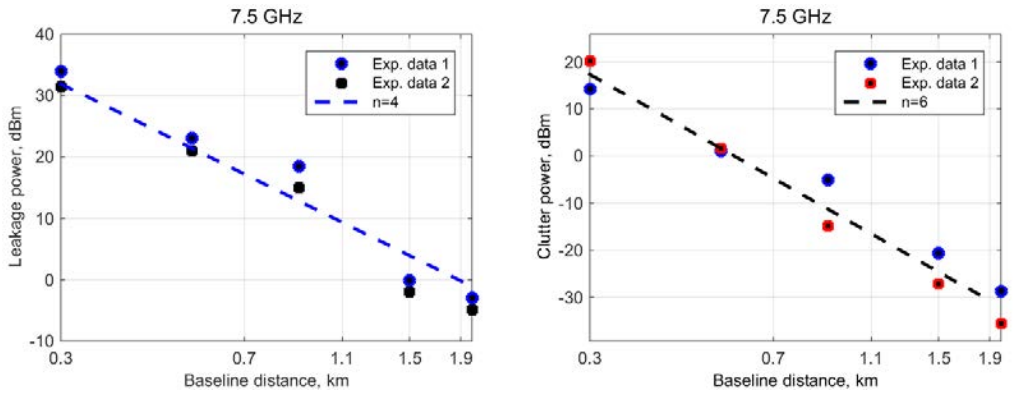

Figure 3.3.11 Leakage and clutter received powers against range, measured at 7.5 GHz.

07-09 October 2010 - Coniston water, Cumbria, England

In order to determine the maximum detection range of the system, the decision was made to test on the calmest surface possible. Therefore it was decided to move from sea to lake based trials, thus this section contains information gathered from trials on Coniston Water in the Lake District (Figure 3.3.12). This test site also gave us the ability to ground mount the antenna's at a variety of ranges; this is not possible at the Langstone harbour test site [110]. During this trials FSR "Version 3" has been used according to Table 3.1.

Figure 3.3.12 Location of the Tx and Rx and their baseline during the experiments at Coniston water

First RSSI target signatures with omnidirectional antennas have been recorded on the last days of the trials presented on Figure 3.3.13.

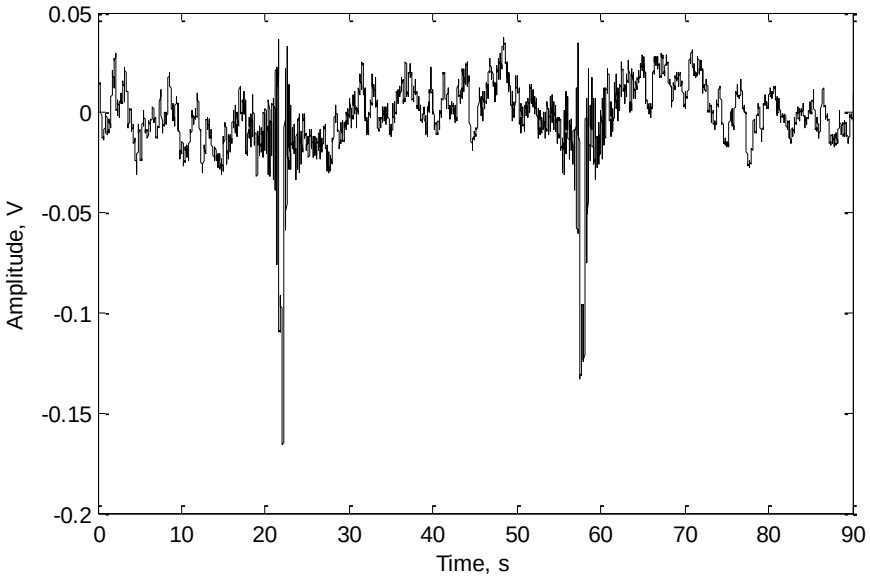

Figure 3.3.13 RSSI signal of MISL boat crossing the 730m baseline using omnidirectional antennas

05-11 July 2011 Sozopol, Bulgaria

In order to compare the effect of the use of omnidirectional antennas on the system, sea trial measurements were performed in Sozopol, Bulgaria and at a later date in the UK to double check some previously obtained results. The configuration of the Buoy mounted radar has been shown previously in the dissertation, with the height of the omnidirectional antenna being approximately 1.5 meters. In order to understand the effect of the antenna movement on the Doppler Spectrum, measurements with fixed antennas on the edge of the sea and with swaying antennas in open sea have been made. FSR "Version 3" (Table 3.1) has been used throughout the trials in Bulgaria.

In Figure 3.3.14 the topology of the test site indicating the position of transmitter and receiver for the case of fixed antennas is shown. The receiver is placed on a rock on St. Ivan's island approximately 1m above sea level, mounted with an omni-directional antenna.

At the other side the transmitter was mounted near the edge of the sea also approximately 1 meter from sea level. The Transmitter configuration was 7.5GHz CW and a distance between the transceivers of approximately 350 meters.

Figure 3.3.14 Topology of the islands and position of the Transmitter and Receiver

In order to compare the effect of the antenna movement on the Doppler spectrum the Transmitter mounted on the Ringo tube has been moved to open sea, the position is shown on Figure 3.3.15 including a photo of the equipment. The distance between the Transmitter and Receiver was about 450m.

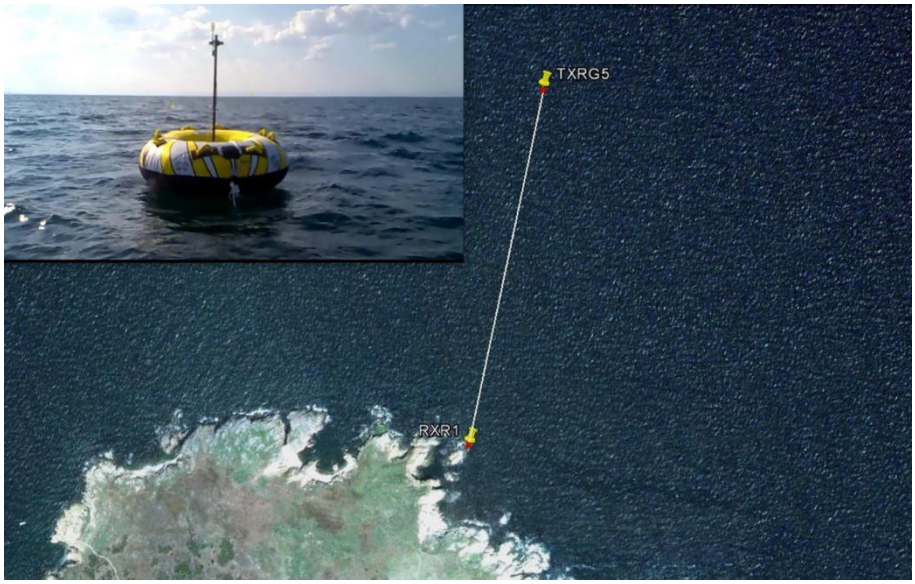

Figure 3.3.15 The transmitter is mounted on a Ringo about 450m from the stationary receiver

30 April – 3 May, 26 – 28 Nov 2013 Weymouth, UK

Few maritime measurements were performed in Weymouth using FSR "Version 5" equipment (Table 3.1). Because of the easy access to the Weymouth shore and harbour, MISL team was able to perform sea clutter measurements at 4 different distances (0.8 km, 1.6 km, 2.4 km and 3.4 km) with 7.5 GHz equipment and 24 GHz equipment which is presented on Figure 3.3.16.

Attempts to record high sea states have been made but unfortunately few of the times the high sea state was too low and in other cases the wind and sea state was too high which was dangerous to perform any kind of measurements in such kind of environment.

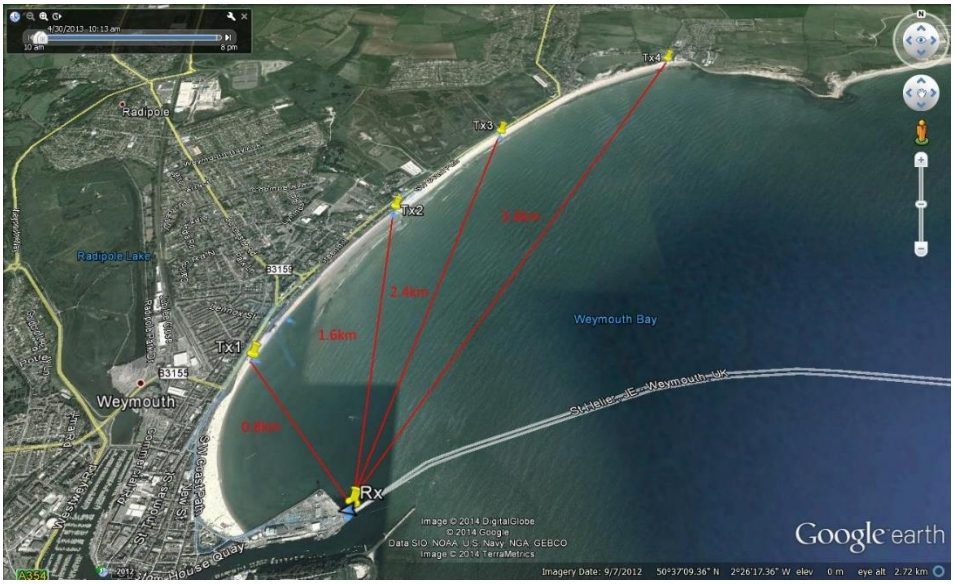

Figure 3.3.16 Topology of trial area and positions of the transmitter and receiver equipment

3.3.3 Presenting and storing measurements data

Since the beginning of the FSR trials, a method for storing the data has been developed. As it has been discussed previously each record is saved on computer's hard drive in '*. dat' format. Files have been stored in folders depending the day of the measurement and its trial location. In each folder GPS and weather data is located for most of the measurements. Photos and video records have been saved in folders linked with the measurements folders.

Different databases has been created which allowed easier manipulation with all the information available for each measurement. More information will be included in the following section.

All the data has been stored on at least 3 hard drives reducing the risk from data losses.

3.4 Data base structure

After each FSR trial, a database has been created in Microsoft Word and later on in Microsoft Excel and Access to store and sort all the available information about the measurements. A concept for a database template has been created but didn't fit the needs for the separate measurements.

The databases included information about the Radar system and parameters used throughout the whole experiment process. Data about the topology and scenarios of the measurements has been added as well. Also collected data from different sources concerning the weather condition, sea state and data truth which are extremely important, has been inserted in the tables.

The trials databases are organised in order of appearance – time order from 2009 till 2013. Every single measurement in the database obtains unique number, name and time and date. The importance and influence of specific parameters during each trial was changing and often one has been excluded and new has been added in the databases. Navigation key for each measurement in the trials is comments at the beginning or the end of the column row.

3.4.1 Radar parameters

Throughout the development and upgrades of the FSR system and the database some parameters became constant numbers or less influential and have been excluded from the databases and stored in the general description of the trial.

Table 3.3 Radar parameters database

Transmitter					**Receiver**				
Tx (GHz)	Signal type	Band (GHz)	PRF (MHz)	Vpp Level (V)	RF Filter	Doppler Receiver			Fs (Hz)
						RSSI Gain (dB)	Doppler Gain (dB)	Fc (Hz)	
7.5	CW	-	-	1	3GHz	10	10	164	200
7.5	CW	-	-	1	3GHz	30	30	164	200
7.5	CW	-	-	1	3GHz	20	20	164	200
7.5	Pulse	0.1	1	1	3GHz	10	20	164	200
7.5	Pulse	0.1	1	1	3GHz	10	20	164	200
7.5	Pulse	0.1	1	1	3GHz	10	20	164	200

An example for the parameters included in the radar description section part of the first database is shown on Table 3.3. On the end of each database short explanations and abbreviations has been enclosed as well.

As it is shown below Transmitter and Receiver has been separated in two main groups followed by their most influential parameters for these measurements.

The green colour in the table represents that the signals were analysed and the results were good for extraction clutter or target data. Three colour system have been used: Green colour- good results; orange – not so good results but with easily extractable information and red for distorted or damaged signals.

The transmitter parameters in the table above are:

- Tx – which stands for the centre frequency of the transmitted signal.
- Signal type – Continuous wave mode or Pulse mode of the transmitting device.
- Band – In case that the signal was Pulse, information about the pulse width has been provided.
- PRF - In case that the signal was Pulse, its Pulse repetition frequency.
- Vpp – Transmitted Voltage level peak to peak.

And explanation of the Receiver parameters is provided below:

- RF filter – It is the RF filter mounted after the receiver antenna. Two filters are available – 30MHz and 3GHz.
- Doppler Receiver – the Doppler receiver has 2 hardware amplifiers which could be controlled through the ADC and respectively through the PC software.
- RSSI gain – The gain loaded on the first amplifier in the Doppler receiver.
- Doppler gain – The gain loaded on the second amplifier in the Doppler receiver.
- Fc – Cutoff frequency of the receiver.

- Sample frequency – Sampling rate of the analog-to-digital converter. During most of the trials 200Hz frequency has been used.

The latest version of the Radar parameters in the database is shown on Table 3.4. The 'Vpp' parameter has been excluded from the Transmitter section and added in to the general description of the trial. Attenuation on the transmitted signal became an influential element of the system and it has been added into the Transmitter characteristics in the Database. Also the transmitter and receiver positions have been recorded with GPS devices and stored in to folders with the recorded radar data. The waypoint name is saved in the database and could be found in the GPS folders.

Table 3.4 Newest version of the Radar parameters database

Transmitter		**Receiver**					
Tx / Signal / Band / PRF / Att (GHz) type (GHz) (MHz) (dB)	Tx position	RF Filter	Doppler Receiver			Fs (Hz)	Rx position
			RSSI Gain (dB)	Doppler Gain (dB)	Fc (Hz)		
7.5 / Pulse / 0.1 / 1 / 0	Tx1	3 GHz	-	-	164	200	RX 1
7.5 / Pulse / 0.03 / 1 / 0	Tx1	3 GHz	-	-	164	200	RX 1
7.5 / Pulse / 1 / 1 / 0	Tx1	3 GHz	-	-	164	200	RX 1
7.5 / Pulse / 1 / 1 / 0	Tx1	3 GHz	-	-	164	200	RX 1
7.5 / CW / - / - /0	Tx1	30 MHz	-	-	164	200	RX 1

A column with antenna characteristics such as type of the antenna, polarisation and height is provided for every measurement. Additional information for the available antennas used during the FSR trials is included in a small database shown on Table 3.5.

Table 3.5 Antenna database

Antenna Number	Antenna Type	Beamwidth	Frequency
A1-A2	Flann antennas	20 & 20	7.5GHz
A3-A4	Wide (Ed's) antennas	30 & 6	7.5GHz
A5-A6	White Antennas	N/A	7.5GHz
A7-A8	Omni-Directional	N/A	7.5GHz

3.4.2 Topology and Scenarios

Information about the transmitter and receiver position, system baseline and antenna heights have been stored in the database for every single measurement. The data truth of the measurements and the analysis afterwards were strongly related with the preciseness of these topology parameters. GPS devices [107] were used for recording the transceivers positions. Afterwards the GPS coordinates were applied on software program such as Google earth and information about baseline of the system has been extracted. Very small location and baseline error is possible due to the GPS device (less than 10 m).

The height of the antennas is measured using tape measure starting from the mean sea level. The position and the height of the antennas needed constant observation and adjustment throughout the trials because of the fast moving sea tides. Tide tables were used to synchronise this process.

Different types of measurements have been performed throughout the data collection process. Clutter, range and target measurements crossing the baseline have been recorded and each of them had its own specifications. Other types of measurements have been collected as well. Comments specifying these properties of the records have been included in the database for each record.

Often during the trials targets of opportunity have crossed the baseline of the radar. Various maritime targets such as ships, boats, yachts, jet skis, windsurfers and others have been recorded. Usual interference during the trials is seagulls, dogs and people crossing the baseline of the system. Another possible interference throughout specific measurements has been the nearby maritime radar at Portsmouth harbour which worked at relatively close frequency to our radar. Comments about these targets have been included in the database in the same field as the measurement properties.

When target measurements crossing the baseline were conducted, the data truth of parameters such as position of the Transmitter and Receiver, speed and direction of the reference inflatable boat were quite important for further processing of the data.

Various methods were used to make sure the precision of the measurements;

- GPS tracking devices – as discussed previously in the hardware subchapter, waterproof GPS devices have been used for recording the position of the Transmitting and Receiving radar system. Also a tracking device has been mounted on the reference inflatable

Figure 3.4.1 GPS track of the target crossing the FSR baseline forming a 52 degree crossing angle

boat and it recorded the speed, direction and coordinates. Using track and waypoint data, calculation of the target's FSR baseline crossing angle has been made through Matlab script written by Mr. Liam Daniel. Figure 3.4.1 shows the recorded trajectory for a target crossing the baseline at an angle of 52°.

The GPS records were saved separately for each target measurement and stored in folders which allowed easier manipulation of the data afterwards. A link to the GPS folders has been provided in the trial database for each measurement.

- Video records and photos – Different video recording devices have been used through the trials. CCTV camera mounted on the top of our university vehicle was recording the first FSR measurements. The camera used a car battery as an energy supply and the video records were directly recorded on a laptop. A replacement of the CCTV camera was a portable video camera which offered relatively long lasting and removable battery and enough memory storage. The next generation cameras were waterproofed GoPro's Generation 2 with 170 degree viewing angle and excellent video resolution.

3.4.3 Parameters to be presented in Database

In this section the most influential parameters would be displayed;

- **Weather**

Atmospheric condition data has been collected throughout every conducted trial. A weather station was the main source for gathering data about wind speed and direction, temperature, humidity, rainfall and etc. The device shown on Figure 3.4.2 has been mounted close to the experimental area. The software provided with the weather station has been set to record the

atmospheric condition every 5 minutes and store its data in excel data sheet. All the weather data has been stored in folders with the radar records. Weather websites have been used as well as a source of weather forecasts.

Figure 3.4.2 Weather station mounted on 3m poll

Atmospheric information such as wind direction and speed and general weather condition for example sunny, cloudy or rainy has been included for each measurement in the trial database. But further data can be extracted if needed for each experiment from the weather database records.

- **Sea state**

For estimation of sea state level, different approaches and scales has been used. Video records, photos and visual notices have been used to measure the Douglas sea scale [49]. This scale estimates the height of waves and also measures the swell of sea. Weather station has been used throughout the whole experiment process to record the wind speed and direction. This allows observation of sea condition using the Beaufort wind force scale. Other tools for describing the sea condition used during trials were tide tables and weather forecasts for the area.

- Video records have been captured throughout all the measurements which provided visual data of sea condition, weather and external interference. During the records, trial number, date, time and start of the measurement has been taped for easier synchronisation with the radar trial. Videos have been stored in folders and for each FSR measurement a link in the database leading to this specific folder has been provided. Figure 3.4.3 shows a snap shot extracted from video for specific trial including sea state condition, MISL boat and external boat.
- Photos have been captured during the measurements and information about the sea state, weather and external interference could be extracted as well. As in the case with the videos, photographs have been stored in folders and linked in the database for each measurement.

Figure 3.4.3 Harborne master crossing the baseline during MISL boat measurement in relatively bumpy sea

- Tide tables - they were used for tidal prediction and to show the daily times and heights of high water and low water, for the particular location. These tide charts were usually saved with all the data for the measurement and mentioned in the general description file for the trials.

3.5 Conclusions

In this chapter, the stages of development of the novel FSR system are described in detail. This system is designed to establish the feasibility of this mode of operation for detection of small, low RCS targets in the environment of sea clutter. The FSR have been tested in laboratory environment and the results showed that extremely low Doppler frequencies (< 1 Hz) can be measured with the system. Same equipment has been a subject of outdoors trials in order to evaluate the field operation of the system. Targets crossing have been performed and the results showed that the clutter level is low in comparison with MISLs old ground equipment. All performed maritime trials from 2009 to 2013 have been discussed in the chapter giving mainly the purpose of the experiments and their topology settings. Methodology of the data collection procedure is presented as well. The vast amount of measurements data created the need of data storage strategies and construction of various databases explained in details in the chapter.

My personal involvement in the work discussed in this chapter is:

- Took part in all MISLs maritime experiments and the collection of target signals and sea clutter data.
- Was in charge of the data storage and handling (sorting the all the available measurement data into databases including all the GPS, weather and video data).
- Partially involved in the development of the FSR system.

Chapter 4 Sea Clutter Analysis

In order to develop Forward Scatter Radar systems for use in maritime applications a fundamental understanding of the operating environment is required as presented in [24]. Currently there is a lack of published experimental forward-scatter radar sea clutter data at very low (near zero) grazing angle over the sea. This data is essential when developing forward-scatter radar systems for maritime applications. Therefore, to facilitate further investigation, clutter data for such a system has been recorded at frequencies of 7.5 GHz and 24 GHz with static, medium gain antennas for low sea states 1-3 on the Douglas scale [20], [24], [91]. Analysis of forward scatter propagation phenomena is presented previously in Chapter 2 and Chapter 3. In this chapter, spectral and statistical analysis of forward scatter clutter is performed.

4.1 Radar Operational regimes

A program of measurement has been undertaken at sea to establish a comprehensive database of sea clutter measurements at almost zero grazing angles, to understand the mechanism of clutter generation and to validate on-going modelling and simulation work [20]. The topology of the radar assumes relatively short baselines (up to 2-3 km) and, therefore, atmospheric effects and ducting are assumed negligible over the radar operational area. Laboratory measurements have been made to establish the sensitivity of Doppler FSR (as discussed previously in Chapter 3 and Appendix A) and, therefore, its ability to measure low frequency clutter. To perform the measurements in real sea conditions, an FSR system has been deployed

at different sites providing a wide set of environmental conditions ranging from an almost perfect mirror surface (Lake Coniston) to rough, long range, deep water sea states (Bulgaria). Test sites are summarised in Table 4.1. More detailed description of the test site topologies have been provided in Chapter 3.2.

Table 4.1 Maritime experiments - different test sites.

Site	Experiment Location	Water	Depth, m
A	Portsmouth area, UK	Littoral water, across Langstone harbour	10-15
B	Portsmouth, Hampshire, UK	Littoral water, off coast	10-15
C	Sozopol, Bulgaria[3]	Deep water	25-35
D	Coniston Water, Cumbria, UK	Fresh water	10-20
E	Weymouth , Portland,UK	Littoral water	10-15

Continuous wave and pulse forward-scatter measurements were accompanied by simultaneous weather and sea condition recordings including wind speed and direction. Video records and

[3] This experiment was performed in collaboration with Prof. Hristo Kabakchiev's group from the Department of Software Technologies in Faculty of Mathematics and Informatics, Sofia University, St. Kliment Ohridski, Bulgaria.

GPS positioning provided data truth. Received clutter signals are recorded at the output of the RSSI channel, which represents a composition of the dc component due to coherent propagation and the Doppler shifted scattered components. More information about the receiver output can be found in Chapter 3 and Appendix A.

The radar hardware parameters were varied throughout the measurements by changing the antenna properties, system operating frequencies (7.5 GHz and 24GHz) and operation modes (CW and Pulse). Spectral and statistical analyses for these measurements are outlined below.

4.1.1 Influence of Carrier Frequency over Sea Clutter

The results shown here are obtained with MISL's equipment at frequencies of 7.5GHz and 24GHz and compared with data acquired by other laboratories at 1GHz, 9.3GHz and 37.5GHz. The antenna heights varying from 1 m to 7 m and baseline ranges from hundreds of metres to many kilometres [20], [24], [91].

The 7.5 GHz and 24 GHz (prototype version 4 and 5 as described on Table 3.1) equipment has been described in Chapter 3 and Appendix A. Both radar channels have been used successively or simultaneously to record forward-scatter clutter data. Maritime FSR trials were performed at Langstone harbor in November 2011 where the baseline range was 260m at SS 1 and at Weymouth harbour in April 2013 where the baseline was 2.3 km at SS 1. During both trials the Tx and Rx antennas were stationary mounted on the edge of the shore.

Low grazing angle maritime FSR measurements were completed in the early 90s by Pedenko and Razskazovsky in [116] in Sebastopol, Ukraine. Clutter measurements were undertaken at 9.3 GHz and 37.5GHz at rough sea (SS 3) and baseline range of 14.5 km.

The PSD of 1 GHz signal numerically simulated for shipboard communication systems with a baseline of 2.45 km is also reconstructed for a comparison [117].

Figure 4.1.1 shows the PSDs of seven completely separate clutter measurements acquired during the maritime trials. The results at 9.3 GHz and 37.5 GHz are replicated from [116]. The results have been normalized to illustrate that the overall forward scatter clutter spectrum is found to be independent of the transmit/receive baseline distance and radar frequencies within 1 – 37.5 GHz and as defined by a 10 dB power drop is limited to a maximum width of 1 Hz [20]. According to our simulations and measurements, the clutter does not depend on the distance because practically all the clutter is collected in the vicinity of the transmitter or the receiver. As the result the clutter to leakage ratio remains the same irrelevant to the baseline length. All clutter is collected from transmitter and receiver surrounding where there are no strict rule how to calculate. But further investigations are needed in this direction.

Also the PSD data clearly demonstrates that the PSD slope corresponds to approximately 30-40 dB per decade and therefore to maximum inverse fourth power of Doppler frequency. This result is in good agreement with the findings of Ungan and Johnson (1 GHz numerical simulation) in [117], where the fitted power spectrum model that decays as $\underline{O}\left(\frac{1}{f^4}\right)$ (where $\underline{O}$ is the order) was suggested.

The experimental measurements show that the amplitude fluctuations rise proportionally to sea roughness and inversely proportionally to the transmitting antenna height [91]. It has also been noted in [78] that there are no isolated discrete lines in the spectrum in all of the frequency bands studied. The main maximum of the spectra is located in the frequency range 0.2 – 0.7

Hz and above these frequencies the spectral density decreases according to the power law $G(F) \approx F^{-n}$ where $n = 1.8 - 2.5$.

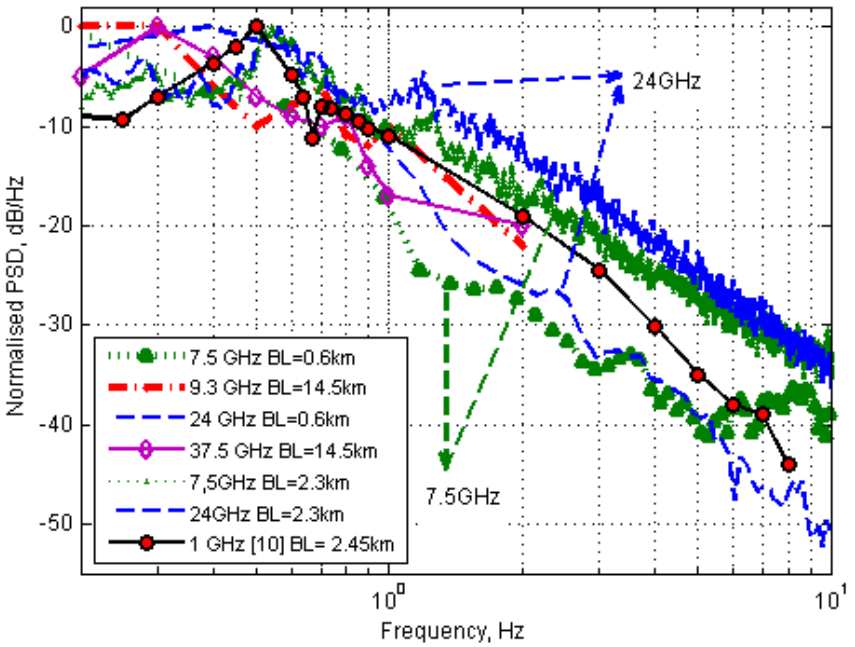

Figure 4.1.1 Normalized PSDs of FSR sea clutter recorded at varying ranges, frequencies, sea states and test sites

The clutter amplitude distribution is the most determinative characteristic to enable theoretical estimation of radar detection performance in terms of false alarm rate and probability of detection [20]. Figures 4.1.2 and Figure 4.1.3 show the probability density functions (PDFs) and the cumulative distribution functions (CDFs) of long clutter data (around 30 minutes each) recorded at 7.5 GHz and 24GHz. Rayleigh, Rice and Weibull distributions fits have been applied in the preliminary sea clutter analysis of the FSR data PDF's and CDF's and it was observed that Weibull fit is almost always with shape parameter around 2 (1.8 up to 2.1). From theory we know that Weibull distribution with shape parameter 2 is Rayleigh distribution [53].

We are not claiming that the best distribution is Rayleigh. We are only using this distribution as a reference because the major power well fitted into it. The tales on the PDFs are natural,

simply measurement results which not necessary should follow the Rayleigh. There are other approximations which may be better fit. The big spread observed on the PDFs is the result of what we are considering as events with very low probability, less than 10^{-4}. And this spread is rather natural, so called "spread" on the tails of distribution. Any experimentation will eventually give this.

The Rayleigh fit has been used as a reference in both plots and the parameters for the Rayleigh fit has been estimated using the maximum-likelihood estimation (MLE) method [118]. It has been found useful to present the CDF on Weibull paper [119] (on which the Rayleigh fit is a straight line) where y-axis shows log(ln(1/1 − CDF(a))) whereas the x-axis corresponds to log(a) where a is the intensity of the signal.

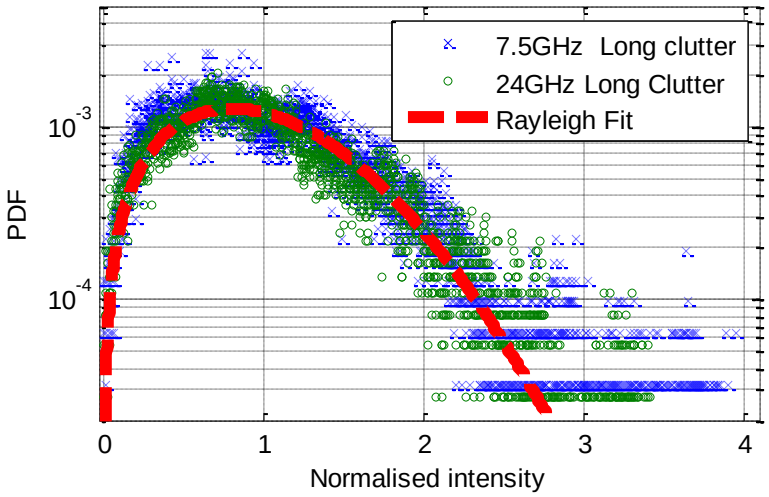

Figure 4.1.2 Comparison of PDFs of normalized FSR sea clutter measured at 7.5 GHz and 24GHz

The data has been normalized by taking the ratio of the signal power (after subtraction of the DC level) to the standard deviation of the clutter signal power to demonstrate the similarity between clutter in terms of the distribution of their amplitude probabilities.

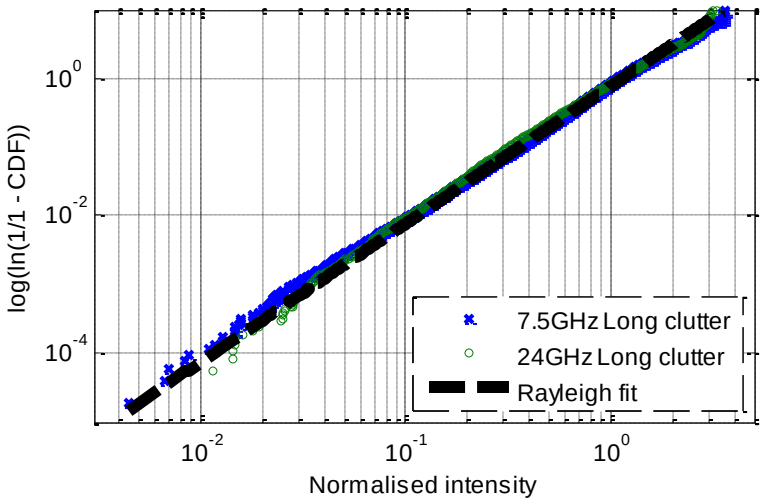

Figure 4.1.3 CDFs corresponding to Figure 4.1.2, on Weibull paper

According to the results shown in Figure 4.1.2 and Figure 4.1.3, the clutter distribution in FSR is close to Rayleigh for the considered frequency ranges, especially for the main body of the clutter distribution [20], [24]. It is worth underlining here that this conclusion may only be true for relatively low sea states. Significantly rougher seas may demonstrate different effects on propagation at low grazing angles. However, such a study is still to be performed.

4.1.2 CW and Pulse Mode (100MHz, 1 GHz and 3 GHz)

In order to investigate the nature of the variations of clutter with respect to transmitted pulse width, we have taken measurements with different bandwidth signals [24]. Shown here are results using 7.5GHz CW and another using 100MHz, 1GHz and 3GHz bandwidth pulse centred on 7.5GHz with a PRF of 1MHz. All data for the analysis has been collected during three different trials across Langstone Harbour during 2009 and 2010 (hardware version 1 and 2 according to Table 3.1). We applied an experimental system using Tektronix Arbitrary Waveform Generator AWG7102 for transmitting device and the Doppler receiver. Further information about the hardware is provided in Chapter 3 and Appendix A. The antennas used

were equal height (1 m) and vertically polarized. The FSR topology is presented on Figure 3.15 and the baseline was approximately 350 m. Throughout the measurements sea state varied between 1 and 2 with wind speeds between 1 m/s and 5.1 m/s.

A comparison of the Clutter spectra for CW mode and Pulse mode (100MHz, 1 GHz and 3GHz) of the Doppler radar are shown in Figure 4.1.4. For accurate comparison, the PSDs of the clutter data have been normalized to have a maximum of 0 dB The comparative clutter plot of Figure 4.1.4 shows that the clutter spectral width is relatively the same for all transmitted signals and as defined by a 10 dB power drop is limited to a maximum width of 1 Hz [110]. The use of wider (narrower pulse) interrogating signals is theoretically shown to reduce the level of clutter returns in FSR. However, this is only prevalent in high sea states [43], [44], [48]. It cannot be said that our measurements are made at a particularly high sea state (approximately sea state 2) and so the benefits of higher bandwidth are not necessarily seen. At low sea states most clutter will originate from a narrow region along the baseline between transmitter and receiver. The differences in the lower frequencies of the 4 presented signal PSDs could be explained with the slightly different sea state, weather condition and position of transmitter and receiver during the data recording.

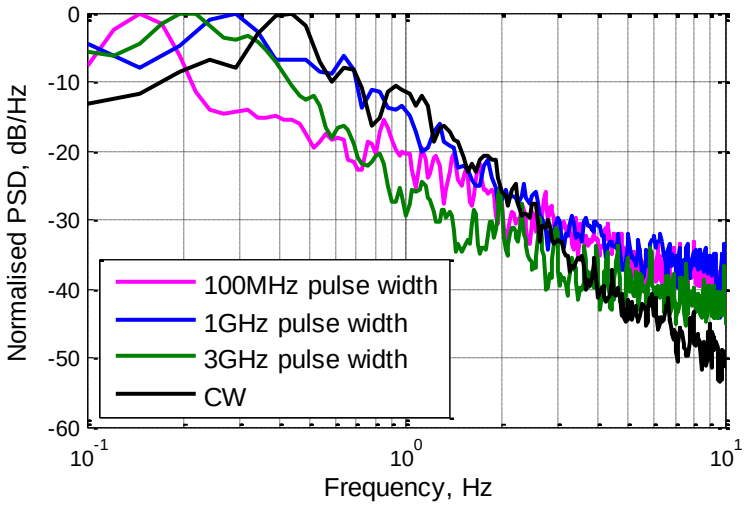

Figure 4.1.4 Normalized PSD of FSR sea clutter from CW mode and Pulse mode (100MHz, 1GHz and 3GHz)

The PSD data distinctly demonstrates (as in the influence of the carrier frequency case) that the PSD slope corresponds to approximately 25-40 dB per decade, and therefore, to maximum inverse fort power of Doppler frequency [20], [120].

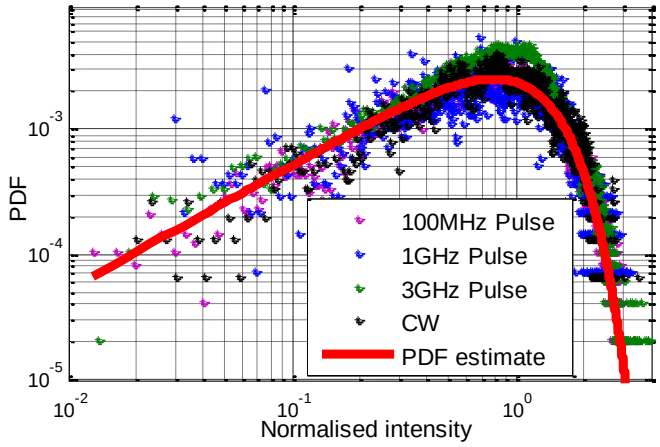

Figure 4.1.5 Normalized PDFs of FSR sea clutter from CW mode and Pulse mode (100MHz, 1GHz and 3GHz)

Figure 4.1.5 and 4.1.6 show the normalized PDFs and CDFs of the clutter data from Figure 4.1.4. The Rayleigh fit has been used as a reference in both plots which allows direct

comparison of the distribution shapes. Please note that the rapid drop of the measured distributions at lower amplitudes is caused by the radar operating in the lower non-linear region of the diode detector [24]. The results indicate that the distribution type of the clutter amplitude distribution is very close to Rayleigh for the different bandwidth signals.

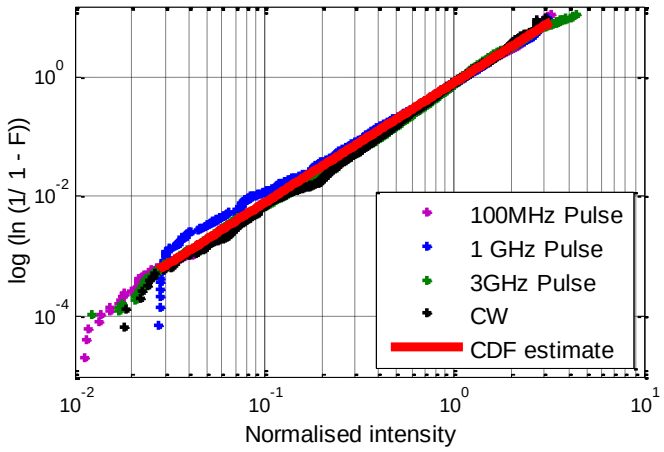

Figure 4.1.6 Normalized CDFs of FSR sea clutter of CW mode and Pulse mode (100MHz, 1GHz and 3GHz)

4.1.3 Antenna Properties

4.1.3.1 Variation of Clutter with Antenna Polarisation

Sea clutter measurements over a long period of time (30 minutes) were recorded using horizontally and vertically polarised antennas [120]. The purpose of the trial was to comprehend the effect of the antenna polarisation on the clutter spectra and its statistical properties and to give us an idea if there were any advantages in using one polarisation over another. The trials were performed over the Portland sea coast where the FSR system baseline was set to approximately 800 m (shown in Figure 4.1.7). Antennas with 20 degree beamwidth in both planes were used for the clutter measurements, operating simultaneously at frequencies of 7.5 GHz and 24 GHz in CW-mode.

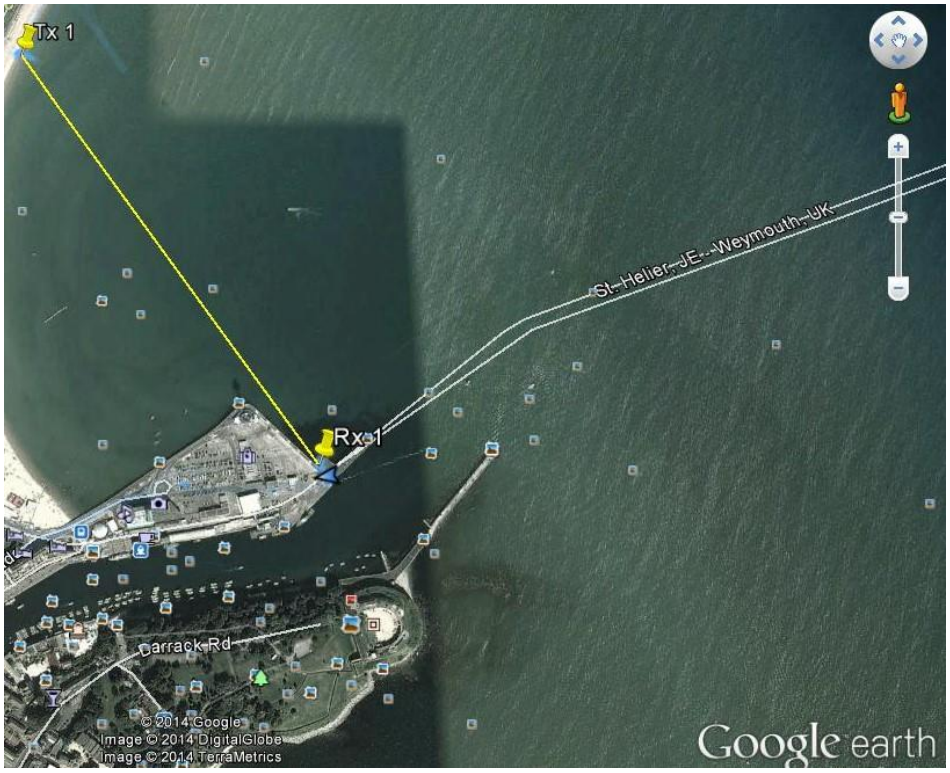

Figure 4.1.7 830m FS radar baseline during the antenna polarisation trials

The illuminated footprint during these measurements was approximately 0.0564 km^2. Figure 4.1.8 shows the normalized PSD of sea clutter recorded with horizontal and then vertical polarisations at 7.5GHz channel and 24GHz channel, respectively. The PSDs clearly show that the spectral shape is reasonably invariant to the antenna polarization in both frequencies and major part of clutter is below 1 Hz [120]. Plots also confirm expected spectral slope of approximately 20-35 dB per decade. These results are in a good agreement with the findings of [74] where horizontal and vertical total signal spectra were found to be the same.

The reason why horizontal and vertical polarisation were found to be the same is that FS components have fundamentally the same polarization as the illuminating field, so at the fundamental level we cannot expect depolarization. We can see difference between 7 and 24

only for very small targets. As soon as the target size is much bigger than the wavelength (this is our case) it should not be any visible difference.

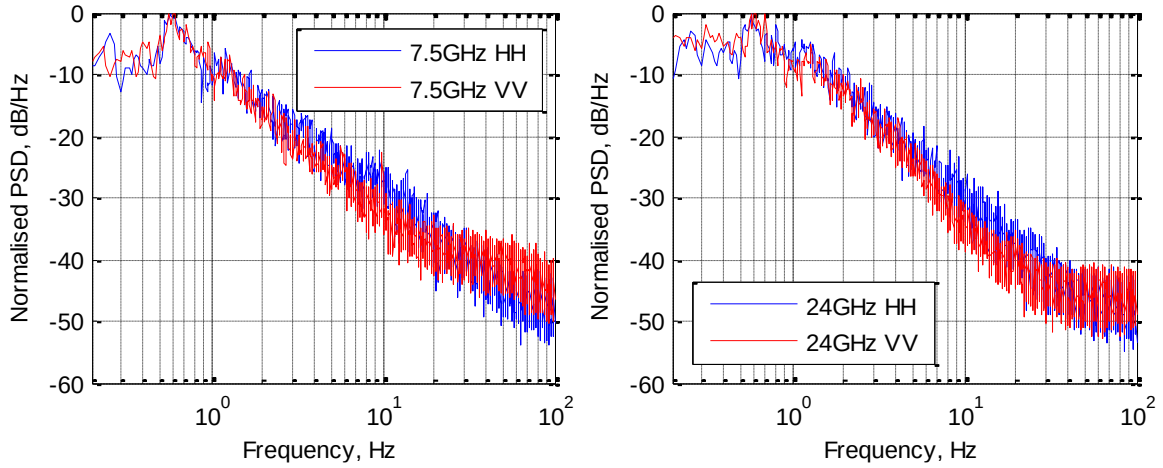

Figure 4.1.8 Normalized PSDs of FSR clutter recorded at 7.5 GHz (a) and 24GHz (b) with horizontal and vertical antenna polarisation

Normalized PDFs and CDFs of this FSR sea clutter measured at 7.5 GHz and 24 GHz are shown in Figure 4.1.9 and Figure 4.1.10. Rayleigh analytic fit has been used as reference in all plots. It follows from the analysis of the results shown in Figure 4.1.9 and 4.1.10 that the clutter distribution in FSR is close to Rayleigh for the considered polarisations and frequency ranges; especially for the main body of the clutter distribution as presented in [120].

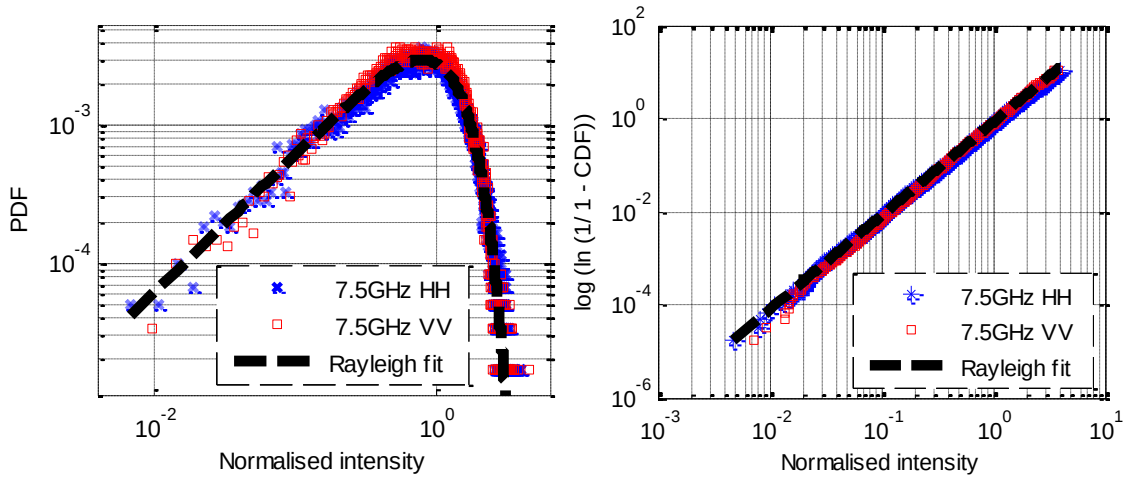

Figure 4.1.9 Normalized PDFs (a) of FSR sea clutter recorded at 7.5GHz from Fig. 4.1.8(a) and corresponding CDF's (b) on Weibull paper

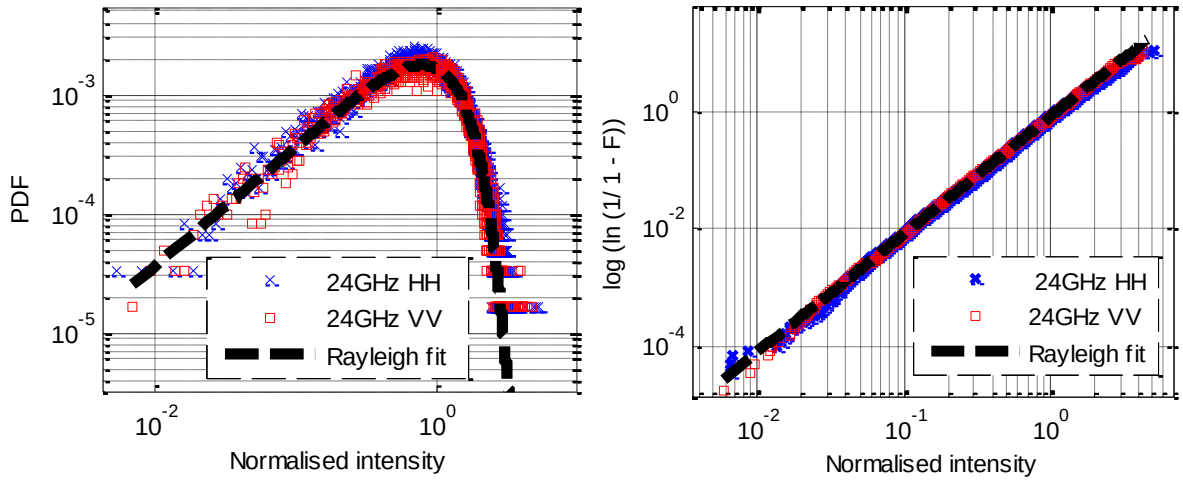

Figure 4.1.10 Normalized PDFs (a) of FSR sea clutter recorded at 24 GHz from Fig. 4.1.8 (b) and corresponding CDF's (b) on Weibull paper

4.1.3.2 Signal-Clutter Dependence on the Antenna Elevation

A series of clutter measurements were performed with modification of antenna height to investigate dependence of the clutter characteristics on grazing angle with respect to the mean sea level [120]. Two channels were used for this purpose: 7.5 GHz and 24 GHz. Transmitter's antennas were positioned on the shore of Weymouth coast (UK) one meter above the sea level while the receivers were located 800m away with 1.31m antenna height (Figure 4.1.11). During

five consecutive measurements the receiver's antenna height was gradually increased by 0.185 m reaching 2.05 m at its highest point. Throughout the experimentation the weather and the sea were relatively calm (sea state 1-2 by Douglas scale).

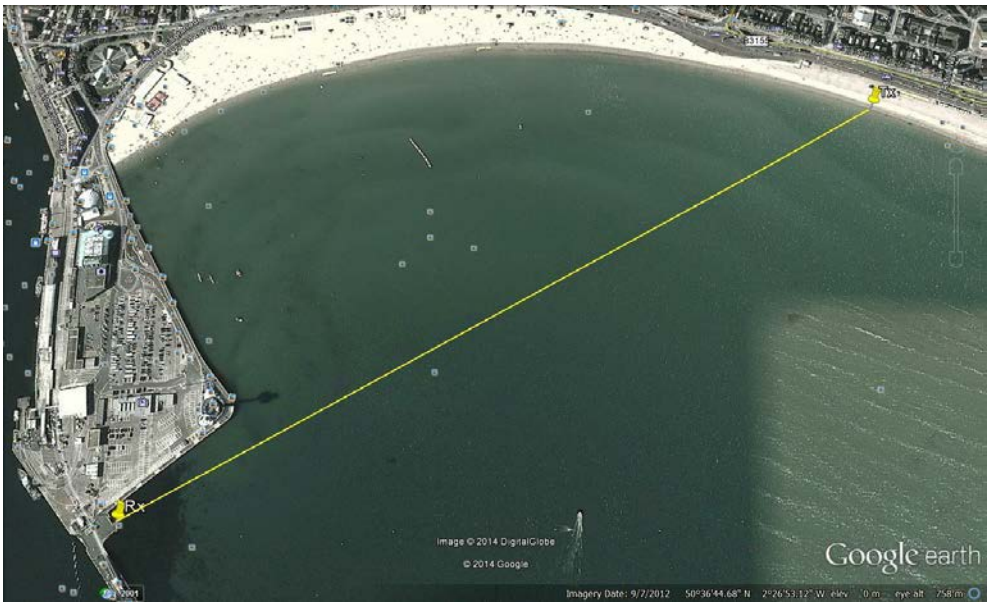

Figure 4.1.11 Topology of trial area and transmitter and receiver positioning

Figure 4.1.12 (a) and (b) illustrate the change of average signal level at 7.5 GHz and 24 GHz due to the increments in antenna heights. As one can observe the leakage power is increasing linearly with the increase of antenna height, which corresponds to theoretical estimations.

Two-ray path propagation model has been used for calculations of the expected received average power level and has proved to be quite accurate for large database of measurements [120]. According to this model, the change of received power (in dB) for different heights of the receiver's antenna h_r can be calculated by

$$dP_r = P_r^{(2)}(dB) - P_r^{(1)}(dB) = 20\log\left(1+\frac{\delta}{h_r}\right) \qquad (4.1)$$

where $P_r^{(2)}$ is the received average power from the higher position of the Rx antenna and $P_r^{(1)}$ is the power from the lower antenna position, respectively. δ is the difference in the antenna heights.

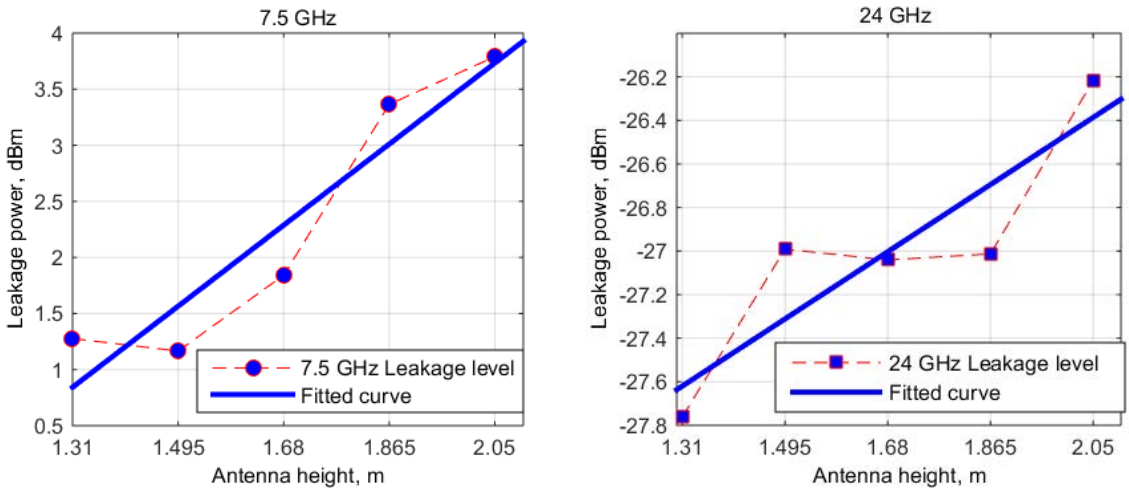

Figure 4.1.12 Leakage power against the Antenna height at 7.5GHz (a) and 24 GHz (b)

The change of received average signal level due to rising antenna height from lowest (1.31m) to its highest (2.05m) height has been calculated by (1). Comparison with the measured leakage power is presented in Table 4.2. The results demonstrate an overall reasonable agreement which emphasises an independence of frequency, inherent for the two-ray propagation model, at least for the 7.5 GHz channel.

Some discrepancy can be explained by the inaccuracy of the antenna height estimation above the mean sea level and sea level change itself. Possible antenna mispointing is another cause which can produce discrepancy.

Table 4.2 Power change due to the antenna height

	Power change dP_r, dB	
	Calculated	Measured
7.5 GHz	2.48	2.52
24 GHz		1.54

4.1.3.3 Influence of the Antenna (Stationary) Beamwidths

During clutter measurements, trials with various antennas were performed. The purpose of the experiments was to understand the effect of antenna azimuth beamwidth over clutter spectrum and its statistical properties [120]. Dozens of maritime trials have been undertaken on the Black sea where the distance between the transmitter and receiver was 350m. Throughout two days of experiments three antennas with different beams such as 12°, 20° and omnidirectional pattern were used which allowed us to see if there is an influence of the surface area illuminated by radar on the magnitude and distribution of clutter. Sea and weather condition were relatively similar during the maritime trials.

We used our notation for antennas as follows (shown on Table 4.3):

±6° – 'Wide'

±10° – 'Flann'

±30° – 'Omni-directional'

Table 4.3 Illuminated surface footprint

Illuminated surface footprint		
Antenna type	Ant. beamwidth	Measured footprint, km^2
Wide	±6°	0.0087
Flann	±10°	0.0108
Omni-directional	> ±30°	> 0.0353

Normalized power spectral densities are shown for clutter signals recorded with the different antennas as shown in Figure 4.1.13. It can easily be seen that the spectral shape is reasonably invariant to the antenna beamwidth and the major part of clutter is within 1 Hz beamdwidth [120]. This also confirms that the slope is approximately 20-35 dB per decade as discussed in [20], [24], [91].

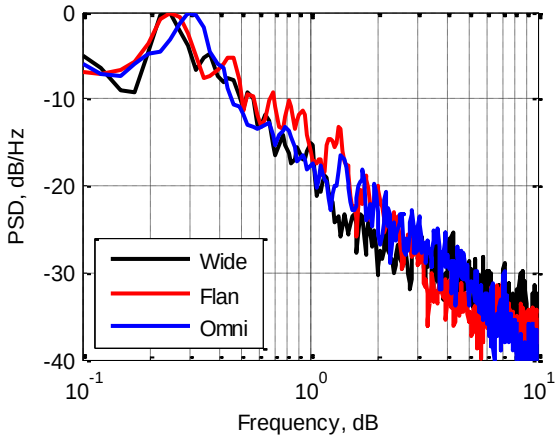

Figure 4.1.13 Normalized PSD of Clutter from 3 different antennas

The PDF and CDF for the same clutter data are plotted in Figure 4.1.14. The Rayleigh fit has been used as a reference in both plots. To allow direct comparison of the distribution shapes, the clutter data from each trial has been normalized by taking the ratio of the signal power (after subtraction the DC level) to the standard deviation of the clutter signal power, to demonstrate the similarity between clutters in terms of the distributions of their amplitude probabilities.

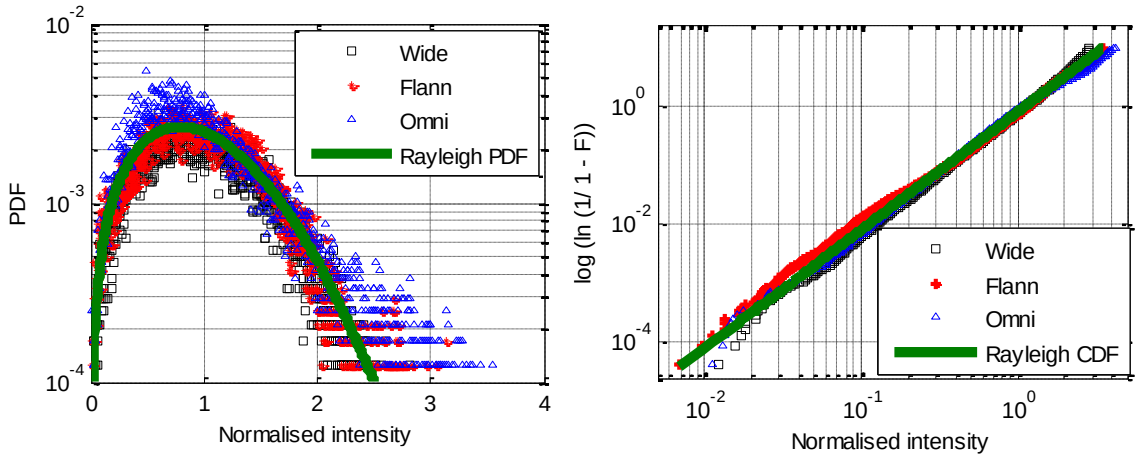

Figure 4.1.14 Comparison of PDFs (a) for FSR sea clutter for different antenna beamwidths and corresponding CDFs (b) plotted on Weibull paper

Also we found it useful to present the CDF on Weibull paper [119]. The results indicate that the distribution type of the clutter is very close to Rayleigh for the different antenna beamwidths.

4.1.3.4 Effects of Antenna Movement on the Doppler Spectrum when Employing Omni-Directional Antennas

In order to compare the effect of the use of omni-directional antennas on the system, sea trial measurements were performed in Sozopol, Bulgaria and at a later date in the UK to double check some previously obtained results [110]. The configuration of the Buoy mounted radar

has been shown previously in Chapter 3 and Appendix A, with the height of the omni-directional antenna being approximately 1.5 meters. In order to understand the effect of the antenna movement on the Doppler Spectrum, measurements with fixed antennas on the edge of the sea and with swaying antennas in open sea have been undertaken.

In Figure 4.1.15 you can see the topology of the test site indicating the position of the transmitter and the receiver for the case of fixed antennas. The receiver is placed on a rock on St. Ivan's Island approximately 1m above sea level, mounted with an omni-directional antenna. At the other side the transmitter was mounted near the edge of the sea also approximately 1 meter from sea level. The Transmitter configuration was 7.5GHz CW with a distance between the transceivers of approximately 350 meters.

Figure 4.1.15 Topology of the islands and position of the Transmitter and Receiver

Figure 4.1.16 shows the received signal of the sea clutter after removed DC level. The wind that day blew South East 5 m/s, the sea state was approximately SS 2 by Douglas scale [121] and the weather was sunny with temperatures around 30 degrees Celsius. In Figure 4.1.17 the power spectral density of the clutter is shown.

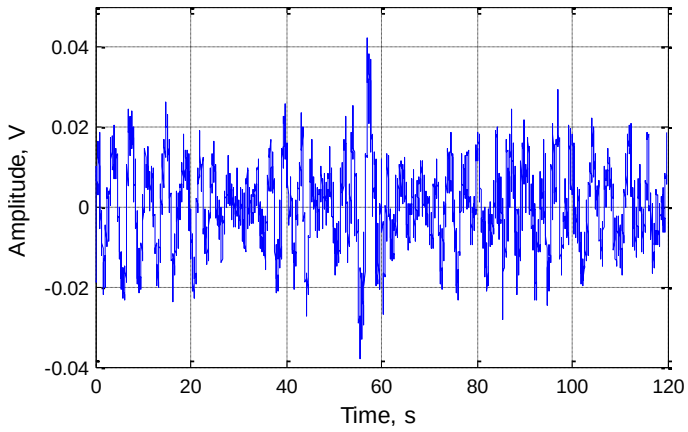

Figure 4.1.16 RSSI signal (after removed DC level) of the sea clutter

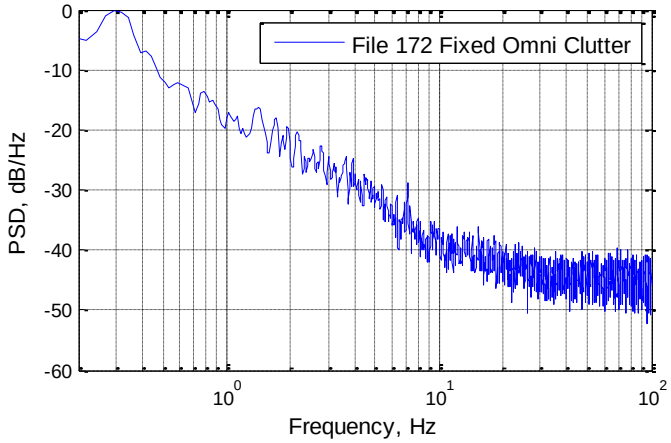

Figure 4.1.17 PSD of the sea clutter with fixed omni-directional antennas

In order to compare the effect of the antenna movement on the Doppler spectrum the transmitter mounted on the Ringo tube has been moved to open sea [110]. The position is shown in Figure 4.1.18 including a photo of the equipment. The distance between the Transmitter and Receiver was about 450m. RSSI (with removed DC) and PSD of a sea clutter record with this FSR configuration are shown in Figure 4.1.19 and Figure 4.1.20 respectively.

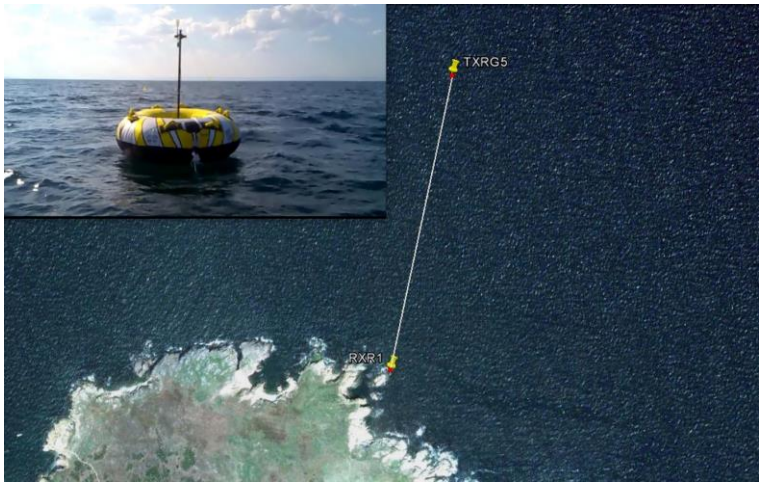

Figure 4.1.18 Position and photo of the Transmitter in open sea

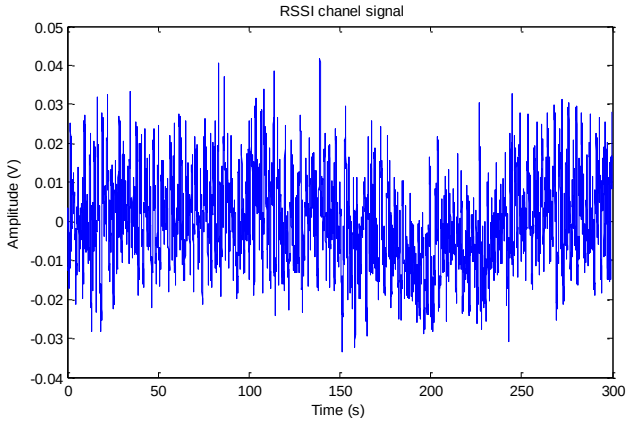

Figure 4.1.19 RSSI signal of sea clutter for swaying omni-directional antenna measurement

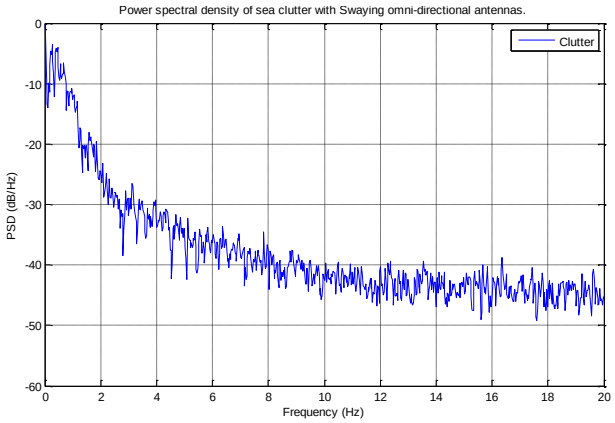

Figure 4.1.20 PSD of the clutter from swaying antenna measurements

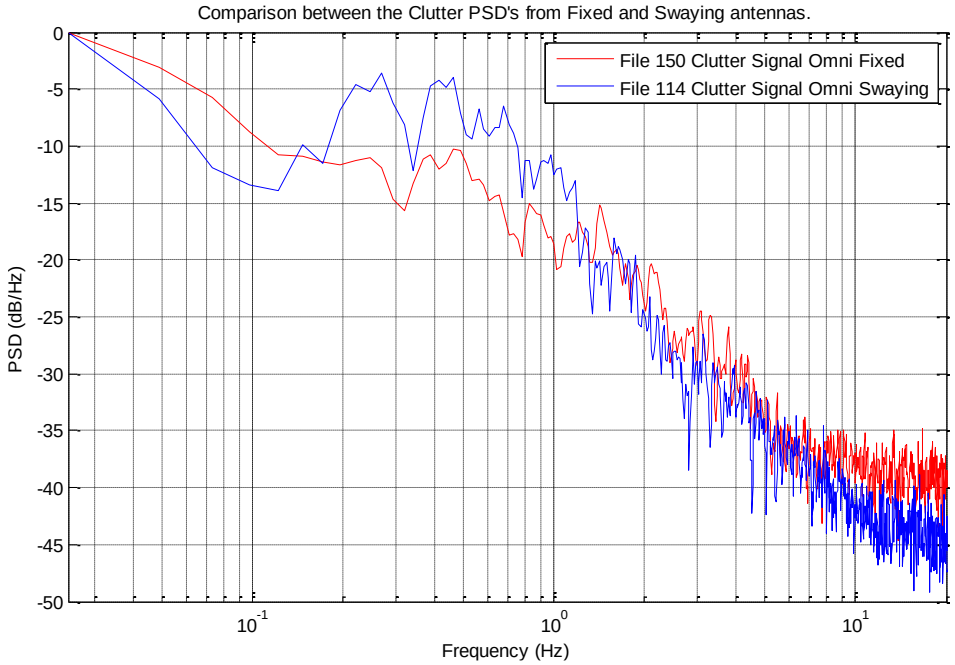

Figure 4.1.21 Comparison between the PSD's in stationary and swaying position

A comparison between the PSD's of swaying and stationary omni-directional antennas has been presented in Figure 4.1.21. The horizontal axis on this graph is in logarithmic scale. Above 1 Hz the spectra are nearly equal. There is some increase (5 dB) in the spectrum for swaying antennas between 0 and 1 Hz, but this is the area of filter rejection. It looks like the only extra spectral components are due to the buoy variation [110].

4.2 Test Scenarios

4.2.1 Influence of Test Sites Topology

A program of forward-scatter clutter measurements has been undertaken starting with littoral water measurements made at the entrance to Langstone Harbour, Portsmouth, U.K. and subsequently into the English Channel [20], [24], [91]. These measurements were made at ranges varying from 300 m up to 2 km under varying sea states (1-2 on the Douglas scale). Further measurements were made at Coniston Water U.K. at a range of 1.3 km, with a relatively calm water state. Furthermore open deep sea measurements were made on the Black Sea, Bulgaria, with 1km transmit/receive baseline between Sozopol and St Ivan Island. Additional measurements were undertaken with baselines ranging from 100 m to 1 km and a wide range of sea states between the mainland and the island as well as in the open sea.

Comparison of PSDs, PDFs and CDFs of the clutter data from the previously mentioned maritime experiments has been used to assess if and how the change of the maritime operational environment and distance affects the clutter and its properties.

Figure 4.2.1 shows the PSDs of representative clutter spectra from each of the measurements overlaid for comparison [91]. The figure shows clutter spectrum recorded with 7.5 GHz CW from Langstone Harbour, Coniston Water and Sozopol at sea state 1-2. Directional antennas with 1 m. height above the mean sea level and vertical polarization were used during all measurements as mentioned above.

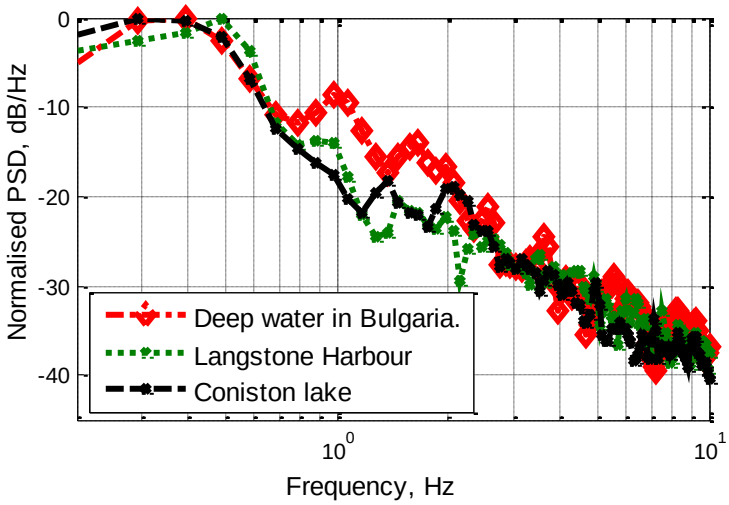

Figure 4.2.1 Clutter spectra from Langstone Harbour, Bulgaria and Coniston using vertical polarisation

The analysis of the data shows that forward-scatter sea clutter produces a relatively constant frequency clutter component around 1 Hz and the shape appears relatively invariant to the particular maritime environment [20], [24].

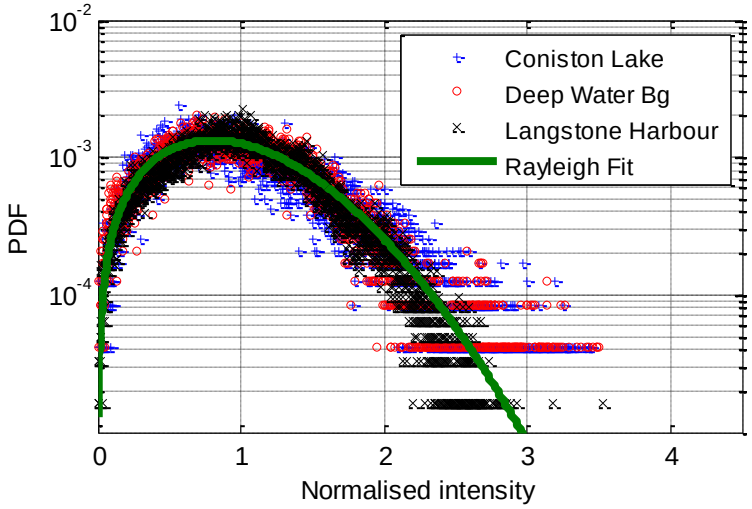

Figure 4.2.2 Corresponding PDFs of normalized FSR sea clutter from Figure 4.2.1

In Figure 4.2.2 and 4.2.3 the PDFs and CDFs of clutter spectra from Figure 4.2.1 are presented. As for previous cases the Rayleigh fit has been used as a reference in both plots. The results of

initial analysis show that the clutter distribution in FSR follows Rayleigh for the considered maritime environments [24].

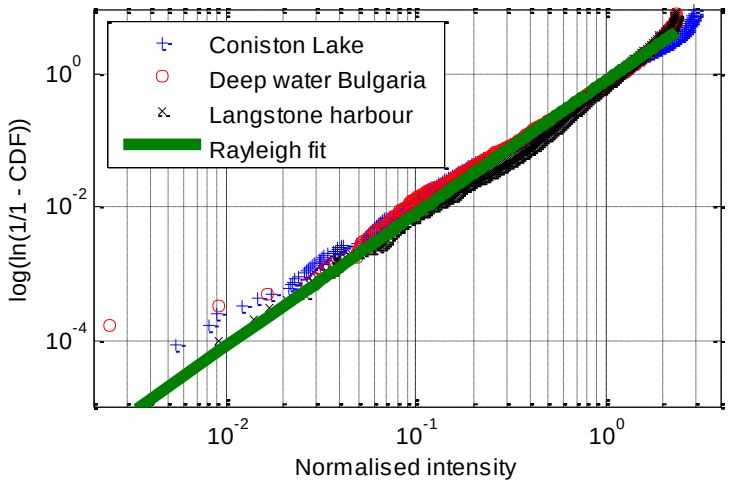

Figure 4.2.3 Corresponding CDFs plotted on Weibull paper from Figure 4.2.1

4.3 Environmental Conditions

4.3.1 Clutter Power Dependence as a Function of the Transmitter-Receiver Distance.

The leakage level depends mainly on the large scale geometry of the FS radar link, while the clutter power reflects the randomness of the deviations from the leakage component due to time-varying deviation of the surface from its mean level [20]. In this section we discus sea clutter and more specifically the time variation of power from its mean level as defined by the leakage power - so rather illustrative examples of clutter and leakage power observation will be presented.

The analysis of path loss is well known for radar [10], [12] and communication system [122], [123]. Two propagation models are usually used:

- the free space propagation model in case of no ground reflections, and
- the two ray path model which includes ground reflections.

In order to provide insight into how clutter power depends upon the transmitter-receiver distance, the 7.5GHz radar equipment (see Chapter 3.1 and Appendix A) has been tested over ranges up to 3.4 km. The first set of trials was performed in 2013 and analysis have been presented in [20]. Leakage and clutter powers as a functions of the baseline distance were shown. The findings of these experiments were inconclusive. Therefore further measurements were needed.

Since then MISL has performed two sets of range measurements on Weymouth coast: 1 day in November 2013 and 3 days in May 2014. Radar links at 7.5 and 24GHz have been set at four baselines: 800, 1600 2400 and 3400m. The receiver was positioned on the Weymouth Harbour and the transmitter was moved four consecutive times shown in Figure 4.3.1. Sea clutter measurements over a long period of time (30 minutes) were recorded using horizontally and vertically polarised antennas (for both Tx and Rx side) fixed 1 m. above the sea level. Sea state condition were roughly estimated to be sea state 1-2 on Douglas scale and were slightly changing within the experimentation period. Every range experiment was repeated several times.

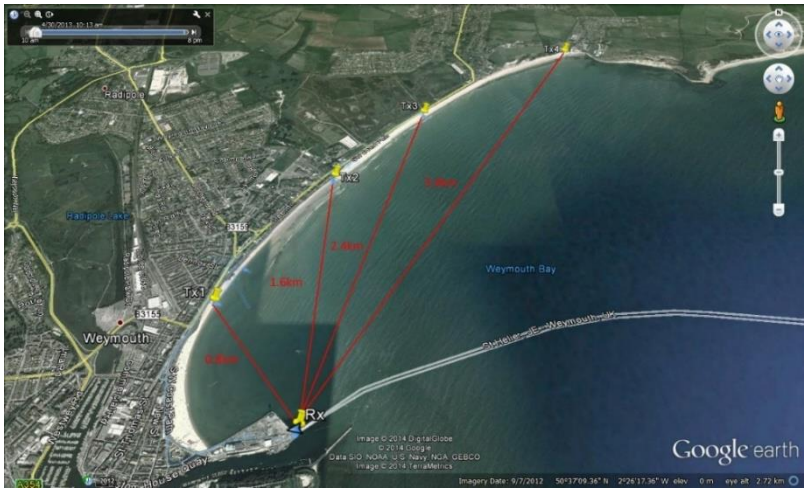

Figure 4.3.1 Topology of trials areas and positions of the Transmitter and Receiver

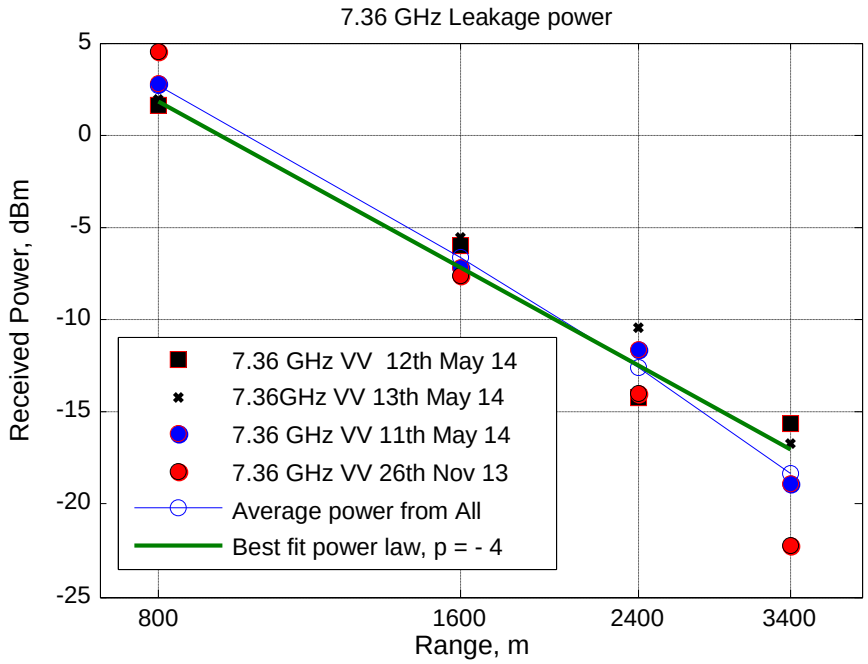

Figure 4.3.2 Leakage power against range, measured at 7.5GHz

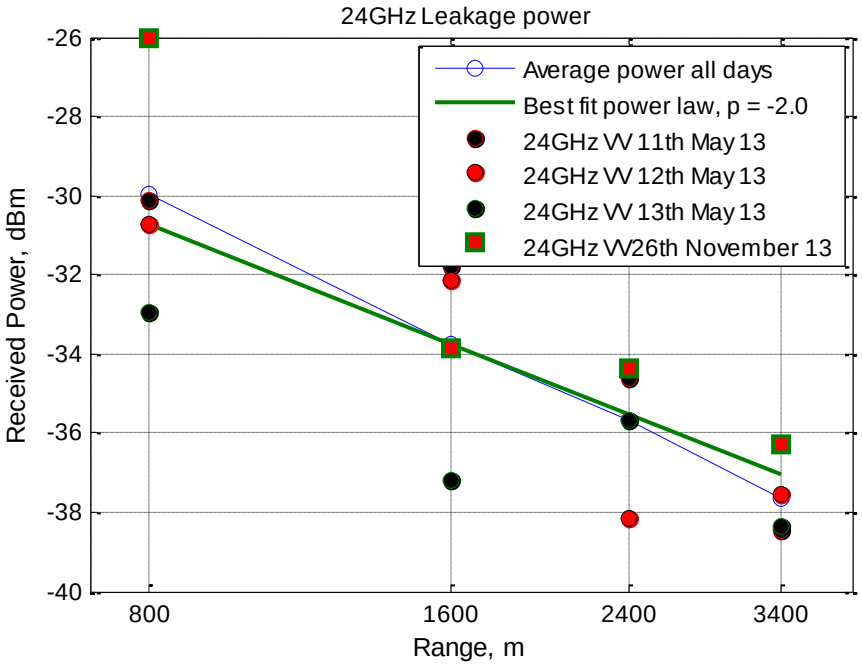

Figure 4.3.3 Leakage power against range, measured at 24GHz

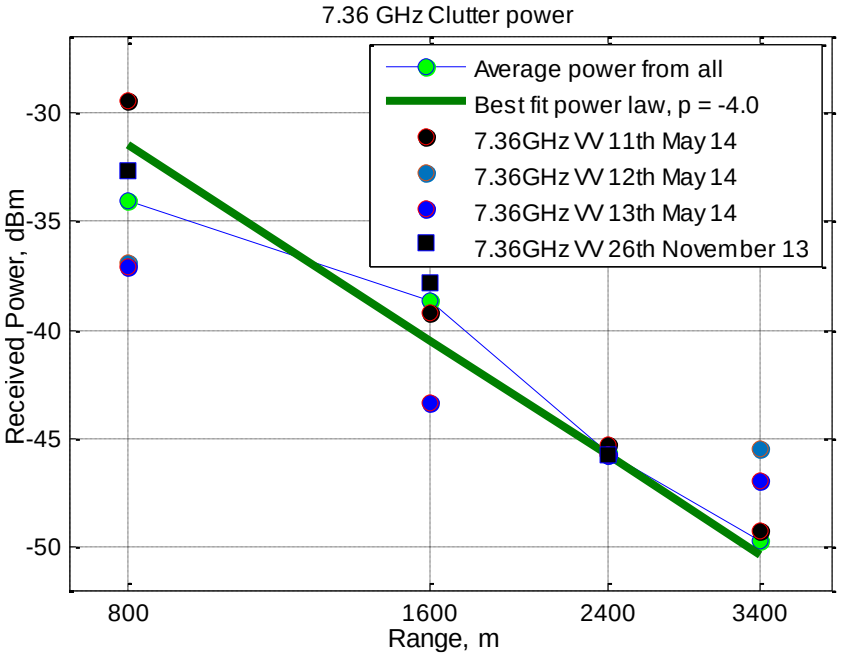

Figure 4.3.4 Clutter power against range, measured at 7.5GHz

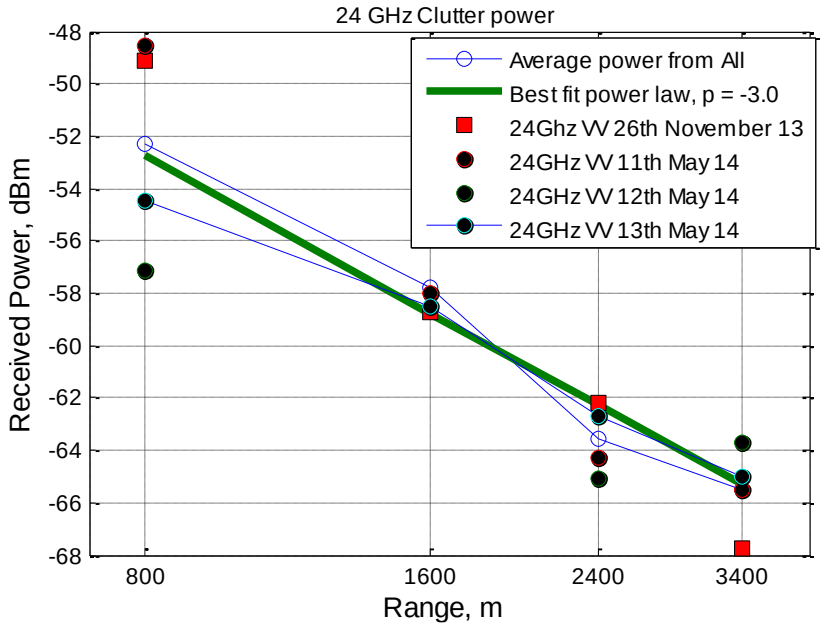

Figure 4.3.5 Clutter power against range, measured at 24GHz

Figure 4.3.2 to 4.3.5 are representing the Leakage and Clutter power over distance for four days of experiments made with the 7.5GHz and 24GHz system. All presented data is from measurements recorded with vertically polarised antennas.

The measure of leakage power is defined as the average value of measured RSSI signal and the measure of clutter amplitude is the standard deviation of the RSSI signal. In the FSR equipment diode detectors are used for the RF signal conversion to the voltage signal, which then could be digitised by ADC and stored in the data file in the computer. Calibration curves of the DRC by standard frequency generator have been made, where the output voltage of the DRC channel is measured (by ADC) in dependence of input CW or pulsed power.

Table 4.4 Clutter-to-leakage ratio for different baseline distances

Clutter to Leakage ratio from the Average values of all vertical polarised measurements, in dB.		
Range/Frequency	7.5 GHz	24 GHz
0.8 km	-36.743	-22.38
1.6 km	-32.1	-24.01
2.4 km	-33.05	-27.85
3.4 km	-31.36	-27.82

Some small discrepancy on the leakage power can be explained by the inaccuracy of the antenna height estimation above the mean sea level and sea level change itself. Possible antenna mispointing is another cause which can produce discrepancy.

We observed from the results above:

- 7.5 GHz channel RSSI average leakage and average clutter power from all the measurements fall off with the distance to the 4^{th} power. In this case we can expect that the clutter-to-leakage ratio should remain the same with the range. This is shown also in Table 4.4 where the average clutter-to-leakage ratio is calculated for all tested

distances. This has clear physical explanation and the effect has previously been observed for ground based FSR and foliage penetration [124], [125]. This also means that for 7.5GHz systems, the TRP can be considered as an accurate model (see also [20]).

- This is not the case with the 24 GHz channel where the average leakage power from all measurements roughly obeys 2nd power fall off with distance. This means that the free space propagation model is more appropriate for the 24 GHz channel. The clutter power follows 3rd power law drop with range so we expect that the clutter to leakage ratio for this channel shown in Table 4.4 should decrease 10 dB per decade. The explanation for this phenomenon is that at high frequency the sea roughness is big enough to decorrelate the second path (reflection from the sea) and as the result at 24 GHz it is like free space model [74].

All conclusion made here are based on sea clutter data recorded in sea state not higher than 3 by the Douglas scale.

4.3.2 Measurements of Clutter Level Dependence over Sea-State

Data has been collected in what might be termed different 'sea states' [20], [24], [91], [110]. Though in the littoral environment of Langstone Harbour it is very difficult to classify in terms of real sea state as defined by the WMO (World Meteorological Organisation) which requires that the area of surface to be classified is large and has been exposed to external conditions for a long period of time. During the course of our trials the surface conditions have visibly changed due to factors including tidal flow of varying strengths and weather conditions influencing waves coming into the harbour – though we cannot say there is a direct relationship between wind speed and surface conditions measured inside the harbour [110].

It has been possible using video recordings of the trials to select a few measurements in which we can say we have different sea states. The actual values of sea state were estimated and in our view this is a very subjective process. We could at least separate lowest visual sea state from highest and some value in between. In order to do so video records, photos, tide tables and visual observation were used.

Measurements presented in this Section were performed using a 7.5 GHz CW signal. The baseline range between the transmitter and receiver was approximately 300 m (Figure 4.3.6). Directional 'Flann' antennas were used during this sea trials, mounted on rocks very close to the shore approximately 1 meter above the sea level.

Figure 4.3.6 Topology of the sea trial test site

An example of RSSI signals after removed leakage level and photos of the different sea states are shown in the following Section.

Clutter at Lowest Estimated Sea State (1-2)

Figure 4.3.7 shows RSSI signal with removed leakage level for what is seemed to be a relatively flat surface with a low sea state of 1-2 by Douglas scale; along with corresponding video

capture stills of the sea surface during the measurement [110]. The recorded average wind speed and direction during the trial was 1.6 ms^{-1} NW.

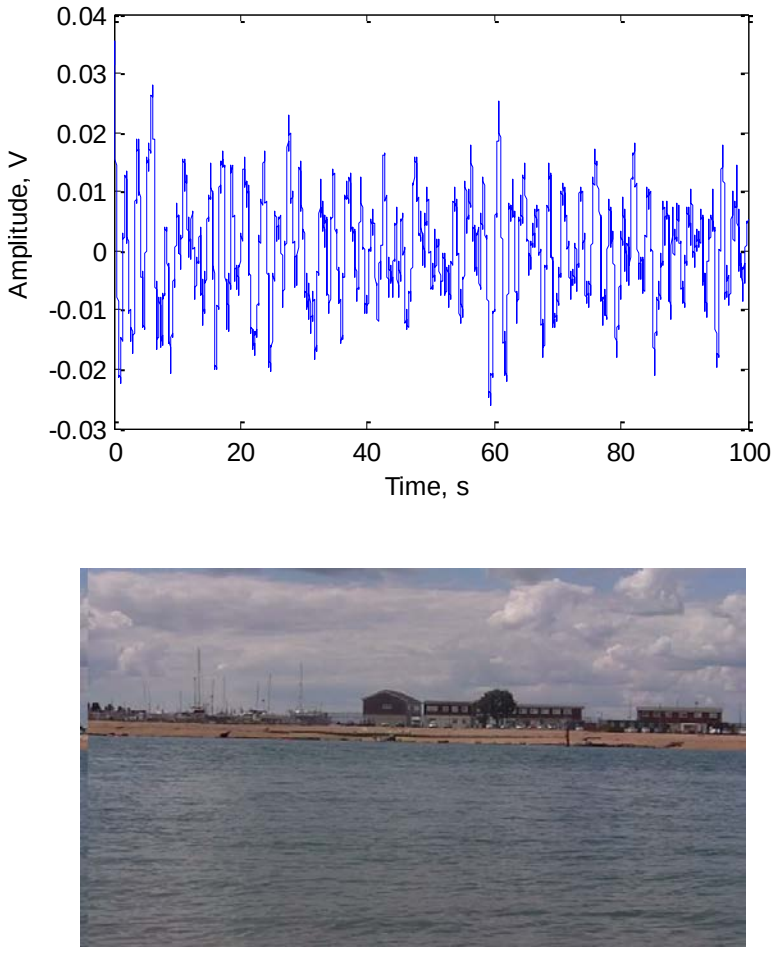

Figure 4.3.7 Recorded Doppler signature and image of lowest sea state (1-2)

Clutter at Mid Estimated Sea State (2-3)

Figure 4.3.8 shows a recorded signature without the leakage level and still cap image of the sea surface for what is estimated to be somewhere in between the lowest and highest sea states found above; an approximate sea state of 2-3 by Douglas scale [110].

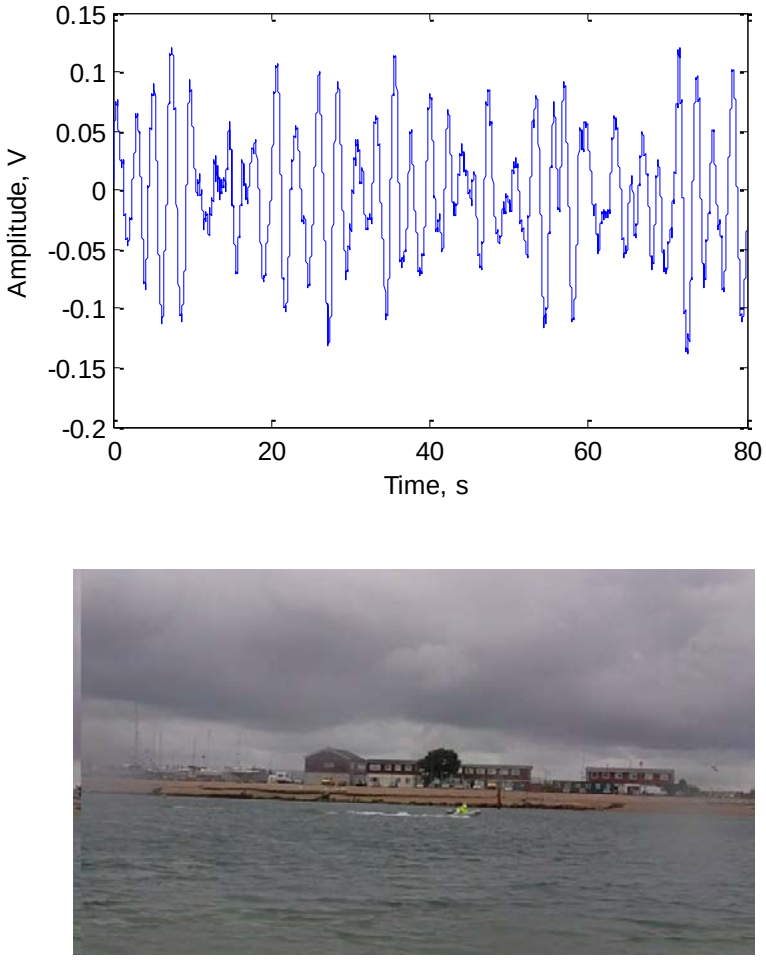

Figure 4.3.8 Recorded Doppler signature and image of mid sea state (2-3)

Clutter at Highest Estimated Sea State

Figure 4.3.9 shows the case of what is seemed to be the highest sea state measurements, around sea state 3 by Douglas scale [110]. The average wind speed and direction measured during the records is 4.4 ms^{-1} SW.

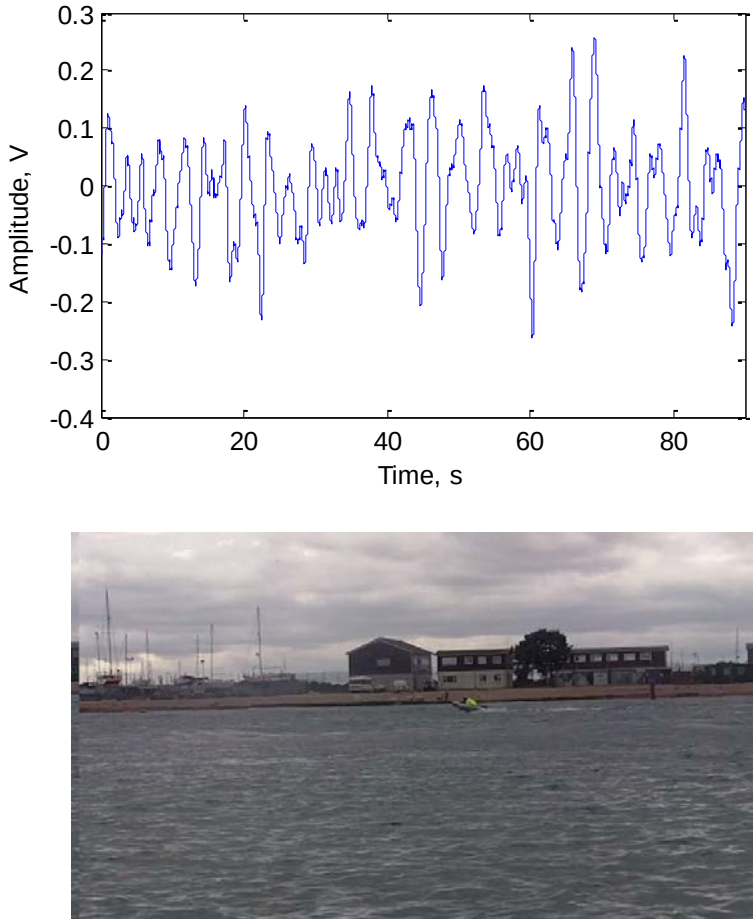

Figure 4.3.9 Recorded Doppler signature and image of highest sea state (3)

PSDs comparison of clutter from different sea states

The PSDs of sections of long term (around 200 s) sea clutter from different sea states has been recorded, analysed and presented in Figure 4.3.10. It can be seen that for the higher estimated sea states there is easily a 30dB increase in the clutter power. The intermediate sea state clutter power lies between the highest and lowest.

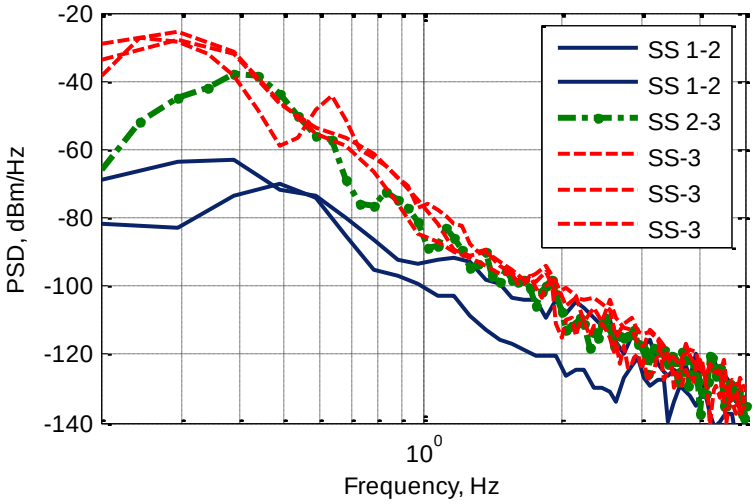

Figure 4.3.10 PSD comparison of clutter at different sea states

Figure 4.3.10 demonstrates that clutter bandwidth remains limited to 1 Hz for all recorded sea states. However there is an initial indication that for higher sea states the spectrum becomes band-limited with slightly narrower bandwidths of higher power - though the pedestals of the spectra coincide reasonably well as described in [20], [24], [91], [110]. This reflects the fact that for higher wind speeds we observe a more developed sea state with an increase in large sea gravity wave amplitudes. These waves have a more regular travelling wave structure and therefore occur periodically rather than the more random behaviour of small background capillary waves typical occurring in an undeveloped sea state. Moreover we can expect that higher sea states will demonstrate the slight shift of bandwidth down to lower frequency because with the increase of the sea state the interval of waves is increasing [110].

PDFs and CDFs of clutter data from different sea states

Using the same sea clutter data as in Figure 4.3.10, a comparison of the PDFs and CDFs for different sea states with their corresponding analytic Raleigh fits is shown in Figure 4.3.11 and 4.3.12. The data indicates once again that the distribution of clutter amplitude is Rayleigh over

the range of sea states measured. It also shows the shift to higher amplitudes at higher sea states [20], [24], [91].

Relationship between signal amplitudes and sea states requires further work/data at high sea states.

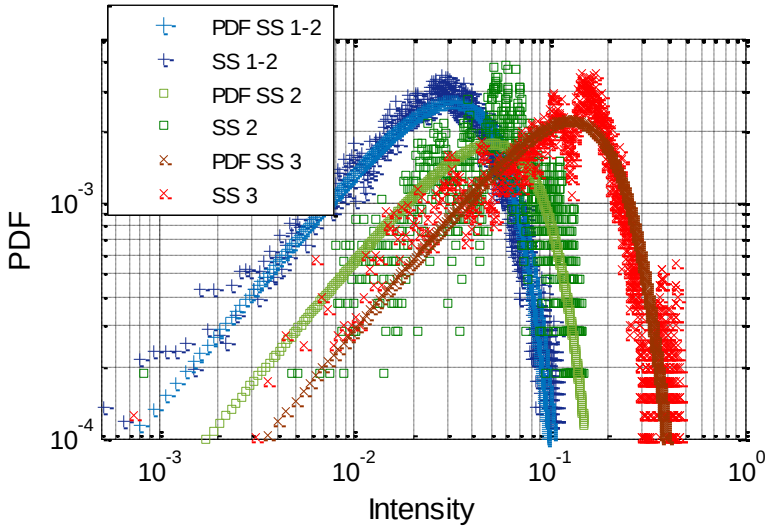

Figure 4.3.11 Comparison of PDFs for long-term sea clutter measurements in different sea states. Legend symbol SS corresponds to the PDF of measured data

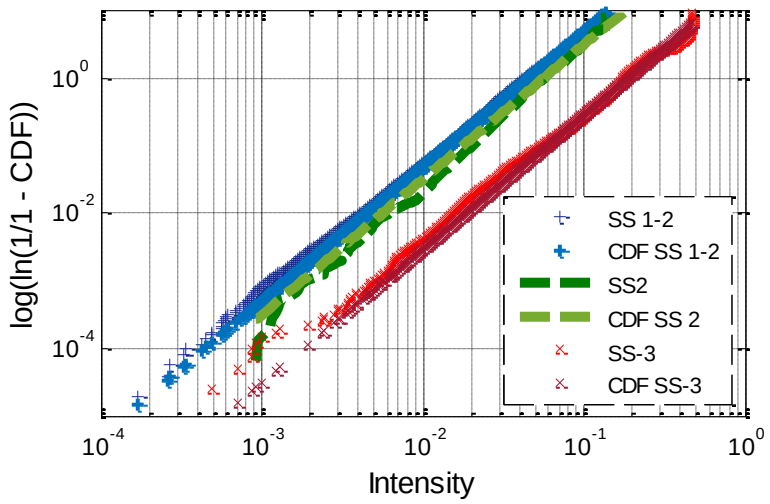

Figure 4.3.12 CDFs corresponding to Figure 4.34, on Weibull paper

4.4 Conclusions

For maximisation of target detectability in FSR, where the system is inherently clutter limited, it is crucially important to analyse the spectrum and statistics of forward-scatter sea clutter. Therefore, this Chapter has been focused on the spectral and statistical analysis depending on the radar operational regimes, environment and scenarios. The operational environment analysis are fundamental in order to develop fully functional FSR system for use in maritime applications. For that reason to facilitate understanding of the sea clutter the various experiments at frequencies of 7.5 GHz and 24 GHz were undertaken. The FSR was deployed at different maritime sites providing wide range of environmental conditions. The measurements were performed in CW mode and Pulse mode. Data on weather and sea conditions has been provided as well.

According to the results from the influence of carrier frequency over sea clutter, the forward scatter clutter spectrum is found to be independent of the transmit/receive baseline distance and radar frequencies within 1 – 37.5 GHz. According to our simulations and measurements, the clutter does not depend on the distance because practically all the clutter is collected in the vicinity of the transmitter or the receiver. As the result the clutter to leakage ratio remains the same irrelevant to the baseline length. All clutter is collected from transmitter and receiver surrounding where there are no strict rule how to calculate. But further investigations are needed in this direction. Also the spectrum is defined by a 10 dB power drop and limited to a maximum width of 1 Hz and depends strongly on the state of the sea surface. In particular, shading strongly influences the spectra characteristics of scattered signals. As well, the PSD data clearly demonstrates that the PSD slope corresponds to approximately 30-40 dB per decade, and therefore, to a maximum inverse forth power of Doppler frequency. This result is

in good agreement with [117], where the fitted power spectrum model that decays as $\underline{O}\left(\frac{1}{f^4}\right)$ was suggested.

The comparison of the clutter spectra for CW mode and Pulse mode (100MHz, 1 GHz and 3GHz) of the Doppler radar showed that the clutter spectral width is relatively the same for all transmitted signals and as defined by a 10 dB power drop is limited to a maximum width of 1 Hz. The use of wider (narrower pulse) interrogating signals is theoretically shown to reduce the level of clutter returns in FSR. However, this is only prevalent in high sea states. It cannot be said that our measurements are made at a particularly high sea state (approximately sea state 2) and so the benefits of higher bandwidth are not necessarily seen. At low sea states most clutter will originate from a narrow region along the baseline between transmitter and receiver. Also the analysis indicated that the distribution type of the clutter amplitude distribution is very close to Rayleigh for the different bandwidth signals. Please note that the rapid drop of the measured distributions at lower amplitudes is caused by the radar operating in the lower non-linear region of the diode detector [24].

The variation of clutter with the antenna polarisations analysis concluded that the spectral shape is reasonably invariant to the antenna polarisations in both 7.5 GHz and 24 GHz and major part of clutter is below 1 Hz. Plots also confirm expected spectral slope of approximately 20-35 dB per decade. These results are in a good agreement with the findings of [74] where horizontal and vertical total signal spectra were found to be the same. The reason why horizontal and vertical polarisation were found to be the same is that FS components have fundamentally the same polarization as the illuminating field, so at the fundamental level we cannot expect depolarization. We can see difference between 7 and 24 only for very small targets. As soon

as the target size is much bigger than the wavelength (this is our case) it should not be any visible difference. Also it follows from the analysis of the results that the clutter distribution in FSR is close to Rayleigh for the considered polarisations and frequency ranges; especially for the main body of the clutter distribution.

The change of the average signal level at 7.5 GHz and 24 GHz due to the increments in antenna heights have been calculated and results showed that the leakage power is increasing linearly with the increase of the antenna height which corresponded to the theoretical estimations. A two-ray path propagation model has been used for calculations of the expected received average power level and has proved to be quite accurate for large database of measurements. Comparison with the measured leakage power demonstrate an overall reasonable agreement which emphasises an independence of frequency, inherent for the two-ray propagation model, at least for the 7.5 GHz channel.

The effect of antenna azimuth beamwidth over clutter spectrum and its statistical properties has been observed. The results showed the spectral shape is reasonably invariant to the antenna beamwidth and the major part of clutter is within 1 Hz bamdwidth. This also confirmed that the slope is approximately 20-35 dB per decade. The results indicate that the distribution type of the clutter is very close to Rayleigh for the different antenna beamwidths.

In order to understand the effect of the antenna movement on the Doppler Spectrum, measurements with fixed antennas on the edge of the sea and with swaying antennas in open sea have been undertaken. A comparison between the PSD's of swaying and stationary omni-directional antennas has been presented and above 1 Hz the spectra are nearly equal. There is some increase (5 dB) in the spectrum for swaying antennas between 0 and 1 Hz, but this is the

area of filter rejection. It looks like the only extra spectral components are due to the buoy variation.

The influence of the test sites topology over clutter has been observed. The analysis of the data shows that forward-scatter sea clutter produces a relatively constant frequency clutter component around 1 Hz and the shape appears relatively invariant to the particular maritime environment. The results of initial analysis show that the clutter distribution in FSR follows Rayleigh for the considered maritime environments.

The clutter power dependence as a function of the transmit-receive distance has been observed. 7.5 GHz channel RSSI average leakage and average clutter power from all the measurements fall off with the distance to the 4^{th} power. In this case we can expect that the clutter-to-leakage ratio should remain the same with the range. This has clear physical explanation and the effect has previously been observed for ground based FSR and foliage penetration [124], [125]. This also means that for 7.5GHz systems, the TRP can be considered as an accurate model. This is not the case with the 24 GHz channel where the average leakage power from all measurements roughly obeys 2^{nd} power fall off with distance. This means that the free space propagation model is more appropriate for the 24 GHz channel. The clutter power follows 3^{rd} power law drop with range so we expect that the clutter to leakage ratio for this channel shown in Table 4.5 should decrease 10 dB per decade. The explanation for this phenomenon is that at high frequency the sea roughness is big enough to decorrelate the second path (reflection from the sea) and as the result at 24 GHz it is like free space model [74].

Also the clutter level dependence over sea-state was investigated. The results demonstrated that clutter bandwidth remains limited to 1 Hz for all recorded sea states. However there is an initial indication that for higher sea states the spectrum becomes band-limited with slightly

narrower bandwidths of higher power - though the pedestals of the spectra coincide reasonably well. This reflects the fact that for higher wind speeds we observe a more developed sea state with an increase in large sea gravity wave amplitudes. These waves have a more regular travelling wave structure and therefore occur periodically rather than the more random behaviour of small background capillary waves typical occurring in an undeveloped sea state. Moreover we can expect that higher sea states will demonstrate the slight shift of bandwidth down to lower frequency because with the increase of the sea state the interval of waves is increasing. The data indicates once again that the distribution of clutter amplitude is Rayleigh over the range of sea states measured. It also shows the shift to higher amplitudes at higher sea states. Relationship between signal amplitudes and sea states requires further work/data at high sea states.

Following the analysis above, the overall forward scatter clutter spectrum:

- Is found to be independent of the transmit/receive baseline distance and radar frequencies within 1 – 37.5 GHz.
- Is found to be invariant to the transmitting mode (CW or Pulse), antenna properties, test scenarios and environmental conditions.
- Is defined by a 10 dB power drop and limited to a maximum width of 1 Hz.
- Depends strongly on path geometry and the state of the sea surface. In particular, shading strongly influences the spectra characteristics of scattered signals.

Also, the PSD data clearly demonstrates that the PSD slope corresponds to approximately 20-40 dB per decade, and therefore, to a maximum inverse forth power of Doppler frequency.

It follows from the analysis of the results that the clutter distribution in FSR is close to Rayleigh for the presented radar operational regimes, test scenarios and environmental conditions; especially for the main body of the clutter distribution [20]. It is worth to underline here that this conclusion may only be true for relatively low sea states. Significantly rougher seas may demonstrate different effects on propagation at low grazing angles, however such a study is still to be performed. Also this is not a claim that the best distribution is Rayleigh. The distribution is used as a reference because the major power well fitted into it. The observed tales on the PDFs are natural, simply measurement results which not necessary should follow the Rayleigh. There are other approximations which may be better fit. The big spread observed on the PDFs is a result of what we are considering as events with very low probability, less than 10^{-4}. And this spread is rather natural, so called "spread" on the tails of distribution.

Chapter 5 Preliminary FSR Target Analysis

Measurements included in this thesis have been recorded in a number of test areas, mainly across the entrance of Langstone Harbour near Portsmouth, but also on Lake Coniston in the Lake District and on the Black Sea in Bulgaria. At sites such as Langstone harbour and Lake Coniston, it is very difficult to classify the sea in terms of the classical sea state description, tidal effects play a large role in the state of the surface (littoral regions). However wind speed and direction data has been recorded for all trials along with much video and photographic data and attempts at sea surface classification have been made. Certain sites in the Black Sea trials may have made for more 'deep sea' like testing, however were still performed close to land of some nature (i.e. from smaller islands).

Target measurements have been made with MISL's own small 3m long inflatable boat. GPS data has been collected for nearly all trials, consisting of markers for antenna positions and track data for target trajectories. This allows us to calculate target speed, FSR baseline crossing point, angle and FSR baseline length.

Unless otherwise stated, for the 2009 to 2012 results the FSR system used in trials will be of the same configuration (gain, filters, Flann horn antennas, V-V polarisation, 1 m antenna heights) for each section of analysis. The same applies for the assumption of the sea state, measurements within each section are assumed to have been recorded close enough in time to assume the same sea state unless otherwise stated [110].

5.1 Received Signal Characterization in FSR

Power Budget in Maritime FSR

According to the radar equation, received power P_r from a target in bistatic and forward-scatter radar is defined as

$$\frac{P_r}{P_t G_r G_t} = \frac{4\pi\sigma}{\lambda^2} L_{T-tg} L_{tg-R}, \tag{5.1}$$

where L_{T-tg}, L_{tg-R} are the transmitter-to-target and target-to-receiver propagation loss as it was described in [41].

Above the sea surface the TRP (two-ray path) propagation model gives the propagation loss as practically the same value as for perfectly conducting ground:

$$L_{T-tg} \approx \frac{h_T^2 h_{tg}^2}{R_t^4}, \; L_{tg-R} \approx \frac{h_{tg}^2 h_R^2}{D_r^4}, \tag{5.2}$$

where h_T, h_{tg}, h_R are the heights of transmitter antenna, target and receiver antenna, respectively, D is the baseline length, so that

$$\frac{P_r}{P_t G_r G_t} = \frac{4\pi\sigma}{\lambda^2} \cdot \frac{h_T^2 h_{tg}^4 h_R^2}{R_t^4 R_r^4}. \tag{5.3}$$

In FSR as explained in [41], the target signal cannot be received separately from the direct leakage from the transmitter to the receiver as both transmitter and receiver antennas are directed towards each other. The moving target signal interferes with the leakage and creates a small Doppler frequency modulation.

For the leakage signal we have the received power:

$$\frac{P_L}{P_t G_r G_t} = L_{T-R} = \frac{h_T^2 h_R^2}{D^4}, \tag{5.4}$$

where L_{T-R} is TRP propagation loss at 7.5 GHz (free space propagation loss at 24 GHz) between transmitter and receiver.

In order to estimate measured target FS RCS it is helpful to use the target-to-leakage ratio (TLR) as it was done in [41]:

$$\frac{P_r}{P_L} = \frac{4\pi\sigma}{\lambda^2} \cdot \frac{h_T^2 h_{tg}^4 h_R^2}{R_t^4 R_r^4} \cdot \frac{D^4}{h_T^2 h_R^2} = \frac{4\pi\sigma}{\lambda^2} \cdot \frac{D^4 h_{tg}^4}{R_t^4 R_r^4}, \tag{5.5}$$

this does not contain any hardware parameters (radiated power, antenna gains and heights) and rejects any possible errors in the estimation of these parameters. The ratio depends only on target parameters (target effective height and RCS) and FSR geometry (baseline distance and cross-point position).

Moreover, if the target crosses the baseline in the middle and $R_t = R_r = D/2$, equation (5) can be further simplified:

$$\frac{P_r}{P_L} = \frac{4\pi\sigma}{\lambda^2} \cdot \frac{D^4 {h_{tg}}^4}{(D/2)^8} = \frac{1024\pi\sigma}{\lambda^2} \cdot \left(\frac{h_{tg}}{D}\right)^4. \tag{5.5,a}$$

For a system wavelength of 4.0 cm (for frequency 7.5 GHz) the scattering from any target of interest (swimmer, boat, jet-ski) may be considered as an optical diffraction mechanism as it was explained in [41], i.e. its FSCS (forward scatter cross section) is defined through the target plane shape A (silhouette) as

$$\sigma = \frac{4\pi A^2}{\lambda^2}. \tag{5.6}$$

The FSCS value obtained by this simplest equation is in very good accordance to the results of more powerful 3D EM simulation of the target body by CST Studio Suite 2010 [106].

The target effective height h_{tg} for simple shapes (sphere, rectangular plate) is the position of target centre of symmetry. For a complex target shape we need to use the integration technique to define the target shape centre, i.e. target effective height. As an example, in Figure 5.1.1 the simplified shape of a complex target (boat with engine and sitting driver) is shown as in [41].

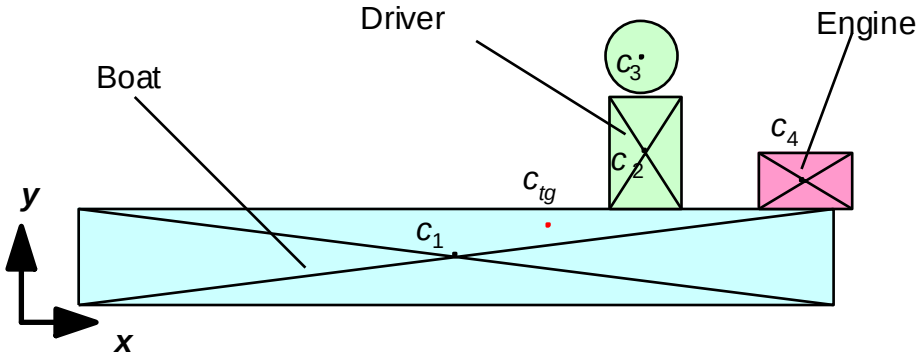

Figure 5.1.1 Presentation of complex target shape

The complex shape is divided into a few partial shapes, for which the partial area A_i and partial shape centre position $c_i = \{x_i, y_i\}$ can be easily defined. Thus, the total target shape aperture A is a sum of the partial areas [41]

$$A_{tg} = \sum_i A_i \,, \tag{5.7}$$

the position of the shape centre can be defined as the mass centre:

$$c_{tg} = 1/A_{tg} \sum_i c_i A_i \,. \tag{5.8}$$

If we define the TLR in dB units, the equation (5.5,a) may be written in the form:

$$10\lg\frac{P_r}{P_L} = 35.1 + 10\lg\sigma - 20\lg(\lambda) + 40\lg(\frac{h_{tg}}{D}), \qquad (5.9, \text{a})$$

all lengths are in m, and $10\log_{10}\sigma$ is the target RCS in [dBm^2], or for a wavelength of 0.04m:

$$\frac{P_r}{P_L}\Big|_{dB} = 62.88 + \sigma\Big|_{dBsm} + 40\lg(\frac{h_{tg}}{D}). \qquad (5.9, \text{b})$$

Small Inflatable Boat and Towed Sphere Trials

To test the relationship of target forward scatter cross section (FSCS) with Doppler signature, boat and swimmer targets have been measured [41]. During a number of MISL boat target measurements, a metallic sphere of known diameter (0.65 m) has also been towed approximately 15m behind, the sphere FSCS can be very accurately predicted from EM theory (Equation 5.6) to provide a calibration signature. Figure 5.1.2 shows one such signature of the MISL inflatable and the towed ball where baseline distance was 298 m and a central crossing point. The signature shown is actually an RSSI (received signal strength indicator) signal, with DC component representing the leakage/direct path signal amplitude.

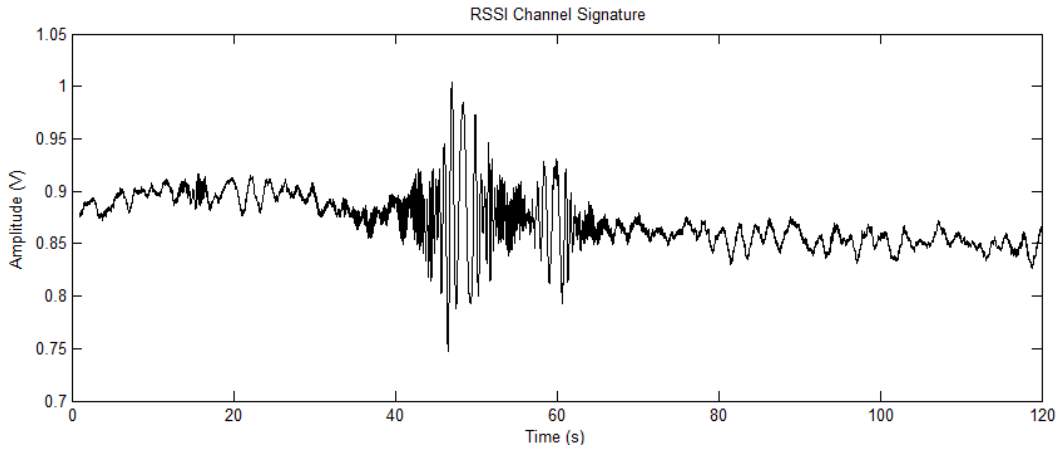

Figure 5.1.2 RSSI signature of MISL boat towing a metallic sphere of 0.65 m diameter

A comparison is made between the model theoretical target-to-leakage ratio, calculated using Equation (5.9,b), and that which is measured from the measured signature; the results of which are shown in Table 5.1. This comparison is made for the sphere target and the MISL inflatable.

In order to use Equation (5.9,b) the dimensions of the targets must be known to calculate the effective target height (Equation 5.8) and the FSCS (Equation 5.6). The metallic sphere has diameter of 0.65m and the MISL inflatable dimensions are shown in Figure 5.1.3 and presented in [41].

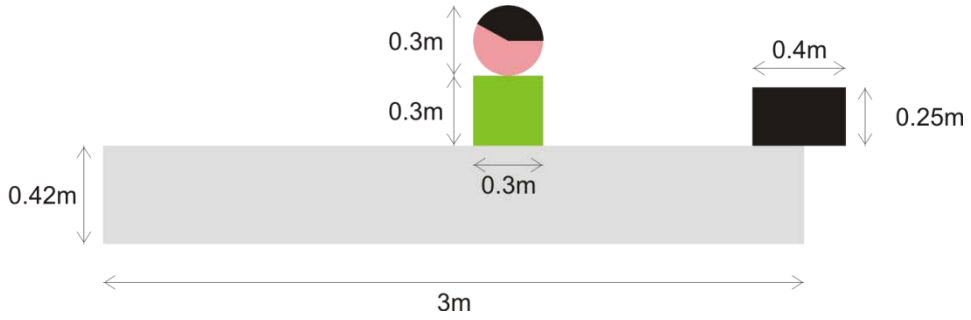

Figure 5.1.3 MISL inflatable boat dimensions for calculating effective target height and FSCS

The calculated target areas, FSCSs and effective target heights are included in Table 5.1. Two effective heights are included for the inflatable boat, one for the full boat and the other taking into account that the target in reality sits a lower in the water by approximately 8 cm. The sphere on the other hand is very light and travels full height on the surface.

In order to calculate the measured TLR, the power that is present at the detector diode for both the direct leakage signal and the peak target signal must be found. The TLR is then calculated (in dB) using

$$TLR = 20\log\left(\frac{\delta P}{8.686}\right) \tag{5.10}$$

Where δP is the difference between target and leakage power (in dBm) [41]. This is found through use of the diode calibration curve and measurement of leakage and peak target voltages from the RSSI data, the leakage voltage is the mean of the RSSI signal. The table indicates that the model fits the measurements very well in both cases.

Table 5.1 Comparisons of predicted and measured target-to-leakage ratios for sphere and boat target

Target	Planar Area [m^2]	Calculated FSCS (@7.5 GHz) [dBm^2]	Effective Target Height [m]	Calculated TRL [dB]	Measured TLR [dB]
Reference Target (Sphere, 65cm in diameter)	0.33	29.4	0.325	-26.0	-26.1
MISL Inflatable Boat	1.52	42.6	0.284 (full) 0.204 (partially submerged)	-15.2 -20.9	-20.3

The swimmer target has been measured at a much shorter range and in very different conditions to the other target measurements, Doppler records have been collected in a swimming pool environment over a baseline distance of 25 m presented in [110]. It was envisaged that the target signature from a swimmer is very different from that of other targets, the swimmer is mostly submerged and has the added complexity that depending on swimming method, the target is more or less visible in a periodic manner. Front crawl and backstroke involve the cyclic appearance and disappearance of arms and breaststroke requires the head to bob in and out of the water. Tests were performed in a more controlled environment so as to see the

potential signature types. Figure 5.1.4 shows a section of recorded Doppler data for the swimmer performing front crawl (1m antenna heights and CW 7.5GHz signal).

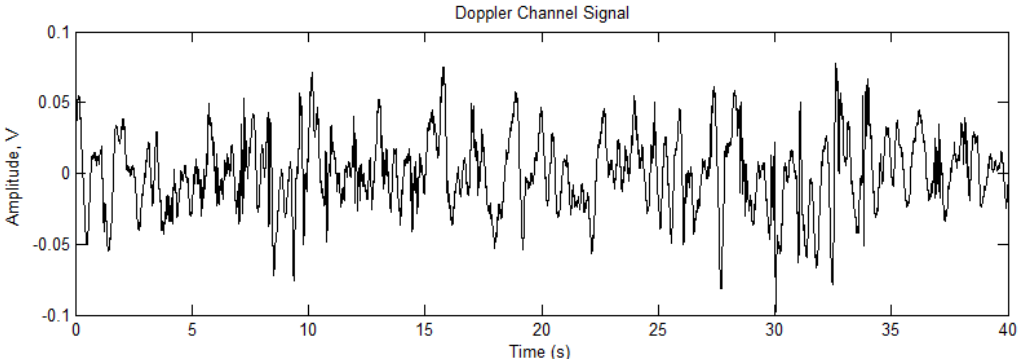

Figure 5.1.4 Doppler signature of swimmer performing front crawl

With the application of a 2Hz HPF (high pass filter) the target can be seen more clearly, this is shown in Figure 5.1.5. Here two baseline crossings of the swimmer target can be seen, one in the time frame 0-20 s and the other 20-40 s according to our video records and notes. Our opinion is that each of these is composed of a set of spikes corresponding to where the arms are raised out of the water to form the stroke but further investigation is needed. Video records of the measurements were also made allowing us to have better understanding the observed effect.

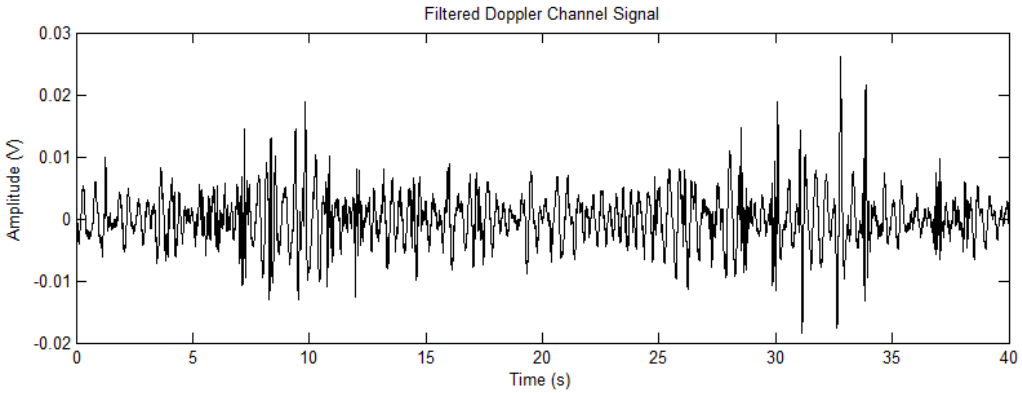

Figure 5.1.5 Filtered Doppler signature of swimmer performing front crawl

Figure 5.1.6 shows Doppler data for swimmer target performing breaststroke (0-20 s) and then backstroke (20-40 s) according to video records and notes. In this case, the (spike like) signatures for the back stroke are more prominent than those for the crawl in Figure 5.1.4 and can be seen pre-filtering [110]. On the application of a 2 Hz HPF it appears that the back stroke spikes are visible but it is not the case with the breaststroke swimming where it is not possible to see the signature of the head on top of the water – Figure 5.1.7.

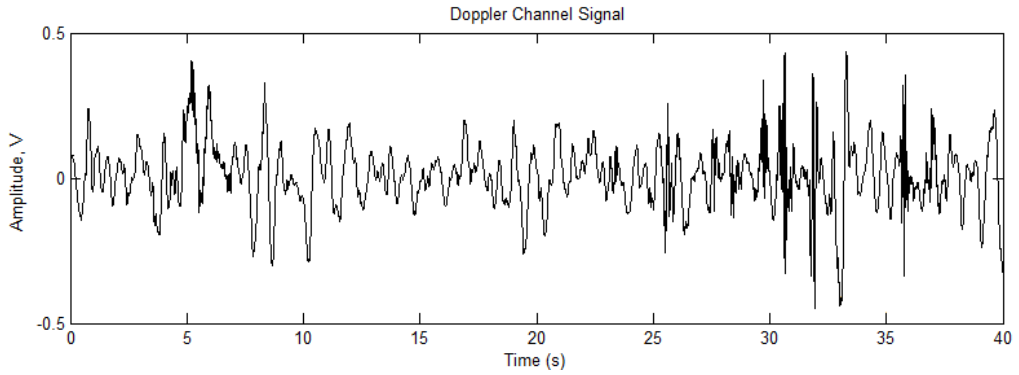

Figure 5.1.6 Doppler signature of swimmer performing breaststroke (0-20s) followed by back stroke (20-40s)

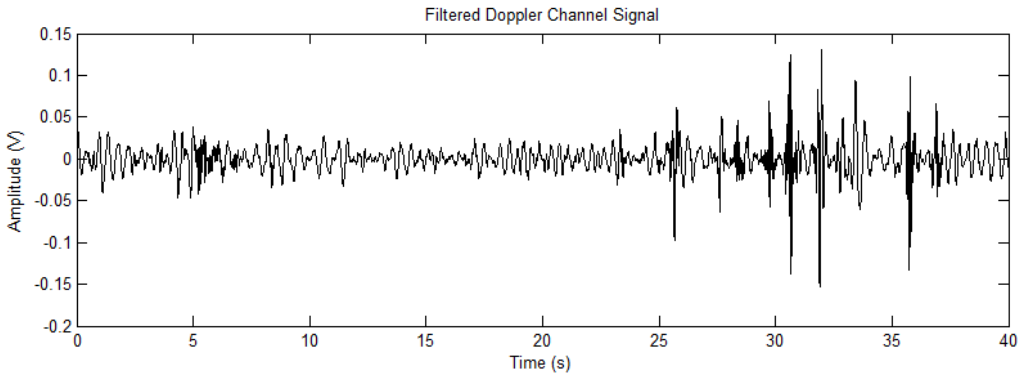

Figure 5.1.7 Filtered Doppler signature of swimmer performing breaststroke followed by back stroke

Summary and Conclusions

The sphere FSCS is well known and has an analytic expression which is easily confirmed by modelling in CST microwave studio. The estimation of boat FSCS depends on how accurately the dimensions are introduced into the FSCS modelling [110]. As one can see the measured and modelled value of TLR are very similar for the sphere and for the boat, which implies that the boat FSCS is estimated adequately. This TLR model therefore allows the prediction of expected signature strengths for targets of any cross section and effective height, given a particular FSR baseline length for which the leakage can be calculated.

Doppler records have been collected for different swimming styles over short ranges to give an idea of expected signature structure.

5.2 Variation of Target Signature with Baseline Crossing Angle

A set of experimental measurements have been performed to determine the variation of target signature with FSR baseline crossing angle [110].

The measurements presented here were recorded at Langstone Harbour over a range of 298 m with antenna heights of 1 m using a 7.5 GHz CW signal. The target shown in each of the following measurements is the MISL small inflatable and using GPS track and waypoint data it is possible to retrieve the trajectories for the target in each measurement. Measurements were taken quite close in time to try to ensure a constant sea state.

Attempts were made to achieve baseline crossing angles of 90°, 45° and 22.5°. The sea conditions makes such trajectory's hard to achieve precisely and the outcome is a set of measurements at 78°, 52° and 34° and as close to along the baseline as possible.

Recorded Signatures for 78° Baseline Crossing of Small Inflatable Boat

Figure 5.2.1 shows the GPS track data corresponding to a 78° target-baseline crossing. The speed of the target was found to be 11 km/h (5.9 knots). The Doppler record is shown in Figure 5.2.2, containing two MISL inflatable signatures of which the second highlighted in red is related to the GPS data above. The PSDs of the highlighted target signature and the highlighted clutter section (green) are shown in Figure 5.2.3 (in corresponding colours).

Figure 5.2.1 GPS track data for target trajectory. Blue shows full track and red indicates section used for analysis

It can be seen both from time domain and PSD that the target signatures have a high signal-to-clutter ratio (SCR); the target is clearly visible over clutter and occupies a much wider spectral bandwidth as observed in [110].

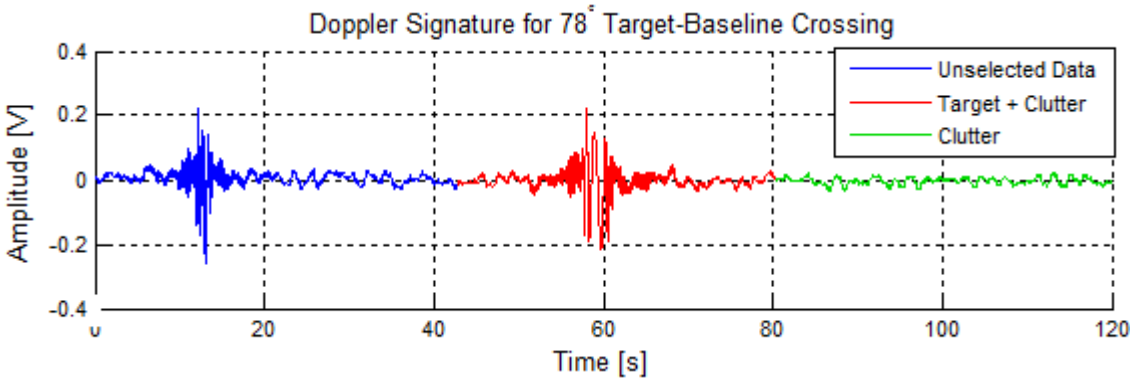

Figure 5.2.2 Doppler signature for two baseline crossings of the MISL inflatable. Red indicates target selection corresponding to a 78° crossing angle and green indicates a clutter selection

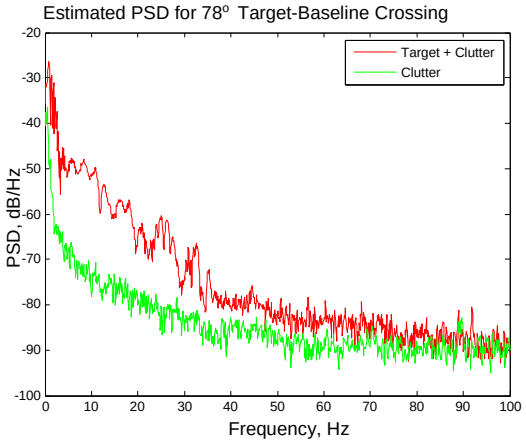

Figure 5.2.3 Power spectral density of target plus clutter for a target-baseline crossing angle of 78°

Recorded Signatures for 52° Baseline Crossing of Small Inflatable Boat

Figure 5.2.4 shows the recorded trajectory for a target crossing the baseline at an angle of 52°. In this case, the target speed is measured to be 10.6 km/h equivalent to 5.7 knots, which is similar to the speed of the target for the 78° crossing angle and so a good comparison.

Figure 5.2.4 GPS track data for target trajectory. Blue shows full track and red indicates section used for analysis

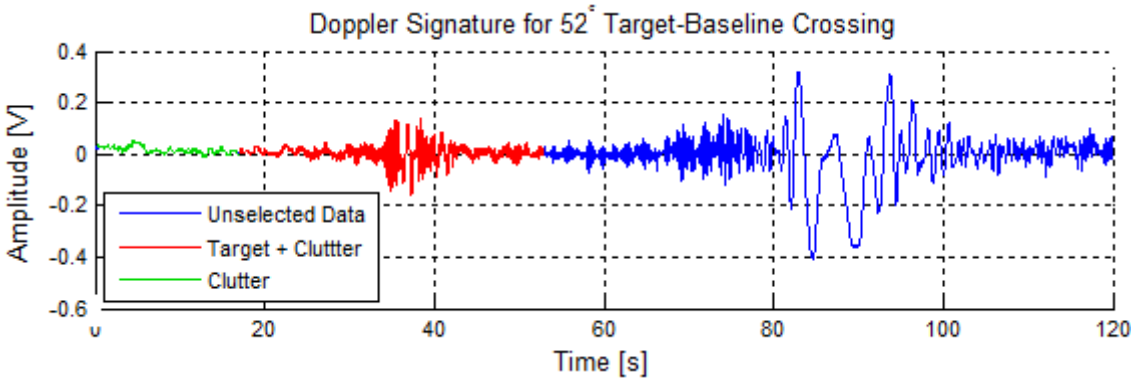

Figure 5.2.5 Doppler signature for baseline crossing of the MISL inflatable. Red indicates target selection corresponding to a 52° crossing angle and green indicates a clutter selection

The Doppler record containing the target signature relating to the above trajectory is shown in Figure 5.2.5. This record contains the target selected in red, the signature of a sailboat as it crossed the baseline in the blue section and a clutter selection in green. The PSDs for the target (plus clutter) and clutter selection are shown in Figure 5.2.6. Again target is clearly separable from the clutter in both time and frequency domains as discussed in [110].

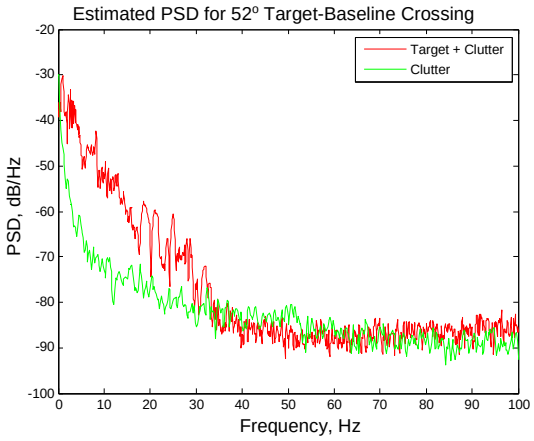

Figure 5.2.6 Power spectral density of target plus clutter for a target-baseline crossing angle of 52°

Recorded Signatures for 34° Baseline Crossing of Small Inflatable Boat

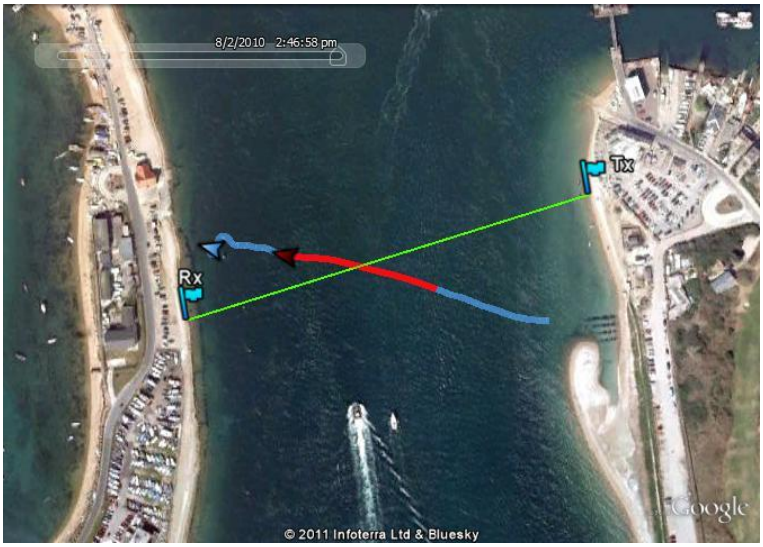

Figure 5.2.7 GPS track data for target trajectory. Blue shows full track and red indicates section used for analysis

Figure 5.2.7 shows the recorded trajectory for the target present in the Doppler signature in Figure 5.2.8. The GPS track of the target gives a velocity of 10.2 km/h or 5.5 knots. Figure

5.2.9 shows the PSD of the selected (red) target signature and the selected (green) clutter section.

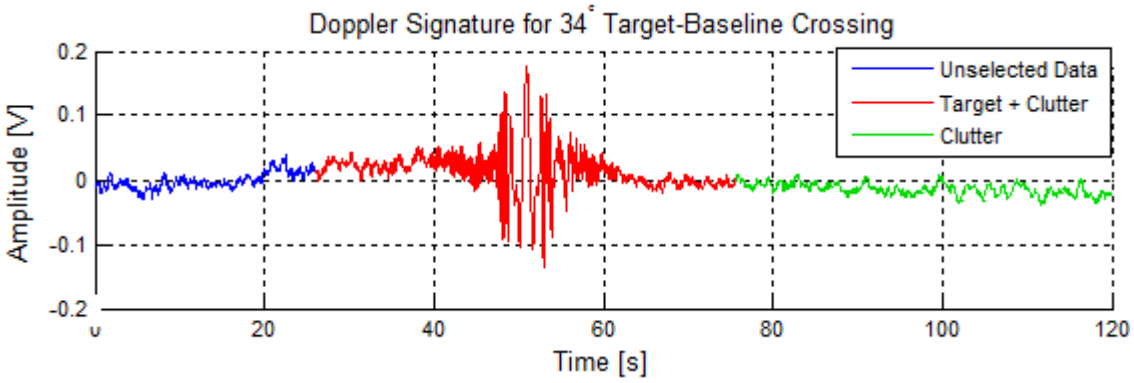

Figure 5.2.8 Doppler signature for baseline crossing of the MISL inflatable. Red indicates target selection corresponding to a 34° crossing angle and green indicates a clutter selection

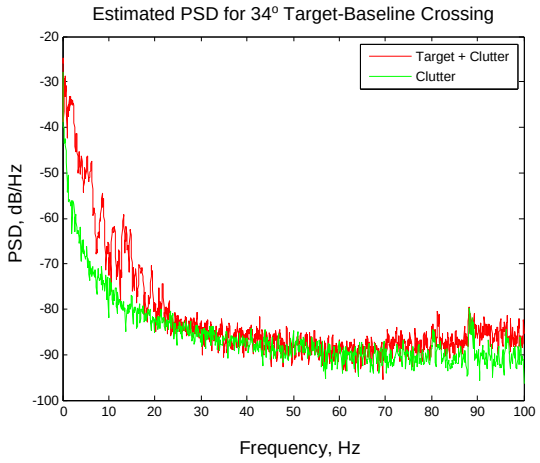

Figure 5.2.9 Power spectral density of target plus clutter for a target-baseline crossing angle of 34°

Yet again the target can clearly be seen above clutter, however it is noted that the spread of the target spectrum is reduced for the lower crossing angles – this is expected from the FSR (forward scatter radar) topology [110].

Comparison of Target PSD's for Three Baseline Crossing Angles

Figure 5.2.10 shows a comparison of all three target crossing angle PSDs plus one selected example of a clutter spectrum.

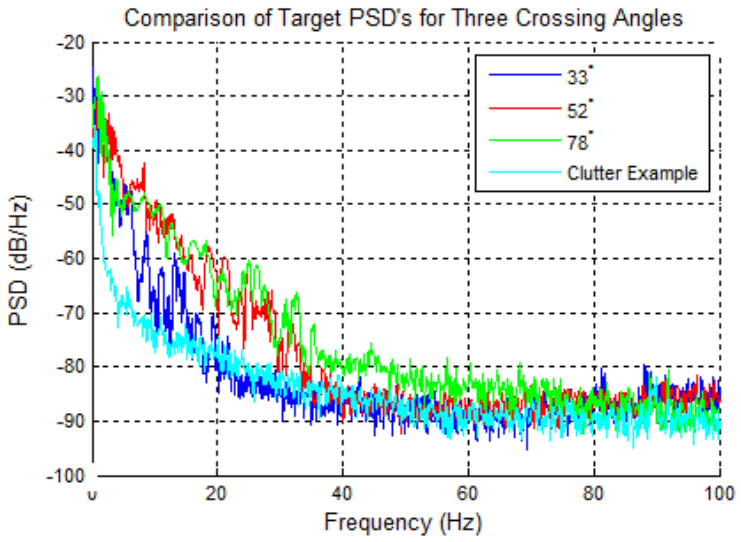

Figure 5.2.10 Comparison of target signature PSDs for target-baseline crossing angles of 78, 52 and 33°

Summary and Conclusions

It can be seen from the PSDs in Figure 5.2.10, that the lower the crossing angle, the narrower the target spectrum (when target speeds are more or less constant). This behaviour is expected from FSR geometry due to the velocity components of the target being larger with respect to transmitter and receiver at greater angles – thus higher Doppler.

The smaller the crossing angle the longer the observation time as the target occupies the region around the baseline for a longer time. This can be seen especially so by comparing the highlighted target signatures in the Figures 5.2.2 and Figure 5.2.8; observing the relative widths in the time domain [110].

Comparing the target signal strength in the Doppler signatures indicates that the peak (when on the baseline) does not essentially depend on the crossing angle and follows the RCS (radar cross section) of the target as discussed in [110]. Deviations may occur due to slightly different baseline crossing points.

5.3 Quantification of Doppler Signature with Velocity

To determine the variation of target signature with respect to target velocity, Doppler recordings were made of the MISL inflatable boat target crossing the FSR baseline approximately mid-way at 90°, with 1m antenna heights using a CW 7.5GHz signal discussed in [110]. Various target speeds have been measured over the full period of our trials, here two speeds are shown, 10 knots and 5 knots which have been recorded when travelling with and against the tide in Langstone Harbour.

Recorded Signature for 10 knot Target Velocity

Figure 5.3.1 (a) shows recorded/measured Doppler data for the small inflatable boat target, red indicates the target signature and green the clutter which are then used to form the PSD's in Figure 5.3.1 (b). The signature denotes the boat travelling with the tidal flow into the harbour.

In Figure 5.3.1 (b) the spectral width of the target signature is quite wide due to the relatively high speed of the target, noticeable above the clutter level up to approximately 60Hz.

Figure 5.3.2 is an image of the target trajectory as measured by the GPS tracker. The blue line shows the complete measured trajectory and the red, the trajectory used to measure target speed and baseline crossing parameters. The speed is estimated using the GPS at an average of 9.8

knots (10.5 knots across the baseline), with a crossing angle of 68°, crossing a 276m baseline 106 m from the transmitter Tx [110].

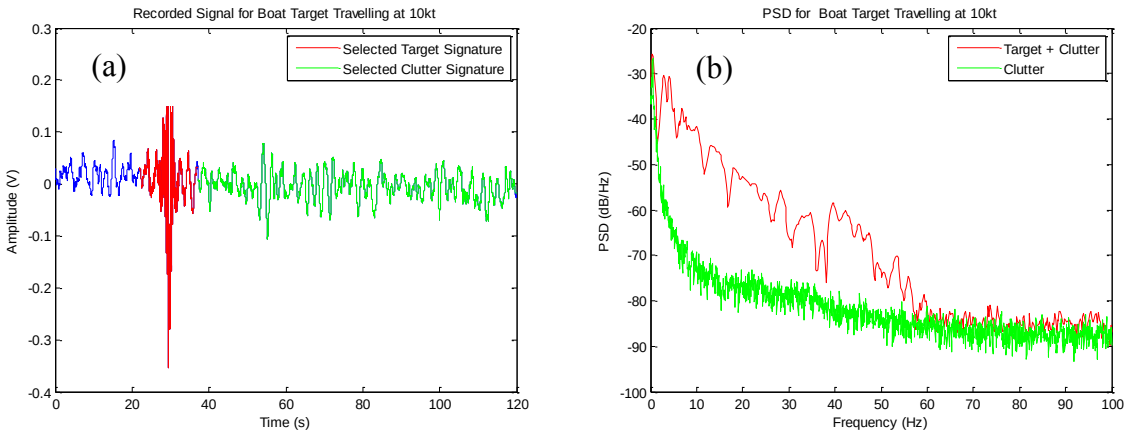

Figure 5.3.1 Doppler signature (a) and PSD (b) for sea clutter and target with speed of 10 knots

Figure 5.3.2 Map showing the measured target trajectory for the signature in Figure 5.18

Recorded Signatures for 5 knot Target Velocity

Figures 5.3.3 (a) and (b) are Doppler data and PSDs from data corresponding to a slower target velocity, where the target is competing against the tide.

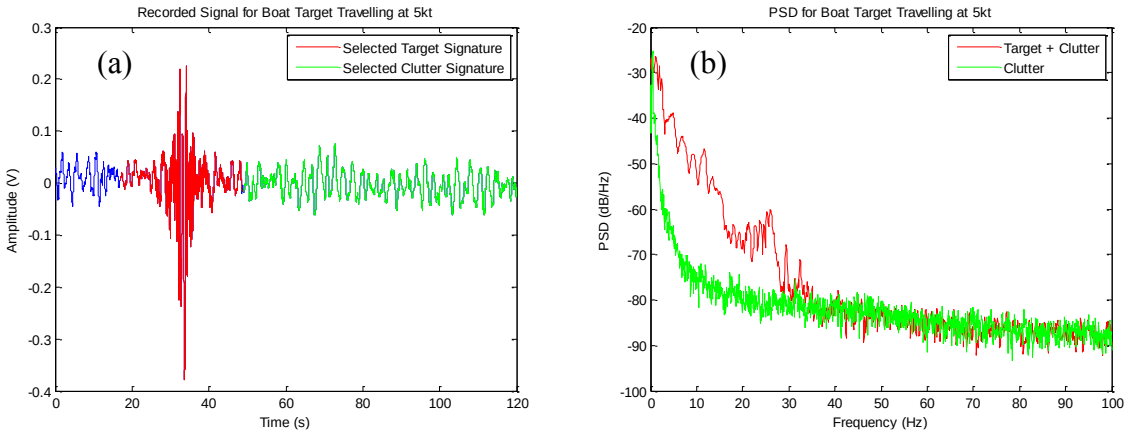

Figure 5.3.3 Doppler signature (a) and PSD (b) for sea clutter and target with velocity 5 knots

Figure 5.3.4 is an image of the target trajectory as measured by the GPS tracker. The blue line shows the complete measured trajectory and the red, the trajectory used to measure target speed and baseline crossing parameters. The speed is estimated at an average of 4.8 knots (5.4 knots across the baseline), with a crossing angle of 83°, crossing a 276m baseline 127m from the transmitter Tx [110].

Figure 5.3.4 Map showing the measured target trajectory for the signature in Figure 5.3.3

In Figure 5.3.3 (b) the spectral width of the target signature is about half as wide as in Figure 5.3.1 (b) for the faster moving target (as expected as the target is travelling at half the speed), the target spectrum is visible above the clutter level up to a frequency of approximately 30Hz in this case [110].

Comparison of Calculated PSD's for Faster and Slower Speed Targets

Figure 5.3.5 PSD comparison for boat target moving at speeds of 5kt and 10kt

Visual Comparison of Width of Target Signatures

Figures 5.3.6 and Figure 5.3.7 show the zoomed target signatures at 10 and 5 knots respectively to allow visual comparison of the signature width.

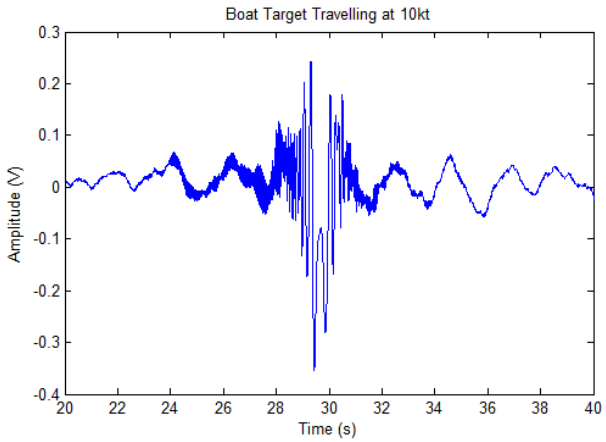

Figure 5.3.6 Zoomed signature for target with speed of 10 knots

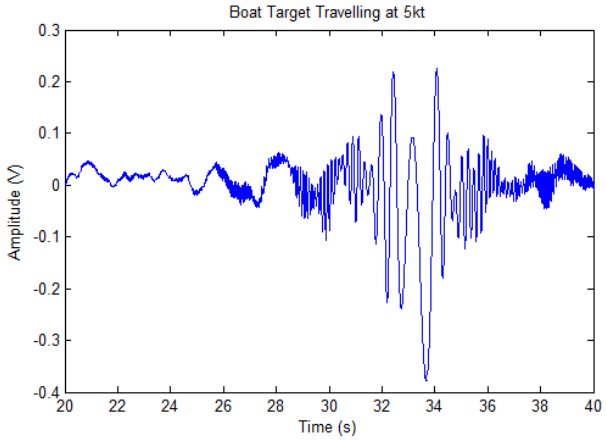

Figure 5.3.7 Zoomed signature for target with speed of 5 knots

On inspection of the zoomed target signatures (which have the same time scale) it can be seen that the slower target has a wider signature. It may even be stated that the slower target signature is approximately twice the width of the faster, corresponding to half the speed [110].

Summary and Conclusions

Figure 5.3.5 shows the comparison of the two target PSDs at the faster and slower speeds. The bandwidth of the PSD is greater for the faster moving target, by two times. This is (as expected) in proportional to the speed being two times faster and all other conditions being reasonably

equal. This proportional speed difference is also visible in the target signatures themselves, with the slower speed target having a twice longer duration signature in Figure 5.3.3 (a) than the faster target in Figure 5.3.1 (a), purely because the target has spent longer in the vicinity of the baseline [3]. The hypothesis above depends on the angle that the target is approaching the baseline and it will not be true if the angle of crossing is different for the various speed measurements.

The measured power of the received signal (related to amplitude in the case of the plots above) does not depend on the target speed, as expected due to the target FSCS (forward scatter cross section) remaining constant.

5.4 Variation of Target Signature with Polarisation

Measurements have been performed to estimate the system performance with respect to varying antenna polarisation [110]. The horns used in the trials presented here are equal beamwidth in both planes (±10°), ensuring no effect of antenna pattern when changing polarisation.

The MISL small inflatable boat is used as the target and measurements are made using a CW 7.5GHz signal with 1m antenna heights. On inspection of the recorded GPS track data the target trajectories for each measurement appear to have similar baseline crossing points and angles, the speeds are not so relevant to this analysis but are in the range 10-12 knots.

Absolute peak signal value for the target and received DC signal level are indicated, the DC level gives an indication of the received signal (leakage/direct path) strength and is removed from signatures shown before plotting.

Recorded Signatures for Vertical (V-V) Polarisation

Doppler data recorded with both the receiving and transmitting antennas having vertical polarisation is shown in Figure 5.4.1 (a). The red highlight indicates the small boat target signature and green a selection of clutter. Figure 5.4.1 (b) shows the corresponding PSDs for these sections of the signature.

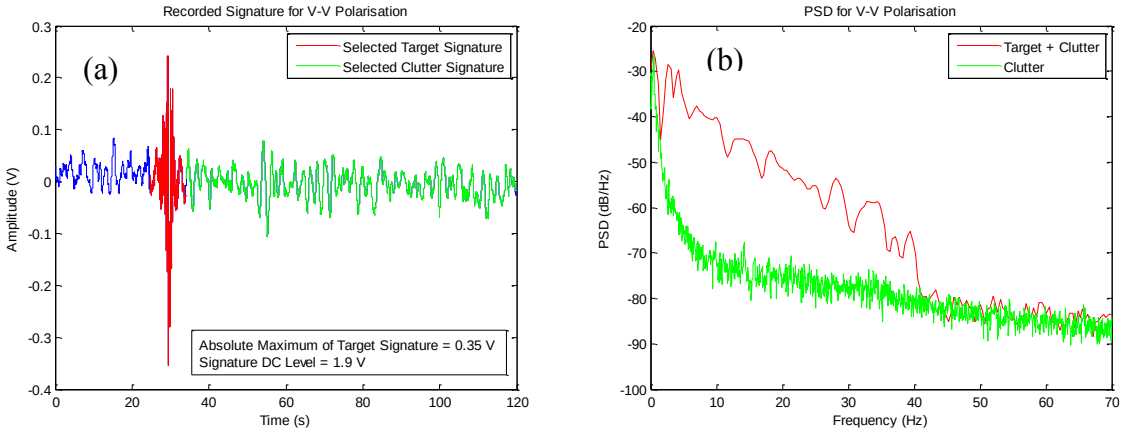

Figure 5.4.1 Doppler signature (a) and PSD (b) for target and clutter recorded with V-V polarisation

Recorded Signatures for Horizontal (H-H) Polarisation

Results for the case where both antennas have horizontal polarisation are depicted in Figure 5.4.2, again (a) showing Doppler signature and (b) the PSDs of the selections.

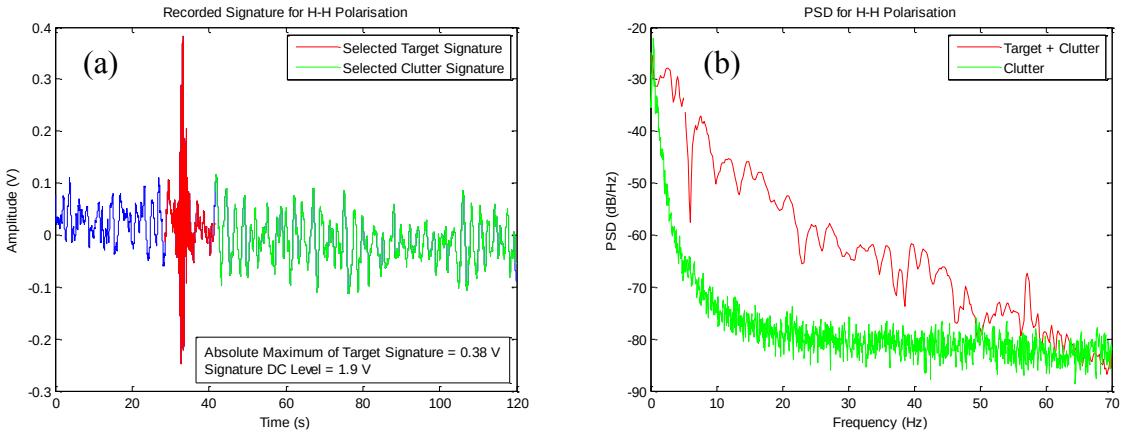

Figure 5.4.2 Doppler signature (a) and PSD (b) for target and clutter recorded with H-H polarisation

Recorded Signatures for Cross (H-V) Polarisation

Cross polarisation results are contained in Figure 5.4.3, again (a) showing the full and selected parts of the recorded Doppler signature and (b) the corresponding PSD's. Note that 5.4.3 (a) also contains the signature of a larger boat crossing the baseline (blue section).

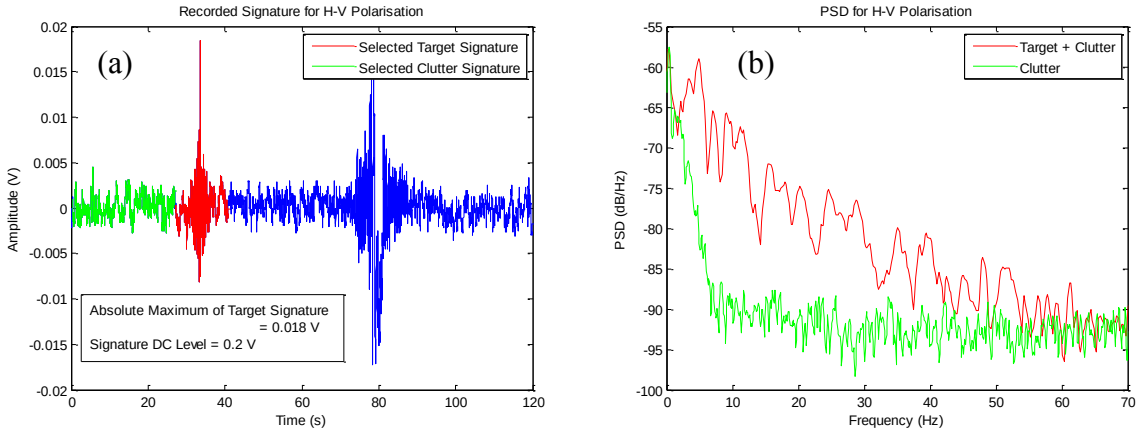

Figure 5.4.3 Doppler signature (a) and PSD (b) for target and clutter recorded with H-V polarisation

Comparison of Received Signature Levels and Spectra for the Various Polarisations

Figure 5.4.4 shows a comparison of the clutter PSDs for the three polarisation combinations of V-V, H-H and H-V.

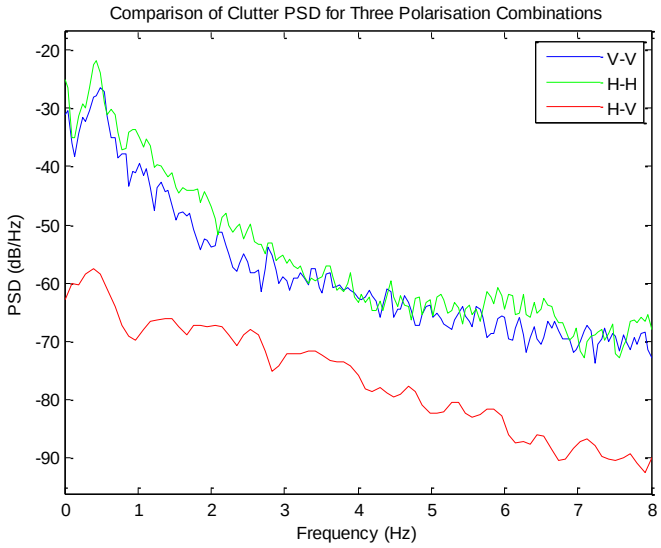

Figure 5.4.4 Comparison of clutter PSDs for V-V, H H and H-V polarisations

Figure 5.4.5 shows a comparison of received DC level of the signatures, along with the peak target signature amplitude. Due to the fact that the FSR configuration between trials remained the same, the trajectories of the targets were similar and all measurements were taken within a short time frame of each other, any differences are due to the polarisation change [110].

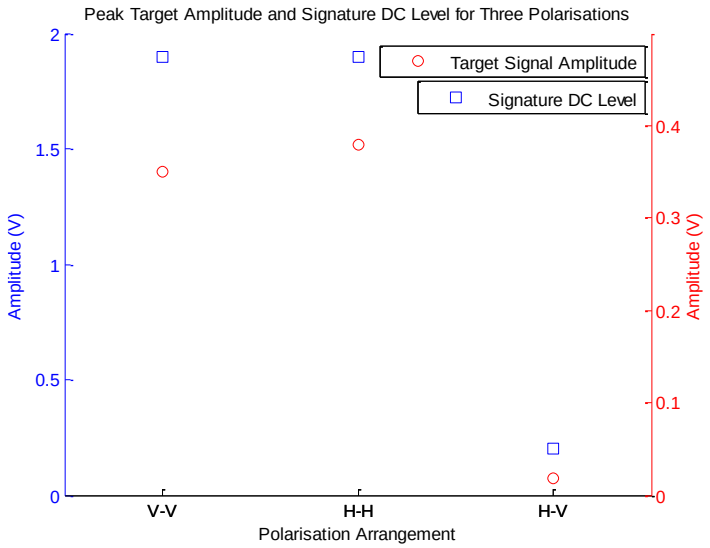

Figure 5.4.5 Target signal amplitude and recorded signature DC level for V-V, H-H and H-V polarisations

Summary and Conclusions

The clutter PSDs in Figure 5.4.4 show approximately a 30dB drop for the cross polar case, however looking at the corresponding target signature PSDs in Figure 5.4.1 to 5.4.3 this is also true for the target signature, implying no real benefit from cross polar antenna configuration. This same effect is shown (Figure 5.4.5) in the DC level of received signal remaining similar for both V-V and H-H but dropping drastically for H-V with similar trends in target amplitude. All in all V-V and H-H appear to have similar signatures/SCR. H-V gives much reduced returns both in target and clutter with no visible increase in SCR to justify the need for higher transmit power.

Ultimately these conclusions are based on measurements where it is assumed that the system is designed to function at very low grazing angles [110].

5.5 Quantification of Doppler Spectrum with Variation in Antenna Height

Antenna height measurements in Langstone Harbour

A set of experimental measurements have been made to attempt to determine the variation of target signature and clutter with antenna height as discussed in [110].

Measurements were recorded at Langstone Harbour over a range of approximately 300m with antenna heights of 0.5 m, 1.5 m and 2 m. Target trajectories were similar for each antenna height measurement and the same MISL inflatable crossed the baseline near perpendicularly approximately mid-way between transmitter and receiver, target speeds are not necessarily similar in the results shown. Measurements were performed using CW 7.5GHz signal and were taken within a relatively short time period of each other, so sea state remains relatively stable from signature to signature.

To note, in this instant a metallic sphere is being towed for calibration purposes which accounts for the two signatures shown in each plot, the sphere being the latest occurring signature.

As an estimation of SCR, the absolute peak target signature for both boat and sphere is compared to 0.7σ of the clutter selection for each signal shown. Absolute peak signal value for sphere target and received DC signal level are also indicated, the DC level gives an indication of the received signal (leakage/direct path) strength and is removed from signatures shown before plotting.

Signatures Recorded for 0.5 m Antenna Elevation

Figure 5.5.1 (a) shows recorded Doppler data for the MISL inflatable and towed sphere with antenna heights of 0.5 m. Red indicates the selected target signatures and green the selected clutter used to form the PSDs for clutter and target in Figure 5.5.1 (b).

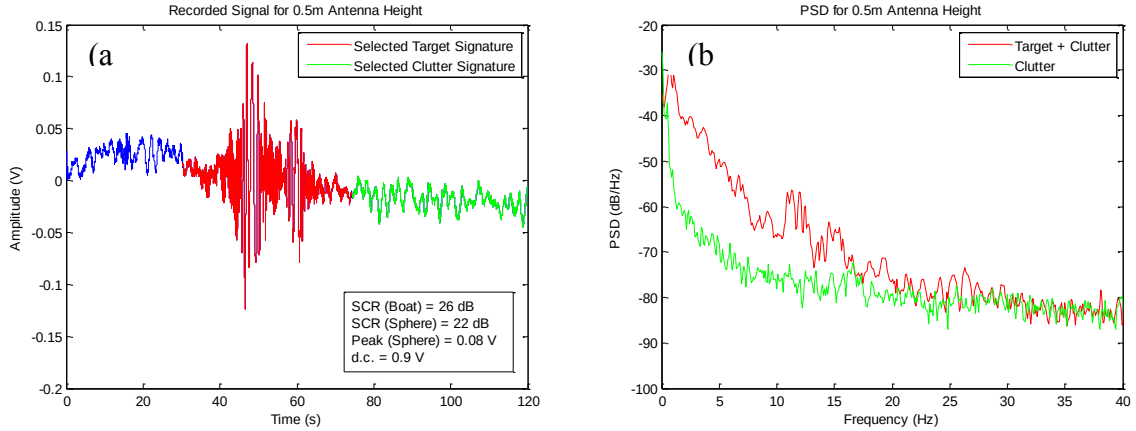

Figure 5.5.1 Doppler signature (a) and PSD (b) for target and clutter with 0.5m antenna height

Signatures Recorded for 1.5 m Antenna Elevation

Figures 5.5.2 (a) and (b) are similar to those above except with antenna height of 1.5m. Again, the selected signature consists of the small boat target and a towed metallic sphere.

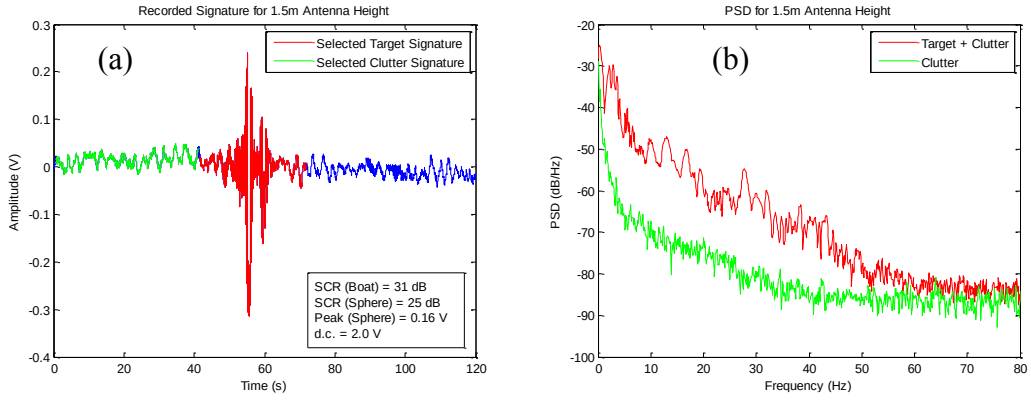

Figure 5.5.2 Doppler signature (a) and PSD (b) for target and clutter with 1.5m antenna height

Signatures Recorded for 2 m Antenna Elevation

Figure 5.5.3 corresponds to recorded Doppler data (a) and PSDs (b) for a 2m elevation antennas.

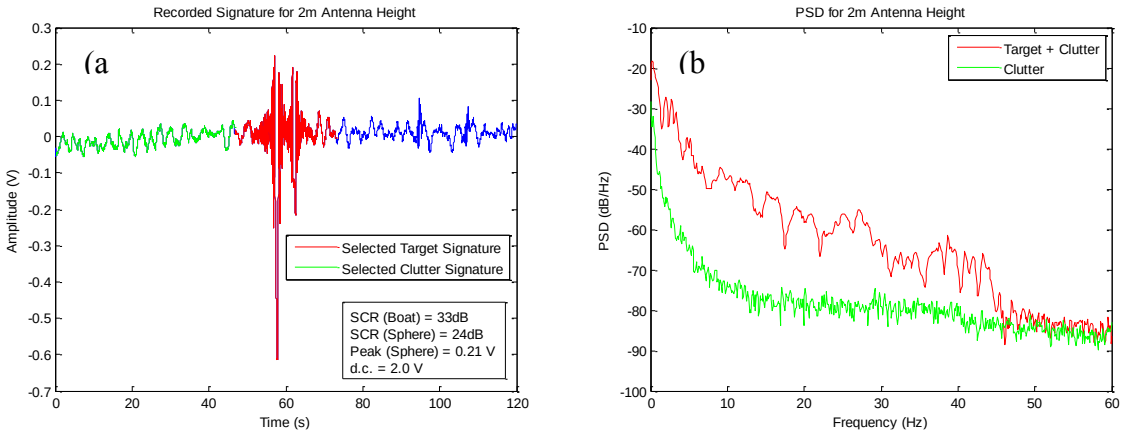

Figure 5.5.3 Doppler signature (a) and PSD (b) for target and clutter with 2 m antenna height

Comparison of Calculated SCR's and Signature Amplitudes

The following plots show SCR's (Figure 5.5.4) for both boat and sphere with respect to the tested antenna elevations and corresponding DC/received signal strength and sphere amplitude level (Figure 5.5.5).

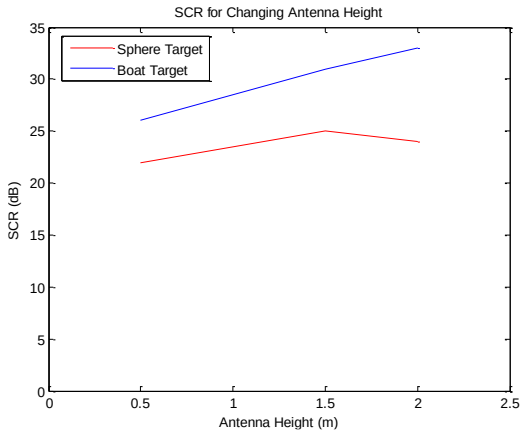

Figure 5.5.4 Boat and spherical target SCR variation with antenna elevation

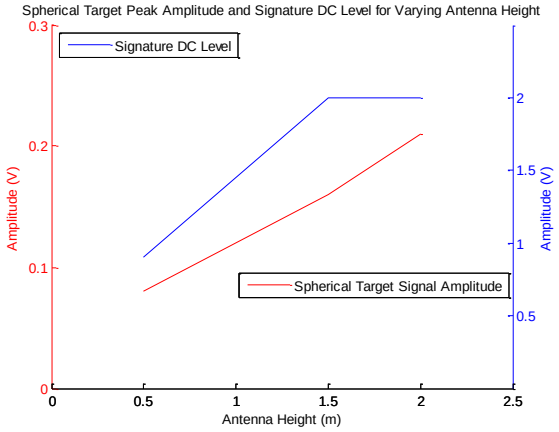

Figure 5.5.5 Spherical target signal amplitude and 'Doppler' signature DC level with respect to antenna

Summary and Conclusions

It is predicted that received power for the FSR radar over a perfectly conducting flat surface is in proportion to the product of the square of the antenna heights. Admittedly the sea is not an ideal flat surface and so we may not expect strict adherence to the theory [110].

Looking at Figure 5.5.5 there is a definite increase in the received power (DC) level of the received signatures as the antenna height increases, this has not been classified numerically yet as it appears that the detector diode may be saturated as the antenna heights were increased, shown by the levelling off of the DC value for taller antenna heights.

Antenna height measurements in Bulgaria

During the trials in Bulgaria, measurements with varying antenna height have been made [110]. The transmitter and receiver positions are shown on Figure 5.5.6. During the trials only the Receiver antenna height has been altered from 1 meter to 7 meters.

Figure 5.5.6 Topology of trial area and transmitter and receiver positions

Figure 5.5.7 shows a RSSI signature of the MISL boat crossing the middle of baseline, both antennas in this measurement are 1 meter above sea level. The transmitted signal uses 7.5 GHz CW with directional Flann horn antennas. The following figures (Figures 5.5.7-5.5.10) show

the power spectral density of the target and clutter signatures, along with coresponding high pass filtered versions of the RSSI and the PSD.

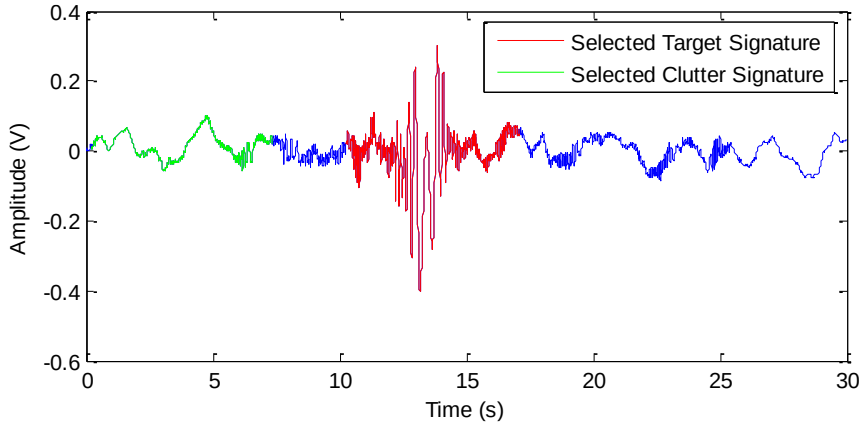

Figure 5.5.7 Target and clutter signatures with antenna heights of 1 metre

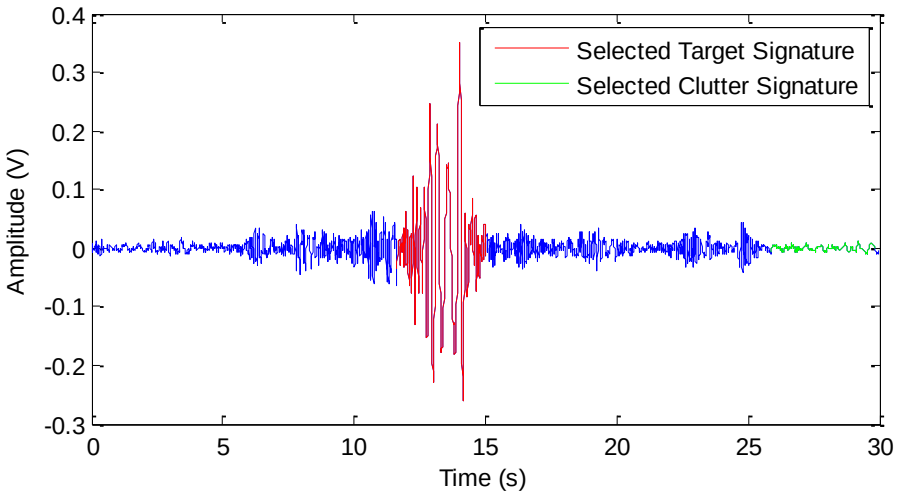

Figure 5.5.8 Same signature as previous figure after application of 2 Hz

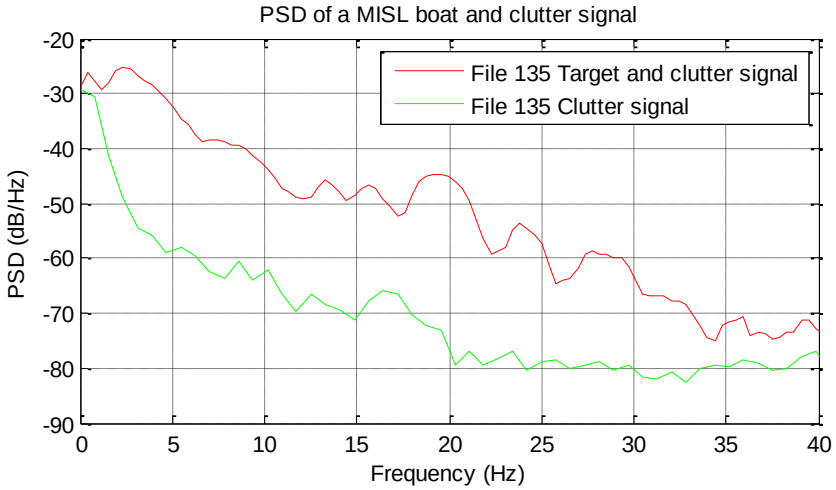

Figure 5.5.9 Target and clutter PSD's for 1m antenna height

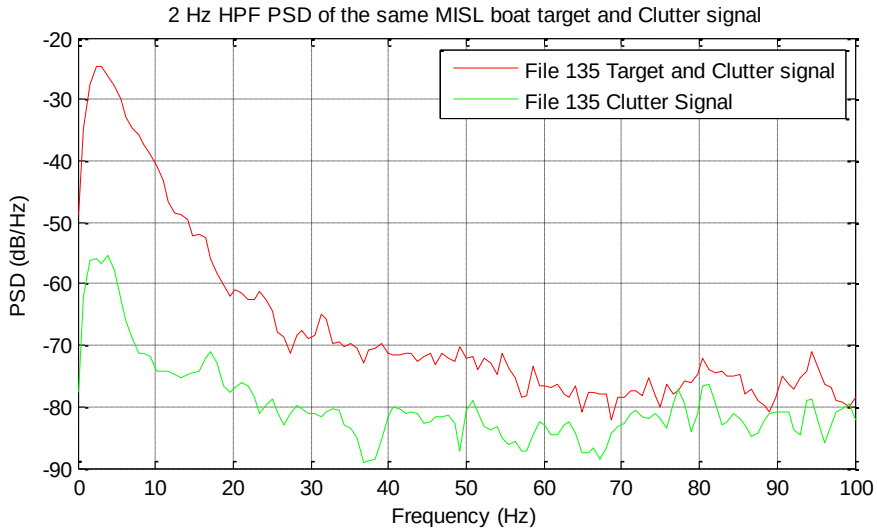

Figure 5.5.10 Target and clutter PSD's from previous figure after 2 Hz HPF

In order to compare the signal to clutter dependence of the antenna elevation, measurements with increased antenna height have been made. The raised antenna was aproximately 7 metres from sea level, the target signature of the MISL boat has been recorded and the RSSI signal and the power spectral density are shown in Figure 5.5.11 and Figure 5.5.13. A 2 Hz high pass filtered version of the RSSI and the PSD have been displayed in Figure 5.5.12 and Figure 5.5.14.

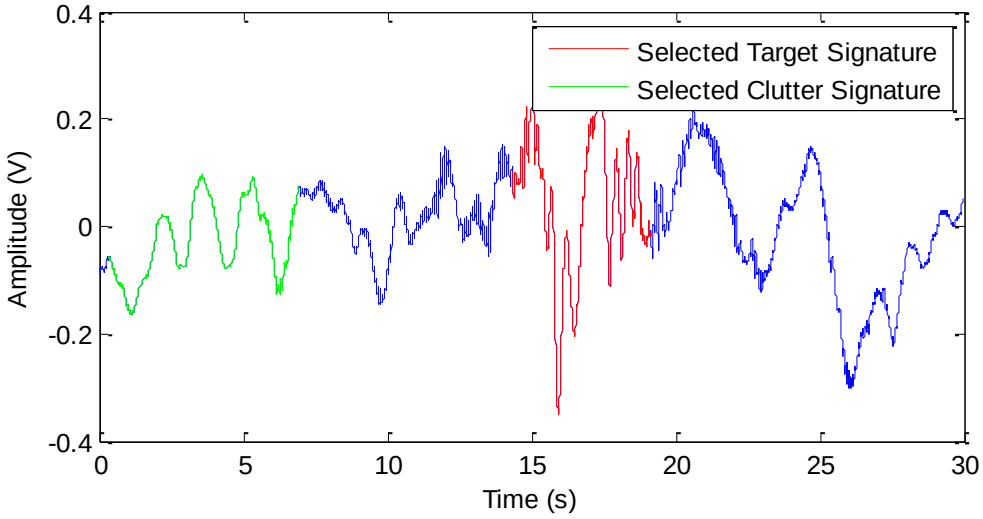

Figure 5.5.11 Target signal and clutter with antenna height of 7m

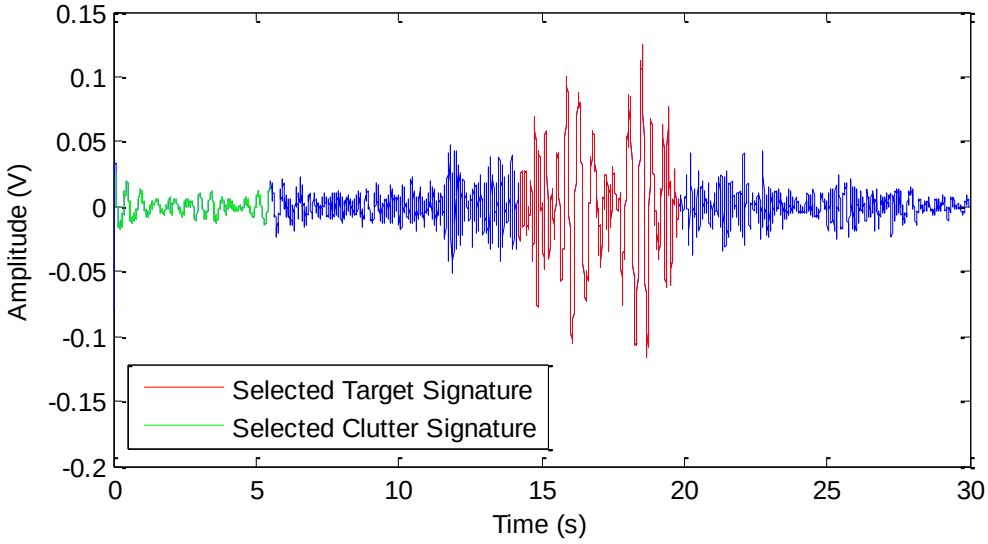

Figure 5.5.12 Target signal and clutter with antenna height of 7m filtered with 2Hz filter

The signal to clutter ratio has been calculated for the two different heights and the results are shown in Table 5.2, calculation of the signal to clutter ratio after 2 Hz HPF are shown in the same table.

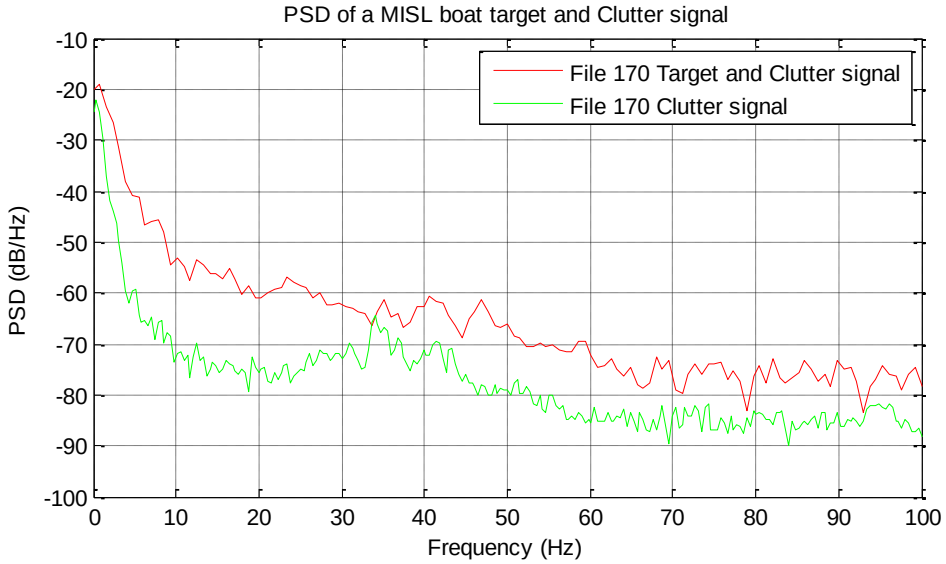

Figure 5.5.13 Target and Clutter signal PSD's with 7m antenna height

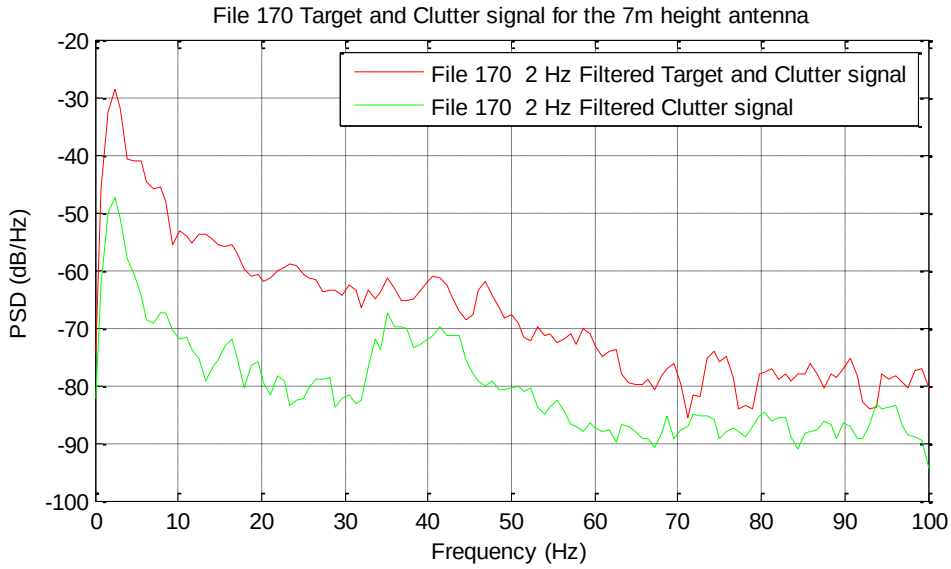

Figure 5.5.14 Target and Clutter signal PSD's with 7m antenna height

Table 5.2 Signal-to-clutter calculations for 1 and 7 meter antenna heights before and after 2Hz filter

File #	Signal type	Rx filter	Range, m	Tx attenuation, dB	RSSI gain, dB	Antennas	Height of antenna, m	Signal to Clutter Ratio, dB
135	CW	3GHz	350	10	10	Flann Antennas V V -Fixed	1	24.29 (before HPF) 42.63 (after applying 2 Hz HPF)
170	CW	3GHz	350	10	10	Flann Antennas V V – Fixes	7	17,19 (before HPF) 28.3(after applying 2 Hz HPF)

From this table it follows that there is some reduction of SCR with the increasing antenna height. Further experimentation and modelling is needed to properly understand the physics behind this effect [110].

Effect of Antenna Height (Grazing Angle) and Polarisation

The complex reflection coefficient for specular reflection of EM waves from a plane surface of given conductivity σ and relative permittivity ε_r varies depending on the grazing angle Ψ, polarisation and frequency of the wave. A plot to show the change in the magnitude of the reflection coefficient for sea water (σ=5 S and ε_r = 81) at our chosen radar frequency of 7.5 GHz is presented in Figure 5.5.15. The blue line indicates vertically polarised and the green indicates horizontally polarised incident waves [110].

The plot itself indicates that for a vertically polarised incident wave there is large drop in reflectivity at 6.3° (Pseudo Brewster angle), this can be very useful as it limits the intensity of surface reflected waves received by the radar – effectively implementing a free space

propagation approximation. However if we look at the comparison between antenna height and baseline distance needed to maintain this angle in our system we obtain the plot in Figure 5.5.16.

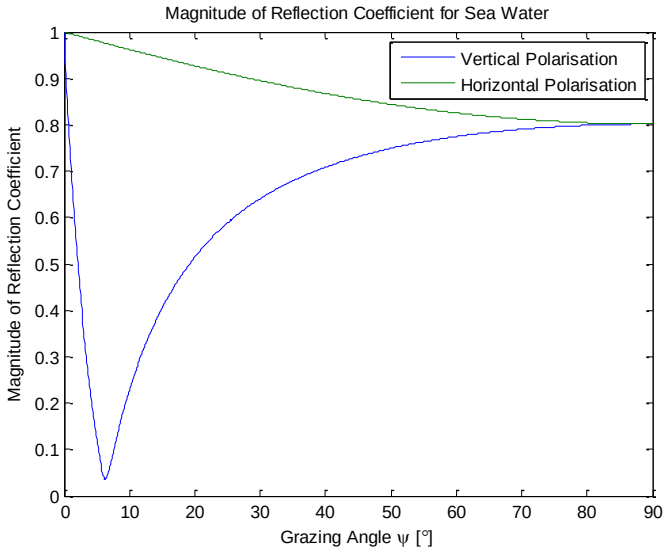

Figure 5.5.15 Magnitude of reflection coefficient of air-sea water interface with respect to grazing angle for both horizontal and vertical polarisation incident waves at a frequency of 7.5 GHz

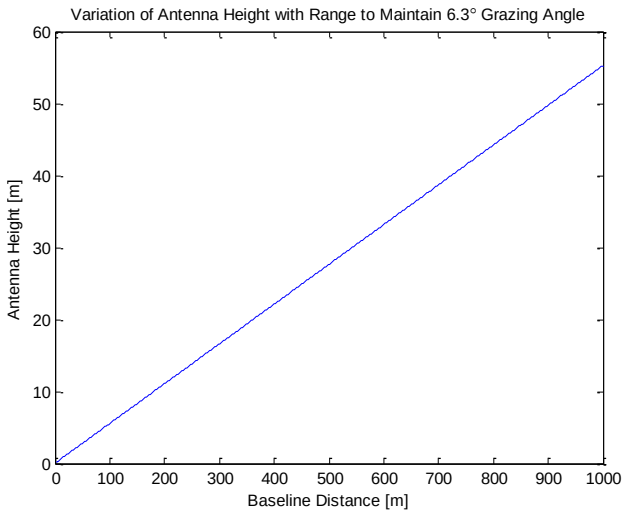

Figure 5.5.16 Relationship between antenna height and baseline range to maintain a grazing angle of 6.3°

From the above plot it can be seen that for a baseline distance of 300m we would require a 16.5 m antenna height and if we were to expect a 1 km baseline, thus reducing the amount of FSR sensor nodes required in any final system, this would imply a 55m high antenna. This sort of antenna height may pose problems when being implemented on relatively unstable sea based buoys.

The instability due to the sea surface motion would also constantly change the grazing angle as the antenna height effectively varies as the buoy sways (the plot shows the reflection coefficient increases in a steep manor either side of the Brewster angle). The sea surface is also highly multifaceted contributing what could be seen as many specular reflections at many widely spread incidence angles apart from the central baseline grazing angle. Ultimately maybe it is not useful to attempt to utilise the effect of pseudo Brewster angle for such a dynamic system [110].

5.6 Coherent processing for Maximum Effective Detection Range

In order to determine the maximum detection range of the system, the decision was made to test on the calmest surface possible [110]. Therefore it was decided to move from sea to lake based trials, thus this section contains information gathered from trials on Coniston Water in the Lake District. This test site also gave us the ability to ground mount the antenna's at a variety of ranges; this is not possible at the Langstone harbour test site.

The signatures shown in this section are all recorded using a CW 7.5 GHz signal and an approximate antenna height of 1 m. The target used is the MISL small inflatable and signatures contain either one or two passes of the boat. It can be noticed in some of the signatures there appears to be a reasonable amount of external interference and this is noted where applicable.

Target Doppler Signatures for 726 m Baseline

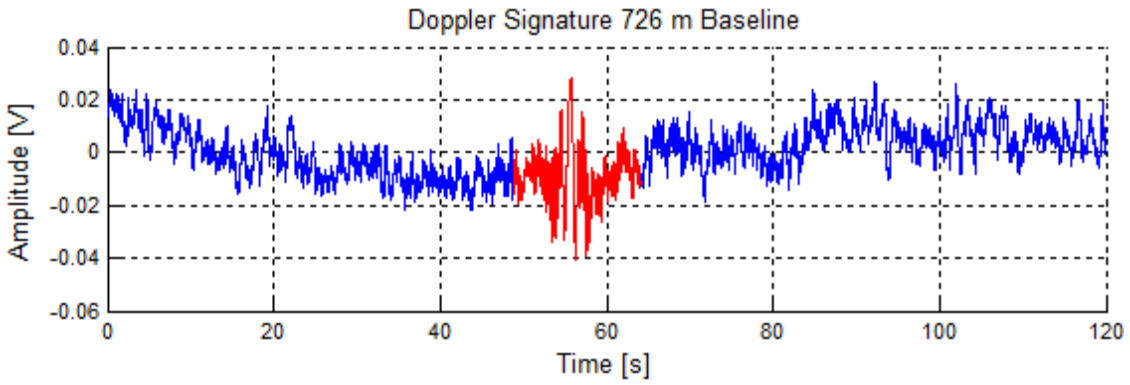

Figure 5.6.1 Doppler signature recorded with a 726 m baseline, target signature highlighted in red

Figure 5.6.1 shows the signature for a target detected at a range of 726m. The red highlight indicates the target signature itself (with clutter) and the blue the background noise and clutter. It is noticeable when comparing this signature to others, there is a large amount of interference contained in the record; however the target signature is still visible. The calculated SCR is 18.5 dB.

Figure 5.6.2 shows the GPS track data for the target trajectory in Figure 5.6.1. The target crossed 370 m from the transmitter (356 m from the receiver) at an angle of 82° to the baseline, with a velocity of 12.5 kmh^{-1} or 6.8 knots. The blue line shows the full trajectory and the red the section used for the GPS track analysis.

With the introduction of a 2 Hz HPF (high pass filter), much of the clutter can be removed, however this being quite a noisy signature, the application of a LPF (low pass filter) may also be beneficial. Figure 5.6.3 shows the Doppler signature after the high pass filtering where the SCR is 24.1 dB. This is 5.6 dB improvement in the SCR in comparison with the original signal.The target signature is clearly visible around the 50 - 65 s time frame.

Figure 5.6.2 GPS track data for target trajectory. Blue shows full track and red indicates section used for analysis

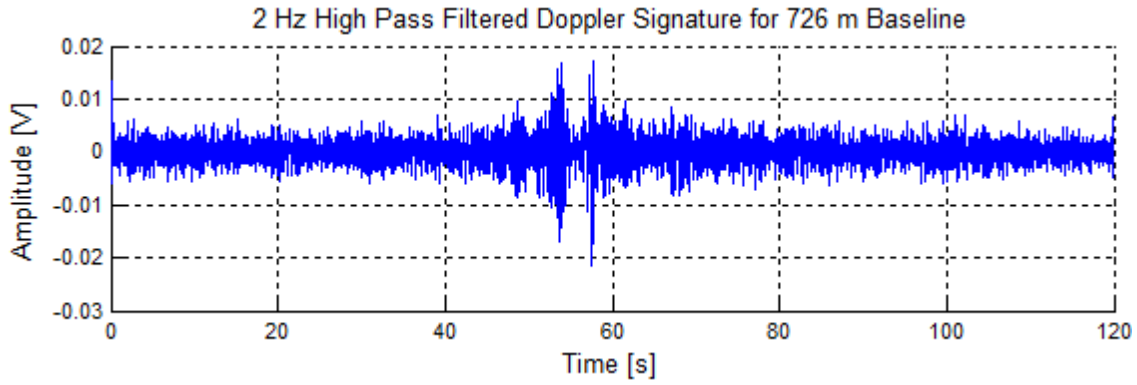

Figure 5.6.3 Doppler signature recorded with a 726 m baseline, after application of 2Hz HPF

Target Signatures for 935 m Baseline

Figure 5.6.4 shows the Doppler signature for 2 consecutive target measurements over a 935 m baseline range. The target signatures are highlighted in red and are reasonably well resolved by the eye. The signal-to-clutter ration has been calculated for the first crossing and it is 12.1 dB. Again as in the previous measurement, there appears to be an external source of

interference/clutter, a large underlying sinusoidal variation (on top of the usual clutter type variation) is visible in the signature. This is not too much of an issue and can be removed by use of a HPF.

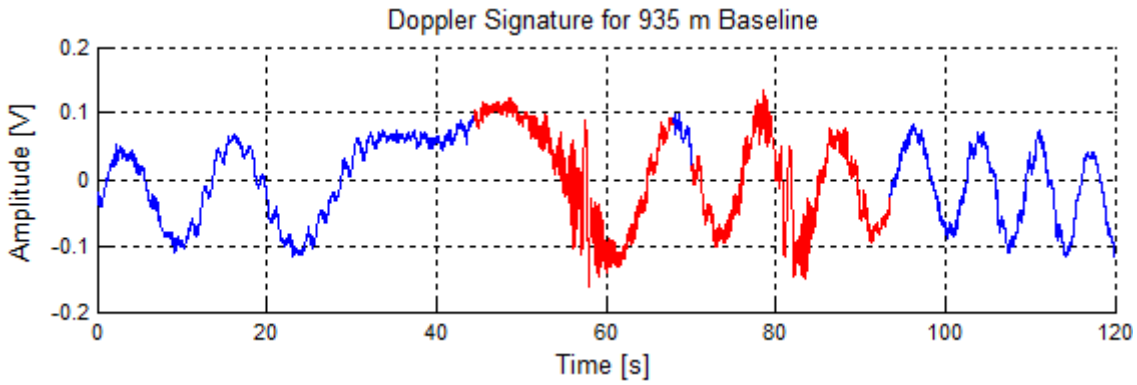

Figure 5.6.4 Doppler signature recorded with a 935 m baseline, target signatures highlighted in red

Figure 5.6.5 show the GPS track data sets used to calculate the target trajectory parameters for both target signatures in Figure 5.6.4, blue showing full track and red the section used for analysis. The crossing points were 617 and 600 m from the transmitter, which makes this trajectory slightly away from a central baseline crossing. The crossing angles were 81 and 71° with velocities of 22.7 and 16.6 kmh^{-1} (12.3 and 9.0 knots).

Figure 5.6.5 GPS track data for target trajectory's, left is for first target signature right for second. Blue shows full track and red indicates section used for analysis

On the implementation of a 2 Hz HPF the two signatures are clearly visible with high SCR (32.9 dB), as shown in Figure 5.6.6. The improvement of the SCR is 20.8 dB by applying 2 Hz HPF.

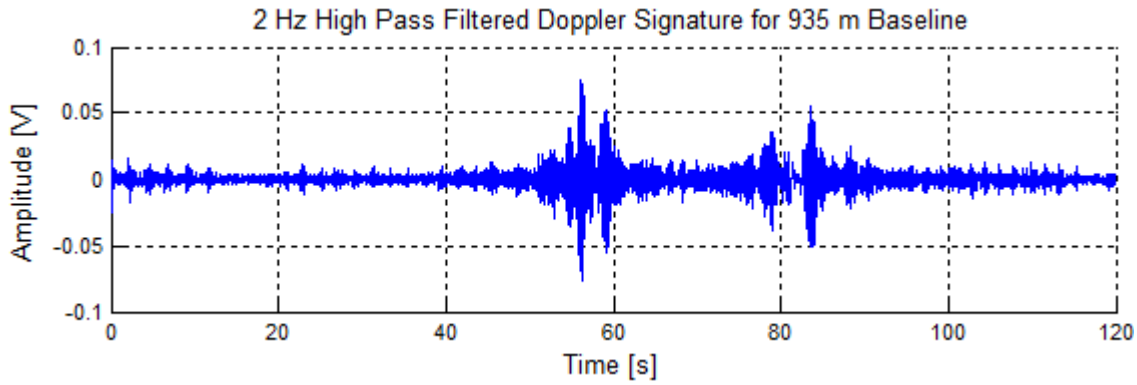

Figure 5.6.6 Doppler signature recorded with a 935 m baseline, after application of 2Hz HPF. Two target signatures are visible

Target Signatures for 992 m Baseline

Target signatures have been recorded on a 992 m baseline; in this case as will be shown in the GPS data, the target-baseline crossing point is more central than the 935 m baseline case. Figure 5.6.7 shows the recorded Doppler signature containing two target-baseline crossings highlighted in red. The signal-to-clutter ration for the first signature and clutter has been calculated to ratio of 18.25 dB.

The GPS track data for both of the target signatures is shown in Figure 5.6.8, the map on the left for the first target signature and the map on the right for the second. The data shows a target-baseline crossing points of 467 and 456 m from the transmitter, crossing angles of 66 and 74° and velocities of 21.8 and 20.2 kmh^{-1} or 11.8 and 10.9 knots.

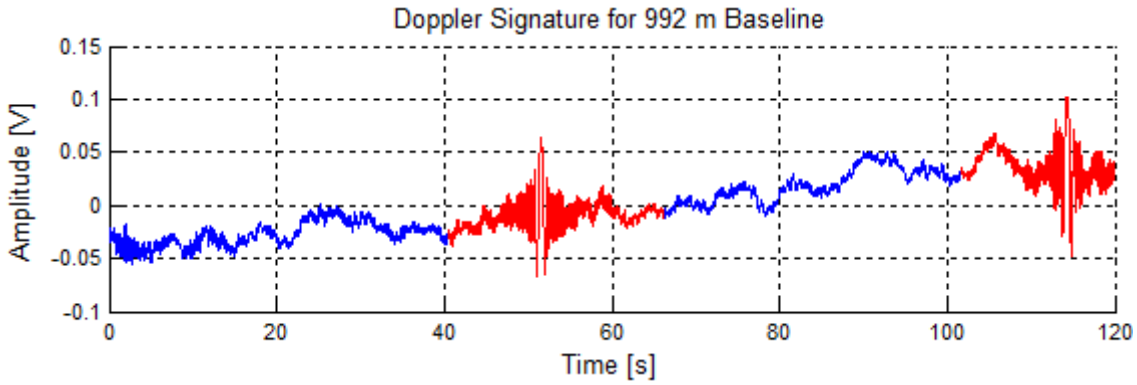

Figure 5.6.7 Doppler signature recorded with a 992 m baseline, target signatures highlighted in red

The 2 Hz high pass filtered signature for this measurement is shown in Figure 5.6.9, showing high SCR for each target signal (one around 52 s and the other 115 s). There is also the end of another signature at the beginning of the record, introduced by other lake users. The SCR for the first signature after the filtration is 33.02dB. This is improvement in the SCR with 14.7 dB by adding 2 Hz HPF.

Figure 5.6.8 GPS track data for target trajectory's, left is for first target signature right for second. Blue shows full track and red indicates section used for analysis

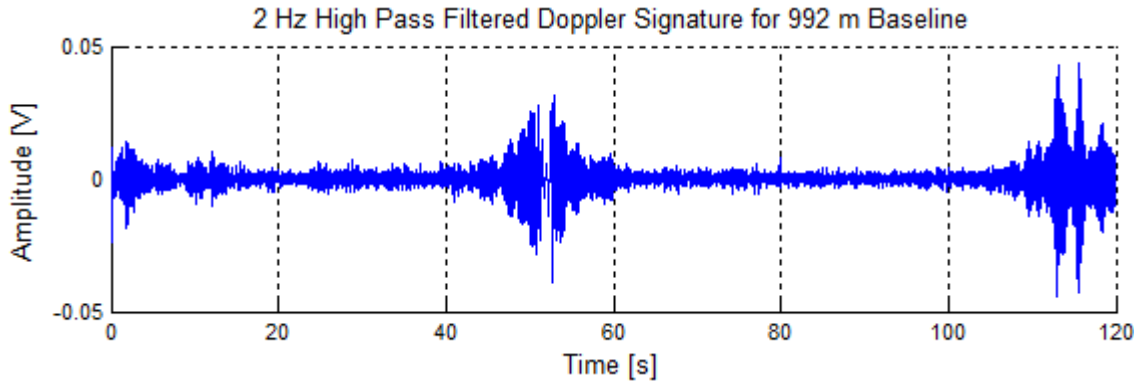

Figure 5.6.9 Doppler signature recorded with a 992 m baseline, after application of 2Hz HPF. Two target signatures are visible (with a third at the beginning of the record)

Target Signatures for 1287 m Baseline

Figures 5.6.10 and 5.6.11 contain Doppler signatures for measurements over a baseline range of 1287m. Target signals contained within these figures are highlighted in red and the corresponding target GPS track data is shown in Figure 5.6.12, left and right maps respectively. The calculated SCR on Figure 5.6.10 is 15.73 dB and on Figure 5.6.11 is 17.85 dB.

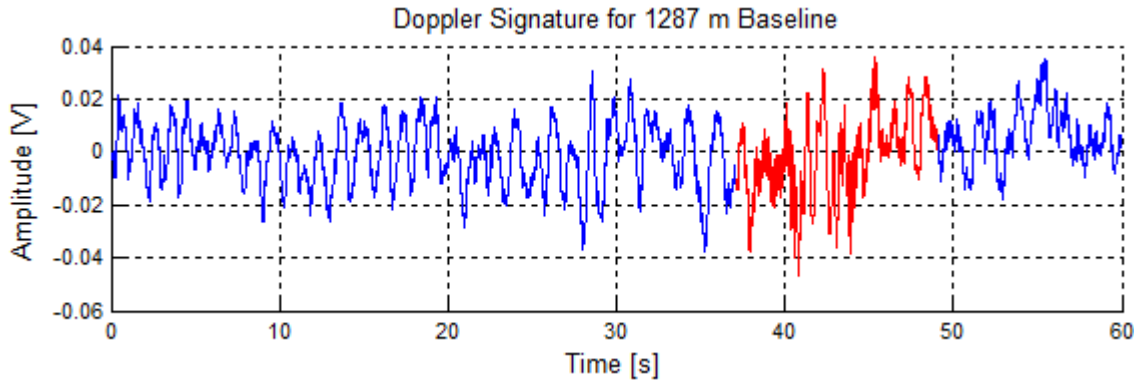

Figure 5.6.10 Doppler signature recorded with a 1287 m baseline, target signature highlighted in red. Calculated SCR of 15.73dB

The trajectory information gives the target-baseline crossing points at 643 and 638 m from the transmitter (almost exactly midpoint crossing), crossing angles at 81 and 84° and target speeds of 22.6 and 14 kmh^{-1} (12.2 and 7.6 knots). Still at this distance the target signature in Figure

5.6.10 is just visible with no pre-processing performed on the data and that in Figure 5.6.11 even more so.

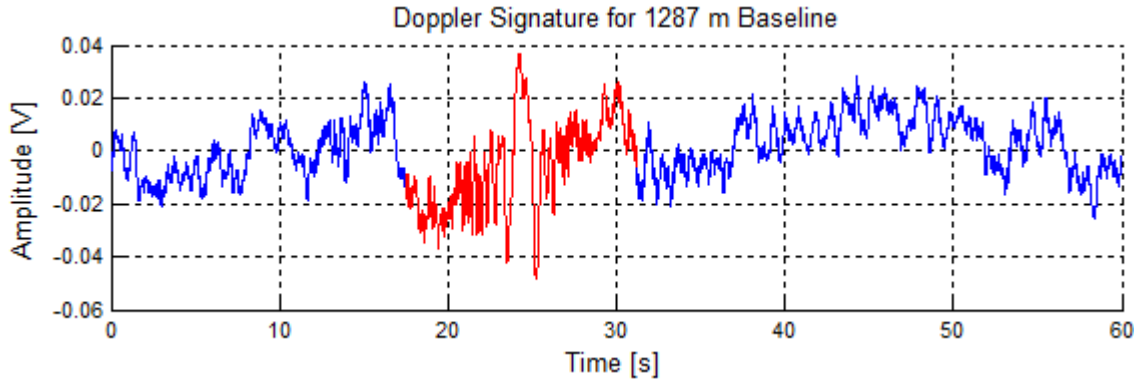

Figure 5.6.11 Doppler signature recorded with a 1287 m baseline, target signature highlighted in red. Estimated SCR of 17.85dB

Figures 5.6.13 and Figure 5.6.14 contain the high pass filtered versions of Figure 5.6.10 and Figure 5.6.11 respectively. There is an obvious improvement into the signal-to-clutter ratio where in Figure 5.6.13 the ratio is 23.69 dB (almost 8 dB improvement) and in Figure 5.6.14 the ratio is 22.49 dB (around 5 dB improvement).

Figure 5.6.12 GPS track data for target trajectory's, left is for target signature in Figure 5.57 right 5.58. Blue shows full track and red indicates section used for analysis

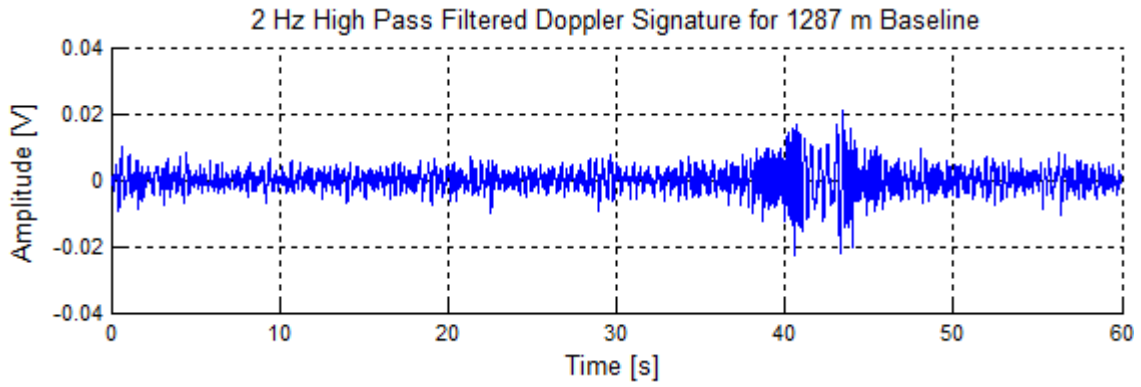

Figure 5.6.13 Doppler signature recorded with a 1287 m baseline, after application of 2Hz HPF. Original signal from Figure 5.57. Estimated SCR of 23.69dB

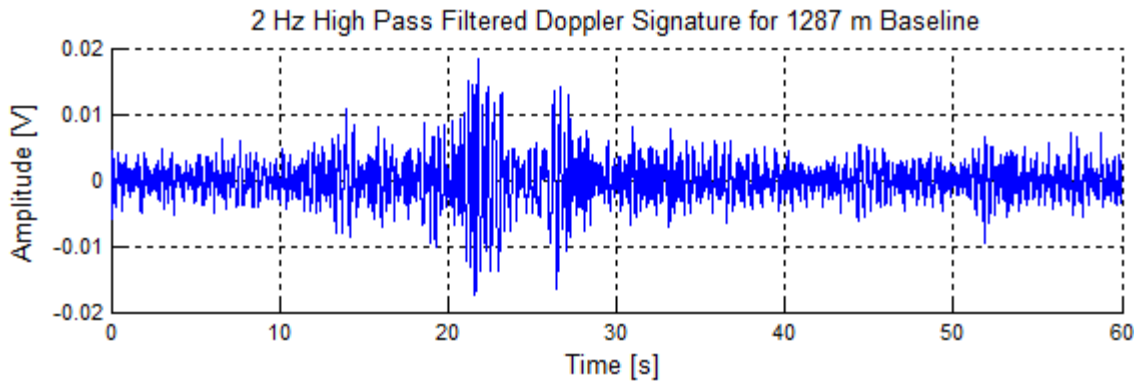

Figure 5.6.14 Doppler signature recorded with a 1287 m baseline, after application of 2Hz HPF. Original signal from Figure 5.58. Estimated SCR of 22.49dB

Coherent Processing to Increase Detection Range

Further to the application of high pass filtering, coherent processing/integration enables further increase in SCR [110]. Figure 5.6.15 shows a Doppler signature consisting of two MISL inflatable crossings, one at around 55 s the other at 100 s overlapping with another larger boat. The sea state is an estimated sea state 3. The estimated SCR for the signature around 55 s is 12.22 dB.

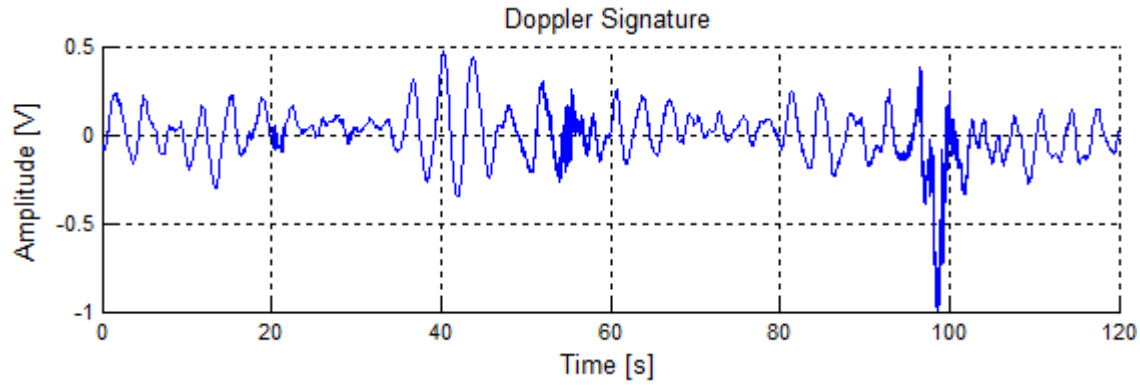

Figure 5.6.15 Doppler signature containing two MISL boat crossings, one overlapping with a larger boat at an estimated sea state 3

In Figure 5.6.16 with the use of a 2 Hz HPF we can see the signatures more clearly; the target(s) positioned around 20 s in time are believed to be seagulls crossing through the FSR baseline.

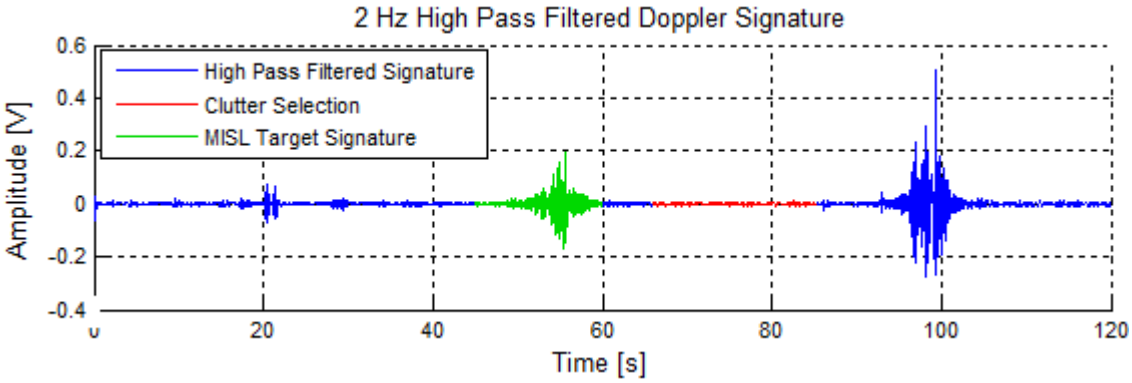

Figure 5.6.16 2 Hz high pass filtered Doppler signature

The red highlighted part of the Figure 5.6.16 indicates a section of filtered clutter for which the standard deviation is 0.003 V. The green highlighted MISL inflatable target signature has a maximum value of 0.20 V, giving an estimated SCR of 36.5dB. This is 24.2 dB improvement in the SCR by applying 2 Hz HPF.

Applying coherent processing/integration to this Doppler signature yields the plot in Figure 5.6.17. The received target signatures are correlated with a stored library signature to produce

the correlation output seen on Figure 5.6.17. Green highlights the compressed target signature and red a section of 'compressed' clutter (with effort to avoid including side lobes of compressed target signature).

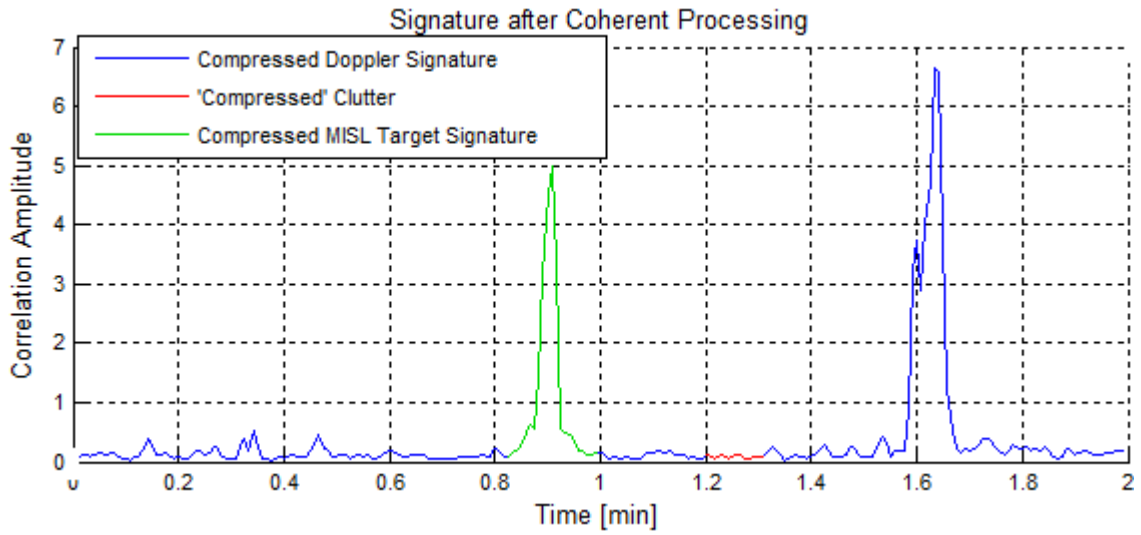

Figure 5.6.17 Doppler signature after coherent processing

The standard deviation of the red highlight is 0.023 and the compressed target signature peak is 5.0, giving an SCR of 46.8dB. Thus after coherent processing the SCR has improved by 10.3dB.

Summary and Conclusions

Sufficient amounts of data have been gathered to show target detection up to at least a 1287 m baseline range with midpoint target baseline crossing on what would be termed a smooth surface – probably sea state 1. Target signatures are visible without pre-processing; the introduction of a HPF allows removal of clutter, improving target visibility. It has been shown that a further 10 dB SCR improvement can be gained from the use of coherent processing and

with this it is predicted that the target may be visible at up to a 1 km baseline at sea state 3 [110].

5.7 Conclusions

Numerous target measurements were recorded at different test sites (Lake Coniston, Langstone Harbour and Sozopol, Bulgaria) by the MISL team. A preliminary analysis of the recorded data are presented here. The received signal characterization in FSR have been observed. Power budget calculation including FS CS estimation have been performed and compared with real experimental data. The results showed good agreement between the analytical calculations and the recorded FSR data. Observation of the target signature have been made with changing of the baseline crossing angles. The measurements showed that the smaller the crossing angle the longer the observation time as the target occupies the region around the baseline for longer time (as expected). Comparison of the targets signal strength in the Doppler signatures indicated that the peak does not depend on the crossing angle and follows the RCS of the target. Also analysis have been performed on data from targets crossing the baseline with different speed. Two measurements of MISLs inflatable boat (our reference target) crossing the baseline with different speed have been observed more specifically and compared. The results showed that the PSD bandwidth was twice wider for the two times faster baseline cross as it was expected. Study on the target signals recorded with different antenna polarisation were made and outcomes indicated that V-V and H-H received signals remain similar in comparison with cross-polarised configuration where considerable drop was observed. Preliminary investigation on target measurements at different antenna heights has been presented. The results from the maximum effective target range detection study are discussed.

My personal contribution in the work in this chapter is:

- Took part in all the maritime trials for acquiring target and sea clutter data.
- Have been involved in analysing all the discussed data in the chapter.

Chapter 6 Conclusions and Future Work

6.1 Summary and Conclusions

A literature survey has been presented in Chapter 1. The operational background and general properties of radar, mainly monostatic, have been introduced. Generic radar configuration, the block diagram, the radar equation, radar resolution and target RCS for monostatic radar have been given and discussed. This provided the background knowledge about radar systems. Then in the chapter different radar systems used in maritime environment and their features, advantages and shortcomings for different applications and robustness to diverse sea conditions have been discussed. Then as a contrast to conventional monostatic and bistatic radar an FSR system has been introduced and applications of such a system have been presented. The buoys mounted FSR sensor network concept has been outlined. The PhD specific research subjects have been explained and the thesis structure provided.

Chapter 2 has described in more details current state-of-the-art research into sea clutter and its effect on the radar performance. Depending on the radar configuration and operation, sea clutter properties may vary quite widely. Three separate cases with regards to the radar topology have been discussed: backscatter, bistatic and forward scatter sea clutters. In the section on backscatter sea clutter its description has been provided and clutter characteristics have been introduced and explained. The brief history of the research on sea clutter modelling and statistical properties at different grazing angles has been given. In the next section on

bistatic sea clutter section the summary of the work done in the last 40 years in this direction has been presented. Particular attention has been paid to experimentation and the radar parameters and, then, sea clutter models have been outlined. Further in the chapter the peculiarities of sea clutter in forward scatter radar mode as well as scattering mechanisms have been discussed. Analytical approaches and computer simulations developed up to date in Forward Scatter systems have been presented where emphasis has been done that the majority of the research in this direction has been related to shipboard and coastal communication.

Also Chapter 2 has been dedicated to the phenomenology of signals in maritime FSR. Detailed explanation was given about the FSR target detection and the physics behind. Forward scattering effect and the increase of RCS in forward direction were also described. The idea of using FSR as 'electronic fence' for target detection has been explained. RSSI measured signatures related to different diffraction mechanism were showed. Then practically useful FS CS approximation has been presented. Next section in the chapter has been focused on the typical targets of interest, their RCS and physical dimensions. 3D simulations using CST modelling and analysis of the targets FS RCS have been presented.

Chapter 3 has given detailed description of the test equipment and experimentation stage methodology. In this chapter a comprehensive explanation of every stage of the development of the FSR system is described including 7.5 GHz and later on the 24 GHz system design and development. Once the radar was build, the FSR was a subject of various laboratory and maritime conditions tests. Experimental maritime test sites have been described in details in the chapter. Methodology of data collection has been explained stressing different stages of experimentation methodology development. And finally structure and design of databases and specifics of organizing them in a convenient format has been explained.

Chapter 4 has been focused on the spectral and statistical analysis depending on the radar operational regimes, environment and scenarios. The operational environment analysis are fundamental in order to develop fully functional FSR system for use in maritime applications. For that reason to facilitate understanding of the sea clutter the various experiments at frequencies of 7.5 GHz and 24 GHz were undertaken. The FSR was deployed at different maritime sites providing wide range of environmental conditions. The measurements were performed in CW mode and Pulse mode. Data on weather and sea conditions has been provided as well.

Description of each separate experiment with its analysis has been placed in separate sections in the chapter. First section has been focused on analysing the influence of the carrier frequency on the sea clutter. Spectra of the collected data have been compared with previously reported spectra in the prior literature of sea clutter records at 9.3 GHz and 37 GHz and modelled spectra for shipborne communications at 1 GHz. The results illustrated that the overall forward scatter clutter spectrum is found to be independent of the transmit/receive baseline distance and radar frequencies within 1 – 37.5 GHz and as defined by a 10 dB power drop is limited to a maximum width of 1 Hz. Also the PSD data clearly demonstrates that the PSD slope corresponds to approximately 30-40 dB per decade and therefore to maximum inverse fourth power of Doppler frequency. According to our simulations and measurements, the clutter does not depend on the distance because practically all the clutter is collected in the vicinity of the transmitter or the receiver. As the result the clutter to leakage ratio remains the same irrelevant to the baseline length. All clutter is collected from transmitter and receiver surrounding where there are no strict rule how to calculate. But further investigations are needed in this direction. Also the

clutter distribution in FSR is found to be close to Rayleigh for the considered frequency ranges, especially for the main body of the clutter distribution.

A comparison of the clutter spectra using 7.5GHz CW mode and 7.5 GHz Pulse mode (100MHz, 1 GHz and 3GHz) of the developed FSR radar has been made in order to investigate the characteristics of clutter with respect to transmitted pulse width. The clutter spectral width was found to be relatively the same for all transmitted signals and as defined by a 10 dB power drop is limited to a maximum width of 1 Hz. The PSD data distinctly demonstrates that the PSD slope corresponds to approximately 25-40 dB per decade, and therefore, to maximum inverse fourth power of Doppler frequency. The use of wider (narrower pulse) interrogating signals is theoretically shown to reduce the level of clutter returns in FSR. However, this is only prevalent in high sea states. It cannot be said that our measurements are made at a particularly high sea state (approximately sea state 2) and so the benefits of higher bandwidth are not necessarily seen. At low sea states most clutter will originate from a narrow region along the baseline between transmitter and receiver. Also the clutter amplitude distribution is found to be very close to Rayleigh for the different bandwidth signals.

The next section in the chapter looked at the influence of the antennas over the sea clutter. Aspects such as the variation of sea clutter with antenna polarisation, signal-to-clutter ratio dependences on the antenna elevation, influence of the antenna beam widths and the effects of antenna movement on the Doppler spectrum when employing omni-directional antennas have been examined in this section.

Looking at the antenna polarisation analysis, PSDs clearly show that the spectral shape is reasonably invariant to the antenna polarization in 7.5 GHz and 24 GHz frequencies and major part of clutter is below 1 Hz. Plots also confirm expected spectral slope of approximately 20-

35 dB per decade. These results are in a good agreement with the findings of [74] where horizontal and vertical total signal spectra were found to be the same. The reason why horizontal and vertical polarisation were found to be the same is that FS components have fundamentally the same polarization as the illuminating field, so at the fundamental level we cannot expect depolarization. We can see difference between 7 and 24 only for very small targets. As soon as the target size is much bigger than the wavelength (this is our case) it should not be any visible difference. As in previous cases the clutter distribution in FSR is close to Rayleigh for the considered polarisations and frequency ranges.

The change of the average signal level at 7.5 GHz and 24 GHz due to the increments in antenna heights have been calculated and results showed that the leakage power is increasing linearly with the increase of the antenna height which corresponded to the theoretical estimations. A two-ray path propagation model has been used for calculations of the expected received average power level and has proved to be quite accurate for large database of measurements. Comparison with the measured leakage power demonstrate an overall reasonable agreement which emphasises an independence of frequency, inherent for the two-ray propagation model, at least for the 7.5 GHz channel.

From the experiments with different antenna azimuth beamwidth, it can easily be seen that the spectral shape is reasonably invariant to the antenna beamwidth and the major part of clutter is within 1 Hz beamdwidth. The analysis there also confirmed that the slope is approximately 20-35 dB per decade. Also the results indicate that the distribution type of the clutter amplitude distribution is very close to Rayleigh for the different antenna beamwidths as in every previous analysis.

In order to understand the effect of the antenna movement on the Doppler Spectrum, measurements with fixed antennas on the edge of the sea and with swaying antennas in open sea have been undertaken. A comparison between the PSD's of swaying and stationary omni-directional antennas has been presented and above 1 Hz the spectra are nearly equal. There is some increase (5 dB) in the spectrum for swaying antennas between 0 and 1 Hz, but this is the area of filter rejection. It looks like the only extra spectral components are due to the buoy variation.

In the next section the influence of test sites topology has been explored. The analysis of the data shows that forward-scatter sea clutter produces a relatively constant frequency clutter component around 1 Hz and the shape appears relatively invariant to the particular maritime environment. The results of initial analysis show that the clutter distribution in FSR follows Rayleigh for the considered maritime environments.

The last section of the chapter is focused on the effect of the environmental conditions. The clutter power dependence as a function of the transmit-receive distance and the clutter level dependence on sea states have been examined. 7.5 GHz channel RSSI average leakage and average clutter power from all the measurements fall off with the distance to the 4^{th} power. In this case we can expect that the clutter-to-leakage ratio should remain the same with the range. This has clear physical explanation and the effect has previously been observed for ground based FSR and foliage penetration [124], [125]. This also means that for 7.5GHz systems, the TRP can be considered as an accurate model. This is not the case with the 24 GHz channel where the average leakage power from all measurements roughly obeys 2^{nd} power fall off with distance. This means that the free space propagation model is more appropriate for the 24 GHz channel. The clutter power follows 3^{rd} power law drop with range so we expect that the clutter

to leakage ratio for this channel shown in Table 4.5 should decrease 10 dB per decade. The explanation for this phenomenon is that at high frequency the sea roughness is big enough to decorrelate the second path (reflection from the sea) and as the result at 24 GHz it is like free space model [74].

The clutter level dependence on sea states results demonstrated that clutter bandwidth remains limited to 1 Hz for all recorded sea states. However there is an initial indication that for higher sea states the spectrum becomes band-limited with slightly narrower bandwidths of higher power - though the pedestals of the spectra coincide reasonably well. This reflects the fact that for higher wind speeds we observe a more developed sea state with an increase in large sea gravity wave amplitudes. These waves have a more regular travelling wave structure and therefore occur periodically rather than the more random behaviour of small background capillary waves typical occurring in an undeveloped sea state. Moreover we can expect that higher sea states will demonstrate the slight shift of bandwidth down to lower frequency because with the increase of the sea state the interval of waves is increasing. The different sea states data indicates once again that the distribution of clutter amplitude is Rayleigh over the range of sea states measured. It also shows the shift to higher amplitudes at higher sea states. Relationship between signal amplitudes and sea states requires further work/data at high sea states.

It has been concluded that the overall forward scatter clutter spectrum is:

- independent on the transmit/receive baseline and the radar frequencies within 1- 37 GHz;

- Is found to be invariant to the transmitting mode (CW or Pulse), antenna properties, test scenarios and environmental conditions.
- is restricted to a maximum width of 1-2 Hz defined by a 10 dB power drop;
- PSD slope corresponds to approximately 20-40 dB decay per decade and, therefore, to a maximum inverse forth power of Doppler frequency.

It follows from the analysis of the results that the clutter distribution in FSR is close to Rayleigh for the presented radar operational regimes, test scenarios and environmental conditions, especially for the main body of the clutter distribution. It is worth to stress here that this conclusion may only be true for relatively low sea states. Significantly rougher seas may demonstrate different effects on propagation at low grazing angles, however such a study is still to be performed. This is not a claim that the best distribution is Rayleigh. The distribution is used as a reference because the major power well fitted into it. The observed tales on the PDFs are natural, simply measurement results which not necessary should follow the Rayleigh. There are other approximations which may be better fit. The big spread observed on the PDFs is a result of what we are considering as events with very low probability, less than 10^{-4}. And this spread is rather natural, so called "spread" on the tails of distribution.

Chapter 5 has been dedicated to the preliminary FSR target analysis, where emphasis has been on analysis of the motion of the node positions on SCR. Received Signal Characterization and the power budget in Forward Scatter Radar have been discussed.

6.2 Future Work

- Develop the next generation of multichannel/multistatic FSR operating at different frequencies in order to optimise maritime radar performance in terms of SCR, target detectability and target motion parameters estimation.
- To undertake a comprehensive analysis on the target signals at different radar configurations and topologies.
- Develop the optimised automatic target detection approaches based on coherent and non-coherent processing.
- Develop the target classification and recognition approaches which will take into account a non-liner motion of target in the sea environment
- Perform the sea clutter measurements at high sea states which are currently were unexplored for presented radar configuration.
- To test FSR with both Tx/Rx mounted on buoy and equipped with Omni-directional antennas in real open sea conditions.

References

[1] M. A. Richards, W. A. Holm, and J. A. Scheer, Eds., *Principles of Modern Radar: Basic Principles v. 1*. Raleigh, NC: SciTech Publishing Inc, 2009.

[2] P. Z. Peebles, *Radar Principles*, 1 edition. New York: Wiley-Blackwell, 1998.

[3] F. E. Nathanson, J. P. Reilly, and M. N. Cohen, *Radar Design Principles*, 2 edition. Mendham, N.J.: SciTech Publishing, 1999.

[4] M. I. Skolnik, *Radar Handbook, Third Edition*, 3 edition. New York: McGraw-Hill Professional, 2008.

[5] V. S. Chernyak, *Fundamentals of Multisite Radar Systems: Multistatic Radars and Multistatic Radar Systems*. Amsterdam, The Netherlands: CRC Press, 1998.

[6] S. R. Doughty, "Development and performance evaluation of a multistatic radar system," Doctoral, University of London, 2008.

[7] E. Fishler, A. Haimovich, R. Blum, D. Chizhik, L. Cimini, and R. Valenzuela, "MIMO radar: an idea whose time has come," 2004, pp. 71–78.

[8] N. J. Willis, *Bistatic Radar*, 2nd Revised edition edition. Raleigh, NC: SciTech Publishing Inc, 2005.

[9] M. Cherniakov, Ed., *Bistatic Radars: Principles and Practice*, 1 edition. Chichester, England; Hoboken, NJ: Wiley-Blackwell, 2007.

[10] M. I. Skolnik, *Introduction to Radar Systems*, 3 edition. Boston: McGraw-Hill Higher Education, 2002.

[11] G. Stimson, *Introduction to Airborne Radar*, 2nd Revised edition edition. Mendham, N.J: SciTech Publishing Inc, 1998.

[12] D. K. Barton, *Modern Radar System Analysis*. Artech House, 1988.

[13] M. I. Skolnik, "An Analysis of Bistatic Radar," *IRE Trans. Aerosp. Navig. Electron.*, vol. ANE-8, no. 1, pp. 19–27, Mar. 1961.

[14] M. A. Richards, *Fundamentals of Radar Signal Processing, Second Edition*, 2 edition. New York: McGraw-Hill Professional, 2014.

[15] J. Briggs, *Target Detection by Marine Radar*. Institution of Engineering and Technology, 2004.

[16] N. Friedman, *The Naval Institute Guide to World Naval Weapons Systems, 1997-1998*. Naval Institute Press, 1997.

[17] "Furuno NavNet TZtouch2 Radar Sensor - DRS2D_4D_4A-25A Installation Manual F.pdf."[Online].Available:http://www.furunousa.com/ProductDocuments/DRS2D_4D_4A-25A%20Installation%20Manual%20F.pdf. [Accessed: 23-Jun-2015].

[18] "Maritime Surveillance : Airbus Defence and Space." [Online]. Available: http://www.geo-airbusds.com/en/5713-maritime-surveillance. [Accessed: 21-Aug-2015].

[19] K. D. Ward, R. J. A. Tough, and S. Watts, *Sea clutter scattering, the K distribution and radar performance*. Stevenage, U.K.: Institution of Engineering and Technology, 2013.

[20] M. Gashinova, K. Kabakchiev, L. Daniel, E. Hoare, V. Sizov, and M. Cherniakov, "Measured forward-scatter sea clutter at near-zero grazing angle: analysis of spectral and statistical properties," *IET Radar Sonar Navig.*, vol. 8, no. 2, pp. 132–141, Feb. 2014.

[21] M. Cherniakov, Ed., *Bistatic Radars: Principles and Practice*, 1 edition. Wiley-Blackwell, 2007.

[22] N. J. Willis and H. D. Griffiths, Eds., *Advances in Bistatic Radar*. Berkeley, Calif: SciTech Publishing Inc, 2007.
[23] M. Gashinova, L. Daniel, V. Sizov, E. Hoare, and M. Cherniakov, "Phenomenology of Doppler forward scatter radar for surface targets observation," *IET Radar Sonar Navig.*, vol. 7, no. 4, pp. 422–432, Apr. 2013.
[24] K. Kabakchiev, L. Y. Daniel, E. G. Hoare, M. Gashinova, and M. Cherniakov, "Near zero grazing angle forward-scatter sea clutter measurement statistical properties," in *Radar Symposium (IRS), 2013 14th International*, 2013, vol. 2, pp. 620–624.
[25] Rohling H., "100 years of radar," Bonn, 2004.
[26] M. Gashinova, L. Daniel, K. Kabakchiev, V. Sizov, E. Hoare, and M. Cherniakov, "Phenomenology of signals in FSR for surface targets detection," in *IET International Conference on Radar Systems (Radar 2012)*, 2012, pp. 1–6.
[27] A. R. S. A. Raja, "Forward scattering radar for vehicle classification." 2007.
[28] G. Honey, *Electronic Access Control*, 1 edition. Oxford ; Boston: Newnes, 2000.
[29] A. B. Blyakhman and I. A. Runova, "Forward scattering radiolocation bistatic RCS and target detection," in *The Record of the 1999 IEEE Radar Conference, 1999*, 1999, pp. 203–208.
[30] A. B. Blyakhman, A. G. Ryndyk, and S. B. Sidorov, "Forward scattering radar moving object coordinate measurement," in *Radar Conference, 2000. The Record of the IEEE 2000 International*, 2000, pp. 678–682.
[31] P. Ufimtsev, "New Insight into the Classical Macdonald Physical Optics Approximation," *IEEE Antennas Propag. Mag.*, vol. 50, no. 3, pp. 11–20, Jun. 2008.
[32] J. I. Glaser, "Bistatic RCS of Complex Objects near Forward Scatter," *IEEE Trans. Aerosp. Electron. Syst.*, vol. AES-21, no. 1, pp. 70–78, Jan. 1985.
[33] L. Daniel, M. Gashinova, and M. Cherniakov, "Maritime target cross section estimation for an ultra-wideband forward scatter radar network," in *Radar Conference, 2008. EuRAD 2008. European*, 2008, pp. 316–319.
[34] "Forward Scatter Radar for Future Systems -." [Online]. Available: http://citeseerx.ist.psu.edu/viewdoc/download;jsessionid=53ECA8DFC1BEDCEE177B4F643C52D7D3?doi=10.1.1.407.1872&rep=rep1&type=pdf. [Accessed: 13-Jul-2015].
[35] G. Mie, "Beiträge zur Optik trüber Medien, speziell kolloidaler Metallösungen," *Ann. Phys.*, vol. 330, no. 3, pp. 377–445, Jan. 1908.
[36] H. C. Hulst and H. C. van de Hulst, *Light Scattering by Small Particles*. Courier Corporation, 1957.
[37] M. Born, E. Wolf, and A. B. Bhatia, *Principles of Optics: Electromagnetic Theory of Propagation, Interference and Diffraction of Light*. Cambridge University Press, 1999.
[38] P. Y. Ufimtsev, *Fundamentals of the Physical Theory of Diffraction*, 1 edition. Hoboken, N.J: Wiley-IEEE Press, 2007.
[39] C. A. Balanis, *Advanced Engineering Electromagnetics*, Solution Manual edition. New York: Wiley, 1989.
[40] "USS Cole Bombing Fast Facts," *CNN*. [Online]. Available: http://www.cnn.com/2013/09/18/world/meast/uss-cole-bombing-fast-facts/index.html.
[41] K. Kabakchiev, L. Y. Daniel, V. Sizov, E. Hoare, M. Gashinova, and M. Cherniakov, "Received signal characterization in forward scatter radar for maritime application," in *Radar Symposium (IRS), 2011 Proceedings International*, 2011, pp. 67–72.

[42] Hoare, E.G., Daniel, L., Sizov, V., Gashinova, M., Cherniakov, M., Svintsov, A., and Kabakchiev, K., "Ultra-Wideband Forward Scatter Radar Fence for Maritime Surveillance," School of Electrical, Electronic and Computer Engineering, University of Birmingham, UK, Final Report, 2009.

[43] L. Y. Daniel, E. G. Hoare, M. Gashinova, A. Svintsov, M. Cherniakov, and V. Sizov, "Ultra-wideband forward scatter radar fence for maritime surveillance - Initial experimental results," in *2010 IEEE Radar Conference*, 2010, pp. 526–531.

[44] M. Cherniakov, M. Gashinova, Cheng Hu, M. Antoniou, V. Sizov, and L. Y. Daniel, "Ultra wideband forward scattering radar: Concept and prospective," in *2007 IET International Conference on Radar Systems*, 2007, pp. 1–5.

[45] M. Antoniou, V. Sizov, C. Hu, P. Jancovic, R. Abdullah, N. E. A. Rashid, and M. Cherniakov, "The concept of a forward scattering micro-sensors radar network for situational awareness," in *2008 International Conference on Radar*, 2008, pp. 171–176.

[46] V. Sizov, M. Cherniakov, and M. Antoniou, "Forward scattering radar power budget analysis for ground targets," *IET Radar Sonar Navig.*, vol. 1, no. 6, pp. 437–446, Dec. 2007.

[47] V. I. Sizov, M. Cherniakov, and M. Antoniou, "Forward scatter RCS estimation for ground targets," in *Microwave Conference, 2007. European*, 2007, pp. 1700–1703.

[48] L. Daniel, M. Gashinova, and M. Cherniakov, "Maritime UWB forward scattering radar network: Initial study," in *2008 International Conference on Radar*, 2008, pp. 658–663.

[49] "Met Office, National Meteorological Library and Archive Fact sheet 6 — The Beaufort Scale," vol. 1. Met Office. © Crown copyright 2010 10/0425 Available at: http://www.metoffice.gov.uk/media/pdf/b/7/Fact_sheet_No._6.pdf.

[50] S. Huler, *Defining the wind: the Beaufort scale, and how a nineteenth-century admiral turned science into poetry*, 1st ed. New York: Crown Publishers, 2004.

[51] D. E. Freund, N. E. Woods, H.-C. Ku, and R. S. Awadallah, "Forward Radar propagation over a rough sea surface: a numerical assessment of the Miller-brown approximation using a horizontally polarized 3-GHz line source," *IEEE Trans. Antennas Propag.*, vol. 54, no. 4, pp. 1292–1304, Apr. 2006.

[52] B. U. Ungan and J. T. Johnson, "Time statistics of propagation over the ocean surface: a numerical study," *IEEE Trans. Geosci. Remote Sens.*, vol. 38, no. 4, pp. 1626–1634, Jul. 2000.

[53] A. Papoulis and S. U. Pillai, *Probability, Random Variables and Stochastic Processes*, 4th edition. Boston, Mass.: McGraw-Hill Europe, 2002.

[54] N. L. Johnson, S. Kotz, and N. Balakrishnan, *Continuous Univariate Distributions, Vol. 1*, 2 edition. New York: Wiley-Interscience, 1994.

[55] N. J. Redding, "Estimating the parameters of the K distribution in the intensity domain," Jul-1999.[Online]. Available: http://dspace.dsto.defence.gov.au/dspace/handle/1947/4203. [Accessed: 20-Jul-2015].

[56] J. A. Rice, *Mathematical statistics and data analysis*, 2nd ed. Belmont, CA: Duxbury Press, 1995.

[57] E. Jakeman and P. N. Pusey, "A model for non-Rayleigh sea echo," *IEEE Trans. Antennas Propag.*, vol. 24, no. 6, pp. 806–814, Nov. 1976.

[58] K. D. Ward, "Compound representation of high resolution sea clutter," *Electron. Lett.*, vol. 17, no. 16, pp. 561–563, Aug. 1981.

[59] K. D. Ward, C. J. Baker, and S. Watts, "Maritime surveillance radar. I. Radar scattering from the ocean surface," *Radar Signal Process. IEE Proc. F*, vol. 137, no. 2, pp. 51–62, Apr. 1990.

[60] S. Watts, C. J. Baker, and K. D. Ward, "Maritime surveillance radar. II. Detection performance prediction in sea clutter," *Radar Signal Process. IEE Proc. F*, vol. 137, no. 2, pp. 63–72, Apr. 1990.

[61] S. O. Rice, "Reflection of electromagnetic waves from slightly rough surfaces," *Commun. Pure Appl. Math.*, vol. 4, no. 2–3, pp. 351–378, Aug. 1951.

[62] G. R. Valenzuela, "Theories for the interaction of electromagnetic and oceanic waves — A review," *Bound.-Layer Meteorol.*, vol. 13, no. 1–4, pp. 61–85, Jan. 1978.

[63] E. Jakeman and K. D. Ridley, *Modeling Fluctuations in Scattered Waves*. Boca Raton, FL: CRC Press, 2006.

[64] H. D. Griffiths, W. A. Al-Ashwal, K. D. Ward, R. J. A. Tough, C. J. Baker, and K. Woodbridge, "Measurement and modelling of bistatic radar sea clutter," *IET Radar Sonar Navig.*, vol. 4, no. 2, pp. 280–292, Apr. 2010.

[65] V. Pidgeon, "Bistatic cross section of the sea," *IEEE Trans. Antennas Propag.*, vol. 14, no. 3, pp. 405–406, May 1966.

[66] DOMVILLE A, "The bistatic reflection from land and sea of X-band radio waves," Part I: Memorandum SLM1802, July 1967; Part II: Memorandum SLM2116,GEC Electronics Ltd, Stanmore, UK.

[67] F. E. Nathanson, J. P. Reilly, and M. N. Cohen, *Radar Design Principles: Signal Processing and the Environment. Second Edition*, 2 edition. Mendham, N.J.: SciTech Publishing, 1999.

[68] EWELL G.W and ZEHNER S.P, "Bistatic sea clutter return near grazing incidence," presented at the Proc. RADAR-82 Conf., London, IEE Conf. Publ. No. 216, 1982, pp. 188–192.

[69] YATES G.A, "Bistatic synthetic aperture radar," PhD thesis, University College London, 2005.

[70] T. P. Kochanski, M. J. Vanderhill, J. V. Zolotarevsky, and T. Fariss, "Low Illumination Angle Bistatic Sea Clutter Measurements At X-band," in *OCEANS '92. Mastering the Oceans Through Technology. Proceedings.*, 1992, vol. 1, pp. 518–523.

[71] M. M. Horst, F. B. Dyer, and M. T. Tuley, "Radar sea clutter model," presented at the Antennas and Propagation, 1978, pp. 6–10.

[72] W. A. Al-Ashwal, A. Balleri, H. D. Griffiths, W. J. Miceli, K. Woodbridge, C. J. Baker, R. Harmanny, M. Inggs, J. S. Sandenbergh, M. A. Ritchie, A. G. Stove, S. Watts, R. J. A. Tough, and K. D. Ward, "Measurements of bistatic radar sea clutter," in *2011 IEEE Radar Conference (RADAR)*, 2011, pp. 217–221.

[73] M. A. Ritchie, W. A. Al-Ashwal, A. G. Stove, K. Woodbridge, and H. D. Griffiths, "Statistical analysis of monostatic and bistatic sea clutter Doppler spectrum," in *2011 IEEE CIE International Conference on Radar (Radar)*, 2011, vol. 1, pp. 816–820.

[74] C. . Beard, "Coherent and incoherent scattering of microwaves from the ocean," *IRE Trans. Antennas Propag.*, vol. 9, no. 5, pp. 470–483, Sep. 1961.

[75] P. Beckmann and A. Spizzichino, *The Scattering of Electromagnetic Waves from Rough Surfaces*, New edition edition. Norwood, MA: Artech House Publishers, 1987.

[76] P. D. L. Williams, H. D. Cramp, and K. Curtis, "Experimental study of the radar cross-section of maritime targets," *IEE J. Electron. Circuits Syst.*, vol. 2, no. 4, pp. 121–136, Jul. 1978.

[77] V. Fabbro, C. Bourlier, and P. F. Combes, "FORWARD PROPAGATION MODELING ABOVE GAUSSIAN ROUGH SURFACES BY THE PARABOLIC SHADOWING EFFECT," *Prog. Electromagn. Res.*, vol. 58, pp. 243–269, 2006.

[78] Zujkov, V. A., Pedenko, Yu. A., and Razskazovsky, V. B., "Characteristics of Radio Propagation in Sea Surface Layer, Propagation of Radio Waves of Millimeter and Centimeter Bands," in *Proceedings of IRE AN USSR*, 1989, pp. 76–82.

[79] Pedenko, Yu.A. and Razskazovsky, V.B., "Multipath propagation over sea, radiophysical study of the world ocean," *Proc IRE USSR*, pp. 2–50, 1992.

[80] Berry, R., "Radar propagation at very low altitude over the sea'.'Radar-present and future,'" in *IEE Conf. Publications*, 1973, vol. 105, pp. 140–145.

[81] C. I. Beard, I. Katz, and L. Spetner, "Phenomenological vector model of microwave reflection from the ocean," *IRE Trans. Antennas Propag.*, vol. 4, no. 2, pp. 162–167, Apr. 1956.

[82] C. I. Beard and I. Katz, "The dependence of microwave radio signal spectra on ocean roughness and wave spectra," *IRE Trans. Antennas Propag.*, vol. 5, no. 2, pp. 183–191, Apr. 1957.

[83] J. R. Smith, S. J. Russell, B. E. Brown, P. M. Haldeman, D. D. Hayden, D. G. Morgan, R. D. Pierce, J. W. Shan, W. T. Stephens, and M. S. Mirotznik, "Electromagnetic forward-scattering measurements over a known, controlled sea surface at grazing," *IEEE Trans. Geosci. Remote Sens.*, vol. 42, no. 6, pp. 1197–1207, Jun. 2004.

[84] K. Anderson, S. Doss-Hammel, D. Tsintikidis, B. Brooks, M. Smith, P. Caffrey, A. Clarke, L. Cohen, A. De Jong, G. De Leeuw, M. Moerman, K. Crahan, K. Davidson, P. Frederickson, D. Dion, C. Friehe, D. Khelif, T. Hristov, J. S. Reid, S. Reising, and E. Terrill, "The RED Experiment: An Assessment of Boundary Layer Effects in a Trade Winds Regime on Microwave and Infrared Propagation over the Sea," *Bull. Am. Meteorol. Soc.*, vol. 85, no. 9, pp. 1355–1365, Sep. 2004.

[85] T. S. Hristov, K. D. Anderson, and C. A. Friehe, "Scattering Properties of the Ocean Surface: The Miller #x2013;Brown #x2013;Vegh Model Revisited," *IEEE Trans. Antennas Propag.*, vol. 56, no. 4, pp. 1103–1109, Apr. 2008.

[86] W. S. Ament, "Toward a Theory of Reflection by a Rough Surface," *Proc. IRE*, vol. 41, no. 1, pp. 142–146, Jan. 1953.

[87] R. M. Brown, A. R. Miller, and NAVAL RESEARCH LAB WASHINGTON DC, *Geometric-Optics Theory for Coherent Scattering of Microwaves from the Ocean Surface.* Ft. Belvoir: Defense Technical Information Center, 1974.

[88] A. Miller, R. M. Brown, and E. Vegh, "New derivation for the rough-surface reflection coefficient and for the distribution of sea-wave elevations," *Microw. Opt. Antennas IEE Proc. H*, vol. 131, no. 2, pp. 114–116, Apr. 1984.

[89] N. Pinel and C. Bourlier, "Forward Propagation over Thick Oil Spills on Sea Surfaces for a Coastal Coherent Radar," in *Geoscience and Remote Sensing Symposium, 2008. IGARSS 2008. IEEE International*, 2008, vol. 4, pp. IV – 1125–IV – 1128.

[90] C. Eckart, "The Scattering of Sound from the Sea Surface," *Acoust. Soc. Am. J.*, vol. 25, p. 566, 1953.

[91] E. G. Hoare, L. Y. Daniel, M. Gashinova, K. Kabakchiev, V. Sizov, M. Cherniakov, V. B. Razskazovsky, G. . Khlopov, S. . Khomenko, and V. E. Morozov, "Near zero grazing angle forward-scatter sea clutter measurement spectrum analysis," in *IET International Conference on Radar Systems (Radar 2012)*, 2012, pp. 1–4.

[92] M. Gashinova, L. Daniel, E. Hoare, V. Sizov, K. Kabakchiev, and M. Cherniakov, "Signal characterisation and processing in the forward scatter mode of bistatic passive coherent location systems," *EURASIP J. Adv. Signal Process.*, vol. 2013, no. 1, p. 36, Feb. 2013.

[93] V. V. Chapurskiy and V. N. Sablin, "SISAR: shadow inverse synthetic aperture radiolocation," in *Radar Conference, 2000. The Record of the IEEE 2000 International*, 2000, pp. 322–328.

[94] J. I. Glaser, "Forward Scatter Radar for Future Systems," in *Forward Scatter Radar for Future Systems*, 2011, vol. 10, pp. 3–8.

[95] V. Schejbal, O. Fiser, and J. Pidanic, "Comparisons of approximate and exact solutions for forward scattering," in *Proceedings of the 5th European Conference on Antennas and Propagation (EUCAP)*, 2011, pp. 2318–2322.

[96] M. Gashinova, M. Cherniakov, N. A. Zakaria, and V. Sizov, "Empirical model of vegetation clutter in forward scatter radar micro-sensors," in *2010 IEEE Radar Conference*, 2010, pp. 899–904.

[97] M. Cherniakov, R. S. A. R. Abdullah, P. Jancovic, M. Salous, and V. Chapursky, "Automatic ground target classification using forward scattering radar," *Radar Sonar Navig. IEE Proc.*, vol. 153, no. 5, pp. 427–437, Oct. 2006.

[98] F. L. Pedrotti, L. M. Pedrotti, and L. S. Pedrotti, *Introduction to optics*, 3rd ed. Upper Saddle River, N.J: Pearson/Prentice Hall, 2007.

[99] D. Halliday, R. Resnick, and J. Walker, *Fundamentals of physics*, 8. ed., regular. Hoboken, NJ: Wiley, 2008.

[100] H. C. Ohanian, *Physics*, 2nd ed., expanded. New York: Norton, 1989.

[101] J. D. Jackson, *Classical Electrodynamics*, 3rd Edition edition. New York: John Wiley & Sons, 1998.

[102] R. E. Hiatt, K. M. Siegel, and H. Weil, "Forward Scattering by Coated Objects Illuminated by Short Wavelength Radar," *Proc. IRE*, vol. 48, no. 9, pp. 1630–1635, Sep. 1960.

[103] "Radar Cross Section Handbook: Volume 1: George Ruck: 9781489953261: Amazon.com: Books." [Online]. Available: http://www.amazon.com/Radar-Cross-Section-Handbook-Volume/dp/1489953264. [Accessed: 29-Jul-2015].

[104] R. A. Ross, "FORWARD SCATTERING FROM A FINITE, CIRCULAR CYLINDER," *Prog. Electromagn. Res. C*, vol. 2, pp. 207–215, 2008.

[105] N. E. A. Rashid, M. Antoniou, P. Jancovic, V. Sizov, R. Abdullah, and M. Cherniakov, "Automatic target classification in a low frequency FSR network," in *Radar Conference, 2008. EuRAD 2008. European*, 2008, pp. 68–71.

[106] "CST MICROWAVE STUDIO - 3D EM simulation software." [Online]. Available: https://www.cst.com/Products/CSTMWS. [Accessed: 27-Nov-2014].

[107] "Locosys Technology." [Online]. Available: http://www.locosystech.com/product.php?zln=en&id=30. [Accessed: 05-Aug-2015].

[108] "MKU ATV 24-2, ATV Transmitter Module | Kuhne electronic Shop." [Online]. Available: http://shop.kuhne-

electronic.de/kuhne/en/shop/amateur/signalquellen/mikrowellen-tv-sende/MKU+ATV+24-2+ATV+Transmitter+Module/?card=552. [Accessed: 27-Nov-2014].

[109] "MKU 24 G2 432 USA, Transverter | Kuhne electronic Shop." [Online]. Available: http://shop.kuhne-electronic.de/kuhne/en/shop/amateur-radio/converter-transverte/transverter/MKU+24+G2+432+USA++Transverter/?card=1023. [Accessed: 27-Nov-2014].

[110] Kabakchiev, K., Daniel, L., Hoare, E.G., Gashinova, M., Sizov, V., and Cherniakov, M., "Sea Barrier - Selex Report," Microwave Integrated Systems Laboratory, School of Electrical, Electronic and Computer Engineering, University of Birmingham, UK., Final Report Draft, 2011.

[111] "GoPro Official Website - Capture + share your world." [Online]. Available: http://gopro.com/. [Accessed: 27-Nov-2014].

[112] "Nikon UK." [Online]. Available: http://www.europe-nikon.com/en_GB/. [Accessed: 27-Nov-2014].

[113] "Home - Canon UK." [Online]. Available: http://www.canon.co.uk/. [Accessed: 27-Nov-2014].

[114] "MATLAB - The Language of Technical Computing - MathWorks United Kingdom." [Online]. Available: http://uk.mathworks.com/products/matlab/. [Accessed: 27-Nov-2014].

[115] V. Sizov, C. Hu, M. Antoniou, and M. Cherniakov, "Vegetation clutter spectral properties in VHF/UHF bistatic doppler radar," in *IEEE Radar Conference, 2008. RADAR '08*, 2008, pp. 1–6.

[116] Pedenko, Yu. A. and Razskazovsky, V. B., "Multipath Propagation over Sea, Radiophysical study of the World Ocean," in *Proceedings of IRE AN USSR*, 1992, pp. 2–50.

[117] B. U. Ungan and J. T. Johnson, "Time statistics of propagation over the ocean surface: a numerical study," *IEEE Trans. Geosci. Remote Sens.*, vol. 38, no. 4, pp. 1626–1634, Jul. 2000.

[118] L. L. Cam, "Maximum Likelihood: An Introduction," *Int. Stat. Rev. Rev. Int. Stat.*, vol. 58, no. 2, p. 153, Aug. 1990.

[119] J. V. Toporkov and M. . Sletten, "Statistical Properties of Low-Grazing Range-Resolved Sea Surface Backscatter Generated Through Two-Dimensional Direct Numerical Simulations," *IEEE Trans. Geosci. Remote Sens.*, vol. 45, no. 5, pp. 1181–1197, May 2007.

[120] Kabakchiev, K., Daniel, L., Gashinova, M., Sizov, V., and Cherniakov, M., "Radar Parameters Influence on the Clutter in Maritime Forward Scatter Radar," in *Manuscript submitted for publication in EuRad*, Rome, Italy, in press.

[121] F. R. Met Office, "Factsheets," *Met Office*, 18-Jan-2011. [Online]. Available: http://www.metoffice.gov.uk/learning/library/publications/factsheets. [Accessed: 06-Nov-2014].

[122] J. D. Parsons, *The Mobile Radio Propagation Channel, 2nd Edition*, 2nd Edition edition. Chichester : New York: Wiley-Blackwell, 2000.

[123] T. S. Rappaport, *Wireless Communications: Principles and Practice*, 2 edition. Upper Saddle River, N.J: Prentice Hall, 2001.

[124] V. Sizov, M. Cherniakov, and M. Antoniou, "Forward scattering radar power budget analysis for ground targets," *IET Radar Sonar Navig.*, vol. 1, no. 6, pp. 437–446, Dec. 2007.

[125] V. Sizov, M. Gashinova, N. Zakaria, and M. Cherniakov, "VHF communication channel characterisations over complex wooded propagation paths with applications to ground wireless sensor networks," *IET Microw. Antennas Propag.*, vol. 7, no. 3, pp. 166–174, Feb. 2013.

[126] "Standard Gain Microwave Horn," *Flann Microwave*. [Online]. Available: http://www.flann.com/Products_Home/Antennas/Standard_Gain/standard_gain.html. [Accessed: 27-Nov-2014].

[127] "Ranger 290 Inflatable dinghy | Seago Yachting." [Online]. Available: http://www.seagoyachting.co.uk/ranger-290-p-26.html. [Accessed: 04-Aug-2015].

[128] "USB 8 Simultaneous 16-Bit Analog Inputs and 8 Digital I/O DAQ Device - Measurement Computing." [Online]. Available: http://www.mccdaq.com/usb-data-acquisition/USB-1608FS.aspx. [Accessed: 05-Aug-2015].

Appendix A: Hardware Development

Hardware development 2009

The main goal of this equipment development was to create MISL's first low grazing angle maritime FSR which could be used for testing in maritime environment and demonstrate that the radar could be used for detection of difficult small targets (such as small inflatable boat and Jet Ski) in relatively rough sea conditions. A block diagram of the first MISL's low grazing angle maritime FSR is shown on Figure A1.

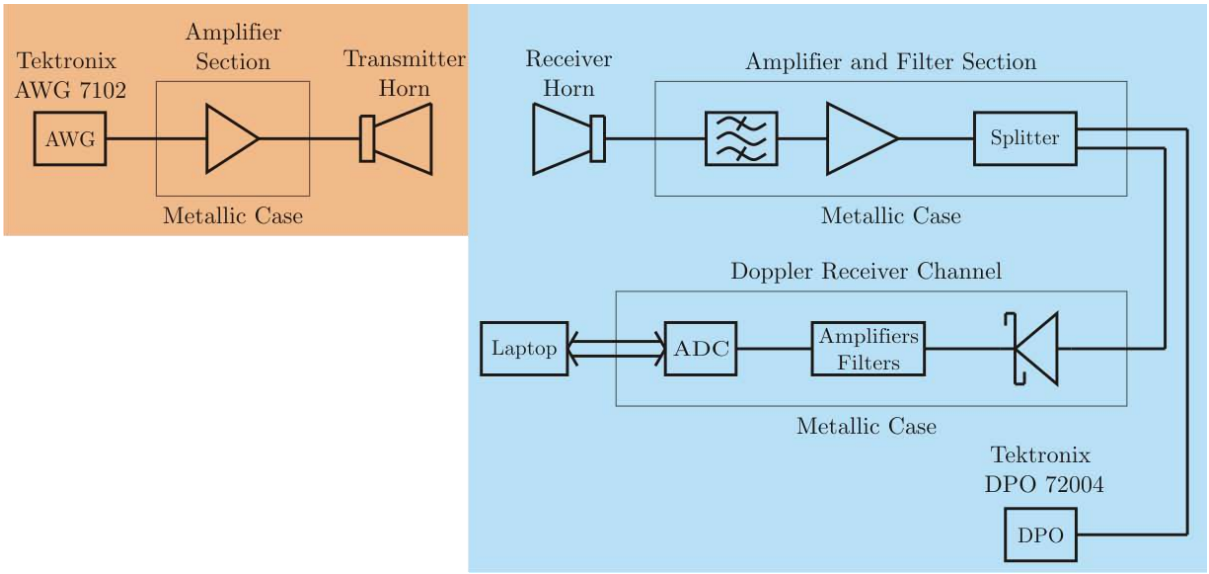

Figure A1 Block diagram of experimental system for FSR data gathering

The first experimental system used Tektronix Arbitrary Waveform Generator AWG7102 as transmitting source (Figure A2). The suite of waveforms programmed into the AWG for experimental use consisted of a 7.5 GHz CW signal and a 100 MHz, 1 GHz, 2 GHz and 3 GHz bandwidth Gaussian modulated pulse centred at 7.5 GHz [42], [43].

The receiver provided two RF output channels, the first to capture the received raw RF pulsed signals, the second supplies the Doppler receiver channel (DRC). Raw data capture was

accomplished through the use of a Tektronix Digital Phosphor Oscilloscope DPO72004, with a 50GS/s sample (Figure A2). A deep memory enables minutes of pulse signals to be recorded for subsequent analysis. The second RF channel in the radar receiver fed the Doppler processor to allow simultaneous capture of Doppler data on a PC along with the raw RF signal in the oscilloscope [42], [43].

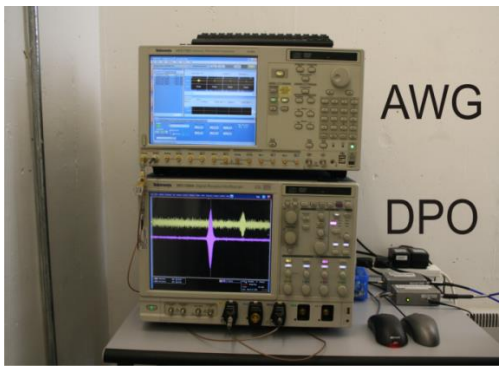

Figure A2 Tektronix DPO 72004 digital phosphor oscilloscope for raw data acquisition and AWG7102 arbitrary waveform generator for waveform generation

A low noise, radar receiver with 60 dB gain was developed along with a transmit amplifier. The receiver and transmitter are shown in Figure A3 with 20dB standard gain horn antennas attached. A set of broader (±30°) azimuthal beamwidth sectoral horns, with narrow (±6°) elevation beamwidth have also been developed. These were designed to allow short range testing, where the physical antenna beamwidth of the standard horns is narrower.

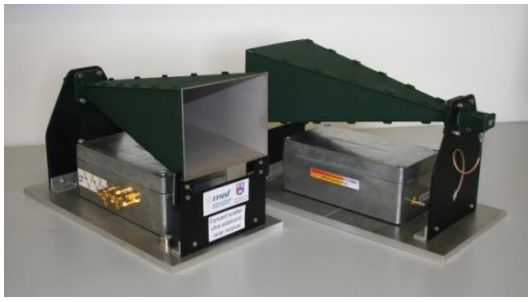

Figure A3 MK1 Transmitter and Receiver units

This thesis is focussed on the CW mode of the system and Pulse signals will not be discussed.

Transmit and receive hardware

The forward scatter radar hardware is comprised of two units, the transmitter and the receiver, based on a common mechanical design.

The transmit and receive hardware was developed through a series of iterations. The initial low gain design was used to perform short range measurements in the anechoic chamber. Subsequently, longer range measurements required more receiver gain, finally the units were provided with simultaneous RF and Doppler measurement capability and additional transmit power.

Mechanical design

The radar units are built on a 10 mm thick solid aluminium baseplate. This is tapped 5/8 inch BSW (standard tripod thread) in the centre of mass to accommodate a tripod support. The antenna fixtures and electronics box fixings are tapped 4 mm and 5 mm respectively directly into the baseplate.

The electronics enclosures are waterproof aluminium diecast boxes screwed to the baseplate with sealed SMA connectors for input and output. All fixing nuts, bolts and washers are stainless steel.

The antenna supports are aluminium plates designed to enable the horn antennas to be mounted to produce either vertical or horizontal polarisation shown on Figure A3. This is achieved by removing the two front clamps and the four throat bolts, rotating the horn and reseating the aperture into the front support, replacing the front clamps and the throat bolts.

An alternative option comprises a heavy duty bracket which allows the entire transmitter or receiver assembly to be rotated trough 90° and re-mounted on the tripod. This is the preferred field option as no antenna dismantling is required. The antennas are connected by semi-rigid coaxial leads terminated in SMA connectors.

Electronic design Transmitter

The transmit amplifier architecture employed two wideband microwave amplifiers and a bias T. The preamplifier is a Minicircuits ZX60-14012L and the power amplifier is a Mini Circuits ZVA 183+. Overall gain is 30 dB. Maximum output power (1 dB compression) is 24 dBm. 3dB attenuators are used as pads between the amplifiers to improve matching and stability.

To reduce the number of connectors and cables in the system the operating 12V DC (400 mA) power is supplied along with the RF signal, via the RF input connector. The DC component is removed by a bias T within the enclosure to provide the DC power to operate the transmitter amplifiers.

The transmitter may also be used as a standalone general purpose microwave amplifier of 30dB gain, from 700 MHz-18 GHz, with 24 dBm output power capability (1 dB compression point) if required. 0dBm drive is required and is available from the arbitrary waveform synthesizer at 7.5 GHz (this allows for losses in the bias Ts, connectors and cable from the AWG to the transmitter).

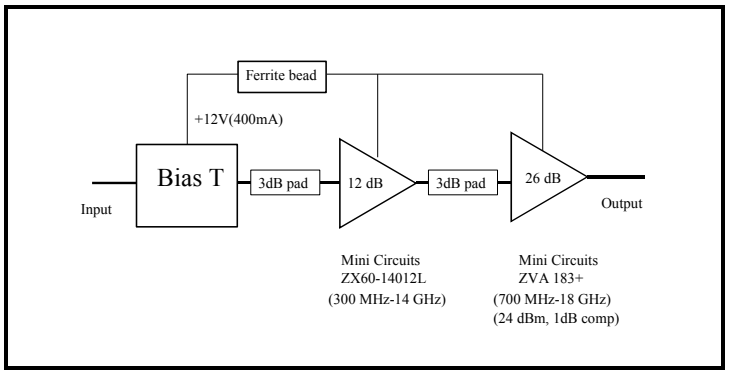

Figure A4 Transmitter block diagram

MK3 Receiver

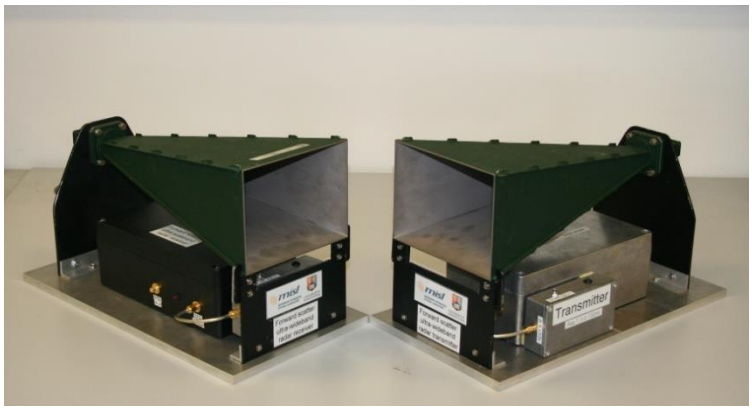

Figure A5 MK3 Transmitter & Receiver units

To reduce the number of connectors and cables in the system the operating 12V (250 mA) DC power is supplied via the RF output connector along with the RF output signal. The DC component is removed by a bias T within the enclosure to power the receiver.

The MK3 receiver (MK2 was an interim intermediate gain receiver design) comprises a Hittite HMC-C001 low noise, 2-20 GHz, amplifier, followed by four additional Hittite HMC-001 amplifiers (Figure A5).

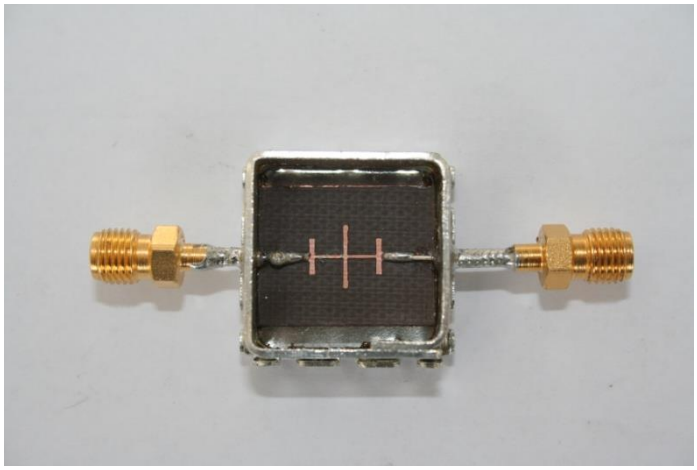

Figure A6 Microstrip low pass filter designed using CST, 9 GHz cut-off frequency

Frequency limiting is achieved by the use of a Mini Circuits VHF 4400+ 4.4GHz high pass filter and a 9 GHz low pass filter (Figure A6) designed using CST Studio Suite 2010 [106] and built by Mr. Liam Daniel [42], [43]. A Mini Circuits 2-way splitter was used to supply separate Doppler channel and RF channel outputs to enable simultaneous data collection from both channels. The bias T is fed via the main RF output channel connector, the Doppler channel has a DC block. The lid of the enclosure is lined with RAM foam to prevent the possibility of instability with the high level of gain used.

A RF monitor output is provided at the side of the receiver enclosure via an SMA connector. This port provides 40B gain and was used for real time RF spectrum analysis during trials to assess interference signals. When not used this is terminated with a 50 ohm load. A detailed block diagram of the MK 3 receiver is provided on Figure A7 and on Figure A8 a photo of the equipment has been shown [42].

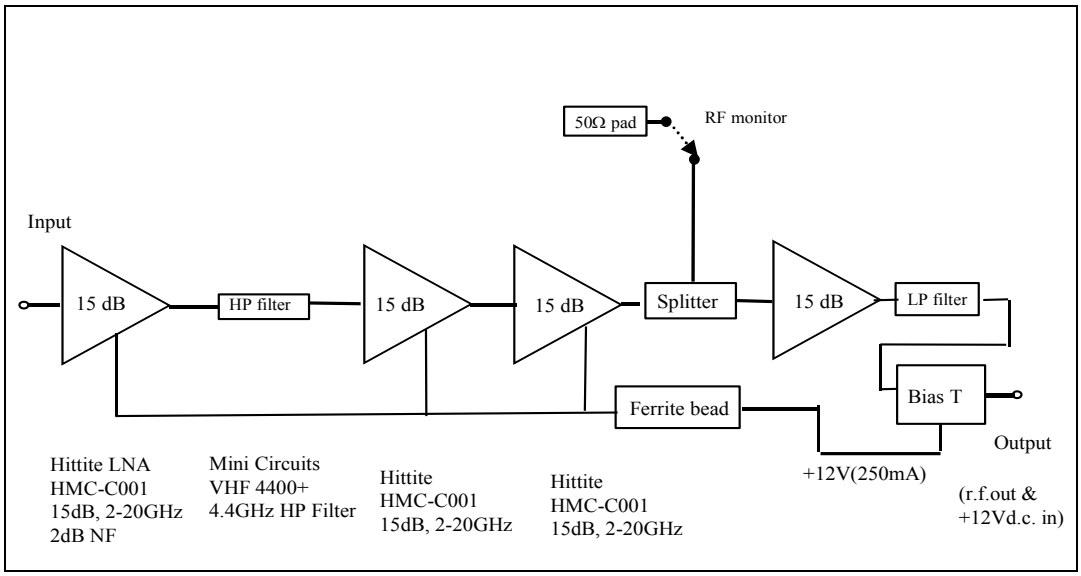

Receiver block diagram

Figure A7 MK 3 Receiver block diagram

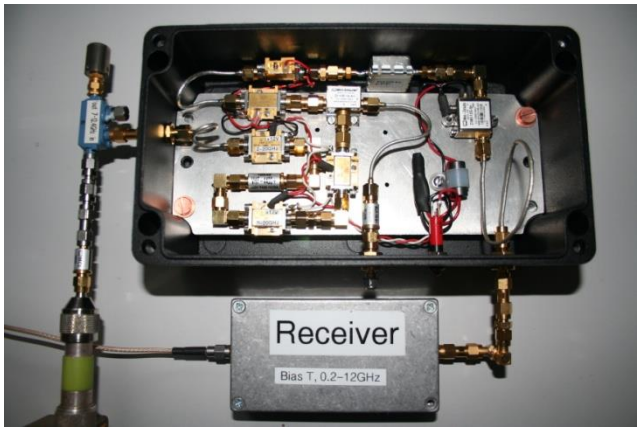

Figure A8 MK3 receiver hardware

The final iteration of hardware design incorporated identical wide beamwidth horn antennas and marine radar notch filters (cavity band-pass filters at 9.3 GHz), as shown in Figure A9. Design of the antennas and filters will be discussed in the following sections of this chapter.

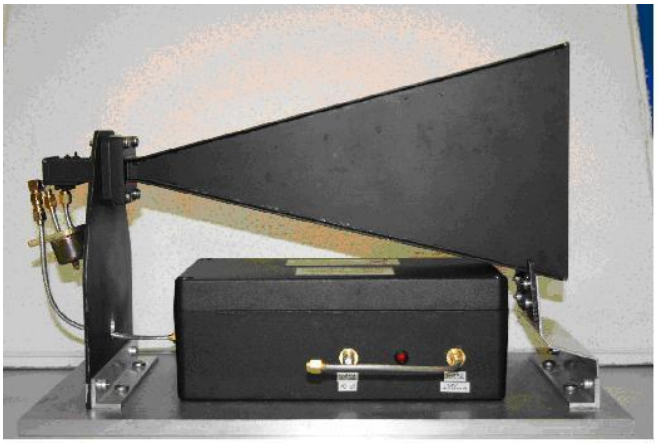

Figure A9 MK3 receiver with wide beam horn and marine radar filter

Doppler receiver channel (DRC)

The Doppler receiver consists of a microwave detector diode, programmable amplification and programmable band pass filtering followed by an ADC for storage of data via USB and also digital control of the adjustable Doppler filter bandwidth and amplifier gains (adjustable from 20 to 80dB). The detector has two output channels, a received signal strength indicator (RSSI) and the Doppler signature output [42].

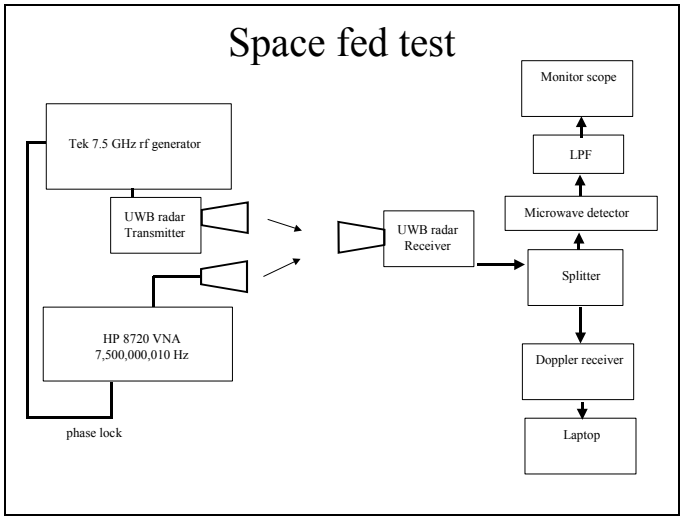

Figure A10 Space fed test of Doppler receiver

To evaluate the operation of the Doppler receiver three separate tests were performed. As a basic test of operation a simple Doppler signature was simulated by amplitude modulating a 7.5 GHz carrier. Secondly, two phase locked synthesizers operating at 7.5 GHz and separated by a very small offset (the offset was varied between 1Hz and 200 Hz) were combined using a microwave combiner and the Doppler frequency detected by the receiver measured. Thirdly to replicate real operation the phase locked synthesizers were fed to antennas and the microwave signals space combined by the receive antenna and the Doppler again was measured and compared with the known offset. All three tests verified the correct operation of the Doppler receiver. Input RF power versus output Doppler amplitude calibrations were also carried out [42].

Marine radar filters

To address the issue of contamination of maritime radars at 9.3 GHz, cavity band-pass filters were designed with deep notches at 9.3 GHz. For CW operation narrow receiver band-pass filters were designed with 40 MHz bandwidth to optimise the signal to noise ratio and an additional deep notch at marine radar frequencies, as shown in Figure A11. For pulse operation receiver band-pass filters have been designed with 100 MHz, 1GHz and 3GHz bandwidth to optimise the signal to noise ratio and the additional deep notch at marine radar frequencies has been included as explained in [42].

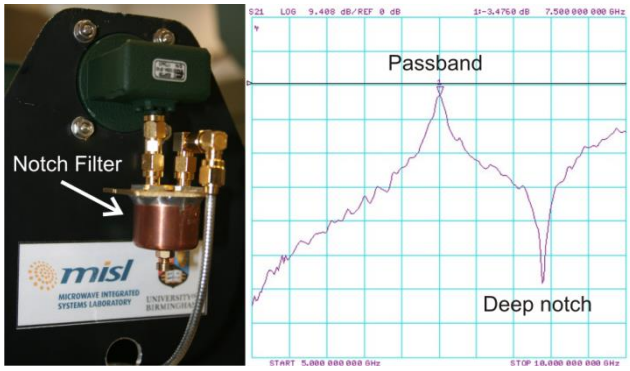

Figure A11 Cavity band pass filter fitted to receiver antenna, and measured performance

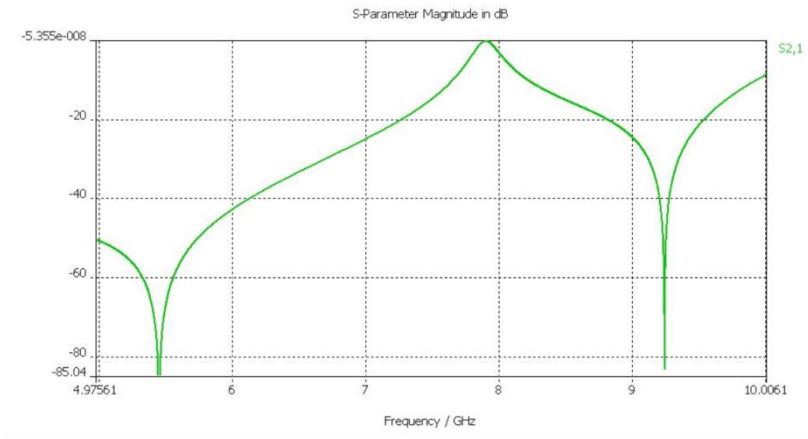

Figure A12 CST simulation of the cavity band pass filter shown in Figure A11

Antenna design and manufacture

Two Standard gain horn antennas Series 240 have been purchased by company called 'Flann'. The used model 15240 shown on Figure A5 has frequency range 6.58 to 10 GHz with standard mid band gain of 20 dB [126]. The Flann antennas have 20 degrees beamwidth in both planes.

At very short ranges the physical beamwidth of the commercially available standard gain horn test antennas used in the prototype measurement system exceeds the pseudo-beamwidth (first ellipse) and therefore sectoral horns with wide azimuth (±30°) and narrow elevation beamwidth (±6°) were designed and made by Dr. E. Hoare [42] in order to make short range measurements (Figure A13 and Figure A14). These antennas (named later in the thesis as 'Wide' antennas)

were also used to enable measurements to be made with antenna characteristics closer to omnidirectional antennas than the high gain horns. These antennas were designed to have beamwidth of ±6° in the elevation plane and ±30° in the azimuth plane.

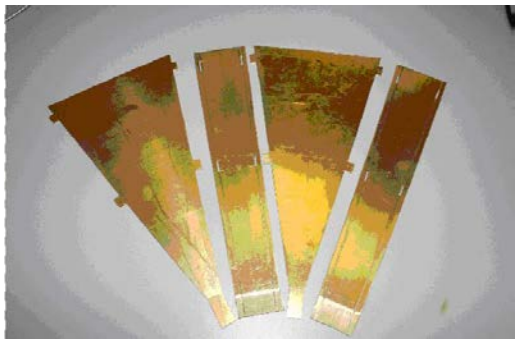

Figure A13 Brass components of the wide beamwidth horn antennas

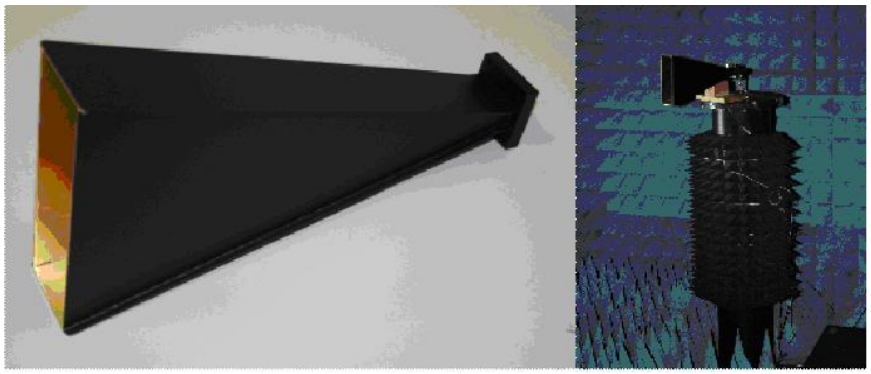

Figure A14 Completed horn and measurement in the anechoic chamber

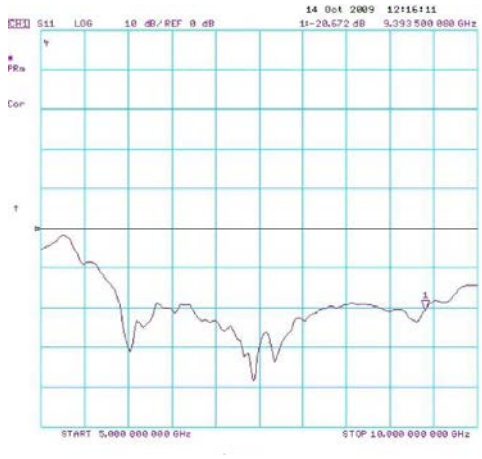

Figure A15 Measured S11 of the final horn (No2) antenna

Omnidirectional antennas have been designed and manufactured by Dr. Vladimir Sizov. The antennas are shown on Figure A16. Measured voltage standing wave ratio (VSWR) of two samples of the antenna are shown in Figure A17.

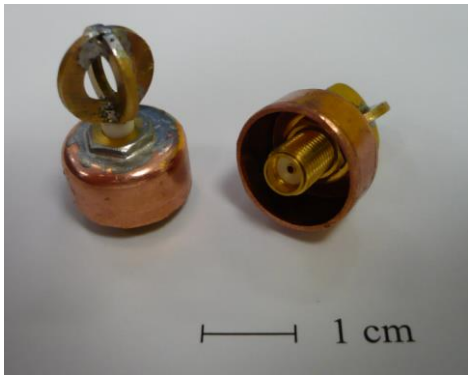

Figure A16 Omnidirectional antennas

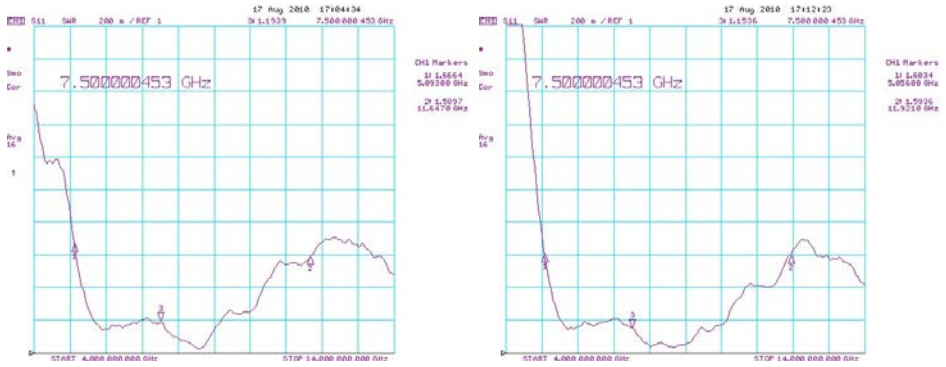

a) b)

Figure A17 Antenna #1 VSWR a) and #2 VSWR b)

The antennas have around 8 GHz bandwidth (from 4.5 GHz to 11.5GHz) at VSWR<1.6, and VSWR<l.25 in working band 6-9GHz. The tests of antenna's beamwidth were simulated by CST Studio Suite 2010. The simulated antenna patterns for different frequencies are presented in Figure A18.

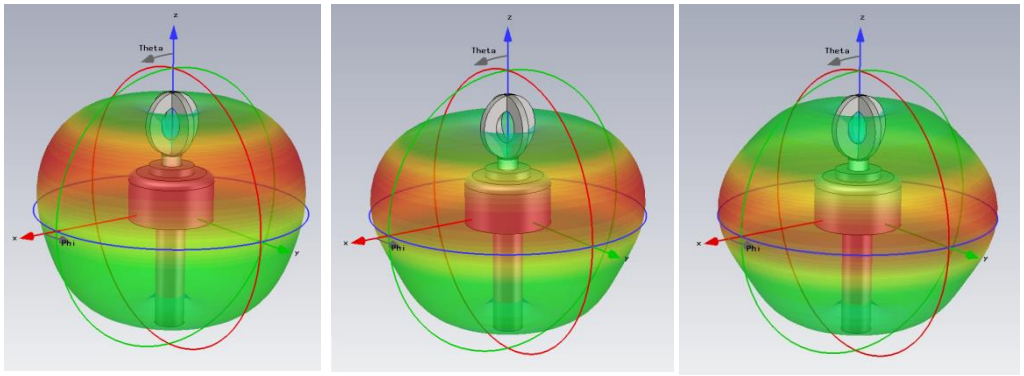

6GHz 7.5GHz 9GHz

Figure A18 Antenna simulated pattern

The antenna have an omnidirectional pattern in azimuth plane and slightly deflected one in elevation. Estimated antenna gain is presented in Table A1.

Table A1 Antenna gain

Frequency, GHz	Maximal gain, dB/at elevation	Gain in zero elevation, dBi
6	2.26/22°	0.82
7.5	2.9/10°	2.2
9	2.8/5°	2.6

Measured antenna pattern is shown in Figure A19, which coincides very well with simulated results.

So, we can assume that antenna has about 0dB gain at 7.36 GHz and perfect omnidirectional pattern.

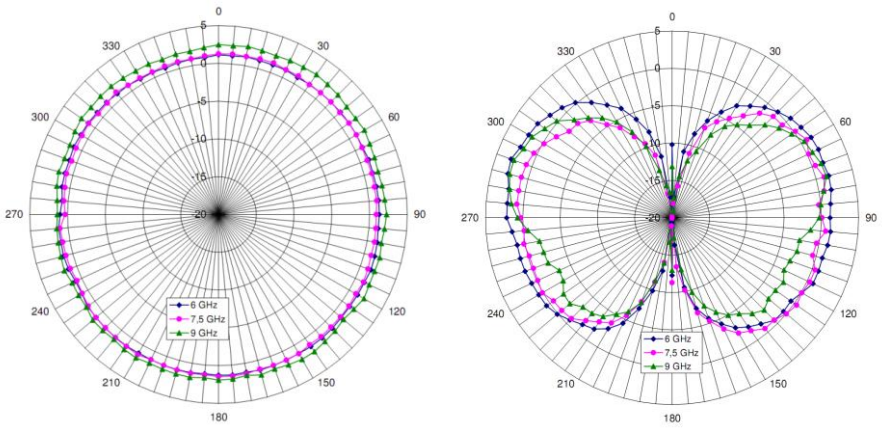

a) b)

Figure A19 Measured antenna pattern in azimuth (a) and in elevation (b)

Hardware development 2010

An obvious drawback of the described FSR equipment was its size. The AWG and DPO shown on Figure A2 are considerably big and heavy and they both require a petrol generator as a

power source. This was making transportation and setting up of the equipment a difficult procedure. Neither the AWG nor the DPO are waterproof which is creating another obstacle for using them in outdoors experiments close to maritime environment. Also in order to be able to create the desired FSR equipment on sea based platform as discussed in Chapter 1, MISL's team needed to develop a portable substitute of the bulky Oscilloscope and Wave generator which automatically excludes the use of petrol generators.

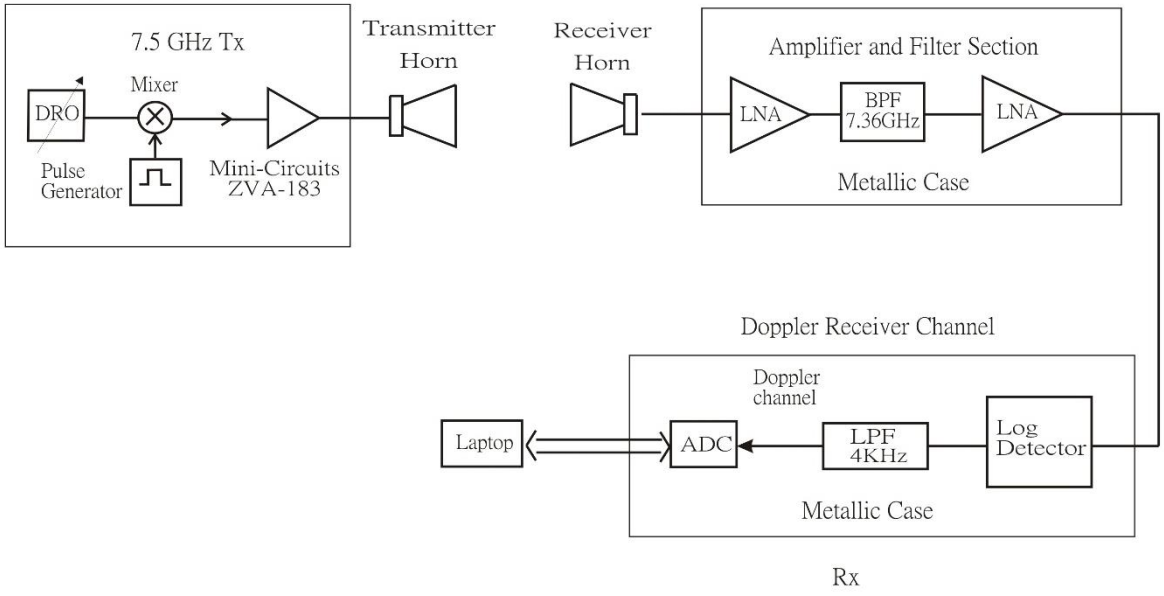

Figure A20 Block diagram of the upgraded 7.5 GHz FSR

As a consequence in 2010 a new portable, low cost wave generator was developed by Dr. E. Hoare and after sequence of test it replaced the Tektronix Arbitrary Waveform Generator AWG7102. Figure A20 shows the block diagram of the upgraded transmitter and receiver module of the FSR system. The transmitter works in 7.5 GHz CW mode and also in 30 MHz, 100 MHz and 1 GHz bandwidth Gaussian modulated pulse centred at 7.5 GHz. A hardware switch is used for changing the transmitting bandwidths and pulse repetition frequencies (PRF) shown on Figure A21.

Figure A21 7.5 GHz Wave generator box

Figure A22 presents the new portable transmitter equipment during experiments in Lake Coniston lake, UK. The fuel generator for the AWG has been replaced with small 12V battery supply.

Figure A22 The new FSR transmitter during measurements on Coniston Water Lake

Hardware development 2011-2012 – 7.5 GHz and 24 GHz Test equipment

The current portable design of the 7.5 GHz equipment used for trials during 2012 is shown in Figure A23. The transmitter and receiver have been redesigned to fit in portable, watertight, crushproof and dustproof cases 'Pelican 1500'. Lightweight 12V lithium-polymer batteries are used as power supply in each case - each battery pack has a 22Ah capacity. A heatsink pad and metal plate have been located underneath the equipment for reducing the temperature inside the cases. Grommets have been placed to let the SMA cables outside. A pole holder has been installed on the transmitter box which allowed mounting an omni-directional antenna on the top of an adjustable pole shown on Figure A23.

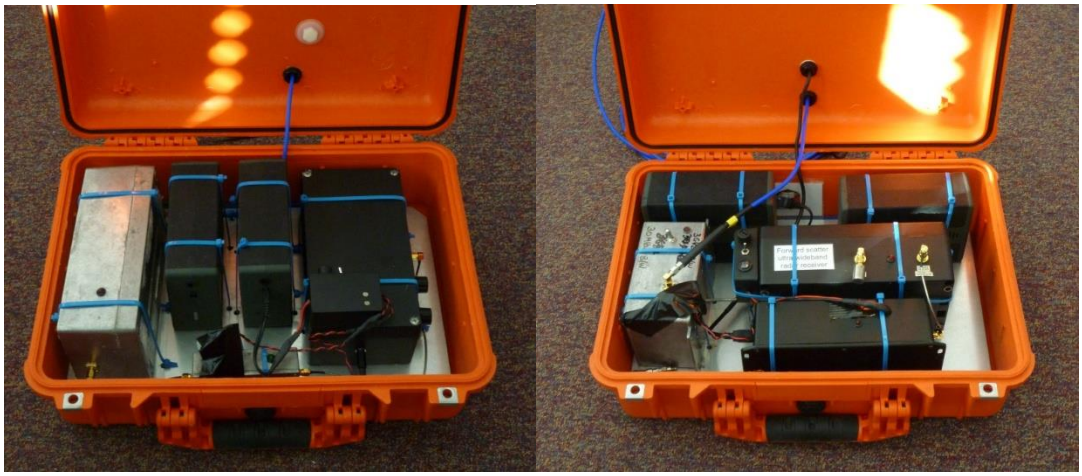

Figure A23: Upgraded 7.5 GHz prototype transmitter (on the left) and receiver (on the right)

- **Buoy Mounted 7.5 GHz Transmitter Equipment**

During improvement and reconstructions of the equipment, MISL invested time in finding a solution to mount the radar on a Buoy [110]. The procurement of a standard maritime buoy posed logistic and financial issues. So after much consideration a buoy substitute was developed in a form of a 60 inch Ringo tube, which is shown on Figure A24.

Figure A24 7.5 GHz transmitter mounted on a 60 inch Ringo. Attached are 2 anchors with 40m. of rope on each

Appendix B: MISL inflatable boat

Microwave integrated system laboratory acquired a small inflatable boat SeaGo Ranger 290 [127] and a 9.9 HP Mariner FourStroke engine in order to perform all the maritime experiments and to have a reference target throughout all the sea/ocean based measurements. The MISL's inflatable boat dimensions are presented on Figure B2 and a photograph of the boat during one of the measurements is shown on Figure B1.

Figure B1 MISL's inflatable boat during maritime test trials

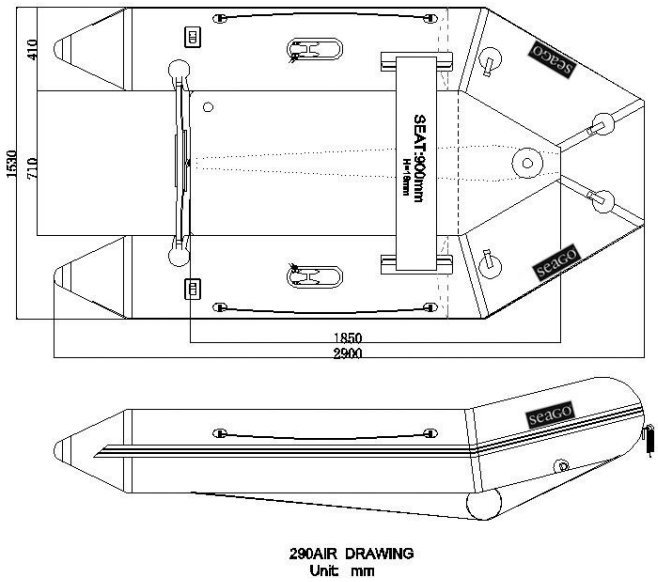

Figure B2 Dimensions of the SeaGo Ranger 290

Appendix C: ADC USB-1608FS

The same ADC USB-1608FS [128] has been used in both 7.5 GHz and 24 GHz radar equipment. The specifications of the hardware are included underneath and further information could be found on their website.

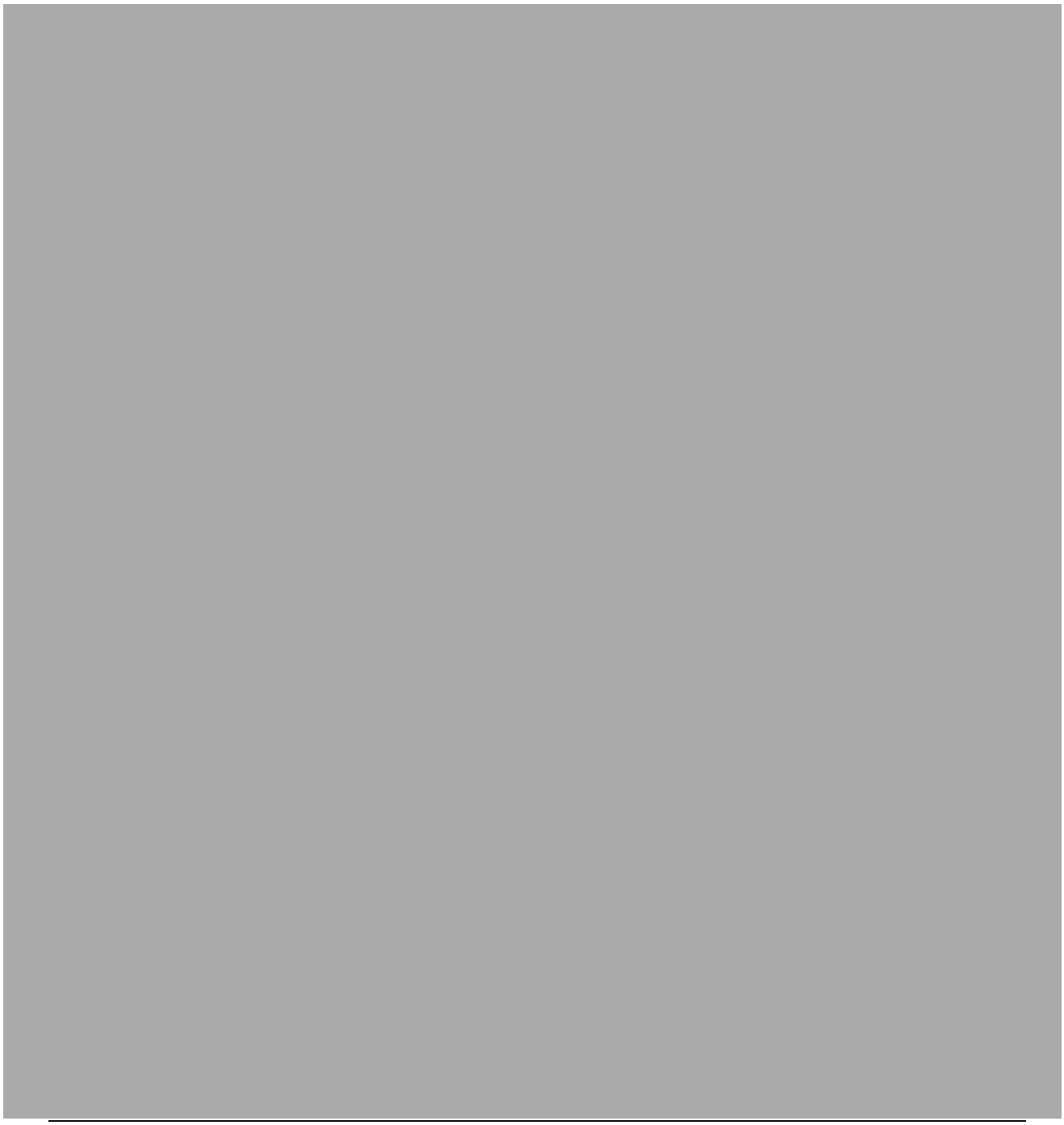

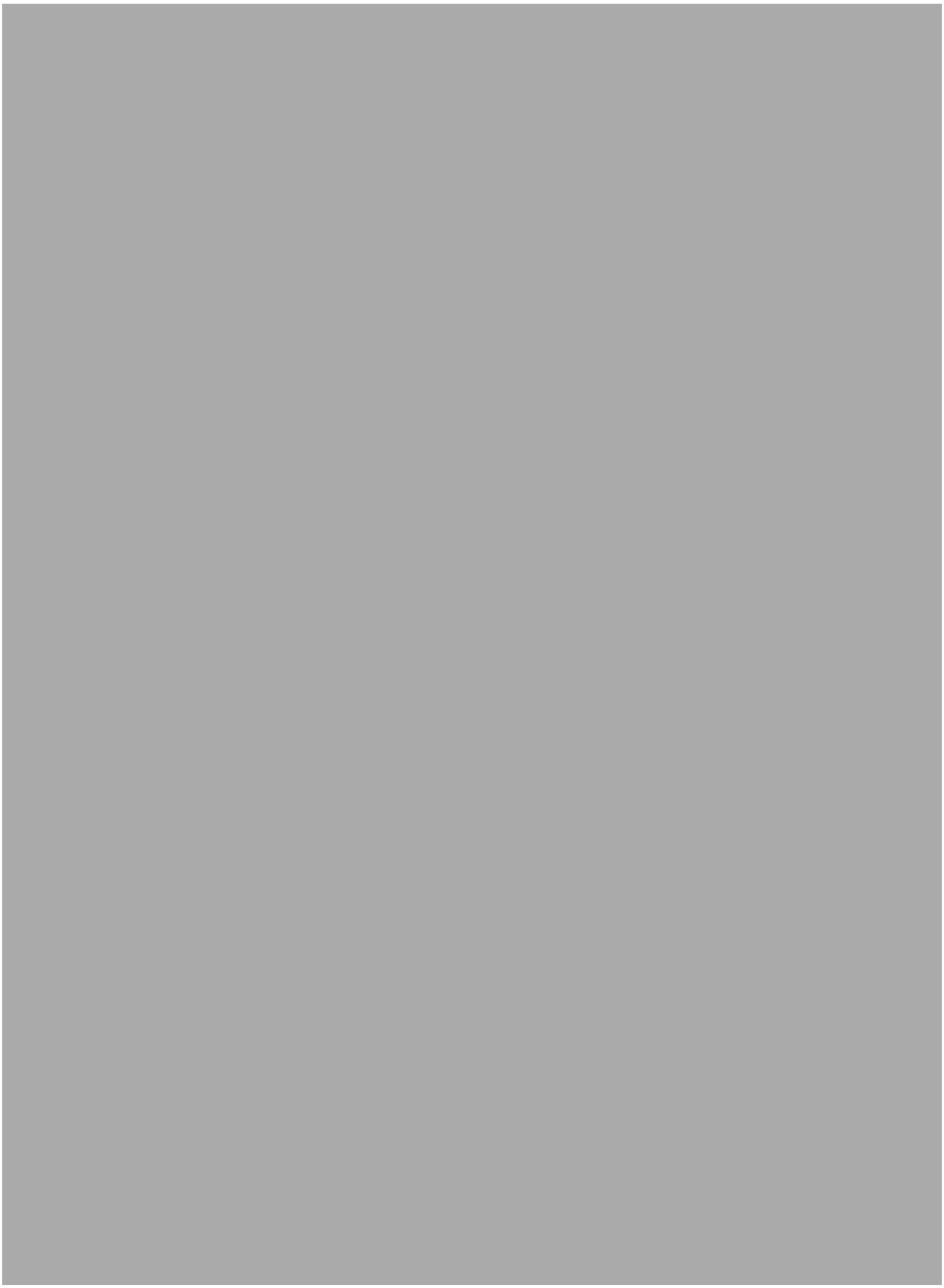

Appendix D: Publications

List of Authored/Co-authored Publications

1. K. Kabakchiev, L. Y. Daniel, V. Sizov, E. Hoare, M. Gashinova, and M. Cherniakov, "Received signal characterization in forward scatter radar for maritime application," in *Radar Symposium (IRS), 2011 Proceedings International*, 2011, pp. 67–72.

2. M. Gashinova, L. Daniel, K. Kabakchiev, V. Sizov, E. Hoare, and M. Cherniakov, "Phenomenology of signals in FSR for surface targets detection," in *IET International Conference on Radar Systems (Radar 2012)*, 2012, pp. 1–6.

3. E. G. Hoare, L. Y. Daniel, M. Gashinova, K. Kabakchiev, V. Sizov, M. Cherniakov, V. B. Razskazovsky, G. I. Khlopov, S. I. Khomenko, and V. E. Morozov, "Near zero grazing angle forward-scatter sea clutter measurement spectrum analysis," in *IET International Conference on Radar Systems (Radar 2012)*, 2012, pp. 1–4.

4. M. Gashinova, L. Daniel, E. Hoare, V. Sizov, K. Kabakchiev, and M. Cherniakov, "Signal characterisation and processing in the forward scatter mode of bistatic passive coherent location systems," *EURASIP Journal on Advances in Signal Processing*, vol. 2013, no. 1, p. 36, Feb. 2013.

5. K. Kabakchiev, L. Y. Daniel, E. G. Hoare, M. Gashinova, and M. Cherniakov, "Near zero grazing angle forward-scatter sea clutter measurement statistical properties," in *Radar Symposium (IRS), 2013 14th International*, 2013, vol. 2, pp. 620–624.

6. M. Gashinova, L. Daniel, E. Hoare, K. Kabakchiev, M. Cherniakov, and V. Sizov, "Forward scatter radar mode for passive coherent location systems," in *2013 International Conference on Radar (Radar)*, 2013, pp. 235–239.

7. M. Gashinova, K. Kabakchiev, L. Daniel, E. Hoare, V. Sizov, and M. Cherniakov, "Measured forward-scatter sea clutter at near-zero grazing angle: analysis of spectral and statistical properties," *IET Radar, Sonar Navigation*, vol. 8, no. 2, pp. 132–141, Feb. 2014.

8. K. Kabakchiev, L. Daniel, M. Gashinova, E. Hoare, M. Cherniakov, and V. Sizov, "Radar parameters influence on the clutter in maritime forward scatter radar," in *European Radar Conference (EuRAD), 2014 11th*, 2014, pp. 113–116.

Publications Related to This Work

1. M. Cherniakov, M. Gashinova, Cheng Hu, M. Antoniou, V. Sizov, and L. Y. Daniel, "Ultra wideband forward scattering radar: Concept and prospective," in *2007 IET International Conference on Radar Systems*, 2007, pp. 1–5.

2. L. Daniel, M. Gashinova, and M. Cherniakov, "Maritime UWB forward scattering radar network: Initial study," in *2008 International Conference on Radar*, 2008, pp. 658–663.

3. L. Daniel, M. Gashinova, and M. Cherniakov, "Maritime target cross section estimation for an ultra-wideband forward scatter radar network," in *Radar Conference, 2008. EuRAD 2008. European*, 2008, pp. 316–319.

4. L. Y. Daniel, E. G. Hoare, M. Gashinova, A. Svintsov, M. Cherniakov, and V. Sizov, "Ultra-wideband forward scatter radar fence for maritime surveillance: Initial experimental results," in *2010 IEEE Radar Conference*, 2010, pp. 526–531.

5. M. Gashinova, L. Daniel, V. Sizov, E. Hoare, and M. Cherniakov, "Phenomenology of Doppler forward scatter radar for surface targets observation," *IET Radar, Sonar Navigation*, vol. 7, no. 4, pp. 422–432, Apr. 2013.